Increased lifetime of Organic Photovoltaics (OPVs) and the impact of degradation, efficiency and costs in the LCOE of Emerging PVs

BALDER ADAD NIETO-DIAZ

Increased lifetime of Organic Photovoltaics (OPVs) and the impact of degradation, efficiency and costs in the LCOE of Emerging PVs

Balder Adad Nieto-Díaz

A Thesis presented for the degree of

Doctor of Philosophy

Department of Engineering

Durham University

September 2021

Dedicated to my mother, the bravest and most loving woman I know.

Gracias por todo amá, te amo!

ABSTRACT

Increased lifetime of Organic Photovoltaics (OPVs) and the impact of degradation, efficiency and costs in the LCOE of Emerging PVs

Balder Adad Nieto-Díaz

Emerging photovoltaic (PV) technologies such as organic photovoltaics (OPVs) and perovskites (PVKs) have the potential to disrupt the PV market due to their ease of fabrication (compatible with cheap roll-to-roll processing) and installation, as well as their significant efficiency improvements in recent years. However, rapid degradation is still an issue present in many emerging PVs, which must be addressed to enable their commercialisation. This thesis shows an OPV lifetime enhancing technique by adding the insulating polymer PMMA to the active layer, and a novel model for quantifying the impact of degradation (alongside efficiency and cost) upon levelized cost of energy (LCOE) in real world emerging PV installations.

The effect of PMMA morphology on the success of a ternary strategy was investigated, leading to device design guidelines. It was found that either increasing the weight percent (wt%) or molecular weight (M_W) of PMMA resulted in an increase in the volume of PMMA-rich islands, which provided the OPV protection against water and oxygen ingress. It was also found that adding PMMA can be effective in enhancing the lifetime of different active material combinations, although not to the same extent, and that processing additives can have a negative impact in the devices lifetime.

A novel model was developed taking into account realistic degradation profile sourced from a literature review of state-of-the-art OPV and PVK devices. It was found that optimal strategies to improve LCOE depend on the present characteristics of a device, and that panels with a good balance of efficiency and degradation were better than panels with higher efficiency but higher degradation as well. Further, it was found that low-cost locations were more favoured from reductions in the degradation rate and module cost, whilst high-cost locations were more benefited from improvements in initial efficiency, lower discount rates and reductions in install costs.

TABLE OF CONTENTS

LIST OF FIGURES

LIST OF TABLES

LIST OF ABBREVIATIONS

AFM	atomic force microscopy
AM	air mass
AUS	Australia
a-Si	amorphous silicon
B	burn-in
BHJ	bulk-heterojunction
BRA	Brazil
c-Si	crystalline silicon
D	degradation rate
D-A	donor-acceptor
DCR	discount rate
EF	fermi level
EFL	Energy Fiji Limited
ESP	Spain
ETL	electron-transporting layer
E_b	exciton binding energy
E_g	energy band gap
FF	fill factor
GA	genetic algorithm
GBR/UK	United Kingdom
HJ	heterojunction
HOMO	highest occupied molecular orbital
HTL	hole-transporting layer
IND	India
ISOS	International summit on OPV stability
JPN	Japan
J_{sc}	short-circuit current
JV	current density-voltage
kWh	kilowatt hour

LCOE	levelized cost of energy
LUMO	lowest unoccupied molecular orbital
M_W	molecular weight
NPV	net present value
OPV	organic photovoltaic
PCE	power conversion efficiency
PCE_B	post burn-in efficiency
PCE_i	initial efficiency
PHJ	planar-heterojunction
PV	photovoltaic
PVK	perovskite
RH	relative humidity
SEM	scanning electron microscopy
Si	silicon
T_{S80}	stabilised lifetime
USA	United States of America
UV-vis	ultraviolet visible
V_{OC}	open-circuit voltage
Wp	watt peak
wt%	weight percent
ZAF	South Africa

DECLARATION

The work in this thesis is based on research carried out in the Engineering Department of Durham University. I hereby declare that the work carried out in this thesis has not been previously submitted for any degree and is not currently being submitted in candidature for any other degree, and it is all my own work unless otherwise mentioned in the text. Parts of this work have been published as detailed in the list of publications and conferences section.

Balder Adad Nieto-Díaz

September 2021

STATEMENT OF COPYRIGHT

LIST OF PUBLICATIONS AND CONFERENCES

Publications

- Nieto-Díaz, B. A., et al. (2021). "Enhanced lifetime of organic photovoltaic diodes achieved by blending with PMMA: Impact of morphology and Donor:Acceptor combination." **Solar Energy Materials and Solar Cells** Volume 219, Page 110765. https://doi.org/10.1016/j.solmat.2020.110765.
- Nieto-Díaz, B. A., et al. (2021). "A levelized cost of energy approach to select and optimise emerging PV technologies: The relative impact of degradation, cost and initial efficiency." **Applied Energy** Volume 299, Page 117302. https://doi.org/10.1016/j.apenergy.2021.117302.

In preparation

- Nieto-Díaz, B. A., et al. (2022). "How does location determine the economic competitiveness of grid-scale Emerging PV?" **Energy Technology** (submitted in Nov 2021).
- Gonabadi, H., Yadav, A., Nieto-Díaz, B.A., Groves, C., Bull, S. (2022). "Mechanical Testing of organic semiconductor films for flexible devices".

Conferences

- Nieto-Díaz, B. A., et al. (2019). "Organic Photovoltaic blends diluted with inert polymers for enhanced lifetime: Impact of blend microstructure and processing additives" **nanoGe Fall Meeting**, Germany.
- Nieto-Díaz, B. A., et al. (2020). "Emerging Photovoltaics Levelized Cost of Energy: Impact of Initial Efficiency, Degradation and Module Cost" International Conference on Renewable Energy (**ICREN**), Italy (online conference).
- Nieto-Díaz, B. A., et al. (2021). "Emerging Photovoltaics levelized cost of energy: Impact of initial efficiency, degradation and module cost" Innovations in Large-Area Electronics (**innoLAE**), UK (online conference).

ACKNOWLEDGEMENTS

I give thanks to God for answering my prayers about my wish to study a postgraduate degree in England, it was certainly not an easy task but I know he never leaves me alone. Many thanks to CONACYT-SENER and all the people in Mexico involved with granting me a scholarship, the work done in this thesis would have not been possible without all the resources provided by the Mexican administration.

My most sincere thanks to Dr. Chris Groves for being my mentor since day one in Durham University, always having time to discuss my research, for giving me constant advice, writing tips and quick feedback whenever I asked for it, but specially for being a comprehensive supervisor and a leader who would push me to increase my academic level. Special thanks to Dr. Christopher Pearson for sharing his technical knowledge, helping me with several laboratory measurements throughout the first part of my PhD, and for his patience when teaching me something or helping to solve an issue related to laboratory equipment.

Thanks to Dr. Michael Cooke, Amy Tate and everyone involved in keeping the clean room in the best possible conditions to work. Thanks to all my colleagues in the Engineering department, especially to Dr. Mujeeb for his advice and support, and David Palacios for always desiring to work together and being truly a friend, I highly appreciate all the time we spent together during and after working hours. I also thank Andrew Crossland and Cai Williams for their collaboration during the second half of my PhD.

I thank my former professors of the Instituto Tecnológico de Nuevo Laredo for their teachings and motivating me to pursue a postgraduate degree abroad. Special thanks to Dr. César Contreras Faz, Dr. Gustavo Rojo and Dr. Daniel Olivares for their advice and support in my scholarship candidature.

I would like to thank all my friends in Mexico for keeping in touch and cheer for me from the distance, and to all the friends I met during my time in Durham for all the experiences we shared and making these some of the best years of my life. Thanks to The Pollers (David, Diego & Pepe) for all the laughs and amazing memories, including all the trips and Friday pizza-gaming sessions. Thanks to my amigue Itzel

for everything we shared during the first part of the pandemic, it was really fun living together. Many thanks to Javier, my best friend in the world, for continuing to strengthen our friendship despite the distance and for always understanding me.

I can’t thank my girlfriend Diana enough, but I am extremely grateful with her for being the kindest and most comprehensive person. I thank you amor for always being with me, even in the distance. I thank you for your warm heart and for helping me grow in so many ways. I thank you for all the days and nights we have spent together since I met you. I thank you for everything and I love you!

Finally, I am extremely thankful with my family, it was hard being physically away from them but they were always in my heart and in my thoughts, and I know I was in theirs as well. Thanks to my grandparents Alfredo and Olinda for their advice and teachings based in love, to my brother Eros for always wishing me the best and sharing an amazing childhood together, to my little sister Ari for being the simplest and funniest person, you are and will always be the girl of my life. Thanks to my mother Blanca for being the most loving and bravest woman in the world, and for raising me and my siblings the best way she could. I am the man I am in big part because of you, amá!

CHAPTER 1
INTRODUCTION, OBJECTIVE AND ORGANISATION

1.1 Introduction

Oil, coal, and natural gas-based conventional energy sources have shown to be successful drivers of economic growth in the last century, but they are also harmful to the environment and human health.[1] To tackle the climate change issue "The Paris Agreement" was adopted by 196 countries in 2015, which goal is to limit global warming to well below 2, preferably to 1.5 degrees Celsius, compared to pre-industrial levels.[2] Solar energy harvesting technologies are one of the most appealing ways to address this challenge since solar power is clean, renewable, and abundant.[3] Commercial solar photovoltaic (PV) technology is mainly based on inorganic semiconductors (silicon, cadmium telluride).[4]

Although inorganic photovoltaics are already established technologies, they still present some issues such as high amount of materials required for panels manufacturing, production involving vacuum processing, high installation costs and their rigidity and weight,[3] as well as issues with recycling and use of scarce materials,[5] which makes them unsuitable for some applications. However, emerging PV technologies such as organic photovoltaics (OPVs) and perovskites may be able to cover the remaining inorganic PV gaps by their compatibility with scalable, roll-to-roll manufacture on flexible substrates[6] and the associated benefits of reduced cost.[7] Therefore, emerging PV installations could be very useful not only minimising carbon dioxide (CO_2) emissions, but also powering remote places, considering that ~770 million people in the world do not have access to electricity.[8] Still, a significant remaining challenge in the commercialisation of OPVs and perovskites is achieving an acceptable lifetime,[9] which should be considered alongside with the efficiency and costs of panels and installation to assess the viability of emerging PV technologies by techno-economic analysis tools such as levelized cost of energy (LCOE) models.

1.2 Thesis Objective

The main objectives of this thesis are to showcase a simple and efficient technique to enhance the lifetime of Organic Photovoltaics (OPVs) and to demonstrate the real world impact of degradation using a novel LCOE model to make a quantitative analysis of current state of the art devices, specifically including rapid degradation (burn-in) which is a critical issue in such devices. The lifetime enhancing technique provides materials processing guidance and allows researchers to improve stability of their OPVs while reducing the amount of donor:acceptor material required, thus also reducing cost. In the other hand, the LCOE model allows developers of emerging PV technology to calculate the cost of energy from their technology while taking into account the impact of realistic degradation for the first time, allowing people to see whether the low cost of manufacture outweighs the poor lifetime and low efficiencies that characterise these materials, which is often debated but not quantified.

1.3 Thesis Organisation

The thesis is structured in eight chapters (counting this Introduction Chapter) as follows:

Chapter 2: Background

This chapter presents a brief summary of PV technologies history and main characteristics, followed by a discussion of OPVs operation and its parameters, alongside with economical concepts and factors that need to be considered in PV installations. Chapters 4 and 5 introductory sections expand the discussion on degradation of OPVs and viability of emerging PV panels, respectively.

Chapter 3: Experimental methods

This chapter provides details of the experimental methods and materials used in Chapter 4 lab based experiments. The fabrication processes are explained and illustrated, from the cleaning of substrates to the Al evaporation deposition as the

electrode and final layer of the OPVs, as well as the measuring techniques and laboratory equipment used to characterise the OPVs initial performance and lifetime.

Chapter 4: Enhancing the lifetime of OPVs using a ternary blend strategy

In this chapter, ternary P3HT:$PC_{61}BM$:PMMA and PTB7:$PC_{71}BM$:PMMA devices are fabricated and their lifetime is compared with their binary counterparts (P3HT:$PC_{61}BM$ and PTB7:$PC_{71}BM$). The effect of PMMA on device performance and lifetime is investigated by varying the molecular weight and weight percent of PMMA in the ternary blend. The impact of processing additive DIO is also investigated. Results were published in: Nieto-Díaz, B. A., et al. (2021), Solar Energy Materials and Solar Cells 219.

Chapter 5: LCOE Model Development

This chapter shows the development of a novel LCOE model which is based on degradation characteristics observed in real emerging PV devices for the first time. Unlike other models, this one considers the impact of fast degradation at the beginning of a module's life (burn-in), which is common in emerging PV technologies. Chapters 6-7 results are obtained by using this LCOE model.

Chapter 6: Emerging PV degradation, efficiency and module cost impact on LCOE

This chapter presents for the first time the relative impacts of realistic degradation, initial efficiency and module cost upon LCOE of emerging PV devices in the case study location (Fiji). The competitiveness of specific, state-of-the-art perovskite PV (PVK) and OPV reported in the literature are assessed for a realistic grid-scale PV installation. Additionally, a brief analysis of the emerging PV embodied carbon is presented and compared against silicon (Si) PV. Results were published in: Nieto-Díaz, B. A., et al. (2021), Applied Energy 299.

Chapter 7: Feasibility of Emerging PV at different locations

This chapter presents an LCOE analysis that evaluates the potential of emerging PV technologies in eight different countries all around the world to cover a range of economies and insolation levels. The impacts of PV parameters as well as location specific parameters (e.g. discount rate and install costs) are quantified and allow for comparisons between countries, while showcasing their ideal optimisation strategies.

Chapter 8: Conclusions

This is the final chapter, which shows the summarised conclusions and provides future work suggestions.

1.4 References

1 EOLSS - Renewable Energy Sources. (2001). http://rael.berkeley.edu/old_drupal/sites/default/files/old-site-files/2001/Herzog-Lipman-Kammen-RenewableEnergy-2001.pdf

2 UNFCCC - The Paris Agreement. (2015). https://unfccc.int/process-and-meetings/the-paris-agreement/the-paris-agreement.

3 Mazzio, K. A. & Luscombe, C. K. (2015). The future of organic photovoltaics. *Chem Soc Rev* 44, 78-90.

4 NREL Best Research-Cell Efficiency Chart. (2021). https://www.nrel.gov/pv/cell-efficiency.html.

5 Freiman, S. W. & Madsen, L. D. (2012). Issues of scarce materials in the United States. *American Ceramic Society Bulletin* 91, 40-45.

6 Krebs, F. C., Tromholt, T. & Jørgensen, M. (2010). Upscaling of polymer solar cell fabrication using full roll-to-roll processing. *Nanoscale* 2, 873-886.

7 IRENA Renewable Power Generation Costs in 2019. (2020). https://www.irena.org/publications/2020/Jun/Renewable-Power-Costs-in-2019.

8 IEA - Access to Electricity. (2020). https://www.iea.org/reports/sdg7-data-and-projections/access-to-electricity.

9 Zhang, Y., Samuel, I. D. W., Wang, T. & Lidzey, D. G. (2018). Current Status of Outdoor Lifetime Testing of Organic Photovoltaics. *Adv Sci (Weinh)* 5, 1800434.

CHAPTER 2
BACKGROUND

2.1 Introduction

The declining module cost of silicon-based solar cells has facilitated the rapid increase in overall photovoltaic (PV) electricity production. Between December 2009 and December 2019, crystalline silicon (c-Si) module prices declined between 87% and 92% for modules sold in Europe, depending on the type.[1] Similar cost reductions have been observed globally as shown in **Figure 2.1** learning curve of the International Technology Roadmap for Photovoltaic (ITRPV). The learning curve indicates that for every doubling of cumulative PV module shipment, the average selling price decreases according to the learning rate (LR), which reached 23.5% by the end of 2019.[2] The LR predicts that module cost will continue to fall and although some regional differences apply, the established c-Si PV technology has reached "grid parity" in many countries all around the world,[3] arising the question: Can new PV technologies compete in the current and future electricity market?

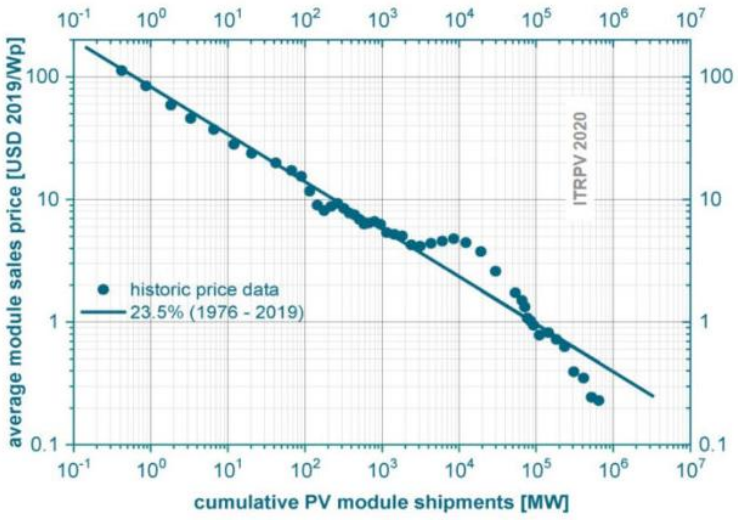

Figure 2.1 Learning curve for module cost as a function of cumulative shipments

In the last two decades, emerging PV alternatives, such as dye-sensitized cells, tandem cells, organic photovoltaics (OPV), quantum dot cells and perovskite (PVK) have all been object of intensive research[4] due to their potential to disrupt current silicon-based solar cells because of their low long-term $/W potential and compatibility with applications not suitable for silicon PV,[3] such as installations in some remote places or within building structures, as well as indoor applications under low-light conditions. For example, flexible and light weight emerging PV panels could be more easily transported to remote locations than rigid and heavier Si PV panels, therefore making PV technology accessible worldwide. Also, emerging PV films could be installed in curved windows while keeping transparency, or in the walls of modern buildings with very unique structures and shapes while tuning the colour of the panels to blend with the background. Niche applications of emerging PV technologies also include artistic installations in sculptures, vehicle integrated panels to provide auxiliary power and indoor applications. The effectiveness of silicon solar cells for indoor applications is limited by the spectrum sensitivity mismatch of frequently used indoor illumination, such as fluorescent and LED lights,[5] contrary to emerging PV which usually present a good spectral response in the visible region (~400-700 nm) characteristic of those light sources, allowing them to reach power conversion efficiencies above 30% under ambient light.[6]

This thesis mainly focuses on Organic Photovoltaics (OPVs), which convert solar energy to electrical energy. They are made from organic semiconducting materials such as polymers and small molecules[7] and promise to be a cheap commercial technology if their short lifetime can be resolved. With OPV solar panels, a manufacturing approach known as "roll-to-roll" processing is possible due to the all-carbon nature of the polymers employed, which might result in very low-cost and high-volume production-line output.[3] This, along with the material's physical flexibility and potential for transparency, makes it appealing for exotic uses such as building integration.[3]

In this chapter, a brief summary of PV technologies is presented, followed by a discussion of OPVs operation and its parameters, alongside with economical concepts and factors that need to be considered in PV installations.

2.2 Photovoltaic generations

The photovoltaic effect was first observed in 1839 when French physicist Alexandre-Edmond Becquerel was working with metal electrodes in an electrolyte solution and noticed that small electric currents were produced when the metals were exposed to light.[8] Charles Fritts, an American inventor, created the first selenium solar cells in 1883 and thought his solar cells would compete with Edison's coal-fired power plants by coating the semiconductor selenium with a thin layer of gold to create the junctions, but they were only 1% effective in converting sunlight to electricity and therefore not particularly practical.[9] The efficiency of a solar cell is the most widely used metric for comparing its performance to that of another. Efficiency is defined as the ratio of energy output from the solar cell to input energy from the sun[10] (more details about efficiency and PV parameters in section 2.6). For the following few decades, some research on selenium photovoltaics continued, and a few applications were discovered, but they were not widely used. The first workable photovoltaic cell was not made until 1954 at Bell Laboratories by Daryl Chaplin, Gerald Pearson, and Calvin Souther Fuller. Those first silicon (Si) solar cells were about six percent efficient at converting the energy in sunlight into electricity, a huge improvement over any previous solar cells.[8] Since then there have been many advances in the PV field and solar cells have been classified into three generations according to their efficiency and cost potential (**Figure 2.2**). The three PV generations are discussed below.

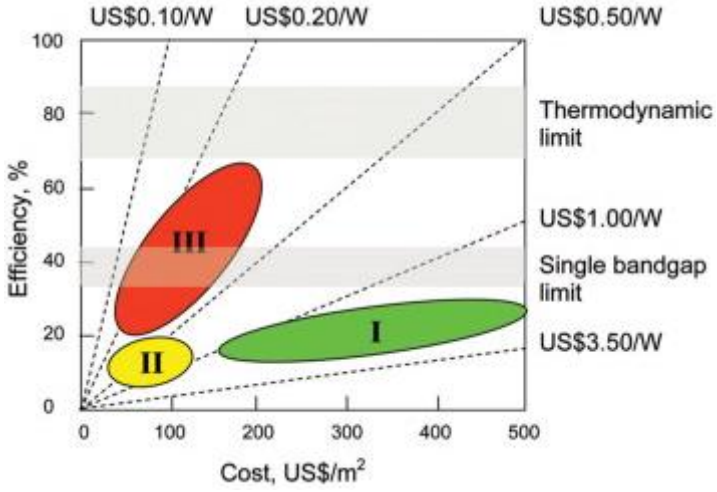

Figure 2.2 Efficiency and cost projections for first- (I), second- (II), and third- generation (III) PV technologies[11]

2.2.1 First PV Generation

Solar cells of the first generation are made of silicon wafers, each of which can produce 2-3 watts of power.[12] Solar modules, which are made up of numerous cells, are used to enhance power. First-generation solar cells are divided into two kinds based on their crystallisation levels. A single crystal solar cell is one in which the entire wafer is made up of only one crystal, while multicrystal solar cells are made out of crystal grains on a wafer. Monocrystalline and multicrystalline solar cells universally have a single-junction structure and its theoretically highest efficiency is ~33% (Shockley–Queisser limit).[13] This maximum theoretical efficiency was calculated taking into account standard solar cell test conditions (AM 1.5 G spectrum and solar cell temperature of 25 °C) and detailed balance considerations proposed by William Shockley and Hans-Joachim Queisser in 1961.[14] They assumed that in an ideal solar cell the only recombination path which cannot be reduced to zero is radiative recombination (where a photon is released), and that photons with energies below the energy band gap (energy required to promote a valence electron bound to an atom to become a conduction electron) do not interact with the solar cell, but photons with energies above the band gap are transformed into electron–hole pairs with a quantum efficiency of 100%.[13] It is however important to note that in reality there are losses due to light reflection or material defects. Still, first generation PV cells typically last longer and have a greater efficiency than later-generation PV cells. The record efficiency for cell-size Si PV has increased from 16% in 1980 to ~26% in the present day,[4] but the record efficiency has remained almost the same for the last 5 years, suggesting that further improvements in efficiency may be difficult to achieve. For monocrystalline panels, the commercial efficiency ranges between 16% and 24%,[15] whilst the efficiency of polycrystalline panels varies in the range of 14–18%.[15] Although monocrystalline solar cells have a greater efficiency than multicrystalline solar cells, wafer manufacturing of the latter is easier and less expensive, thus they are competitive with monocrystalline solar cells.[12] First-generation panels are typically warrantied to lose no more than 0.7% of their output each year over the course of their 25-year lifespan.[16] Their production processes, on the other hand, are expensive in terms of energy usage and labour, and their performance is quickly degraded at high temperatures.[17] First-generation cells are currently the most efficient and the most

widely used cells amongst all the three generations, occupying approximately 80% of the PV market.[15]

2.2.2 Second PV Generation

Second-generation PV cells aim to reduce the cost of first-generation cells through use of smaller amounts of semiconductor material. The reason of this cost reduction is that the film thickness of second-generation solar cells varies from a few nanometres (nm) to tens of micrometres (µm), much thinner than thin-film's first-generation crystalline silicon solar cell (c-Si) that uses wafers of up to 200 µm thick.[18] When compared to silicon-based first-generation cells, second-generation cells show lower efficiencies since they use less semiconductor material. Amorphous silicon (a-Si), CdTe, and CIGS are the three primary kinds of cells in this generation. Together, they occupy approximately 20% of the total PV market. In amorphous silicon cells, the efficiency typically varies from 4% to 10%,[15] but has a record efficiency of 14%,[4] whilst record efficiency for a laboratory CdTe solar cell is 22.1%[4] and commercial CdTe modules have reached 18% efficiency.[19] CIGS efficiency is in general higher, with a cell-size record efficiency of 23.4%[4] and module-size record efficiency of 19%.[20] These thin-film solar cells can be growth on large areas up to 6 m^2,[18] and due to their compatibility with flexible devices they can be used in applications on building integrations, cars, windows, etc. A few specific advantages and disadvantages of each thin-film technology are now mentioned. Amorphous silicon panels have strong absorption in the visible spectrum and are more lightweight than c-Si,[21] but they have low efficiencies and potential photo-induced degradation issues.[22] CdTe solar cells are processed at low-temperature, allowing flexible and cheap manufacturing, however, cadmium is toxic and tellurium is an extremely rare material.[21] CIGS panels have the highest efficiency among thin-film technologies and have a tunable bandgap that allows the possibility of tandem CIGS devices,[23] however, CIGS cells are expensive and require difficult manufacturing processes.[21,23]

2.2.3 Third PV Generation

The main objective of third-generation PV cells is to create high-efficiency devices that employ thin-film technology similar to second-generation PV cells, allowing them to be used in applications not suitable for c-Si panels (e.g. building integrations and indoor applications under low-light conditions). These cells use a range of novel materials to make solar PV technology more efficient and less costly. This includes organic photovoltaics (OPVs), copper zinc tin sulphide (CZTS), perovskite solar cells, dye-sensitized solar cells (DSSCs), and quantum dot solar cells.[4,20,24-27] The majority of third-generation PV technology research and development is currently carried out in laboratories by university or company research groups.[4] Unlike previous generations, third generation PV panels are not commercial yet. However, German company Heliatek has implemented more than 30 OPV pilot projects worldwide,[28] while English company Oxford PV is building the world's first volume manufacturing line for perovskite-on-silicon tandem solar cells and will commence production in 2022.[29] A brief summary of these emerging PV technologies is added below.

CZTS cells have a kesterite crystal structure and an active layer with the general form Cu_2ZnSnS_4.[30] These cells make use of more abundant and non-toxic components than CIGS cells, and they don't require the use of poisonous cadmium or rare indium. The record efficiency for a pure CZTS cell is 11.0%.[31] However, owing to the addition of selenium, this has been surpassed, resulting in a CZTSSe cell with a 13% efficiency.[4,32] Still, both CZTS and CZTSSe are difficult to further optimise due to their material complexity.[33]

Perovskites active material is based on a generic ABX_3 structure, where A is an organic cation such as methyl ammonium ($CH_3NH_3^+$), B is an inorganic cation, typically lead (Pb^{2+}) and X is a halogen anion, such as chloride (Cl^-) or iodide (I^-).[33] Perovskites are remarkable for their quick growth in reported efficiencies and for achieving performance levels equivalent to second-generation inorganic cells, clearly putting them ahead of competing third-generation solar technologies, with a cell-size record efficiency of 25.5%.[4] However, perovskites need to overcome significant stability difficulties, including quick degradation by the presence of moisture and

toxicity concerns, because some perovskite based solar cells could contaminate the environment if encapsulation fails to contain the toxic compounds.[33]

The longest-running third-generation solar technology is DSSCs, which makes use of organic dye-absorbers in a liquid electrolyte to fabricate coloured devices. DSSCs share similar benefits and characteristics with OPVs, such as the availability of solution-processable materials and compatibility with transparent and flexible devices.[33] However, the record-certified efficiency for DSSCs is only ~13% and has stayed roughly the same for nearly a decade,[4] suggesting that they may only be suitable for niche applications.

Quantum dot solar cells refer to a group of devices that use semiconductor nanocrystals to generate electricity from sunlight (commonly metal chalcogenide nanocrystals such as PbS or PbSe).[33] The record efficiency for a quantum dot cell-size device is 18.1%.[4] Quantum dot solar cells benefit from low-temperature solution-processable manufacturing and a readily adjustable band gap[30], but frequently employ hazardous or rare materials (e.g. selenium).

OPVs feature photoactive layers made up of a semiconducting polymer or small molecule and a fullerene derivative or non-fullerene acceptor (NFA), which when intermixed form a bulk heterojunction (BHJ) (further explained in section 2.3). Due to the development of novel NFAs, the cell efficiency record of OPVs has improved from 2.5% in 2013 to 18.2% in 2021.[4] Organic photovoltaic devices have a number of benefits over Si PV devices, including inexpensive material costs, lightweight, flexibility, and the compatibility with roll-to-roll printing manufacturing processes.[27] However, photochemical degradation causes stability difficulties in some OPV blends,[27] and oxygen and moisture ingress can lead to considerable drop in efficiency with the passage of time,[34] meaning that they degrade faster than the well-established inorganic solar panels.

In the next sections (2.3-2.7) the operation of organic photovoltaics is further discussed, and helps as background for the experimental methods (Chapter 3) and results presented in Chapter 4, which focus in tackling the moisture and oxygen ingress degradation issue in OPVs. Whilst in section 2.8 the discussion moves forward to some basic economical concepts related to PV installations, which serve as a brief background for the development of a levelized cost of energy model (LCOE) (Chapter

5) with a focus in quantifying the impacts of PV parameters upon LCOE and analysing the feasibility of OPV and perovskite technologies (Chapters 6-7).

2.3 OPVs operation and manufacture

OPVs are solar cells that have an absorbing layer based on organic semiconductors, typically polymers or small molecules. The term "organic semiconductors" refers to materials that are mainly made up of carbon and hydrogen atoms and exhibit characteristics that are typical of semiconductor materials, such as absorption and emission of light in the visible spectrum and a degree of conductivity to operate semiconductor devices (e.g. light-emitting diodes and solar cells).[35] Organic semiconducting materials are based on chains of sp^2-hybridised carbon[36] (sp^2 relates to σ only) and require a high level of conjugation (alternating between single σ and double π bonds) to become conducting or semiconducting.[7] σ bonds are usually formed by the overlap of hybridised atomic orbitals, while π bonds are formed by the side-by-side overlap of unhybridised orbitals,[37] as shown in **Figure 2.3**.

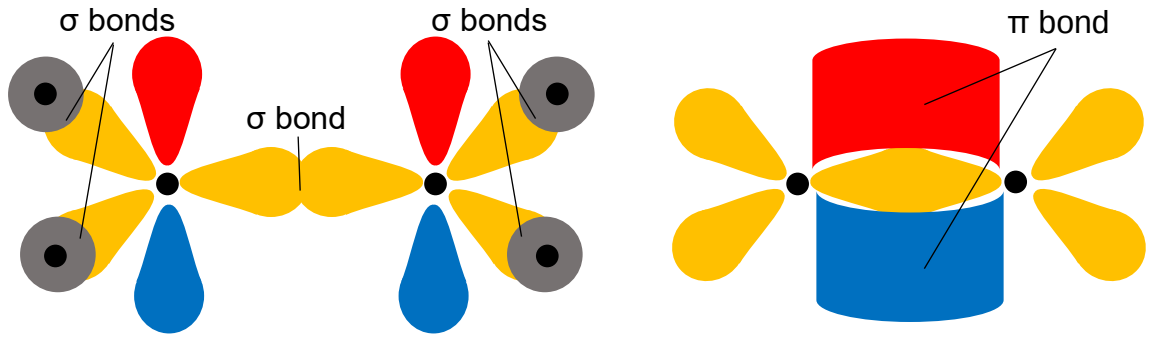

Figure 2.3 Five σ bonds (left) and one π bond (right) in an ethene molecule (C_2H_4). C orbitals are sp^2 (yellow) and p (red and blue), while each H orbital is s (gray). The black dots represent the nuclei of the atoms

The sharing of sp orbitals between adjacent carbons leads to strong σ-bonding, while hybridisation between the remaining $2p_z$ orbitals results in weaker π (bonding) or π* (anti-bonding) orbitals,[36] and the electrons associated with the double bonds get

delocalised over the whole length of conjugations.[7] The highest bonding π-orbital is referred to as the highest occupied molecular orbital (HOMO) and the lowest anti-bonding π*-orbital as the lowest unoccupied molecular orbital (LUMO). The difference between the HOMO and LUMO is called energy band gap (E_g) and it determines the energy required to excite an electron from HOMO to LUMO.[7] The typical band gap of organic semiconductors is between 1.5 and 3.0 eV, which leads to absorption mainly in the visible spectrum,[38] but band gaps can be tuned synthetically to optimise absorption for the AM 1.5 solar spectrum. In the case of inorganic silicon the energy band gap is ~1.1 eV, but the conduction and valence bands take the place of LUMO and HOMO respectively. The Fermi level describes the probability distribution for electrons as function of energy. The main thing in an inorganic semiconductor is that it is mainly crystalline, and that the band structure (and associated gaps) is determined by this regular periodicity. In organic semiconductors the Fermi level can be shifted from a mid-gap position towards the LUMO by n-doping or towards the HOMO by p-doping.[39] Fermi levels can also be influenced by charges injected from contacts. A comparison of organic and inorganic energy band gap diagrams is shown below in **Figure 2.4**.

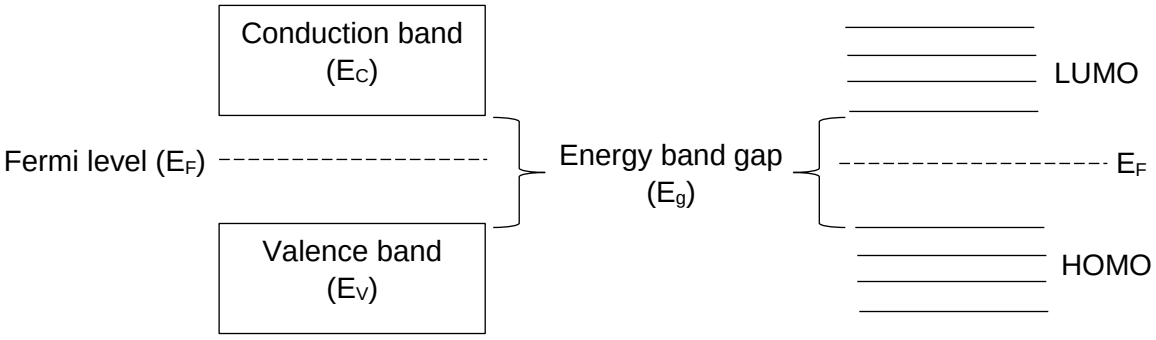

Figure 2.4 Energy band gap diagram of inorganic (left) and organic (right) semiconductors

To create photocurrents in an OPV cell, sunlight is absorbed in a photoactive layer consisting of organic semiconductor donors (polymers or small molecules) and acceptors (fullerenes or non-fullerenes). When the light energy is greater than or equal to the band gap, a bound electron-hole pair (exciton), which is neutral, is created.[7] The exciton binding energy (E_b) refers to the electron and hole attraction

and in the case of inorganic semiconductors the E_b can be easily overcome by thermal energy at room temperature due to its small value (26 meV).[40] However, organic semiconductors have much higher values (~0.3-0.5 eV),[41] hence the exciton does not dissociate spontaneously into free charges. Prior to relaxation, excitons diffuse and may come into contact with a donor/acceptor interface (Exciton Diffusion).[42] Excitons can diffuse ~5-10 nm prior to relaxation, a process in which the solar energy is lost, hence the structure of the donor acceptor interface[43] is very important to avoid recombination (section 2.7) to allow exciton dissociation in its short lifetime (~100 ps-1 ns).[44]

Within an OPV, at least two distinct organic semiconductors (donor and acceptor) are required to offset their individual energy levels to a value higher than E_b and allow exciton dissociation.[7,41] Arriving excitons then split into holes (positive charge carriers) and electrons (negative charge carriers) at the D-A interface (Charge Transfer).[42] Recombination can occur at the interface between the two materials while the electron-hole pair is still attracted in the charge-transfer state.[7] Charges that avoid recombination move away from each other and become free charges (Charge Separation). Following either the donor or acceptor phase, these holes and electrons travel to the corresponding electrodes and are used in an external circuit to produce current (Charge Extraction).[42] **Figure 2.5** summarises the OPV working mechanism.

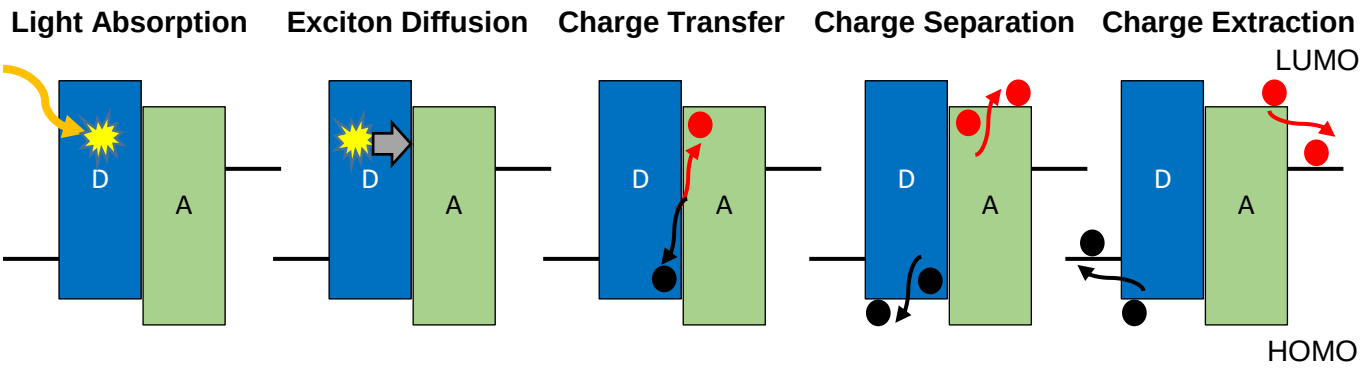

Figure 2.5 Working mechanism of a bilayer organic photovoltaic (D = donor, A = acceptor). Red circles represent electrons and black circles represent holes

Having established the principles of operation of OPVs we now discuss the evolution of the device structures of OPV cells from **Figure 2.6**.

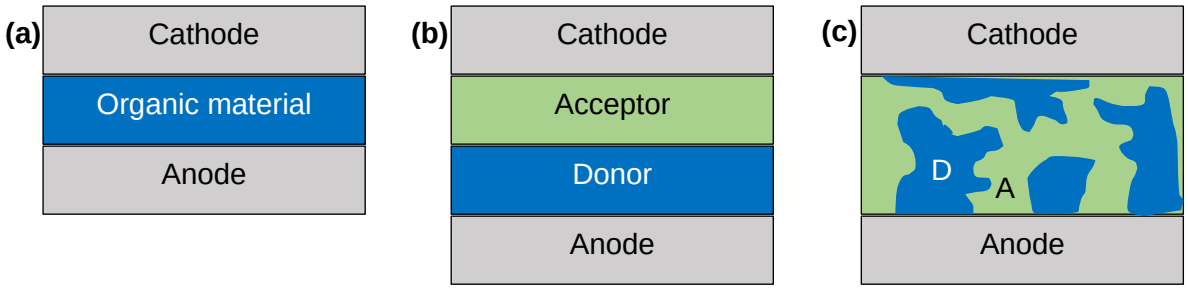

Figure 2.6 Device structure of OPV cells: (a) single layer, (b) bilayer, (c) bulk heterojunction (BHJ). D = donor, A = acceptor

2.3.1 Single layer OPV

Organic photovoltaic cells with a single layer structure are the most basic. These cells are created by sandwiching a layer of organic electronic materials between two metallic conductors, generally a high-work-function layer of indium tin oxide (ITO) and a low-work-function layer of aluminium, magnesium, or calcium. The first single layer OPV was developed by Kearns and Calvin in 1958 and it was based on the molecule magnesium phthalocyanine (MgPc), measuring a photovoltage of 200 mV.[45] However, the potential of single layer OPVs is very limited and typically yields power conversion efficiencies well below 0.1%[46] due to issues with high exciton binding energy (~0.3-0.5 eV),[41] which difficult excitons splitting and results in minimal current output. Also, the field produced by the different work functions of the conductive electrodes is not strong enough to help excitons to dissociate into free carriers.[47] Research continued given the limitations of single layer OPVs, and it was discovered that having an interface between an electron-donor and electron-acceptor improves excitons dissociation, as discussed in the following structures.

2.3.2 Bilayer OPV

The first bilayer OPV was developed by Tang in 1986 from copper phthalocyanine and a perylene tetracarboxylic derivative, showing a power conversion efficiency of 1%.[48] The reason behind this increase in efficiency in comparison with the single layer OPVs was that the bilayer structure, also called planar heterojunction (PHJ), makes use of two materials with different electron affinities and ionisation potentials, which favours excitons dissociation.[46] The material with the highest

electron affinity accepts the electron, whereas the material with the lowest ionisation potential accepts the hole. However, bilayer OPV have their own limitations. Excitons can only dissociate at the donor-acceptor interface, and they can only diffuse for around 10nm before returning back to the ground state.[49] In contrast, to absorb light successfully, a total active layer thickness of over 100 nm is generally required, indicating bilayer cells are either too thin to absorb light properly or too thick for efficient exciton dissociation.[7]

2.3.3 BHJ OPV

To solve the issues presented in bilayer OPVs, a solution was proposed in 1995 by Heeger et al.,[50] which consisted in a bulk heterojunction (BHJ) OPV achieving an efficiency of 1.5%. The absorption layer of bulk heterojunction cells is made up of a nanoscale blend film of donor and acceptor materials. Because this blend's domain sizes are on the order of nanometers, excitons with short lifetimes can reach an interface and dissociate because of the high donor-acceptor interfacial area.[51] Forming a solution comprising the donor and acceptor, casting (e.g. drop casting and spin coating), and then allowing the two phases to separate, generally with the help of an annealing step, is the most common way to make bulk heterojunctions. The two components will self-assemble into a network that connects the two electrodes.[52] Electrons travel to the acceptor domains after capturing a photon, then are transported through the device and collected by one electrode, whereas holes go in the opposite direction and are collected by the other electrode. However, if the dispersion of the two materials is too fine, charge transfer across the layer will be poor.[53]

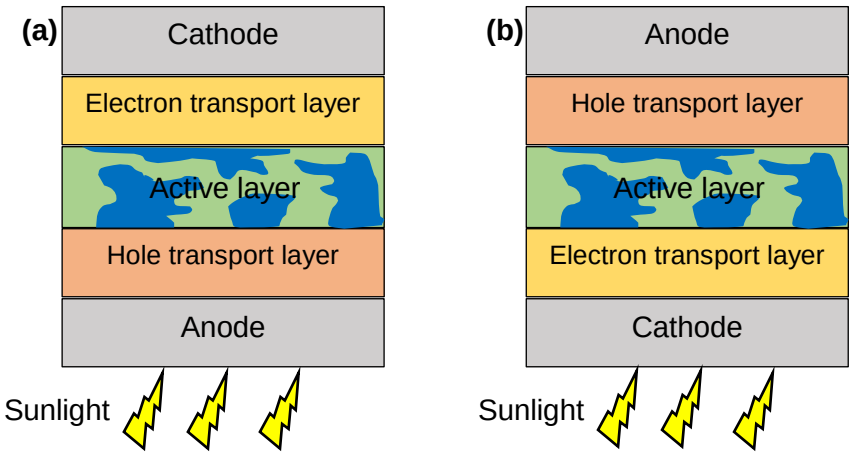

Figure 2.7 Architecture of OPV cells: (a) standard, (b) inverted

Most of the OPVs used in current research are based on the BHJ structure, and their architecture can be classified as standard or inverted as shown in **Figure 2.7**.

The buffer layers (hole transport and electron transport) are the intermediary layers between the electrodes and the active layer, and they are important charge extraction components in standard and inverted OPVs.[54] In standard OPV devices, poly(3,4 ethylenedioxythiophene): poly(styrenesulfonate) (PEDOT:PSS) is commonly used as a hole-transport layer (HTL), which planarises the anode (ITO) surface and lowers leakage current,[55] whilst lithium fluoride (LiF) is a common electron-transporting layer (ETL). Calcium (Ca) is frequently used in conjunction with an aluminium (Al) cathode[7] to collect the electrons generated in the BHJ. Al is used on top of Ca as the former is only slightly reactive, while the latter is very reactive. In the other hand, the inverted OPV design reverses the traditional OPV layer sequence in order to avoid using readily oxidised metals on the exposed cathode and increase device lifetime.[56] The ITO serves as an electron collector (cathode) in this architecture and is generally covered with a transparent metal oxide layer such as zinc oxide (ZnO) or titanium dioxide (TiO_2). On top of the metal oxide layer, the active BHJ layer is deposited, followed by an HTL (typically PEDOT:PSS), and the device is completed with the deposition of a high work-function metal anode such as gold (Au), silver (Ag) or copper (Cu).[57]

The active layer is the core and the most important layer of any solar cell. A light-absorbing electron donor semiconductor, generally a polymer, and an electron acceptor material (fullerene or non-fullerene) make up the active layer in a solution-processed organic photovoltaic system.[58] The morphology and structure of the active layer has to be controlled at the nanoscale to achieve maximum solar efficiency,[54] as mixed donor/acceptor domains are required to provide optimum surface area to enable efficient charge separation.[59] Also, high mobility[60] and enhanced device performance[61] have been linked to increased crystallinity of the donor polymer phase, resulting in reduced charge recombination processes.[62] The active layer thickness in OPVs is usually ~100 nm, leading to optimum performance that results from the compromise between strong light absorption and efficient charge collection.[63] If the thickness is larger it can lead to non-geminate recombination (section 2.7).

In ambient conditions, organic photovoltaics are known for their poor stability, and photodegradation of the active organic layer plays a significant part in this short lifetime.[64] In comparison with most inorganic materials, organic materials utilised in OPVs are more vulnerable to both chemical (from oxygen and water) and physical (from morphological stability) deterioration.[34] Furthermore, degradation can occur in individual layers of OPVs or at their interfaces.[65] The following section discusses the degradation mechanisms of OPVs in more detail.

2.4 OPVs degradation

Organic photovoltaics deteriorate at a higher rate than their inorganic equivalents, thus understanding their degradation mechanisms is crucial. While unencapsulated OPVs normally present lifetimes in the order of tens to hundreds of hours, encapsulated devices have reached lifetimes of several thousands of hours that can be extrapolated to champion lifetimes of >10 years,[63] but most OPVs are still far from the typical lifetime of commercial Si panels (25 years). Degradation in OPVs is categorised as intrinsic or extrinsic and can occur in the active layer, the buffer layers, the electrodes and all the interfaces between them.[66] The primary extrinsic degradation processes found by researchers so far involve water and oxygen, which enter an OPV, react with the materials under illumination, and cause them to lose their capacity to absorb light.[67] However, these mechanisms are in some cases interconnected and occur at the same time, making it difficult to pinpoint the specific degradation mechanisms at work. Furthermore, quantifying the impact of a single degradation process on the total deterioration of OPV devices is more challenging.[68]

Oxygen and water related degradation is particularly critical,[67] as light exposure in combination with molecular oxygen and water entering the device causes photo-oxidation,[69] which results in polymer chains breaking, thus altering the OPV absorption, carriers mobility[66] and mechanical properties.[69] Oxygen and water diffusing through the device can oxidise the cathode and create a transport barrier,[66] therefore decreasing the performance. Furthermore, hygroscopic PEDOT:PSS may absorb water and allow it to penetrate all layers (including the active layer), affecting excitons' dissociation due to a reduction in the donor-acceptor interface area.[66] One way to deal with these issues involves the use of good encapsulants against water.[70]

However, the majority of cost effective encapsulation solutions provide modest protection, leaving the problem mostly unsolved.[71] Chapter 4 shows a complementary approach to minimise water ingress to the active layer, which makes use of a ternary strategy by adding an insulating polymer to the donor-acceptor blend.

Light-induced degradation is also one of the most important extrinsic degradation mechanisms in OPVs. During the first hundreds of hours of operation under sunlight most OPVs show an exponential decrease in performance called burn-in,[67] due to accelerated morphological changes in the blended materials of the active layer by the exposure to light.[72] Photochemical degradation happens when irradiation causes chemical changes in the active layer,[64] regardless of the environment. When oxygen is also present the reaction is called photo-oxidation. The diffusion of oxygen and water into the active layer is also accelerated by excessive illumination,[73] resulting in oxidation of the interface between the cathode and the photoactive materials.[74] Another issue with irradiation is that continuous illumination raises the temperature and leads to thermally induced degradation, which accelerates the intrinsic degradation of organic photovoltaic devices.[75]

Degradation in OPVs includes intrinsic factors that refer to the stability of the materials within the device itself.[7] Extrinsic degradation can be avoided by decreasing or removing the stressors induced by the environment, although this does not guarantee intrinsic OPV stability.[67] Intrinsic degradation arises as a result of internal material modification causing changes in the characteristics of the interface between device layers.[76] For example, commonly used aluminium cathode is very sensitive to oxidation[7] and frequently used HTL PEDOT:PSS can corrode the surface of the ITO anode when it comes into contact with it, causing indium diffusion into the active layer, resulting in charge carrier trapping.[77] Further, some polymers used in the active layer of OPVs have higher photochemical instability than others[78] and the use of light sensitive solvent additives to increase initial efficiency can saturate the polymer conjugated backbone directly or be confined by fullerene moieties,[66] accelerating the active layer photo-oxidation.[79] More details about the stability of specific polymers (P3HT and PTB7) with or without the presence of an additive (DIO) are presented in Chapter 4.

Different strategies have been proposed to tackle the extrinsic and intrinsic degradation of OPVs. For example, the use of inverted architecture and encapsulation has already been mentioned, which is beneficial because it provides high protection against oxygen and water ingress that rapidly degrades OPVs, although it also inflates the price of devices. Other strategies include optimisation of HTL and ETL layers by the use of metal oxides such as NiO, V_2O_5 and CrO_x, Cs_2CO_3 respectively,[79] all of which are highly stable and compatible with roll-to-roll production.[80] More importantly, developing and choosing active layer materials that are not only highly efficient, but also highly stable is critical to allow OPVs commercialisation. Due to their high conductivity, good solubility, and ease of processing, regioregular poly(3-alkylthiophenes) (rr-P3ATs) have been the subject of considerable investigation for many years as OPV active layer components.[81] Researchers have been studying the photochemical stability of polymers in ambient conditions,[82] which requires accurate measurements and standard tests. Having a reliable test method for investigating the stability of organic solar cells will aid in better understanding the degradation mechanisms and improving the devices' stability.

2.5 Standardised lifetime testing

It is difficult to compare organic solar cells with different stack designs, such as standard versus inverted architecture, or those using different materials (active layers, buffer layers and electrodes) since distinct degradation mechanisms are involved. This is further complicated considering that a common issue with OPV stability and lifespan studies is the lack of standardisation of testing. Various experimental conditions, such as temperature, encapsulation, humidity, and others, are used amongst researchers.[83] As a result, comparing the results of different laboratories is challenging. However, the International Summit on Organic Photovoltaics Stability (ISOS) guidelines[84] provide procedures and protocols for evaluating the lifespan of thin film solar cell technologies with accuracy. Although there are stricter standards for technology evaluation, such as those provided by the International Electrotechnical Commission (IEC), they are more suitable for commercial technology or ready-to-market technology, while the ISOS stability standards are ideal for the research phase. There are four main categories for degradation testing and each one of them is divided into three levels:

Basic (Level 1), Intermediate (Level 2) and Advanced (Level 3). A summary of the testing categories protocols is presented below:[84]

Dark storage: The shelf life of samples is determined by keeping them in the dark with no load. These can range from leaving a sample at room temperature, ISOS-D-1 (shelf), to controlling the temperature (65 °C/85 °C) with a hotplate or oven, ISOS-D-2 (high temperature storage), to carefully control both the temperature (65 °C/85 °C) and humidity (85%) with an environmental chamber, ISOS-D-3 (damp heat). The major degradation mechanism in dark storage experiments is exposure to ambient oxygen and moisture, therefore allowing to study the stability of OPVs under these conditions without considering the effect of light-induced degradation (see laboratory weathering).

Outdoor testing: Exposing photovoltaic systems to natural sunshine (outdoors) and monitoring their performance in situ with a solar simulator at regular intervals appears to be the most straightforward method of testing them. While in situ monitoring is the most convenient and perhaps scalable, it can raise a number of difficulties, such as temperature coefficients, cloud cover, non-linearity between performance and irradiance, and wind and seasonal fluctuation in the energy dosage received by the specimen. Furthermore, the differences associated with diverse climates, latitudes, and altitudes should all be given in order to facilitate comparisons across different geographic areas.

Thus, three levels of outdoor testing were established, such as ISOS-O-1, where devices are kept outside and periodically measured inside under solar simulation, ISOS-O-2, where devices are kept outside and measured outside under daylight and ISOS-O-3, where devices are kept and measured outside, but also from time to time measured inside for improving the accuracy of measurements. ISOS-O-1 requires simple ambient temperature and relative humidity (RH) measuring units for monitoring, while ISOS-2 and ISOS-3 require a resistance temperature detector (RTD) and RH sensor with ± 5% capability. Outdoor testing is the most realistic test since it exposes how the samples function in real-world conditions. To document the sample's behaviour to the complete cycle of seasonal variations, the test should be conducted for at least a year. One important note is that the size of the active area has an impact

on efficiency and stability, as generally, enlarging the active area reduces efficiency while increasing stability.[85]

Laboratory weathering: The spectral distribution of the light source to which organic solar cells are exposed has a significant impact on their stability.[86,87] Because the cells are very sensitive to the amount of UV light, they might operate differently depending on the type of light source.[86] A light source that closely mimics the spectral distribution of daylight must be used for realistic comparison of indoor stability testing with real life. Lamps having a spectral mismatch class A in the range 400–1100 nm and a considerable amount of UV light down to 300 nm can also be utilised. Xenon arc, metal halide, sulphur plasma, tungsten halogen, and LED lamp combinations are among the light sources that emit between the aforementioned range. However, only xenon arc and metal halide generate enough UV radiation to initiate photo-degradation reactions. Because the spectra of the lamps might vary with aging, it is critical to track the light source intensity over time for these sorts of studies.

In the ISOS-L-1 level the temperature and relative humidity (RH) are monitored but uncontrolled, while ISOS-L-2 level must have a monitored and controlled temperature (65 °C/85 °C). For ISOS-L-3 both, the temperature (65 °C/85 °C) and RH (50%) must be monitored and controlled. The main goal of these tests is to reveal the photosensitivity of the devices, which is very important as polymers degradation is closely related to the amount of UV-radiation received.

Thermal cycling: Thermal cycling with a temperature range considerably outside the boundaries of regular usage is generally required for final product certification to demonstrate that thermal cycling will not be a degradation mechanism over the product's lifetime. However, because this test necessitates complex equipment and may only offer limited data during development, it may be problematic, especially when samples are vulnerable to heat cycling damage. In other words, a single cycle between 85 and −40 °C may damage a cell completely, thus this test acts as a pass/fail rather than a more progressive deterioration test that might distinguish between cells with similar but different resistances to thermal cycling damage. As a result, there are many types of testing that are dependent on the degree of equipment available as well as the cell's resistance to thermal cycling damage.

Basic (ISOS-T-1) cycling is an initial test in which a sample is cycled from a high temperature (65/85 °C) to room temperature using a hot plate set to the high temperature and a clock-actuated switch to turn the hot plate on/off. Intermediate (ISOS-T-2) cycling is similar except that more advanced equipment such as an environmental chamber or a hot plate with the ability to automatically vary temperature over time is used to precisely cycle the temperature gradually over the course of the cycle period. Advanced (ISOS-T-3) cycling requires the most advanced equipment where the temperature can be cycled from 85 to −40 °C and controlled during the course of the cycle. The purpose of thermal cycling tests is to determine the sample's sensitivity to temperature changes that may arise in real-world circumstances.

Having discussed the basic operation and aging measurement protocols of OPVs, we now focus our attention in the individual parameters that characterise these PV devices.

2.6 PV parameters

The capacity of a solar cell to convert light into electricity is measured by its power conversion efficiency (*PCE*), which is the ratio of incoming light power to output electrical power and is usually measured under standard conditions known as AM 1.5 G (later explained in this section). Current density-voltage (*JV*) measurements are used to calculate the *PCE* and other relevant metrics (see **Figure 2.8**), and to facilitate comparisons between cells with different areas, current density (*J*) is commonly utilised instead of current (*I*).[88]

Figure 2.8 shows a J-V Curve with the following parameters involved in *PCE* calculation:

- J_{MP} – Current density at maximum power
- V_{MP} – Voltage at maximum power
- P_{MAX} – Maximum output power (also known as maximum power point)
- J_{SC} – Short-circuit current density
- V_{OC} – Open-circuit voltage
- *FF* – Fill Factor

The *PCE* can be calculated using the following equation:

$$PCE = \frac{P_{out}}{P_{in}} = \frac{J_{sc} V_{oc} FF}{P_{in}} \qquad (2.1)$$

Here, P_{out} is the output power and P_{in} is the input power of the cell (generally an AM 1.5 G source). Having a higher *PCE* means that the OPV is more efficient converting light into electricity.[89] *JV* curves are performed under illumination so that the OPV has a source to operate with. It is highlighted that *JV* curves parameters are discussed in more detail in subsections 2.6.1 - 2.6.3. Also, *JV* curves in the dark are useful for additional analysis of OPVs and are further explained in **Figure 3.9** of Chapter 3.

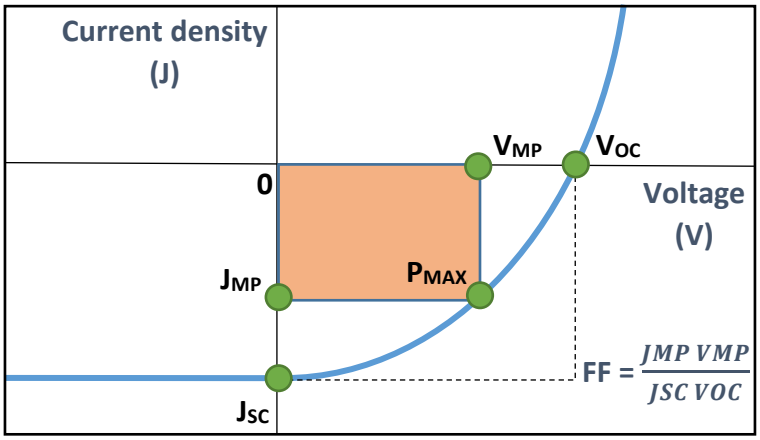

Figure 2.8 J-V Curve showing electrical characteristics of an OPV under illumination

The Air Mass is very important in characterisation of *JV* curves, as it is the length of the journey taken by light through the atmosphere, normalised to the shortest possible path length (i.e. when the sun is directly overhead).[90] As a result, the Air Mass measures the loss of light's power as it travels through the atmosphere and is absorbed by dust and air. The Air Mass is calculated as follows:

$$AM = \frac{1}{cos(\theta)} \qquad (2.2)$$

Where θ is the angle from the vertical (zenith angle). The Air Mass is 1 when the sun is directly overhead (**Figure 2.9**).

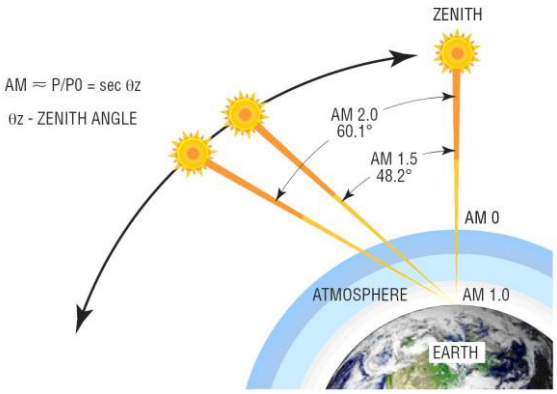

Figure 2.9 Various global (G) air mass (AM)[91]

Variations in both the spectrum and power of incidental light affect the efficiency of a solar cell. A standard spectrum and power density for both radiation outside the Earth's atmosphere and radiation at the Earth's surface has been defined to allow reliable comparison between solar cells recorded at different times and locations.[90] AM 1.5 G is the standard illumination used to characterise PVs. This corresponds to a particular spectrum and intensity of 100 mW/cm^2 (one sun). Because other conditions show distinct spectra, which leads to nonlinear response from some solar cells, most terrestrial solar cells are evaluated under AM 1.5 G conditions.[91] For AM 1.5 standard spectra are defined by the American Society for Testing and Materials (ASTM; see **Figure 2.10**). Having this standard spectrum is particularly important for OPVs, as most organic semiconductors present good absorption in the visible regime (400-700 nm) and some even in the near infra-red (up to ~1000 nm). Using different combinations of donor and acceptor materials with different HOMO and LUMO levels allows to tune the band gap of OPVs and therefore improve their absorption along the AM 1.5 G spectrum.

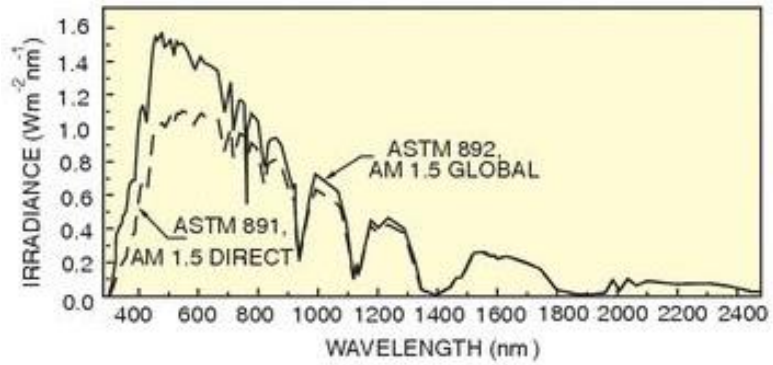

Figure 2.10 ASTM standard spectral irradiance for AM 1.5

Having established the sun spectrum involved in *JV* curves measurement under illumination, we now move on to further describe the main PV characteristics and how these can affect the overall performance of OPVs.

2.6.1 Open-circuit voltage

The open-circuit voltage (V_{OC}) is the maximum voltage across the device when there is no flow of current.[92] The V_{OC} of an OPV can be estimated by the following equation:[93]

$$eV_{OC} = (D^{HOMO} - A^{LUMO}) - 0.3\ eV \quad (2.3)$$

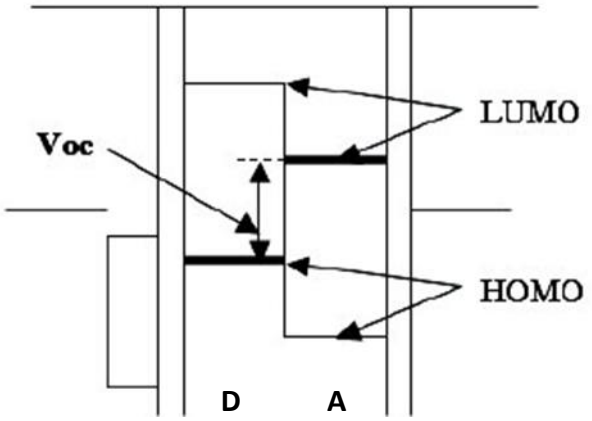

Figure 2.11 V_{OC} under ohmic contacts

Where e is the elementary charge (magnitude of a charge on a single electron or proton = 1.602176 x 10^{-19} C),[94] (D^{HOMO} - A^{LUMO}) is the energy gap between the HOMO of the donor and the LUMO of the acceptor, and 0.3 eV is an empirical factor that accounts for charge separation.[95] This applies when ohmic contacts are present (**Figure 2.11**), meaning that the negative and positive electrodes match the A^{LUMO} and the D^{HOMO}, respectively.[96] Therefore, in OPVs where ohmic-contacts govern, having a semiconductor polymer with a lower HOMO than another polymer leads to a higher V_{OC} if both polymers have the same LUMO level. For example, Jo et al.[97] showed that using PDHF-BT with a HOMO level of -5.47 eV resulted in a V_{OC} of 0.71 V, while using PDHF-TBT with a HOMO level of -5.22 resulted in a V_{OC} of only 0.40 V.

However, if the energetic barrier for hole transfer between the donor and the anode is high, the contact is considered non-ohmic[98] and surface recombination severely restricts the maximum open-circuit voltage,[99] which is determined by the work function difference of the electrodes under non-ohmic contacts. The effect of interface material layers and semiconductor energy disorder on V_{OC} was confirmed by Zampetti et al.[100] In their study they found that when the contacts' work function is within the bandgap, the device's V_{OC} is highly dependent on even small work function changes, while device performance is improved and less sensitive to changes in the work function when it approaches the HOMO and LUMO levels of the active layer components.

2.6.2 Short-circuit current density

The photogenerated current density of the cell when no bias is applied is known as the short-circuit current density (J_{SC}). Only the cell's built-in electric field is employed to push charge carriers to the electrodes in this scenario.[88] In inorganic photovoltaics, mobile electrons and holes seek to disperse evenly within the entire volume due to their random movements over time (diffusion). The free charges recombine as they pass through the junction, leaving behind fixed ions which create a built-in electric field.[101] This built-in electric field affects free electrons and holes, with electrons drawn to positive phosphorus ions and holes attracted to negative boron ions. The number of electrons flowing due to diffusion and the number of electrons flowing back due to the electric field finally achieve a stable equilibrium.[101] In organic photovoltaics the built-in voltage is determined by the difference in work function of the electrodes.[102]

Because the active layer is where the bulk of incident light is absorbed and charge carriers are produced, J_{SC} is roughly proportional to the quantity of light absorbed.[103] Bulk heterojunction (BHJ) OPV materials' absorption spectrum, which typically spans the visible range (~400-700 nm), does not exactly match the solar spectrum, which also includes the ultraviolet and infrared regions (below and above the visible spectrum, respectively), thus limiting their efficiency.[104] The active layer thickness should be substantial in the nm scale (100-150 nm)[105] to absorb a significant quantity of solar incoming light, but within some boundaries to avoid series resistance

or non-geminate recombination[106] (section 2.7) from rising. In OPVs, increasing the series resistance reduces the efficiency of charge collection and transport,[107] resulting in a fast drop in J_{SC}.

2.6.3 Fill Factor

The fill factor is defined as the ratio between the maximum obtainable output power and the product of J_{SC} and V_{OC} (see **Figure 2.8**).[89] The close as possible to 1 the better, however, *FF* will never be exactly 1 because J_{SC} and V_{OC} are the maximum current and voltage respectively from a solar cell, and at both of these operating points the power from the solar cell is zero.[108] *FF* can be calculated using the following equation:

$$FF = \frac{J_{MP}\ V_{MP}}{J_{sc} V_{oc}} \qquad (2.4)$$

Here, J_{MP} and V_{MP} are the current density and voltage of the cell at maximum power respectively. The *FF* is reliant on the OPV's transportation and recombination mechanisms.[109] Fill factor can decrease if there is poor balance in electron-hole transport,[110] as this causes space charges to accumulate and reduces the device's built-in potential.[111] A high series resistance (R_s), which is a parasitic resistance present in every solar cell can also affect *FF*. Any of the interfaces between the layers of the OPV might add resistance, thus the physical origin of the series resistance in any OPV is not evident.[112] What is more clear is that a high series resistance affects the efficiency of OPVs by lowering the *FF*,[113] because it acts as a barrier between the cathode electrode and active layer, by which charge accumulation occurs and inefficient exciton dissociation is obtained.[114]

Resistances arising from energy barriers at interfaces and bulk resistances inside layers are accounted for by the series resistance. The energy barriers across the different interfaces are caused by variations in the HOMO, LUMO, and Fermi levels of the materials utilised for devices, which hinder the transfer of the charge carriers across the interfaces and decrease performance.[115] This should be kept to a minimum

to avoid efficiency losses caused by increased charge carrier recombination, which can be achieved by ensuring that the materials employed in the solar cell have adequate energy level alignment.[88] The next section discusses the main recombination mechanisms that affect the performance of organic photovoltaics.

2.7 Recombination in OPVs

Recombination is a loss mechanism that can happen at different stages of the OPV operation, and it is called that way because it refers to wasted energy due to an electron and hole recombining.[7] Recombination can affect the open-circuit voltage, short-circuit current and fill factor of OPVs, and it can be categorised in two main categories: geminate and non-geminate.[116]

2.7.1 Geminate recombination

This type of recombination occurs when the electron-hole pair recombine before exciton dissociation.[7] Only a fraction of electrons and holes escape their Coulomb attraction and divide into free charges at the donor-acceptor interface.[117] Interfacial geminate pairs (GPs) are formed by electron-hole pairs that have not been able to entirely split, and those interfacial GPs which have relaxed into charge transfer (CT) states can undergo geminate recombination to the ground state.[117]

Geminate recombination happens on a time scale of a few nanoseconds[118] in low mobility, poor conductivity, often disordered semiconductors.[119] However, many studies have concluded that geminate recombination is too weakly dependent on device electric field to have a substantial influence on OPVs *FF* and V_{OC}.[120]

2.7.2 Non-Geminate recombination

Charge separated states are formed when electron-hole pairs escape their mutual Coulomb interaction. If their spatially separated carriers are extracted at the electrodes, charge-separated states contribute to the device's photocurrent. However, free electrons and holes may encounter and recombine during charge transport to the

electrodes. This mechanism is known as non-geminate recombination because the recombining charge carriers come from distinct photoexcitations.[117] In all OPVs the driving force for charge extraction is reduced when the forward bias is applied, as does the charge collecting efficiency.[121] This affects the *FF*, however, when the forward bias is equal to the open circuit voltage, all photogenerated free charge carriers recombine, and the net current flowing out of the device is zero, regardless of the *FF* value. As a result, unlike geminate recombination losses, which may be entirely avoided, all OPV devices are vulnerable to free charge recombination.[116] Non-geminate recombination can be radiative (a photon is released) in the case of band to band recombination, and non-radiative (a photon is not released) such as trap-assisted and Auger recombination.[7]

Band to band recombination

In radiative recombination of inorganic photovoltaics, an electron from the conduction band combines directly with a hole from the valence band, resulting in the emission of a photon.[122] In OPVs the same concept applies but LUMO and HOMO are used instead of the conduction and valence bands. Band to band recombination in a disordered semiconductor with localised charge carriers is restricted by the pace at which oppositely charged carriers locate each other. The rate of this recombination in OPVs is related to the charge carrier mobilities because the quicker charge carriers travel, the faster they will locate one other.[116] This is described by the Langevin equation:[116]

$$R_L = \frac{q}{\varepsilon}(\mu_n + \mu_p)(np - {n_i}^2) \qquad (2.5)$$

Where q is the elementary charge, ε the dielectric constant, μ_n the mobility of the electrons through the LUMO of the acceptor, μ_p the mobility of the holes through the HOMO of the donor, n and p represent the electron and hole charge density respectively and n_i is the intrinsic carrier concentration.

Trap-assisted recombination

When a charge falls into a trap, which is an energy level within the bandgap produced by the presence of a foreign atom or a structural defect, trap-assisted recombination occurs.[122] When the trap is filled, it is unable to absorb any more charges. In a second stage, the trapped charge recombines with a mobile carrier (hole or electron).[121] Defects in the crystal lattice are the most prevalent source of trap-assisted recombination,[122] and the quantity of sites that function as traps and how quickly the free carrier may reach the trapped carrier determine the recombination rate,[123] which is described by the Shockley-Read-Hall (SRH) equation:[116]

$$R_{SRH} = \frac{C_n C_p N_{tr} (np - n_i^2)}{[C_n(n+n_1)C_p(p-p_1)]} \qquad (2.6)$$

Where C_n denotes the probability per unit time that an electron in the conduction band will be captured for the case that the trap is empty and able to capture an electron. Correspondingly, C_p indicates the probability per unit time that a hole will be captured when a trap is filled with an electron and able to capture the hole. N_{tr} is the density of electron traps. And $n_1p_1 = n_i^2$ their product under equilibrium conditions in the case that the Fermi level coincides with the position of the recombination centers where n_i denotes the intrinsic carrier concentration in the sample.

Although most fullerene derivatives are known to be trap-free, many trap-assisted recombination events reported in organic photovoltaics are caused by traps in the donor material or general impurities.[116] However, trap-assisted recombination at interfaces has been found to be the dominant recombination mechanism in emerging PV devices,[124] inducing losses in the photocurrent, but also limiting the open-circuit voltage.[125]

2.8 PV installations

Now that the OPV operation, lifetime, parameters and recombination have been covered, it is also important to discuss some of the factors and concepts involved in PV installations. According to the International Renewable Energy Agency (IRENA) Renewable Capacity Statistics 2021 report, the total worldwide installed capacity of

solar PV now exceeds 700 GW, which represents ten times the worldwide installed capacity by 2011.[126] This large increase in PV installations has been possible largely due to a drop in silicon prices[127] and efficiency gains associated with increased adoption of newer cell architecture types, i.e., passivated emitter and rear contact (PERC) solar cells.[20,128] Higher module efficiencies directly reduce module costs per watt and those balance of system costs related to the area of the solar installation (e.g., racking and mounting structures, cabling, etc.).[1] Cost reductions have also been achieved in the solar PV module manufacturing value chain (e.g., reduced materials usage from diamond wire sawing, higher throughput in factories, automation and reduced labour costs).[1] However, emerging PV technologies like OPVs and perovskites may be able to provide even lower cost solutions by further reductions in module cost and installation costs, if their efficiency and stability reach an adequate level.

Although the National Renewable Energy Laboratory (NREL) in the United States provides charts of the different PV technologies efficiency records per year,[4,20] this information is not enough to demonstrate the feasibility of a technology, as it lacks stability and costs information. Therefore, the ISOS protocols[84] described in section 2.5 are very important to obtain useful and accurate information about the lifetime of devices, leaving only the relevant costs pending to be addressed. This is where the concept of levelized cost of energy (LCOE) comes into play, as it is a way to measure holistically the costs, including the timeline of those expenditures, which go into the production of a kilowatt-hour (kWh).[129] This includes the initial capital investment, maintenance costs, any operational costs and the discount rate (see section 5.3 in Chapter 5 for more information). Thus, an LCOE approach is useful to compare different PV technologies by considering the lifetime of a project and all the associated costs within that time scale.

Chapter 5 continues the discussion of PV installations and presents a novel LCOE model that quantifies the relative impacts of realistic degradation, initial efficiency and module cost of emerging PV technologies. The LCOE results are present in Chapters 6-7.

2.9 References

1 IRENA Renewable Power Generation Costs in 2019. (2020). https://www.irena.org/publications/2020/Jun/Renewable-Power-Costs-in-2019.

2 PV-magazine - Solar costs set to continue falling according to ITRPV roadmap. (2020). https://www.pv-magazine.com/2020/04/28/solar-costs-set-to-continue-falling-according-to-itrpv-roadmap/.

3 ADL - Renewable Energy Emerging PV Technologies. (2015). https://www.adlittle.com/sites/default/files/viewpoints/ADL-Renewable-Energy-Emerging-PV-Technology.pdf.

4 NREL Best Research-Cell Efficiency Chart. (2021). https://www.nrel.gov/pv/cell-efficiency.html.

5 Soyeon, K., Muhammad, J., Jae Hoon, J. & Dong Chan, L. (2019). Recent Progress in Solar Cell Technology for Low-Light Indoor Applications. *Current Alternative Energy* 3, 3-17.

6 Cao, Y., Liu, Y., Zakeeruddin, S. M., Hagfeldt, A. & Grätzel, M. (2018). Direct Contact of Selective Charge Extraction Layers Enables High-Efficiency Molecular Photovoltaics. *Joule* 2, 1108-1117.

7 Ossila - Organic Photovoltaics Introduction. (2021). https://www.ossila.com/pages/organic-photovoltaics-introduction.

8 APS - Physics History. (2009). https://www.aps.org/publications/apsnews/200904/physicshistory.cfm.

9 Renewable Energy Hub - The history of solar power. (2020). https://www.renewableenergyhub.co.uk/main/solar-panels/the-history-of-solar-power/.

10 PVeducation - Solar Cell Efficiency. (2021). https://www.pveducation.org/pvcdrom/solar-cell-operation/solar-cell-efficiency.

11 Conibeer, G. (2007). Third-generation photovoltaics. *Materials Today* 10, 42-50.

12 Kibria, M., Ahammed, A., Sonyy, S., Sony, F. & Hossain, S.-U.-I. in *Conference: 5th International Conference on Environmental Aspects of Bangladesh* (2014).

13 Rühle, S. (2016). Tabulated values of the Shockley–Queisser limit for single junction solar cells. *Solar Energy* 130, 139-147.

14 Shockley, W. & Queisser, H. J. (1961). Detailed Balance Limit of Efficiency of p-n Junction Solar Cells. *Journal of Applied Physics* 32, 510-519.

15 Zhang, T., Wang, M. & Yang, H. (2018). A Review of the Energy Performance and Life-Cycle Assessment of Building-Integrated Photovoltaic (BIPV) Systems. *Energies* 11.

16 Jordan, D. C. & Kurtz, S. R. (2013). Photovoltaic Degradation Rates-an Analytical Review. *Progress in Photovoltaics: Research and Applications* 21, 12-29.

17 Virtuani, A., Pavanello, D. & Friesen, G. in *25th European Photovoltaic Solar Energy Conference and Exhibition/5th World Conference on Photovoltaic Energy Conversion* 4248-4252 (2010).

18 Hisour - Thin film solar cell. (2021). https://www.hisour.com/thin-film-solar-cell-39519/.

19 First Solar - Series 6 Advanced Thin Film Solar Technology. (2021). https://www.firstsolar.com/-/media/First-Solar/Technical-Documents/Series-6-Datasheets/Series-6-Datasheet.ashx.

20 NREL - Champion Module Efficiency Chart. (2021). https://www.nrel.gov/pv/module-efficiency.html.

21 Ossila - Organic Photovoltaics vs 2nd-Generation Solar Cell Technologies. (2021). https://www.ossila.com/pages/organic-photovoltaics-vs-2nd-gen-solar-cell-tech.

22 Jean, J., Brown, P. R., Jaffe, R. L., Buonassisi, T. & Bulović, V. (2015). Pathways for solar photovoltaics. *Energy & Environmental Science* 8, 1200-1219.

23 Solar Energy Technologies Office - Copper Indium Gallium Diselenide. (2021). https://www.energy.gov/eere/solar/copper-indium-gallium-diselenide.

24 Giannouli, M. (2021). Current Status of Emerging PV Technologies: A Comparative Study of Dye-Sensitized, Organic, and Perovskite Solar Cells. *International Journal of Photoenergy* 2021, 6692858.

25 Almora, O., Baran, D., Bazan, G. C., Berger, C., Cabrera, C. I., Catchpole, K. R., Erten-Ela, S., Guo, F., Hauch, J., Ho-Baillie, A. W. Y. *et al.* (2021). Device Performance of Emerging Photovoltaic Materials (Version 1). *Advanced Energy Materials* 11, 2002774.

26 Yan, J. & Saunders, B. R. (2014). Third-generation solar cells: a review and comparison of polymer:fullerene, hybrid polymer and perovskite solar cells. *RSC Advances* 4, 43286-43314.

27 Dracula Technologies - A short overview of the third-generation solar cells: concept, materials, and performance. (2021). https://dracula-technologies.com/what-is-the-third-generation-of-photovoltaic/.

28 Heliatek - The future is light. (2021). https://www.heliatek.com/en/.

29 Oxford PV - The Perovskite Company. (2021). https://www.oxfordpv.com/tandem-cell-production.

30 Lee, T. D. & Ebong, A. U. (2017). A review of thin film solar cell technologies and challenges. *Renewable and Sustainable Energy Reviews* 70, 1286-1297.

31 Sun, K., Yan, C., Liu, F., Huang, J., Zhou, F., Stride, J. A., Green, M. & Hao, X. (2016). Over 9% Efficient Kesterite Cu2ZnSnS4 Solar Cell Fabricated by Using Zn1–xCdxS Buffer Layer. *Advanced Energy Materials* 6, 1600046.

32 Wang, W., Winkler, M. T., Gunawan, O., Gokmen, T., Todorov, T. K., Zhu, Y. & Mitzi, D. B. (2014). Device Characteristics of CZTSSe Thin-Film Solar Cells with 12.6% Efficiency. *Advanced Energy Materials* 4, 1301465.

33 Ossila - Organic Photovoltaics vs 3rd Generation Solar Cell Technologies. (2021). https://www.ossila.com/pages/organic-photovoltaics-vs-3rd-gen-solar-tech.

34 Jørgensen, M., Norrman, K. & Krebs, F. C. (2008). Stability/degradation of polymer solar cells. *Solar Energy Materials and Solar Cells* 92, 686-714.

35 Köhler, A. & Bässler, H. (2015). Electronic Processes in Organic Semiconductors. *Wiley-VCH Verlag GmbH & Co. KGaA*, 1-86.

36 Cavendish Laboratory Cambridge - Organic Semiconductors. (2021). https://www.oe.phy.cam.ac.uk/research/materials/osemiconductors.

37 Lumen - Multiple Bonds. (2021). https://courses.lumenlearning.com/frostburg-chemistryformajorsxmaster/chapter/multiple-bonds-2/.

38 Tregnago, G. *Photophysics and applications of organic semiconductors*, London theses, University College London, (2015).

39 Mayer, T., Hein, C., Mankel, E., Jaegermann, W., Müller, M. M. & Kleebe, H.-J. (2012). Fermi level positioning in organic semiconductor phase mixed composites: The internal interface charge transfer doping model. *Organic Electronics* 13, 1356-1364.

40 Yan, C., Barlow, S., Wang, Z., Yan, H., Jen, A. K. Y., Marder, S. R. & Zhan, X. (2018). Non-fullerene acceptors for organic solar cells. *Nature Reviews Materials* 3, 18003.

41 Nelson, J. (2011). Polymer:fullerene bulk heterojunction solar cells. *Materials Today* 14, 462-470.

42 Sigma Aldrich - Organic Photovoltaics. (2021). https://www.sigmaaldrich.com/materials-science/organic-electronics/opv-tutorial.html.

43 Sunderwirth, S. G. (1970). Donor-acceptor interactions in organic chemistry. *J. Chem. Educ.* 47, 728.

44 Clarke, T. M. & Durrant, J. R. (2010). Charge Photogeneration in Organic Solar Cells. *Chemical Reviews* 110, 6736-6767.

45 Kearns, D. & Calvin, M. (1958). Photovoltaic Effect and Photoconductivity in Laminated Organic Systems. *The Journal of Chemical Physics* 29, 950-951.

46 Spanggaard, H. & Krebs, F. C. (2004). A brief history of the development of organic and polymeric photovoltaics. *Solar Energy Materials and Solar Cells* 83, 125-146.

47 Głowacki, E. D., Sariciftci, N. S. & Tang, C. W. in *Solar Energy* 97-128 (2013).

48 Tang, C. W. (1986). Two-layer organic photovoltaic cell. *Applied Physics Letters* 48, 183-185.

49 Brabec, C. J., Gowrisanker, S., Halls, J. J. M., Laird, D., Jia, S. & Williams, S. P. (2010). Polymer–Fullerene Bulk-Heterojunction Solar Cells. *Adv. Mater.* 22, 3839-3856.

50 Yu, G., Gao, J., Hummelen, J. C., Wudl, F. & Heeger, A. J. (1995). Polymer Photovoltaic Cells: Enhanced Efficiencies via a Network of Internal Donor-Acceptor Heterojunctions. *Science* 270, 1789.

51 Cao, W. & Xue, J. (2014). Recent progress in organic photovoltaics: device architecture and optical design. *Energy & Environmental Science* 7, 2123-2144.

52 Heeger, A. J. (2014). 25th Anniversary Article: Bulk Heterojunction Solar Cells: Understanding the Mechanism of Operation. *Adv. Mater.* 26, 10-28.

53 Scharber, M. C. & Sariciftci, N. S. (2013). Efficiency of bulk-heterojunction organic solar cells. *Progress in Polymer Science* 38, 1929-1940.

54 Wang, Q., Xie, Y., Soltani-Kordshuli, F. & Eslamian, M. (2016). Progress in emerging solution-processed thin film solar cells – Part I: Polymer solar cells. *Renewable and Sustainable Energy Reviews* 56, 347-361.

55 Cao, W. & Xue, J. (2014). Recent progress in organic photovoltaics: device architecture and optical design. *Energy & Environmental Science* 7, 2123.

56 Sigma Aldrich - Inverted Organic Photovoltaic Devices Using Zinc Oxide Nanocomposites as Electron Transporting Layer Materials. (2021). https://www.sigmaaldrich.com/GB/en/technical-documents/technical-article/materials-science-and-engineering/photovoltaics-and-solar-cells/inverted-organic-photovoltaic-devices.

57 Gaspar, H., Figueira, F., Pereira, L., Mendes, A., Viana, J. C. & Bernardo, G. (2018). Recent Developments in the Optimization of the Bulk Heterojunction Morphology of Polymer: Fullerene Solar Cells. *Materials (Basel)* 11, 2560.

58 Nielsen, C. B., Holliday, S., Chen, H. Y., Cryer, S. J. & McCulloch, I. (2015). Non-fullerene electron acceptors for use in organic solar cells. *Acc Chem Res* 48, 2803-2812.

59 Guerrero, A. & Garcia-Belmonte, G. (2016). Recent Advances to Understand Morphology Stability of Organic Photovoltaics. *Nano-Micro Letters* 9, 10.

60 Sirringhaus, H., Tessler, N. & Friend, R. H. (1998). Integrated Optoelectronic Devices Based on Conjugated Polymers. *Science* 280, 1741.

61 Chen, Y., Wan, X. & Long, G. (2013). High Performance Photovoltaic Applications Using Solution-Processed Small Molecules. *Accounts of Chemical Research* 46, 2645-2655.

62 Ripolles, T. S., Guerrero, A. & Garcia-Belmonte, G. (2013). Polymer defect states modulate open-circuit voltage in bulk-heterojunction solar cells. *Applied Physics Letters* 103, 243306.

63 Wu, J., Luke, J., Lee, H. K. H., Shakya Tuladhar, P., Cha, H., Jang, S.-Y., Tsoi, W. C., Heeney, M., Kang, H., Lee, K. *et al.* (2019). Tail state limited photocurrent collection of thick photoactive layers in organic solar cells. *Nature Communications* 10, 5159.

64 Rivaton, A., Chambon, S., Manceau, M., Gardette, J.-L., Lemaître, N. & Guillerez, S. (2010). Light-induced degradation of the active layer of polymer-based solar cells. *Polymer Degradation and Stability* 95, 278-284.

65 Sapkota, S. B., Spies, A., Zimmermann, B., Dürr, I. & Würfel, U. (2014). Promising long-term stability of encapsulated ITO-free bulk-heterojunction organic solar cells under different aging conditions. *Solar Energy Materials and Solar Cells* 130, 144-150.

66 Rafique, S., Abdullah, S. M., Sulaiman, K. & Iwamoto, M. (2018). Fundamentals of bulk heterojunction organic solar cells: An overview of stability/degradation issues and strategies for improvement. *Renewable and Sustainable Energy Reviews* 84, 43-53.

67 Mateker, W. R. & McGehee, M. D. (2017). Progress in Understanding Degradation Mechanisms and Improving Stability in Organic Photovoltaics. *Adv Mater* 29.

68 Srivastava, S. B., Sonar, P. & Singh, S. P. (2016). Analysis of degradation mechanisms in donor–acceptor copolymer based organic photovoltaic devices using impedance spectroscopy. *Materials Research Express* 3.

69 Yousif, E. & Haddad, R. (2013). Photodegradation and photostabilization of polymers, especially polystyrene: review. *Springerplus* 2, 398-398.

70 Manceau, M., Rivaton, A., Gardette, J.-L., Guillerez, S. & Lemaître, N. (2009). The mechanism of photo- and thermooxidation of poly(3-hexylthiophene) (P3HT) reconsidered. *Polymer Degradation and Stability* 94, 898-907.

71 Kawano, K., Pacios, R., Poplavskyy, D., Nelson, J., Bradley, D. D. C. & Durrant, J. R. (2006). Degradation of organic solar cells due to air exposure. *Solar Energy Materials and Solar Cells* 90, 3520-3530.

72 Li, Z., Wu, F., Lv, H., Yang, D., Chen, Z., Zhao, X. & Yang, X. (2015). Side-Chain Engineering for Enhancing the Thermal Stability of Polymer Solar Cells. *Adv Mater* 27, 6999-7003.

73 Eloi, C. C., Robertson, D. J., Rao, A. M., Zhou, P., Wang, K. A. & Eklund, P. C. (1993). An investigation of photoassisted diffusion of oxygen in solid C60 films using resonant alpha-scattering. *Journal of Materials Research* 8, 3085-3089.

74 Norrman, K., Larsen, N. B. & Krebs, F. C. (2006). Lifetimes of organic photovoltaics: Combining chemical and physical characterisation techniques to study degradation mechanisms. *Solar Energy Materials and Solar Cells* 90, 2793-2814.

75 Motaung, D. E., Malgas, G. F. & Arendse, C. J. (2011). Insights into the stability and thermal degradation of P3HT:C60 blended films for solar cell applications. *Journal of Materials Science* 46, 4942-4952.

76 Madogni, V. I., Kounouhéwa, B., Akpo, A., Agbomahéna, M., Hounkpatin, S. A. & Awanou, C. N. (2015). Comparison of degradation mechanisms in organic photovoltaic

devices upon exposure to a temperate and a subequatorial climate. *Chemical Physics Letters* 640, 201-214.

77 Rafique, S., Abdullah, S. M., Sulaiman, K. & Iwamoto, M. (2017). Layer by layer characterisation of the degradation process in PCDTBT:PC71BM based normal architecture polymer solar cells. *Organic Electronics* 40, 65-74.

78 Holliday, S., Ashraf, R. S., Wadsworth, A., Baran, D., Yousaf, S. A., Nielsen, C. B., Tan, C.-H., Dimitrov, S. D., Shang, Z., Gasparini, N. *et al.* (2016). High-efficiency and air-stable P3HT-based polymer solar cells with a new non-fullerene acceptor. *Nature Communications* 7, 11585.

79 Tournebize, A., Rivaton, A., Peisert, H. & Chassé, T. (2015). The Crucial Role of Confined Residual Additives on the Photostability of P3HT:PCBM Active Layers. *The Journal of Physical Chemistry C* 119, 9142-9148.

80 Warren, B. J., Han-Jun, K., Ohseung, K., Bao, Y., Randy, H., Devin, M., Tim, K., Carl, T., Richard, E. & Albert, J. in *Proc.SPIE.*

81 Roncali, J. (1992). Conjugated poly(thiophenes) synthesis, functionalization, and applications. *Chem. Rev.* 92, 711.

82 Manceau, M., Gaume, J., Rivaton, A., Gardette, J.-L., Monier, G. & Bideux, L. (2010). Further insights into the photodegradation of poly(3-hexylthiophene) by means of X-ray photoelectron spectroscopy. *Thin Solid Films* 518, 7113-7118.

83 Hermenau, M., Riede, M., Leo, K., Gevorgyan, S. A., Krebs, F. C. & Norrman, K. (2011). Water and oxygen induced degradation of small molecule organic solar cells. *Solar Energy Materials and Solar Cells* 95, 1268-1277.

84 O.Reese, M., Gevorgyan, S. A., Jørgensen, M., Bundgaard, E., Kurtz, S. R., Ginley, D. S., Olson, D. C., Lloyd, M. T., Morvillo, P., Katz, E. A. *et al.* (2011). Consensus stability testing protocols for organic photovoltaic materials and devices. *Solar Energy Materials and Solar Cells* 95, 1253-1267.

85 Cao, H., He, W., Mao, Y., Lin, X., Ishikawa, K., Dickerson, J. H. & Hess, W. P. (2014). Recent progress in degradation and stabilization of organic solar cells. *Journal of Power Sources* 264, 168-183.

86 Gevorgyan, S. A., Medford, A. J., Bundgaard, E., Sapkota, S. B., Schleiermacher, H.-F., Zimmermann, B., Würfel, U., Chafiq, A., Lira-Cantu, M., Swonke, T. *et al.* (2011). An inter-laboratory stability study of roll-to-roll coated flexible polymer solar modules. *Solar Energy Materials and Solar Cells* 95, 1398-1416.

87 Hermenau, M., Scholz, S., Leo, K. & Riede, M. (2011). Total charge amount as indicator for the degradation of small molecule organic solar cells. *Solar Energy Materials and Solar Cells* 95, 1278-1283.

88 Ossila - Solar Cells: A Guide to Theory and Measurement. (2017). https://www.ossila.com/pages/solar-cells-theory.

89 Hoppe, H. & Sariciftci, N. S. (2011). Organic solar cells: An overview. *Journal of Materials Research* 19, 1924-1945.

90 PVeducation - Air Mass. (2021). https://www.pveducation.org/pvcdrom/properties-of-sunlight/air-mass.

91 LaserFocusWorld - PHOTOVOLTAICS: Measuring the 'Sun'. (2009). https://www.laserfocusworld.com/lasers-sources/article/16566681/photovoltaics-measuring-the-sun.

92 Eftaiha, A. a. F., Sun, J.-P., Hill, I. G. & Welch, G. C. (2014). Recent advances of non-fullerene, small molecular acceptors for solution processed bulk heterojunction solar cells. *J. Mater. Chem. A* 2, 1201-1213.

93 Scharber, M. C., Mühlbacher, D., Koppe, M., Denk, P., Waldauf, C., Heeger, A. J. & Brabec, C. J. (2006). Design Rules for Donors in Bulk-Heterojunction Solar Cells—Towards 10 % Energy-Conversion Efficiency. *Adv. Mater.* 18, 789-794.

94 Study - Elementary Charge: Definition & Overview. (2021). https://study.com/academy/lesson/elementary-charge-definition-overview.html.

95 Brédas, J.-L., Beljonne, D., Coropceanu, V. & Cornil, J. (2004). Charge-Transfer and Energy-Transfer Processes in π-Conjugated Oligomers and Polymers: A Molecular Picture. *Chemical Reviews* 104, 4971-5004.

96 Mihailetchi, V. D., Blom, P. W. M., Hummelen, J. C. & Rispens, M. T. (2003). Cathode dependence of the open-circuit voltage of polymer:fullerene bulk heterojunction solar cells. *Journal of Applied Physics* 94, 6849-6854.

97 Jo, M. Y., Park, S. J., Park, T., Won, Y. S. & Kim, J. H. (2012). Relationship between HOMO energy level and open circuit voltage of polymer solar cells. *Organic Electronics* 13, 2185-2191.

98 Elumalai, N. K. & Uddin, A. (2016). Open circuit voltage of organic solar cells: an in-depth review. *Energy & Environmental Science* 9, 391-410.

99 Liu, J., Shi, Y. & Yang, Y. (2001). Solvation-Induced Morphology Effects on the Performance of Polymer-Based Photovoltaic Devices. *Adv. Funct. Mat.* 11, 420-424.

100 Zampetti, A., Fallahpour, A. H., Dianetti, M., Salamandra, L., Santoni, F., Gagliardi, A., Auf der Maur, M., Brunetti, F., Reale, A., Brown, T. M. *et al.* (2015). Influence of the interface material layers and semiconductor energetic disorder on the open circuit voltage in polymer solar cells. *Journal of Polymer Science Part B: Polymer Physics* 53, 690-699.

101 The Key Centre for Photovoltaic Engineering, UNSW - Understanding the p-n Junction. (2021). http://www2.pv.unsw.edu.au/nsite-files/pdfs/UNSW_Understanding_the_p-n_Junction.pdf.

102 Solak, S., Blom, P. W. M. & Wetzelaer, G. A. H. (2016). Effect of non-ohmic contacts on the light-intensity dependence of the open-circuit voltage in organic solar cells. *Applied Physics Letters* 109, 053302.

103 Kumar, P. & Chand, S. (2012). Recent progress and future aspects of organic solar cells. *Progress in Photovoltaics: Research and Applications* 20, 377-415.

104 Chen, L.-M., Hong, Z., Li, G. & Yang, Y. (2009). Recent Progress in Polymer Solar Cells: Manipulation of Polymer:Fullerene Morphology and the Formation of Efficient Inverted Polymer Solar Cells. *Adv. Mater.* 21, 1434-1449.

105 Park, S. H., Roy, A., Beaupré, S., Cho, S., Coates, N., Moon, J. S., Moses, D., Leclerc, M., Lee, K. & Heeger, A. J. (2009). Bulk heterojunction solar cells with internal quantum efficiency approaching 100%. *Nature Photonics* 3, 297-302.

106 Sylvester-Hvid, K. O., Ziegler, T., Riede, M. K., Keegan, N., Niggemann, M. & Gombert, A. (2007). Analyzing poly(3-hexyl-thiophene):1-(3-methoxy-carbonyl)propyl-1-phenyl-(6,6)C61 bulk-heterojunction solar cells by UV-visible spectroscopy and optical simulations. *Journal of Applied Physics* 102.

107 Shen, Y., Li, K., Majumdar, N., Campbell, J. C. & Gupta, M. C. (2011). Bulk and contact resistance in P3HT:PCBM heterojunction solar cells. *Solar Energy Materials and Solar Cells* 95, 2314-2317.

108 PVeducation - Fill Factor. (2021). https://www.pveducation.org/pvcdrom/solar-cell-operation/fill-factor.

109 Kroon, R., Lenes, M., Hummelen, J. C., Blom, P. W. M. & de Boer, B. (2008). Small Bandgap Polymers for Organic Solar Cells(Polymer Material Development in the Last 5 Years). *Polymer Reviews* 48, 531-582.

110 Yip, H.-L. & Jen, A. K. Y. (2012). Recent advances in solution-processed interfacial materials for efficient and stable polymer solar cells. *Energy & Environmental Science* 5.

111 Yip, H.-L. & Jen, A. K. Y. (2012). Recent advances in solution-processed interfacial materials for efficient and stable polymer solar cells. *Energy & Environmental Science* 5, 5994-6011.

112 Street, R. A., Song, K. W. & Cowan, S. (2011). Influence of series resistance on the photocurrent analysis of organic solar cells. *Organic Electronics* 12, 244-248.

113 Wu, L., Zang, H., Hsiao, Y.-C., Zhang, X. & Hu, B. (2014). Origin of the fill factor loss in bulk-heterojunction organic solar cells. *Applied Physics Letters* 104.

114 Muhammad, F. F., Yahya, M. Y., Hameed, S. S., Aziz, F., Sulaiman, K., Rasheed, M. A. & Ahmad, Z. (2017). Employment of single-diode model to elucidate the variations in photovoltaic parameters under different electrical and thermal conditions. *PLOS ONE* 12, e0182925.

115 Gusain, A., Faria, R. M. & Miranda, P. B. (2019). Polymer Solar Cells—Interfacial Processes Related to Performance Issues. *Frontiers in Chemistry* 7, 61.

116 Proctor, C. M., Kuik, M. & Nguyen, T.-Q. (2013). Charge carrier recombination in organic solar cells. *Progress in Polymer Science* 38, 1941-1960.

117 Laquai, F., Andrienko, D., Deibel, C. & Neher, D. in *Elementary Processes in Organic Photovoltaics* 267-291 (2017).

118 Howard, I. A., Mauer, R., Meister, M. & Laquai, F. (2010). Effect of Morphology on Ultrafast Free Carrier Generation in Polythiophene:Fullerene Organic Solar Cells. *Journal of the American Chemical Society* 132, 14866-14876.

119 Street, R. A., Cowan, S. & Heeger, A. J. (2010). Experimental test for geminate recombination applied to organic solar cells. *Physical Review B* 82, 121301.

120 Credgington, D., Jamieson, F. C., Walker, B., Nguyen, T.-Q. & Durrant, J. R. (2012). Quantification of Geminate and Non-Geminate Recombination Losses within a Solution-Processed Small-Molecule Bulk Heterojunction Solar Cell. *Adv. Mater.* 24, 2135-2141.

121 Cowan, S. R., Banerji, N., Leong, W. L. & Heeger, A. J. (2012). Charge Formation, Recombination, and Sweep-Out Dynamics in Organic Solar Cells. *Advanced Functional Materials* 22, 1116-1128.

122 PVeducation - Types of Recombination. (2021). https://www.pveducation.org/pvcdrom/pn-junctions/types-of-recombination.

123 Chalmers - Radiative and non-radiative recombination. (2021). http://fy.chalmers.se/mbe/WWW/data/presentation.pdf.

124 Sherkar, T. S., Momblona, C., Gil-Escrig, L., Bolink, H. J. & Koster, L. J. A. (2017). Improving Perovskite Solar Cells: Insights From a Validated Device Model. *Advanced Energy Materials* 7, 1602432.

125 Zeiske, S., Sandberg, O. J., Zarrabi, N., Li, W., Meredith, P. & Armin, A. (2021). Direct observation of trap-assisted recombination in organic photovoltaic devices. *Nature communications* 12, 3603-3603.

126 IRENA - Renewable Capacity Statistics 2021. (2021). https://irena.org/publications/2021/March/Renewable-Capacity-Statistics-2021.

127 Bernreuter - Polysilicon Price Trend. (2021). https://www.bernreuter.com/polysilicon/price-trend/.

128 Wilson, G. M., Al-Jassim, M., Metzger, W. K., Glunz, S. W., Verlinden, P., Xiong, G., Mansfield, L. M., Stanbery, B. J., Zhu, K., Yan, Y. *et al.* (2020). The 2020 photovoltaic technologies roadmap. *Journal of Physics D: Applied Physics* 53, 493001.

129 Huff, K. D. in *Storage and Hybridization of Nuclear Energy* 1-20 (2019).

CHAPTER 3
EXPERIMENTAL METHODS

3.1 Introduction

This chapter provides details of the experimental methods used for Chapter 4 in this thesis. The OPVs fabrication processes and devices structure are explained and illustrated in section 3.2, while the materials (polymers and fullerenes) relevant characteristics and OPV batches are briefly described in section 3.3. Finally, the measuring techniques and laboratory equipment used to characterise the OPVs initial performance and lifetime are explained and illustrated in section 3.4.

3.2 Fabrication of devices and structure

Indium tin oxide (ITO) coated glass substrates were cut to size 19.5 mm x 16.5 mm and patterned into stripes by etching with zinc powder and hydrochloric acid, prior to sequential sonication for 15 min each in propanol-2-ol, acetone, Decon 90 solution (2% aqueous), and deionised water, followed by drying with N_2 gas. Cleaned substrates were treated with Oxygen plasma (Yield Engineering Systems Inc., YES-R3) for 5 min with 100 W RF power.

The conductive polymer poly (3,4-ethylenedioxythiophene):poly (styrene sulfonate) PEDOT:PSS (CLEVIOS P VP AI 4083) was filtered using a 0.2 μm poly (tetrafluoroethylene) (PTFE) syringe filter and spin-cast onto the substrate at 2500 rpm for 45s using a spin coater (**Figure 3.1**) prior to annealing at 140 °C for 10 min in ambient atmosphere, to give a layer thickness of ~30-35 nm, as measured by atomic force microscopy (AFM). This recipe was chosen as it was optimised by Al Busaidi et al.[1] for its use in level 4 cleanroom of the Department of Engineering at Durham University, same cleanroom in which Chapter 4 experiments were carried out.

Figure 3.1 Spin coater for buffer and active layers spin coating

The polymer donors considered in this study were P3HT and PTB7, which were purchased from Rieke Metals and 1-Material Inc., respectively, alongside the acceptor fullerenes $PC_{61}BM$ and $PC_{71}BM$, purchased from 1-Material Inc. PMMA with molecular weights M_W = 15 kg mol^{-1}, 97 kg mol^{-1} and 350 kg mol^{-1} were purchased from Sigma Aldrich. P3HT:$PC_{61}BM$ materials were chosen to follow-up and expand a study[1] in which PMMA wt% was increased to improve OPVs stability, while PTB7:$PC_{71}BM$ materials were chosen to study the impact of PMMA in a different active layer with higher initial efficiency, due to PTB7 higher absorption in the infrared and bandgap optimisation by pairing it with $PC_{71}BM$. In all cases the materials were used as provided. Working in a N_2 glovebox, 30 mg ml^{-1} solutions of the individual components were formulated. Details as to solvents used and stirring times are listed in **Table 3.1**.

Two types of OPVs were fabricated, ternary OPVs containing a donor:acceptor and PMMA, and binary OPVs with only a donor and acceptor which served as a control. Binary solutions of P3HT:$PC_{61}BM$ were mixed in a 1:1 volume ratio, while binary blends of PTB7:$PC_{71}BM$ were mixed in volume ratio of 1:1.5, and stirred overnight. Binary OPVs were fabricated by pipetting 150 µl of these mixtures onto the PEDOT:PSS coated substrates prior to spinning at 1000 rpm for 1 min. Ternary OPVs were fabricated in a similar fashion by adding 30 mg ml^{-1} solutions of PMMA to the binary solutions described above, prior to spin coating. In devices that use diiodooctane (DIO), this was added with a concentration of 3% to the binary or ternary solutions, and stirred for 1 h before deposition. P3HT based devices recipe was also chosen following Al Busaidi et al.[1] optimised recipe, whilst PTB7 based devices recipe

resulted as the combination of literature standard[2,3] (ratio and concentration) and in-house experience (pipetting and spinning values) to achieve efficient devices with similar thicknesses observed on P3HT based devices to allow comparisons. Detailed information about solvents used and stirring times are included in **Table 3.1**.

Table 3.1 Active layer preparation summary.

Active layer	Dissolve (30 mg/ml)	Stir (alone)	Mix (binary)	Stir (binary)	Mix (ternary)	Stir (ternary)
P3HT:$PC_{61}BM$	P3HT in DCB	30 min	1:1 ratio	24 hrs	N/A	N/A
	$PC_{61}BM$ in DCB	30 min			N/A	N/A
P3HT:$PC_{61}BM$: PMMA	PMMA in DCB	48 hrs	N/A	N/A	5/10/15 wt%	24 hrs
	P3HT in DCB	30 min	1:1 ratio	3 hrs	95/90/85 wt%	
	$PC_{61}BM$ in DCB	30 min				
PTB7:$PC_{71}BM$	PTB7 in CB	30 min	1:1.5 ratio	24 hrs	N/A	N/A
	$PC_{71}BM$ in CB	30 min			N/A	N/A
PTB7:$PC_{71}BM$: PMMA	PMMA in CB	48 hrs	N/A	N/A	15 wt%	24 hrs
	PTB7 in CB	30 min	1:1.5 ratio	3 hrs	85 wt%	
	$PC_{71}BM$ in CB	30 min				

Spin coating resulted in active layer films of ~100 nm thickness, whilst the solvent is evaporated during spinning. Then, thermal evaporation was used to deposit the Aluminium (Al) cathode, which involved heating the Al to a high temperature with a tungsten filament in a vacuum chamber ($<3x10^{-6}$ mbar) until it reached the point of evaporation. The power supplied to the filament was manually adjusted during deposition while observing a quartz crystal film thickness monitor to maintain a deposition rate of 1 nm/s. An Edwards 306 thermal evaporator (**Figure 3.2**) was used

inside the same glovebox in which the active layer was deposited via spin coating, ensuring a high purity inert atmosphere was kept outside the evaporation chamber. Al cathodes, 150 nm thick, were thermally evaporated through a shadow mask. Finally, the devices were annealed at 120 ◦C for 10 min in the glovebox prior to testing.

Figure 3.2 Evaporator system inside glovebox

A binary control was included in each fabrication run to enable comparison between different formulations and the control, even if slight changes in processing protocols may lead to differences in aging performance. Each batch of OPVs comprised four to six substrates of four devices each that were measured to ensure reliable statistics. The overlap of the patterned ITO and Al electrodes defines the four devices on each substrate, as observed in **Figure 3.3**b. The control devices used in this study were two different binary blend bulk heterojunctions (BHJ) of a donor (polymer) and an acceptor (fullerene) sandwiched between two electrodes (ITO and Al), as illustrated in **Figure 3.3**a. Ternary bulk heterojunction active layers also were fabricated by adding PMMA.

Substrates were handled with tweezers to avoid touching the active area identified in a red tonality in **Figure 3.3**b, as scratching the film could cause failures due to shorting of the anode and cathode. It is important to note that a mask was used

during measurements, which provided an illumination area that is a small fraction of the active area. The benefits of masking are further explained in section 3.4.1.

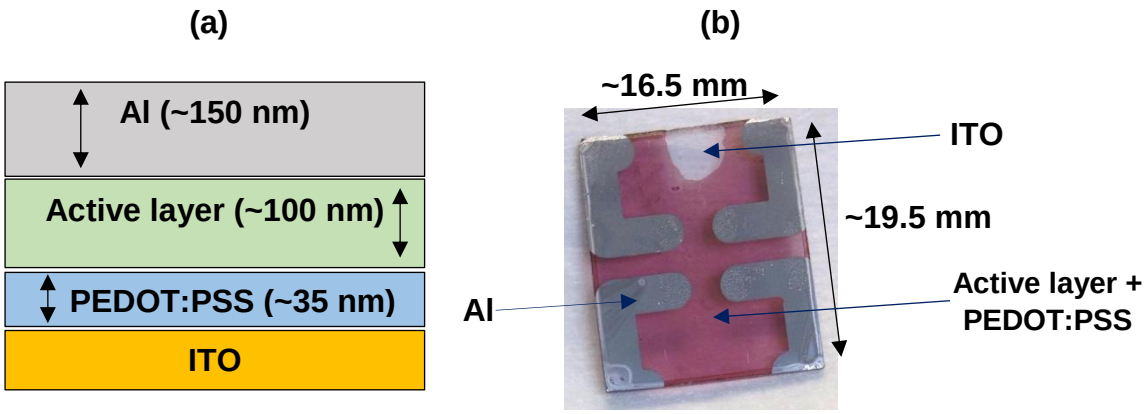

Figure 3.3 OPV layers structure (a) cross section and (b) plan view

3.3 Materials and batches

Poly(3,4 ethylenedioxythiophene): poly(styrenesulfonate) (PEDOT:PSS) (CLEVIOS P VP AI 4083 purchased from Heraeus) is used as an anodic buffer layer in OPV devices, which planarises the anode (ITO) surface and reduces the leakage current.[4] PEDOT:PSS forms a transparent film with high conductivity and has high visible light transmission.[5] Its chemical structure is shown in **Figure 3.4**. PEDOT is conductive but it is not soluble by itself, which is why it is embedded in the insulating, soluble PSS. Doping PEDOT with PSS results in the formation of a water-based complex that allows for spin-coating and enhances processability.[6]

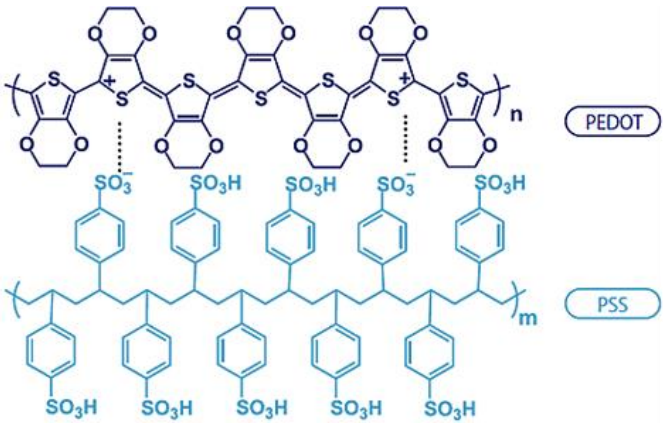

Figure 3.4 The chemical structure of PEDOT:PSS

The active layer is the core of any solar cell. In OPVs it is normally composed of a light absorbing electron donor semiconductor, typically a polymer, and an acceptor, which can be a fullerene.[7] The electron donor used in the first active layer combination was regioregular poly (3-hexylthiophene-2, 5-diyl) (P3HT) (Rieke Metals, M_W=50–70 kg mol^{-1}) which is one of the most studied polymers used for OPV devices.[8] The chemical structure of P3HT is shown in **Figure 3.5**. P3HT has good solubility in common organic solvents[9] and a good hole mobility,[10] which ranges from 10^{-4} cm^2/Vs up to 10^{-1} cm^2/Vs.[11] However, P3HT large energy band gap (~2.0 eV) hamper efficient absorption of the most part of solar radiations (red and infrared region) that is supposed to be the major reason of the low efficiency of P3HT.[12] The average efficiency for P3HT:$PC_{61}BM$ devices is only around 3%,[8] with a maximum efficiency of 7.4% reported with the more expensive fullerene indene-C_{60}-bisadduct (ICBA),[13] which is still low compared to the current OPV record efficiency of 18.2%, which utilises a quaternary approach comprising polymer donors PM6 and PM7, a non-fullerene small molecule acceptor Y6, and the fullerene acceptor $PC_{71}BM$.[14]

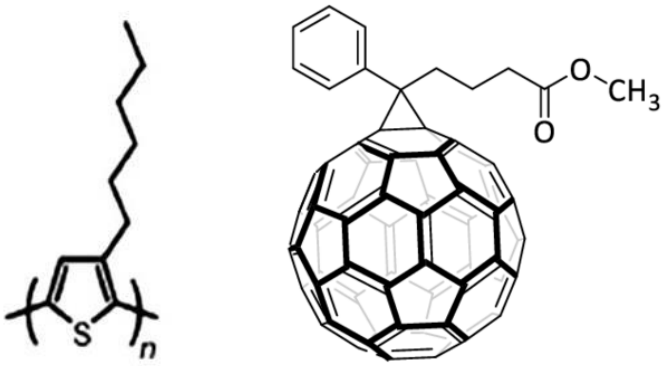

Figure 3.5 The chemical structure of P3HT (left) and $PC_{61}BM$ (right)

The fullerene used to complement the active layer with P3HT was [6, 6]-phenyl C_{61} butyric acid methyl ester ($PC_{61}BM$) (Luminescence Technology Corp., M_W=0.91 kg mol^{-1}), as it can be easily dissolved in common solvents used for donor polymers, allowing the simultaneous casting of polymer and fullerene and the formation of an efficient bulk heterojunction.[15] $PC_{61}BM$ also enables rapid and efficient charge transfer and exciton dissociation when used in a device with a donor polymer.[16] However, although $PC_{61}BM$ stabilizes P3HT films exposed to air, its fullerene cage is found to

undergo a series of oxidations that are responsible for the deterioration of the photoconductivity of the material, and these oxides act as traps for electrons in the $PC_{61}BM$ domains. Another drawback from $PC_{61}BM$ is that it is limited by its poor light-harvesting ability, typical of fullerenes, which has restricted fullerene based OPVs *PCE* to ≈12%,[17] whilst the non-fullerene ITIC breakthrough in 2015 (6.8% *PCE*)[18] has inspired the research community to develop electron acceptors alternatives with efficiencies higher than 17%.[19] The chemical structure of $PC_{61}BM$ is illustrated in **Figure 3.5**.

The electron donor used in the second active layer combination was poly[[4,8-bis[(2-ethylhexyl)oxy]benzo[1,2-b:4,5-b']dithiophene-2,6-diyl][3-fluoro-2-[(2-ethylhexyl)carbonyl]thieno[3,4-b]thiophenediyl]] (PTB7) (1-Material Inc., M_W=80-120 kg mol^{-1}), shown in **Figure 3.6**.

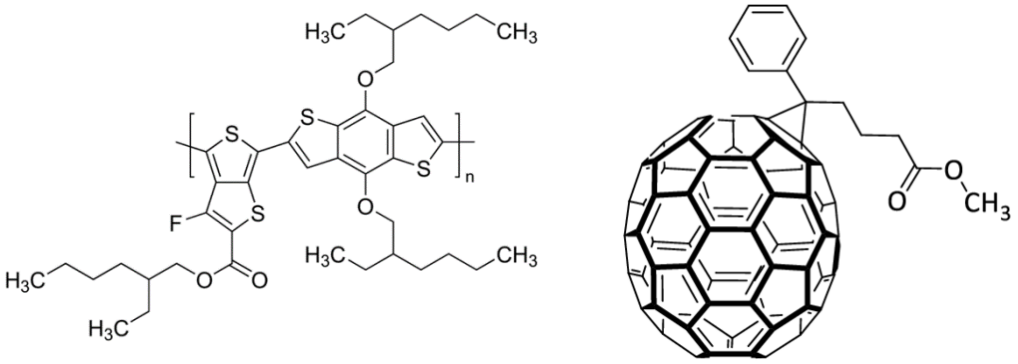

Figure 3.6 The chemical structure of PTB7 (left) and $PC_{71}BM$ (right)

PTB7 is an amorphous polymer and has a hole mobility of about 1×10^{-3} cm^2/Vs.[20] however it gives higher efficiencies than P3HT based OPVs due to its extended absorption into the near infra-red.[21] By using new interface materials and architectures, PTB7 based OPVs have been shown to reach efficiencies of 9.2% *PCE*.[22,23]

The fullerene used to complement the active layer with PTB7 was [6,6]-phenyl-C_{71}-butyric acid methyl ester ($PC_{71}BM$) (1-Material Inc., M_W=1.03 kg mol^{-1}), which is an electron acceptor commonly used in the most efficient organic photovoltaic devices.

The non-symmetrical C_{70} cage of $PC_{71}BM$ enables energetic transitions that are forbidden in C_{60}, improving the absorption characteristics over $PC_{61}BM$ for the visible range of the solar spectrum.[24] The chemical structure of $PC_{71}BM$ is illustrated in **Figure 3.6**.

The insulating polymer used for ternary blend films of Chapter 4 was poly(methyl methacrylate) (PMMA) (Sigma-Aldrich, M_W=15 kg mol^{-1}, M_W=97 kg mol^{-1} & M_W= 350 kg mol^{-1}). This polymer was chosen because it works increasing OPVs lifetime, suggesting it is slightly hygroscopic, which means it has the ability to absorb humidity from the air,[25] and three different molecular weights were used to observe its effect on the lifetime of OPVs. **Figure 3.7** illustrates the chemical structure of PMMA.

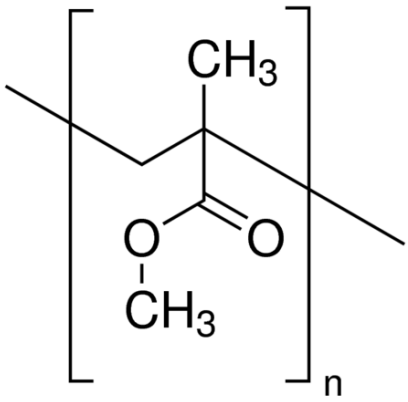

Figure 3.7 The chemical structure of PMMA

PMMA is readily available and dissolves easily in dichlorobenzene (DCB) and chlorobenzene (CB), which were used as the solvents for the P3HT:$PC_{61}BM$ and PTB7:$PC_{71}BM$ OPVs in this work. Al Busaidi et al. showed that the addition of PMMA to P3HT:$PC_{61}BM$ OPVs improves both its initial performance and lifetime.[1] Measurements at a variety of relative humidities suggested that the PMMA acts as a water gettering agent (absorbs water that would otherwise cause degradation). It was also shown that the lifetime improvement with PMMA reduces with increasing relative humidity, suggesting that the polymer can become saturated. Chapter 4 extends this study by considering different molecular weights of PMMA and its effects in different OPV systems, with and without the use of additives.

Although the fabrication of binary and ternary OPVs used for Chapter 4 is explained in section 3.2, it is important to explain the differences between OPV batches and the objective of each one. Control devices of P3HT:$PC_{61}BM$ (1:1 ratio), were compared with ternary P3HT:$PC_{61}BM$:PMMA blends having different concentrations of PMMA. Four main P3HT based batches were prepared comprising the following:

Table 3.2 P3HT based batches with four devices per substrate.

Batch #	PMMA wt% (M_W in kg mol^{-1})			
	Substrate 1	**Substrate 2**	**Substrate 3**	**Substrate 4**
1	0	5 (15)	10 (15)	15 (15)
2	0	5 (97)	10 (97)	15 (97)
3	0	5 (350)	10 (350)	15 (350)
4	0	15 (15)	15 (97)	15 (350)

Each batch was prepared from the same stock solution of P3HT:$PC_{61}BM$ and PMMA. Four devices for each weight ratio of PMMA were prepared for the first three batches. Four devices for each molecular weight of PMMA were prepared for the fourth batch. Batches #1-3 were used to study the effect of varying the wt% of PMMA with a standard M_W, while the batch #4 was used to study the effect of varying the M_W of PMMA with a standard wt%. Initial performance measurements were performed on all OPVs, while lifetime measurements were performed on an average device of each wt% for batches #1-3, and an average one of each M_W of PMMA for batch #4. Between each measurement, OPVs were stored in a dark environment in ambient air at a RH of 40%. An environmental chamber was used to provide and maintain a uniform level of temperature (20-25 ^oC) and humidity (~40–50% RH) in accordance with the standard of the International Summit on OPV Stability ISOS-D-1 shelf aging protocol.[26]

In the case of PTB7 based OPVs, the control devices comprised PTB7:$PC_{71}BM$ in a 1:1.5 ratio, while the ternary devices had a standard 15 wt% of PMMA, having different M_{Ws}. Three main batches were prepared with the following structure:

Table 3.3 PTB7 based batches with four devices per substrate.

Batch #	PMMA wt% (M_W in kg mol^{-1})				DIO additive 3 wt%			
	Sub 1	**Sub 2**	**Sub 3**	**Sub 4**	**Sub 1**	**Sub 2**	**Sub 3**	**Sub 4**
5	0 DCB	0 DCB	0 CB	0 CB	No	Yes	No	Yes
6	0	15 (15)	15 (97)	15 (350)	Yes			
7	0	15 (97)	0	15 (97)	Yes		No	

Again, four devices were prepared for each M_W and initial performance measurements were performed on all OPVs, while lifetime measurements correspond to one average device for each molecular weight of PMMA in both batches. Batch #5 was used to study the effect of using 2 different solvents with and without the DIO additive. Batch #6 was used to study the effect of varying the M_W of PMMA with a standard wt%, while batch #7 was used to study the effect of PMMA without the influence of DIO.

Three extra batches were prepared to briefly analyse the impact of DIO on P3HT based devices, the effect of washing the PTB7 active layer with a small amount of an inert solvent with a low boiling point, and the impact of high amounts of PMMA on P3HT based OPVs, respectively. The same number of devices per substrate and initial and lifetime measurements applied to these three batches:

Table 3.4 Additional batches with four devices per substrate.

Batch #	PMMA wt% (M_W in kg mol^{-1})						DIO additive 3 wt%					
	Sub 1	**Sub 2**	**Sub 3**	**Sub 4**	**Sub 5**	**Sub 6**	**Sub 1**	**Sub 2**	**Sub 3**	**Sub 4**	**Sub 5**	**Sub 6**
8 P3HT	0	15 (97)	0	15 (97)	N/A		Yes		No		N/A	
9 PTB7	0	15 (97)	0	15 (97)	0	15 (97)	Yes		Yes + ethanol wash		No	
10 P3HT	0	15 (97)	40 (97)	50 (97)	N/A		No				N/A	

3.4 Measurement techniques and equipment

3.4.1 Solar Simulator (Light and Dark J-V Characteristics)

A solar simulator (Oriel Sol1A 94021 A) class ABB was used for the measurement of *J-V* under illumination. This solar simulator uses a xenon proprietary filter to meet, efficiently and reliably, class ABB performance parameters without compromising an illumination close to the Air Mass (AM 1.5) solar spectrum, which corresponds to an irradiance of 1000 W/m^2. Spectral match is indicated by the first letter in the solar simulators class rating, meaning that the used solar simulator provide the highest spectral match performance (class A) as defined by the most recent standards from the International Electrotechnical Commission (IEC), Japanese Industrial Standards (JIS) and American Society for Testing and Materials (ASTM).[27] The irradiance uniformity over the working area is indicated by the second letter in a solar simulator class rating. Class B spatial uniformity performance standard is designed to minimize the impact of hot spots, which can otherwise lead to errors in measured cell efficiency. Temporal stability is the third performance parameter of solar simulators, and class B ensures that lamp fluctuations do not significantly distort measurements. At the Department of Engineering level 3 laboratory, the solar simulator intensity output (~1 sun) was checked by myself, using a 91150V calibrated reference cell and meter. However, unless the alignment settings are changed for some other reason, the alignment calibration procedure should only be performed when a new xenon lamp is installed (typical lamp lifetime ~1000 h). Adjustments knobs and an adjustment ladder chain were used by the experimental officer Dr Chris Pearson whenever a calibration was required.

Figure 3.8 shows the test chamber that was used to allow OPV measurements in a protective and controlled environment, which minimized the risk of potential external degradation mechanisms outside the scope of the OPV Stability ISOS-D-1 shelf aging protocol.[26] A 1 mm diameter pinhole defined the illumination area of each device to 0.79 mm^2. A photomask was used following best practices from literature, as lateral electrical conduction or unconsidered scattering or light piping effects may lead to overestimation of photocurrent generation.[28,29] Each substrate had a common ITO anode and four aluminium cathodes, and spring pins were used to allow reliable contact between these electrodes. The test instruments and the device inside the

chamber were connected by a wire to the Al metal and another to the ITO. On the top of the test chamber there was an integrated circuit powered by a 9V battery, which allowed to easily switch between each of the four devices within a substrate for measurements. A Keithley 2400 Source Meter controlled by a LabView PC program applied a -1V to 1V DC voltage sweep to each device. PV characteristics were measured with the solar simulator on, whilst dark *J-V* curves were measured with no illumination. The Keithley 2400 Source Meter was used to create a *J-V* curve similar to a diode characteristic when measuring *J-V* in the dark.

Figure 3.8 Solar simulator (left) and test chamber (right)

Light and dark *JV*-Curves examples of ternary OPVs with different content of insulating polymer are shown in **Figure 3.9**. V_{OC} and J_{SC} can be identified in the light *JV*-Curve, and more details about these parameters are found in Chapter 2 (section 2.6). At low voltages (Region I), the dark *JV* characteristics are primarily determined by a shunt resistance (R_{sh}), at intermediate voltages (Region II) by the diode recombination currents and ideality factor parameters, and at high voltages (Region III) by a series resistance R_s.[30] The ideality factor (n) found in the following Shockley diode equation describes the voltage, or carrier density, dependence of total charge carrier recombination.[31]

$$J = J_0(e^{\frac{qV}{nkT}} - 1) \qquad (3.1)$$

Where:

J = net current flowing through the diode

J_0 = dark saturation current

q = electronic charge

n = ideality factor

k = Boltzmann constant

T = absolute temperature (K)

In Region II, the ideality factor controls the "rectangularity" (FF) of the light J–V characteristic curve. In fact, the overall behaviour, i.e. the shape of the J–V characteristic curve, can largely depend on the value of n.[32] Most OPVs are non ideal to some extent due to recombination arising from their distinctive BHJ structure and their intrinsic large exciton binding energy (about 0.3–0.5 eV).[33,34] Therefore, the recombination effect cannot be neglected, which deviates the ideality factor from the ideal unity value.[31,35] In OPVs the R_s may result from the bulk resistance of the active layer or contact resistance at the electrodes, while R_{sh} may originate from current leakage in the cell.[36] The amount of leakage current at the active layer-electrode interface is indicated by the reverse current, which can affect the open circuit voltage.[37]

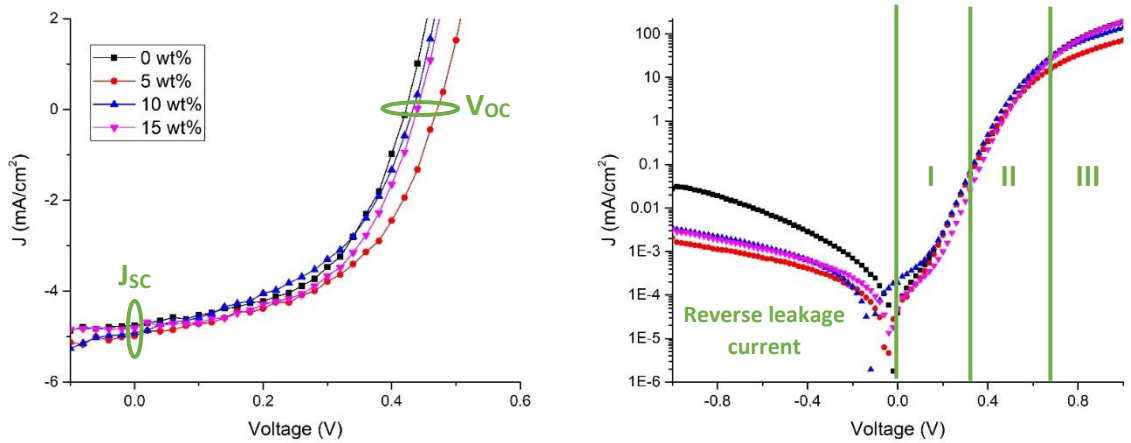

Figure 3.9 Light (left) and dark (right) JV-Curves examples

3.4.2 Atomic Force Microscopy (AFM)

Atomic force microscopy (AFM) is an imaging technique widely used by the scientific community. To measure the force or potential energy between a small tip and a sample, a nm scale probe (cantilever) is employed. AFM tips and cantilevers are typically micro-fabricated from Si or Si_3N_4, and typical tip radius is from a few to 10s of nm. The cantilever provides a force sensor and a force actuator. By pushing the cantilever tip to the sample, its topographic height can be measured, and the interacting force between the tip attached to the cantilever and the sample can be measured by pulling it.[38] Traditionally, most Atomic Force Microscopes use a laser beam deflection system where a laser is reflected from the back of the reflective AFM lever and onto a position-sensitive photodetector.[39] AFM has a feedback loop using the laser deflection to control the force and tip position. As the tip interacts with the surface, the laser position on the photodetector is used in the feedback loop to track the surface for imaging and measuring. The schematic diagram of a basic AFM system is shown in **Figure 3.10**.

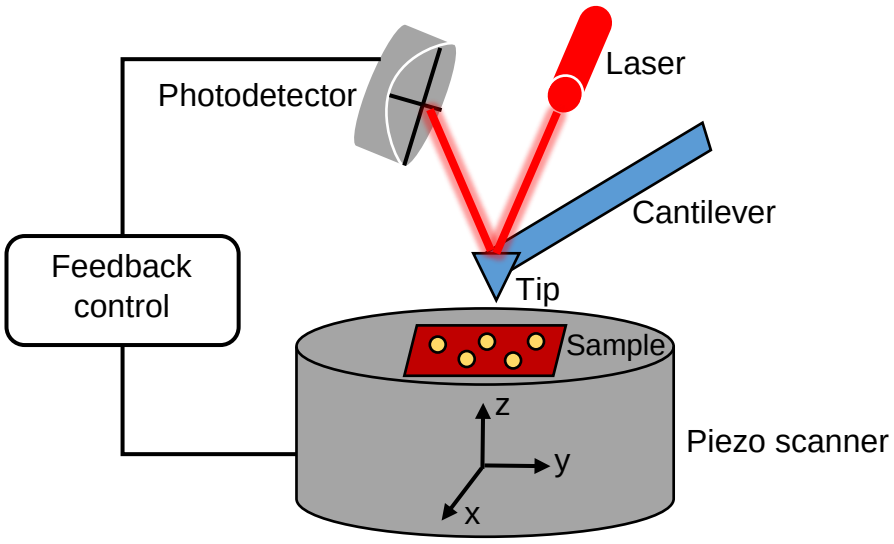

Figure 3.10 AFM schematic diagram

There are three basic modes of operation with an AFM: contact mode, non-contact mode and tapping mode.[38] The simplest mode is the contact mode, also called static, while the non-contact and tapping modes can be grouped as dynamic, which allow the collection of measurements for amplitude, frequency or phase of the

cantilever oscillation. The static mode is done in “contact” with the scanned surface, where the overall force is repulsive, with both long- and short-range forces adding up to the imaging signal (binary or ternary OPVs morphology in this thesis). In the static mode, both tip and sample can be subject to deformation, showing risks regarding collision. The dynamic mode gets its name from the fact that, the cantilever is deliberately vibrated at or close to its resonance frequency and, to allow external excitation for its oscillation, is mounted on an actuator. The resonance of the cantilever is characterised by amplitude, phase and frequency. The variation of these three indicators, due to the interaction force, can be measured and the force will be evaluated from the above registered signals, through a theoretical formalism. The main differences between the non-contact and tapping mode is that the former is dominated by attractive interaction forces with the tip never making contact with the surface and its amplitude of oscillation is of less than 10 nm, while in the latter the tip touches the surface intermittently and gently, with its cantilever amplitude oscillation typically ranging from 100-200 nm.

AFM (Veeco Dimension 3100) shown in **Figure 3.11** was used in tapping mode to measure the thickness of the active layer and the surface morphology of binary and ternary OPVs. AFM probes were from Budget Sensors, model Tap300Al-G with a spring constant of 0.2 Nm^{-1}. AFM measurements were under carried by the experimental officer Dr Chris Pearson in the level 4 cleanroom. A sharp metal point was used to scratch the surface of the OPVs, and by imaging the edge of the scratch it was possible to measure the different layers thicknesses. The scratched area was scanned at a location where all of the OPV layers could be clearly observed, as shown in **Figure 3.12**. After collecting the topography data, the image was flattened using the AFM software. The flatten command eliminates unwanted and uncorrelated to signal features (e.g., noise, bow and tilt) from scan lines. Finally, both the total thickness of the device layers (active layer + PEDOT:PSS layer) and the PEDOT:PSS thickness were determined, separately, from a line profile. The active layer thickness was calculated by subtracting the thickness of the PEDOT:PSS from the total thickness. Gwyddion 2.50 software[40] was used to analyse the characteristics of the PMMA islands that appeared in the ternary OPVs images.

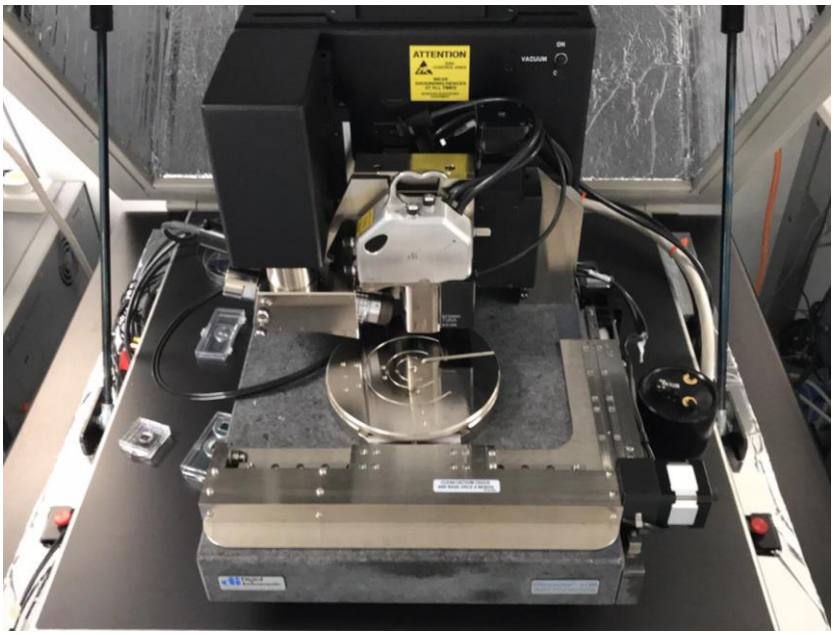

Figure 3.11 AFM equipment

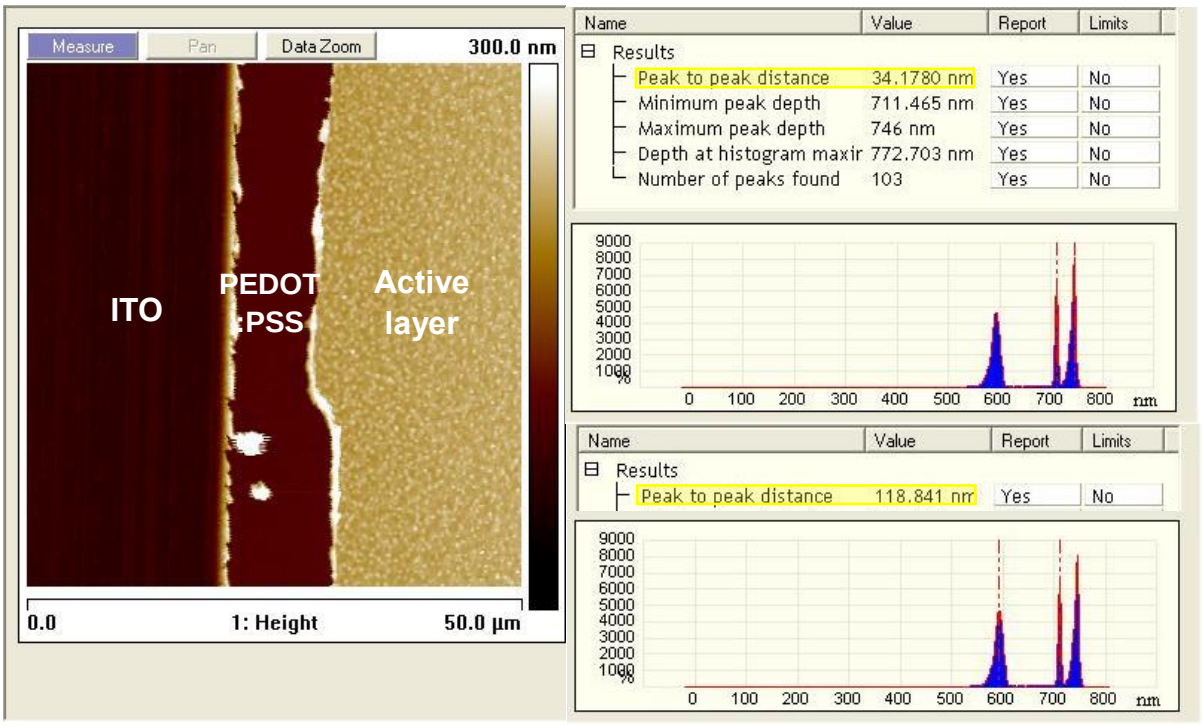

Figure 3.12 AFM flattened image showing OPV layers (left). A sharp metal point was used to scratch the surface of the OPV and allow imaging of the edge of the scratch. Upper right "peak to peak distance" indicates PEDOT:PSS thickness, and lower right "peak to peak distance" indicates active layer thickness

3.4.3 Ultraviolet visible (UV-vis) spectroscopy

UV-vis Spectroscopy (or Spectrophotometry) is a quantitative technique used to measure the absorption of solid thin films.[41] This is done by measuring the intensity of light that passes through a sample with respect to the intensity of light through a reference sample or blank. In this study the reference sample was a clean ITO coated substrate with PEDOT:PSS on the top, whilst the active layer sample was a binary or ternary OPV (**Figure 3.3**).

A Shimadzu UV-1800 spectrophotometer (**Figure 3.13**) was used to measure the absorption of the OPV blend films over the range of 300 to 1100 nm. The spectrophotometer uses a deuterium lamp and a tungsten-halogen lamp to cover the specified wavelength range. A monochromator splits the light into the different wavelengths that pass through the samples, and a silicon photodiode detector measures the photons transmitted through the film. **Figure 3.14** shows the spectrophotometer schematic diagram.

Figure 3.13 UV-vis equipment

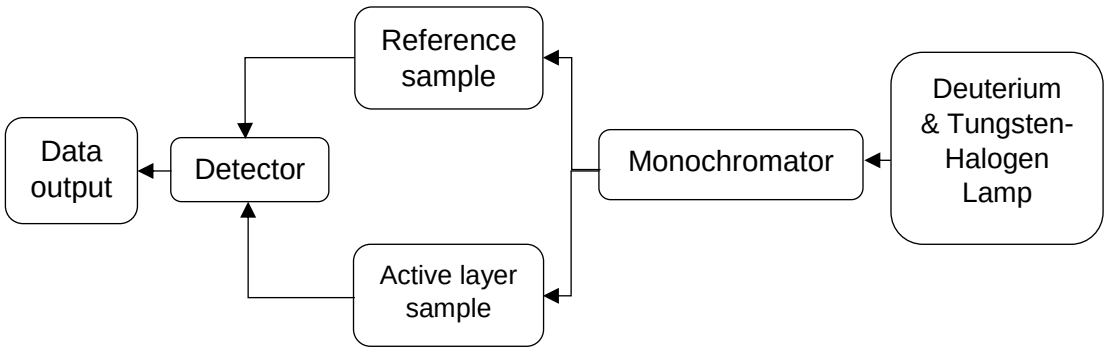

Figure 3.14 Spectrophotometer schematic diagram

3.4.4 External Quantum Efficiency (EQE)

The external quantum efficiency (EQE) is the ratio of the number of carriers collected by the solar cell to the number of photons of a given energy incident on the solar cell.[42] The quantum efficiency may be given either as a function of wavelength or as energy. If all photons of a certain wavelength are absorbed and the resulting minority carriers are collected, then the quantum efficiency at that particular wavelength is 1.0 or 100%. The quantum efficiency for photons with energy below the band gap is zero.

EQE measurements were conducted using a Monochromator System (Oriel Cornerstone™ 130 1/8 m) (**Figure 3.15**) linked to a PC with MatLab software capable of plotting the graphs to observe the effective percentage of photon absorption along the visible spectrum. To ensure the correct operation of the system a weekly calibration was performed with a certificated reference photodiode.

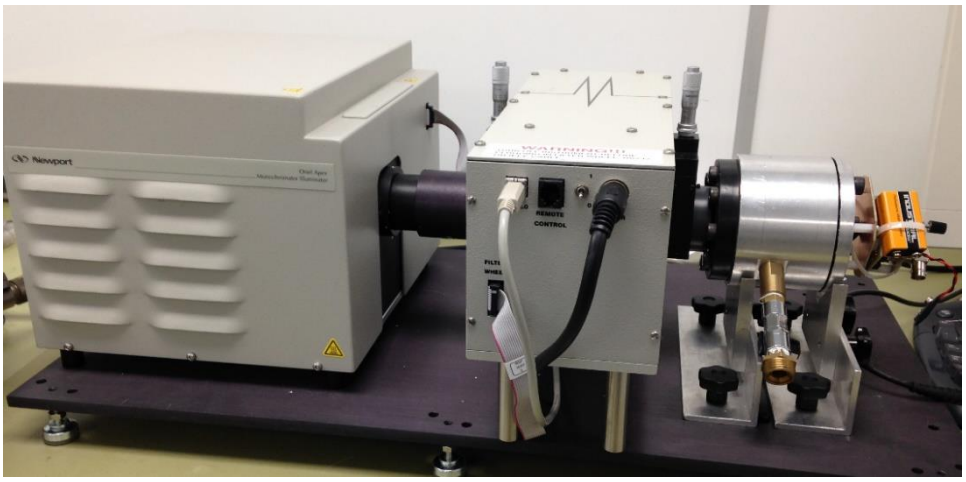

Figure 3.15 EQE measuring system

3.4.5 Scanning Electron Microscopy (SEM)

A scanning electron microscope scans a focused electron beam over a surface to create an image. The electrons in the beam interact with the sample, producing various signals that can be used to obtain information about the surface topography and composition.[43] My analysis reports SEM findings from Al-Busaidi, Zakiya, former PhD student from the Department of Engineering at Durham University.[44] In her

thesis, OPV films were coated with carbon to ensure the material was fully conductive and improve the imaging quality. A focused ion beam (FIB) system was used to cut a cross section of the OPVs, and platinum was used as a protective layer while FIB milling.

SEM measurements were under carried by Leon Bowen, Technical Manager of the Electron Microscopy Laboratory from the Physics Department at Durham University. A Hitachi SU-70 scanning electron microscope (**Figure 3.16**) with a beam energy of 5keV and FEI Helios Nanolab 600 microscope (**Figure 3.17**) were used to create the SEM images.

Figure 3.16 Hitachi SU-70 equipment

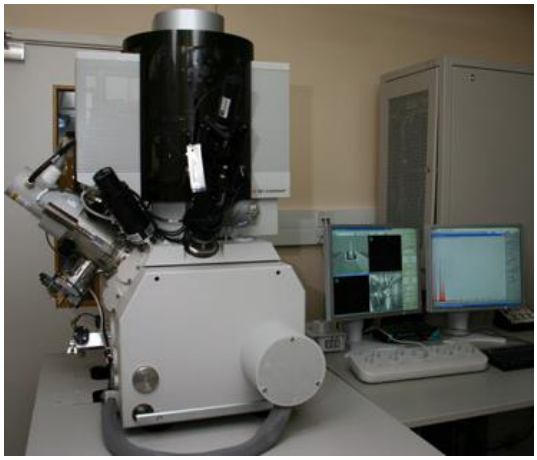

Figure 3.17 FEI Helios Nanolab 600 equipment

3.5 References

1 Al-Busaidi, Z., Pearson, C., Groves, C. & Petty, M. C. (2017). Enhanced lifetime of organic photovoltaic diodes utilizing a ternary blend including an insulating polymer. *Solar Energy Materials and Solar Cells* 160, 101-106.

2 Barreiro-Argüelles, D., Ramos-Ortiz, G., Maldonado, J.-L., Pérez-Gutiérrez, E., Romero-Borja, D., Meneses-Nava, M.-A. & Nolasco, J. C. (2018). Stability study in organic solar cells based on PTB7:PC71BM and the scaling effect of the active layer. *Solar Energy* 163, 510-518.

3 Kettle, J., Ding, Z., Horie, M. & Smith, G. C. (2016). XPS analysis of the chemical degradation of PTB7 polymers for organic photovoltaics. *Organic Electronics* 39, 222-228.

4 Cao, W. & Xue, J. (2014). Recent progress in organic photovoltaics: device architecture and optical design. *Energy & Environmental Science* 7, 2123.

5 Suchand Sangeeth, C. S., Jaiswal, M. & Menon, R. (2009). Correlation of morphology and charge transport in poly(3,4-ethylenedioxythiophene)-polystyrenesulfonic acid (PEDOT-PSS) films. *J Phys Condens Matter* 21, 072101.

6 Stöcker, T., Köhler, A. & Moos, R. (2012). Why does the electrical conductivity in PEDOT:PSS decrease with PSS content? A study combining thermoelectric measurements with impedance spectroscopy. *Journal of Polymer Science Part B: Polymer Physics* 50, 976-983.

7 Nielsen, C. B., Holliday, S., Chen, H. Y., Cryer, S. J. & McCulloch, I. (2015). Non-fullerene electron acceptors for use in organic solar cells. *Acc Chem Res* 48, 2803-2812.

8 Dang, M. T., Hirsch, L. & Wantz, G. (2011). P3HT:PCBM, best seller in polymer photovoltaic research. *Adv Mater* 23, 3597-3602.

9 Hu, R., Zhang, W., Wang, P., Qin, Y., Liang, R., Fu, L. M., Zhang, J. P. & Ai, X. C. (2014). Characterization and distribution of poly(3-hexylthiophene) phases in an annealed blend film. *Chemphyschem* 15, 935-941.

10 Kumar, P. & Chand, S. (2012). Recent progress and future aspects of organic solar cells. *Progress in Photovoltaics: Research and Applications* 20, 377-415.

11 Laquai, F., Andrienko, D., Mauer, R. & Blom, P. W. (2015). Charge carrier transport and photogeneration in P3HT:PCBM photovoltaic blends. *Macromol Rapid Commun* 36, 1001-1025.

12 Ansari, M. A., Mohiuddin, S., Kandemirli, F. & Malik, M. I. (2018). Synthesis and characterization of poly(3-hexylthiophene): improvement of regioregularity and energy band gap. *RSC Advances* 8, 8319-8328.

13 Guo, X., Cui, C., Zhang, M., Huo, L., Huang, Y., Hou, J. & Li, Y. (2012). High efficiency polymer solar cells based on poly(3-hexylthiophene)/indene-C70 bisadduct with solvent additive. *Energy & Environmental Science* 5.

14 NREL Best Research-Cell Efficiency Chart. (2021). https://www.nrel.gov/pv/cell-efficiency.html.

15 Ossila - PCBM. (2021). https://www.ossila.com/products/pcbm?variant=30366226088032.

16 Sariciftci, N. S., Smilowitz, L., Heeger, A. J. & Wudl, F. (1992). Photoinduced electron transfer from a conducting polymer to a buckminsterfullerene.pdf. *Science* 258, 1474-1476.

17 Zhao, J., Li, Y., Yang, G., Jiang, K., Lin, H., Ade, H., Ma, W. & Yan, H. (2016). Efficient organic solar cells processed from hydrocarbon solvents. *Nature Energy* 1.

18 Lin, Y., Wang, J., Zhang, Z. G., Bai, H., Li, Y., Zhu, D. & Zhan, X. (2015). An electron acceptor challenging fullerenes for efficient polymer solar cells. *Adv Mater* 27, 1170-1174.

19 Green, M., Dunlop, E., Hohl-Ebinger, J., Yoshita, M., Kopidakis, N. & Hao, X. (2020). Solar cell efficiency tables (version 57). *Progress in Photovoltaics: Research and Applications* 29, 3-15.

20 Ebenhoch, B., Thomson, S. A. J., Genevičius, K., Juška, G. & Samuel, I. D. W. (2015). Charge carrier mobility of the organic photovoltaic materials PTB7 and PC71BM and its influence on device performance. *Organic Electronics* 22, 62-68.

21 Liang, Y., Xu, Z., Xia, J., Tsai, S. T., Wu, Y., Li, G., Ray, C. & Yu, L. (2010). For the bright future-bulk heterojunction polymer solar cells with power conversion efficiency of 7.4%. *Adv Mater* 22, E135-138.

22 He, Z., Zhong, C., Huang, X., Wong, W. Y., Wu, H., Chen, L., Su, S. & Cao, Y. (2011). Simultaneous enhancement of open-circuit voltage, short-circuit current density, and fill factor in polymer solar cells. *Adv Mater* 23, 4636-4643.

23 He, Z., Zhong, C., Su, S., Xu, M., Wu, H. & Cao, Y. (2012). Enhanced power-conversion efficiency in polymer solar cells using an inverted device structure. *Nature Photonics* 6, 591-595.

24 Zhang, F., Zhuo, Z., Zhang, J., Wang, X., Xu, X., Wang, Z., Xin, Y., Wang, J., Wang, J., Tang, W. *et al.* (2012). Influence of PC60BM or PC70BM as electron acceptor on the performance of polymer solar cells. *Solar Energy Materials and Solar Cells* 97, 71-77.

25 Zohuriaan-Mehr, M. J. & Kabiri, K. (2008). Superabsorbent Polymer Materials A Review. *Iran. Polym. J.* 17, 451-477.

26 Reese, M. O., Gevorgyan, S. A., Jørgensen, M., Bundgaard, E., Kurtz, S. R., Ginley, D. S., Olson, D. C., Lloyd, M. T., Morvillo, P., Katz, E. A. *et al.* (2011). Consensus stability testing protocols for organic photovoltaic materials and devices. *Solar Energy Materials and Solar Cells* 95, 1253-1267.

27 Oriel Sol1A Class ABB Solar Simulators. (2019). https://www.newport.com/medias/sys_master/images/images/h5d/h0f/934193761487 8/DS-031001-Oriel-Sol1A.pdf.

28 Kiermasch, D., Gil-Escrig, L., Bolink, H. J. & Tvingstedt, K. (2019). Effects of Masking on Open-Circuit Voltage and Fill Factor in Solar Cells. *Joule* 3, 16-26.

29 Lin, C. F., Lin, B. H., Liu, S. W., Hsu, W. F., Zhang, M., Chiu, T. L., Wei, M. K. & Lee, J. H. (2012). Optical effects of shadow masks on short circuit current of organic photovoltaic devices. *Phys Chem Chem Phys* 14, 3837-3842.

30 Servaites, J. D., Ratner, M. A. & Marks, T. J. (2011). Organic solar cells: A new look at traditional models. *Energy & Environmental Science* 4.

31 Tvingstedt, K. & Deibel, C. (2016). Temperature Dependence of Ideality Factors in Organic Solar Cells and the Relation to Radiative Efficiency. *Advanced Energy Materials* 6.

32 Jao, M.-H., Liao, H.-C. & Su, W.-F. (2016). Achieving a high fill factor for organic solar cells. *Journal of Materials Chemistry A* 4, 5784-5801.

33 Feron, K., Belcher, W. J., Fell, C. J. & Dastoor, P. C. (2012). Organic solar cells: understanding the role of Forster resonance energy transfer. *Int J Mol Sci* 13, 17019-17047.

34 Halls, J. J. M., Cornil, J., dos Santos, D. A., Silbey, R., Hwang, D. H., Holmes, A. B., Brédas, J. L. & Friend, R. H. (1999). Charge- and energy-transfer processes at polymer/polymer interfaces: A joint experimental and theoretical study. *Physical Review B* 60, 5721-5727.

35 Giebink, N. C., Wiederrecht, G. P., Wasielewski, M. R. & Forrest, S. R. (2010). Ideal diode equation for organic heterojunctions. I. Derivation and application. *Physical Review B* 82, 155305.

36 Qi, B. & Wang, J. (2013). Fill factor in organic solar cells. *Phys Chem Chem Phys* 15, 8972-8982.

37 Brédas, J.-L., Norton, J., Cornil, J. & Coropceanu, V. (2009). Molecular understanding of organic solar cells the challenges. *Acc. Chem. Res.* 42, 1691–1699.

38 Warwick - Atomic Force Microscopy. (2021). https://warwick.ac.uk/fac/sci/physics/current/postgraduate/regs/mpagswarwick/ex5/techniques/structural/afm.

39 Nanoscience - Atomic Force Microscopy. (2021). https://www.nanoscience.com/techniques/atomic-force-microscopy/.

40 Gwyddion Software. (2021). http://gwyddion.net/download.php.

41 UV-vis spectroscopy technique. (2021). https://www.edinst.com/techniques/uv-vis-spectroscopy/.

42 PVeducation Quantum Efficiency. (2021). https://www.pveducation.org/pvcdrom/solar-cell-operation/quantum-efficiency.

43 Scanning electron microscopy technique. (2021). https://www.nanoscience.com/techniques/scanning-electron-microscopy/.

44 AL-BUSAIDI, Z., NASSER,KHALFAN. *Enhanced Lifetime of Organic Photovoltaics based on P3HT: PCBM*, Durham theses, Durham University, (2017).

CHAPTER 4
Enhancing the lifetime of OPVs using a ternary blend strategy

4.1 Introduction

Organic Photovoltaics (OPVs) use a variety of donor and acceptor combinations which lead to devices with different efficiencies, but they all degrade by similar mechanisms mainly linked to ambient light,[1-3] temperature,[4,5] oxygen[6-8] and water.[7,9,10] Coupling the donor with the fullerene acceptors phenyl-C61-butyric acid methyl ester ($PC_{61}BM$)[11] and phenyl-C71-butyric acid methyl ester ($PC_{71}BM$)[12] reduces photo-oxidation, which would otherwise have a negative impact in its mechanical and electronic properties.[13] However, this improvement in photo-oxidation stability is not enough to yield commercial level lifetimes. Water and oxygen can ingress to the active layer through microscopic holes in the electrode,[14] reacting with the donor or acceptor[15] and leading to increased charge recombination,[16] which accelerates the degradation of OPVs performance.[17] Some donor and acceptors are less affected by degradation than others,[11,18,19] but they all need further improvements in active layer stability and compatibility with encapsulation methods in order to achieve acceptable lifetimes. Fluorinated plastic laminates and parylene, Al_2O_3 and ZrO_2[20-22] barrier layers have been proved to be compatible with flexible OPVs. Despite the compatibility between OPVs and these barriers there are some drawbacks. The mentioned barrier layers can greatly increase the cost[23-25] of the final device and still do not assure a long enough lifetime from a commercial point of view, as the water vapour and oxygen ingress protection is not sufficient. It is important to note that the focus of this chapter is looking at intrinsic stability, which is an important contributing part of the lifetime solution, although some sort of encapsulant would still be needed to minimise extrinsic degradation.

A recent study explored a novel method to reduce OPV degradation, which consisted in combining the donor poly(3-hexylthiophene) (P3HT) and acceptor $PC_{61}BM$ with the inert polymer poly-methyl(methacrylate) (PMMA) in a common solvent prior to deposition.[26] It was suggested that the hygroscopic PMMA[27] acts as a gettering agent for water, because experiments revealed that the ternary OPVs had

longer lifetimes than the P3HT:$PC_{61}BM$ control to an extent which depended on the relative humidity. Despite the reduced P3HT:$PC_{61}BM$ content in the active layer, they found that diluting the donor:acceptor layer with PMMA marginally boosted the initial power conversion efficiency (*PCE*) at some concentrations, similarly as observed by Qin et al.[28] in another study. Therefore, blending PMMA with the active layer can potentially reduce the requirements placed on active materials and encapsulants for flexible and rigid OPV devices, whilst minimising their cost. However, it is unclear from past research what role PMMA morphology has in this approach's success, or whether this procedure is relevant to other donor:acceptor mixtures. Here, the PMMA weight percentage (wt%) and molecular weight (M_W) is varied in two different active layer combinations (P3HT:$PC_{61}BM$ and PTB7:$PC_{71}BM$) to further address the unanswered questions of this lifetime increasing method. Fabrication of OPV devices is explained in Chapter 3 (section 3.2), whilst composition of control and ternary devices of each batch is explained in Chapter 3 (section 3.3).

Overall, the goal of this chapter is to improve and explain the lifetime of OPVs through blending the donor:acceptor binary blend with the inert polymer PMMA, which slows performance degradation via the 'gettering' of water.[26] The effect of PMMA morphology on the success of this strategy is investigated, leading to device design guidelines. It is shown that adding PMMA can be effective in enhancing the lifetime of different active material combinations, although not to the same extent, and it is also shown that processing additives can have a negative impact in the devices lifetime. These findings show that blending PMMA with different donor:acceptor pairs is an easy and efficient technique to improve OPVs lifetime, and suggest that combining this approach with newer more stable materials and more efficient encapsulants may enable OPVs to have long lifetimes required for commercial applications.

4.2 Characterisation summary

The current-voltage characteristics of OPVs were measured in the dark and under AM 1.5 illumination (Oriel Sol1A 94021 A) using a Keithley 2400 SourceMeter (section 3.4.1). All measurements under illumination used a mask to restrict illumination to an active area of 0.79 mm^2. Each batch of OPVs comprised four to six substrates of four devices each that were measured to ensure reliable statistics. UV-

vis absorption was measured alongside current-voltage measurements using a UV-1800 Shimadzu UV spectrophotometer (section 3.4.3). EQE measurements were conducted using a Monochromator System (Oriel Cornerstone^{TM} 130 1/8 m) (section 3.4.4). In all cases, measurements of average devices are reported rather than 'champion' devices with the highest performance or lifetime. Following initial characterisation in a N_2 atmosphere, OPVs were stored in a dark environmental chamber in ambient air with controlled temperature (20–25 ^{o}C) and humidity (40–50% RH), thereby following the standard of the International Summit on OPV Stability ISOS-D-1 shelf aging protocol.[29] Devices were removed from the environmental chamber for current-voltage and UV-vis absorption measurements to be taken, prior to being replaced for further aging. This process was repeated until the power conversion efficiency (*PCE*) fell to 20% of its original value. AFM was used in a cleanroom environment to characterise surface topography and measure layer thicknesses (section 3.4.2). Gwyddion 2.50 image processing software [30] was used to analyse the characteristic surface features shown in the ternary OPV blends. Chapter 3 provides more details for the equipment enlisted in this section.

4.3 Impact of PMMA morphology on P3HT:PC_{61}BM lifetime

Two series of ternary P3HT:PC_{61}BM:PMMA OPVs were manufactured to investigate how the distribution of PMMA within the active layer effects OPV lifetime and performance. PMMA weight percent (wt%) and molecular weight (M_W) were varied in each series, respectively. Molecular weight is the average weight of the molecules that make up a polymer and thus gives an indication of the length of the polymer chains. The polymerization process is subject to variation so there is no single chain length, there is actually a wide range of lengths, and the M_W average is found by measuring samples of the material as it is produced.[31] In general, a higher molecular weight improves the mechanical properties of polymers. However, a higher molecular weight also increases the melt and glass transition temperature as well as the solution and melt viscosity which makes processing and forming of the polymeric material more difficult.[32] The molecular weight of polymers is also known to influence phase separation, through its effect on several parameters. For instance, an increasing chain length increases the free energy of mixing in polymer solutions and, thus, promotes

phase separation,[33] which can be described in terms of the Flory-Huggins interactions parameter χ. In the Flory-Huggins theory, each lattice site is taken to be the volume of one solvent molecule and it is assumed that each polymer occupies *N* lattice sites (number of statistical segment lengths). As a consequence, the statistical segment size is calculated at a reference volume of the solvent. For volume fractions φ_1 and φ_2, the following expression for the free energy of mixing per site of a polymer solution applies:[34]

$$\frac{\Delta G_m}{kT} = \left(\varphi_1 ln\varphi_1 + \frac{\varphi_2}{N} ln\varphi_2 + \varphi_1\varphi_2\chi\right) \qquad (4.1)$$

Where k is the Boltzmann constant and T is the absolute temperature. Although Flory-Huggins can be useful to predict the behaviour of mixtures of a conjugated polymer with a solvent, fullerene or another polymer, it is more complicated to predict the behaviour of ternary blends like the two series of ternary P3HT:$PC_{61}BM$:PMMA OPVs here analysed, especially taking in consideration P3HT crystallisation. PMMA is available in a range of M_Ws, hence we varied the M_W from 15 kg mol^{-1} to 350 kg mol^{-1} whilst keeping 15 wt% of PMMA in one series, while the other series kept a constant PMMA M_W of 350 kg mol^{-1} and its concentration was increased from 5% to 15 wt%. In this way, aspects of the ternary blend morphology could be controlled, and the corresponding impact on OPV performance measured. All series included binary P3HT:$PC_{61}BM$ OPV devices to serve as a control (more details in sections 3.2 and 3.3 of Chapter 3). **Figure 4.1**a-d shows the AFM images of the series of blend films in which PMMA M_W was varied. It is observed that domed regions appear in the topology when PMMA is added to the P3HT:$PC_{61}BM$ blend. The corresponding AFM images for the series in which wt% of PMMA was varied are shown in **Figure 4.2**. Experiments from a previous study by Al-Busaidi et al.[26] also showed the appearance of domed regions in the topology of P3HT:$PC_{61}BM$:PMMA OPVs with 14wt% of PMMA with M_W = 97 kg mol^{-1}. They inferred that the domed sections were PMMA-rich because conductive AFM measurements showed that they had low conductivity when compared to the surrounding regions (P3HT:$PC_{61}BM$-rich). **Figure 4.1**e shows a cross-sectional SEM image, here used to further investigate the domed regions.

Surprisingly, it is found that the PMMA-rich domains form beneath the active layer, suggested to be due to the high wettability of the PMMA on the PEDOT:PSS surface.[35] Given that the addition of PMMA extends the lifetime of P3HT:PC_{61}BM-based OPVs in the presence of atmospheric water vapour,[26] this suggests that atmospheric water has significant mobility in the device before reacting with the active materials, be it either through the PEDOT:PSS layer or through the P3HT:PC_{61}BM-rich active layer. This supposition is supported by conductive AFM images of ternary devices reported by Al-Busaidi et al.,[26] since the conductivity of the P3HT:PC_{61}BM-rich regions degrades uniformly across the heterogeneous film. It is important to note that PMMA was kept as part of the active layer blend and not as top-layer because it was found that laminating devices with PMMA can diminish the electrical properties of OPVs.[26]

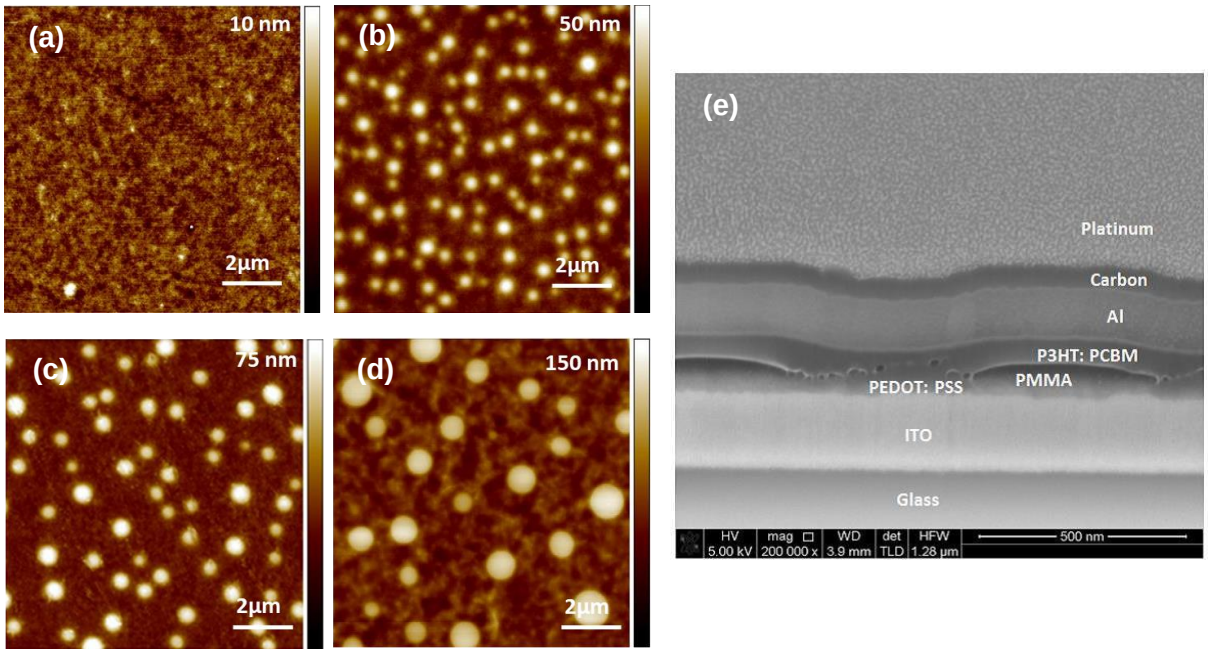

Figure 4.1 AFM topography images of active layers comprising (a) P3HT:PC_{61}BM and P3HT:PC_{61}BM:PMMA with 15 wt% PMMA of M_W (b) 15 kg mol^{-1}, (c) 97 kg mol^{-1} and (d) 350 kg mol^{-1}. (e) Cross-sectional SEM image of a P3HT:PC_{61}BM:PMMA blend film with 14 wt% of M_W = 97 kg mol^{-1} PMMA.

The size of the PMMA-rich domains can be adjusted by the M_W and wt% of PMMA, according to the present P3HT:PC_{61}BM:PMMA devices AFM studies. **Figure 4.1** shows that the size of the PMMA-rich domains increases with PMMA M_W for a constant

wt% of PMMA (**Table 4.1** lists average area, density, and height of the PMMA-rich domes). The solvent evaporates faster from the PMMA-rich phase and solidifies first onto the substrate as M_W increases.[36] This accelerated drop out of the solution results in larger PMMA-rich domains and less PMMA available in the remaining P3HT:$PC_{61}BM$-rich regions, therefore resulting in a total higher volume of isolated PMMA (**Figure 4.3**) that provides increased protection against water vapour.

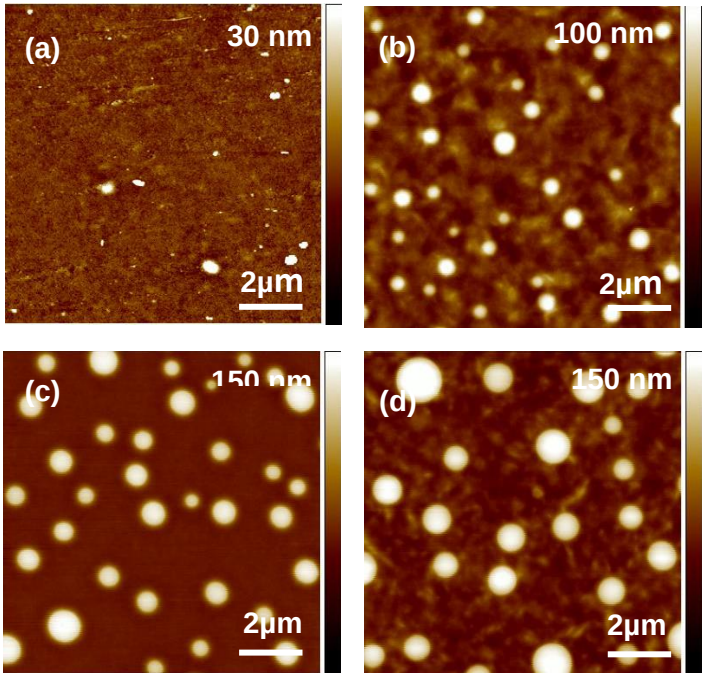

Figure 4.2 AFM topography images of average binary P3HT:$PC_{61}BM$ film (a) and P3HT:$PC_{61}BM$:PMMA ternary films with PMMA at 350 kg mol^{-1} M_W in concentration (b) 5 wt%, (c) 10wt% and (d) 15 wt% of PMMA.

Table 4.1 AFM images showing circular islands characteristic of average P3HT:$PC_{61}BM$:PMMA ternary films with 15 wt% of PMMA and a M_W of 15, 97 & 350 kg mol^{-1}.

Active layer	PMMA M_W (kg mol^{-1})	wt%	Islands			Film thickness (nm)
			Density (# of islands)	Mean Area (µm²)	Mean Depth (nm)	
P3HT: $PC_{61}BM$: PMMA	15	15	152	0.1235	13.57	103.48
	97	15	49	0.4249	25.01	105.22
	350	15	28	0.4985	49.62	121.74
	Average		76	0.3490	29.40	110.14

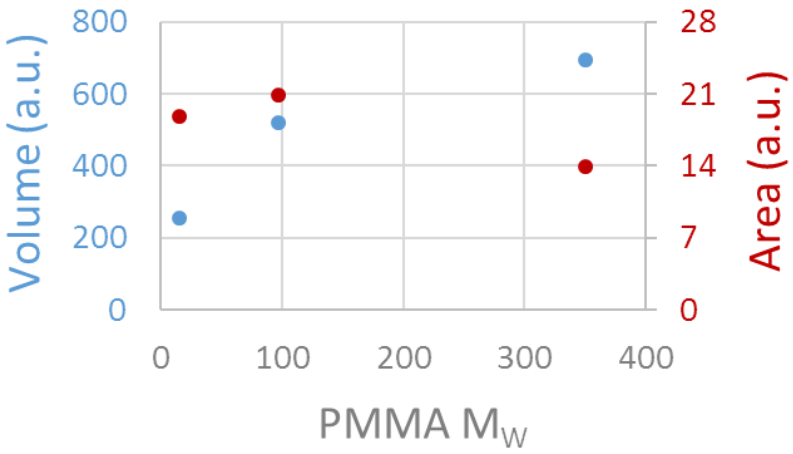

Figure 4.3 Total volume and area coverage of the PMMA islands observed in P3HT:PC_{61}BM:PMMA ternary films in Figure 4.1b-d. Total area = density x mean area, and Total volume = total area x mean depth, from Table 4.1.

Increasing the wt% of PMMA whilst keeping the M_W constant also increases the size of PMMA-rich domains in P3HT:PC_{61}BM:PMMA devices, as shown in **Figure 4.2**. Unlike the first series, changing only the wt% of PMMA and not the M_W, is not expected to change the equilibrium concentration of PMMA in the PMMA-rich and P3HT:PC_{61}BM-rich regions.[37] Bigger PMMA-rich regions are simply a result of the higher concentration of PMMA in solution. Therefore, the two series of P3HT:PC_{61}BM:PMMA devices allow for some degree of control over the amount and location of PMMA within the OPV.

Turning the attention into the lifetime of the ternary OPVs, **Figure 4.4**a illustrates ISOS-D-1 degradation of the *PCE* for average P3HT:PC_{61}BM:PMMA OPVs with 15 wt% PMMA but varying M_W, normalised to the initial value. Similar to Al-Busaidi et al,[26] it is shown that ternary OPVs with PMMA have a longer lifetime than the binary control. **Figure 4.4**b-d shows that this improvement in lifetime is largely due to an improvement of the rate in which J_{SC} degrades when PMMA is added. In the presence of PMMA, the Fill Factor (*FF*) degrades more slowly, while the open-circuit voltage (V_{OC}) remains basically constant for all devices with measurable photovoltaic action. It has been argued that the presence of water in P3HT:PC_{61}BM OPV active layers leads to trap formation and increased recombination,[16] and that water-related trap-formation is slowed in the presence of PMMA.[26] Increased trapping can lead to increased charge recombination, as suggested by other OPV systems data.[38,39] This

in turn effects J_{SC} and *FF* as seen here, hence the data is consistent with this explanation. However, it is important to clarify that although ISOS-D-1 aging protocol is useful to assess the shelf stability of OPVs under oxygen and moisture conditions (focus of this chapter), it does not take into account the effect of light induced degradation as ISOS-L-1 or ISOS-O-1 do, which would change the rate of J_{SC} and *FF* degradation of encapsulated OPVs used in real world applications.

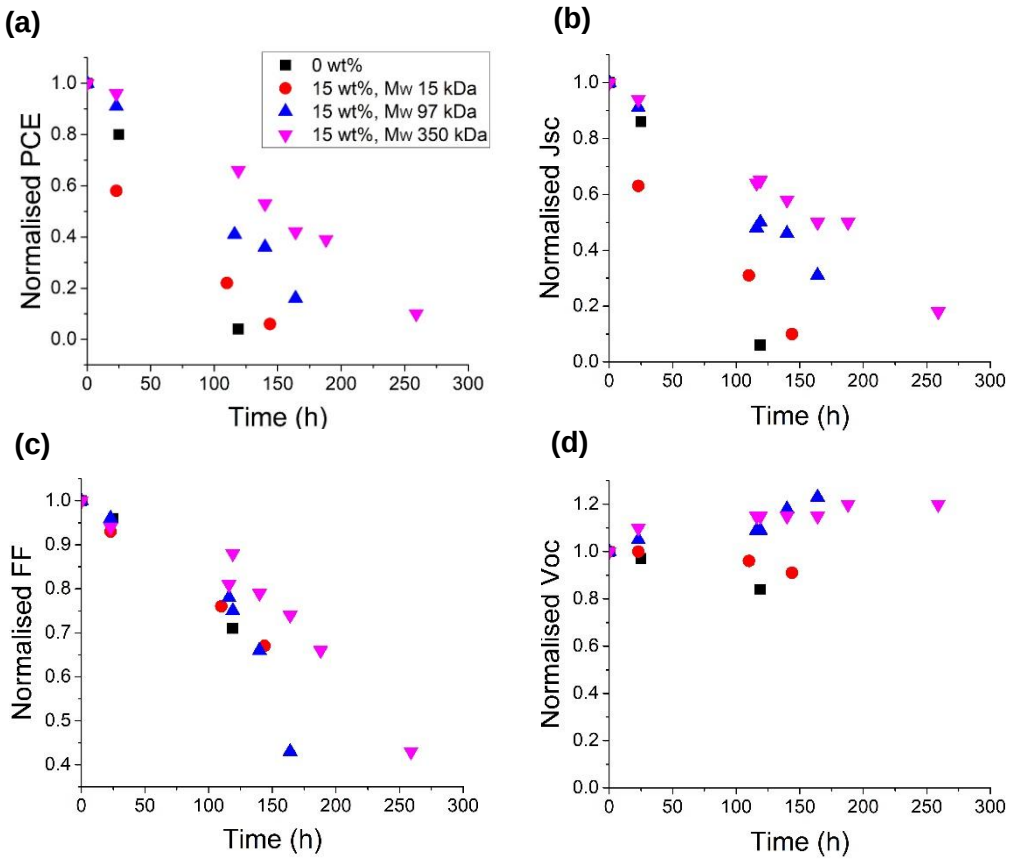

Figure 4.4 Normalised (a) PCE, (b) J_{SC}, (c) FF and (d) V_{OC} as a function of time for average binary P3HT:$PC_{61}BM$ blend (black squares) and ternary P3HT:$PC_{61}BM$:PMMA blend with 15 wt% of PMMA and M_W = 15 kg mol^{-1} (red circles), 97 kg mol^{-1} (blue up triangles) and 350 kg mol^{-1} (pink down triangles). Devices were aged according to ISOS-D-1 standard. Initial PCE range (not normalised): 0.9 - 1.1%.

Figure 4.4a shows a significant variation in OPV lifetime as a function of PMMA M_W. This set of devices contains the same amount of PMMA, but that its distribution varies with M_W (**Figure 4.1**). The positive impacts of PMMA are greatest for the largest M_W (350 kg mol^{-1}), which have the largest, most widely distributed PMMA-rich regions

(**Figure 4.1**d). **Figure 4.5**c shows normalised *PCE* lifetime for the second series of OPVs in which wt% of 350 kg mol^{-1} PMMA was increased from 0% to 15%. It can be seen that lifetime improves with increasing wt% of PMMA, which from **Figure 4.2**, is associated with larger PMMA-rich domains. **Figure 4.6** shows that the improvement in lifetime is again largely due to a reduction in the rate at which J_{SC} degrades. These findings suggest that large, widely spread PMMA-rich zones are most effective at extending OPV lifetime, thus providing design criteria for future ternary OPV devices.

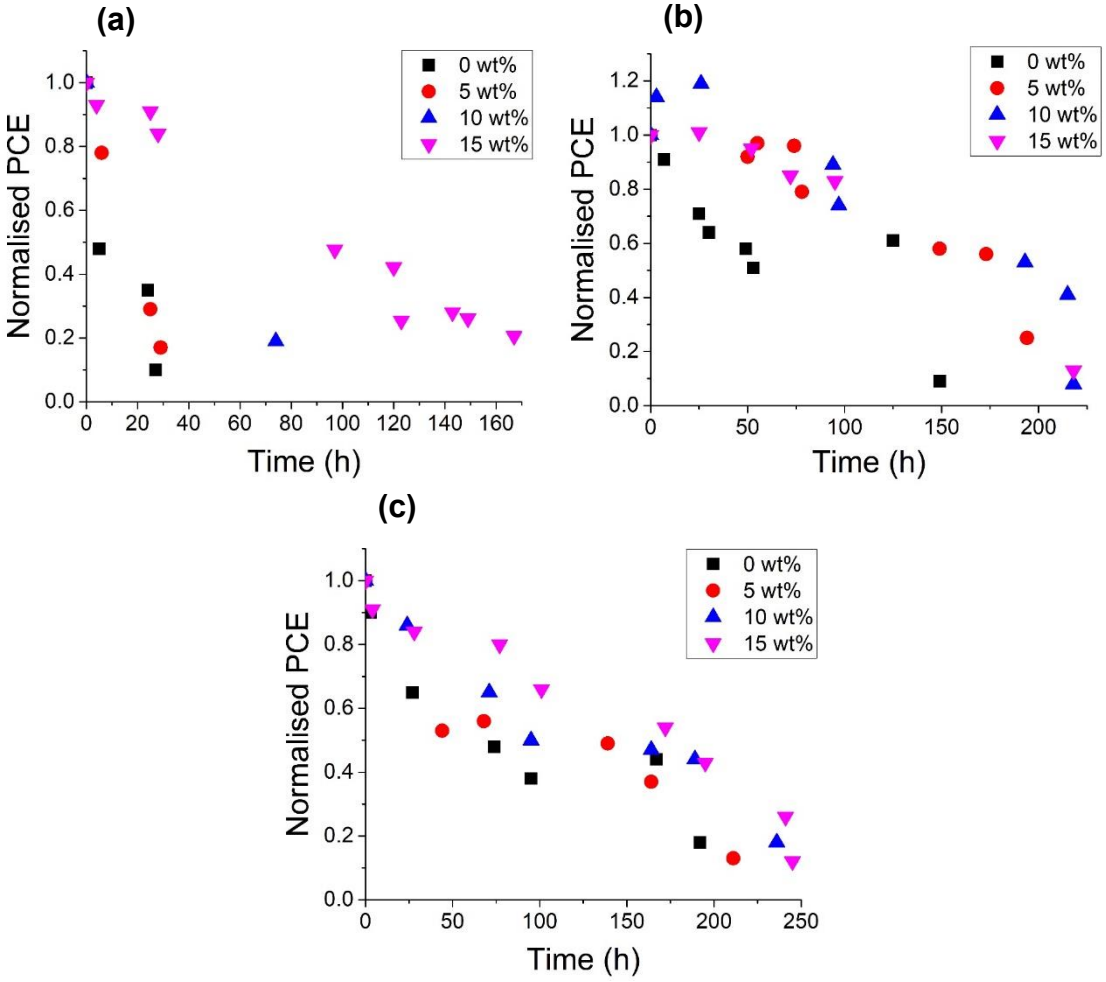

Figure 4.5 Normalised power conversion efficiency (PCE) as a function of time for average devices with different content of PMMA with (a) 15 kg mol^{-1}, (b) 97 kg mol^{-1} and (c) 350 kg mol^{-1} M_W. Binary P3HT:PC_{61}BM blend (black squares) and ternary P3HT:PC_{61}BM:PMMA blend with a 5 wt% (red circles), 10 wt% (blue up triangles) and 15 wt% (pink down triangles) of PMMA. Initial PCE range (not normalised): 0.8 - 1.2%.

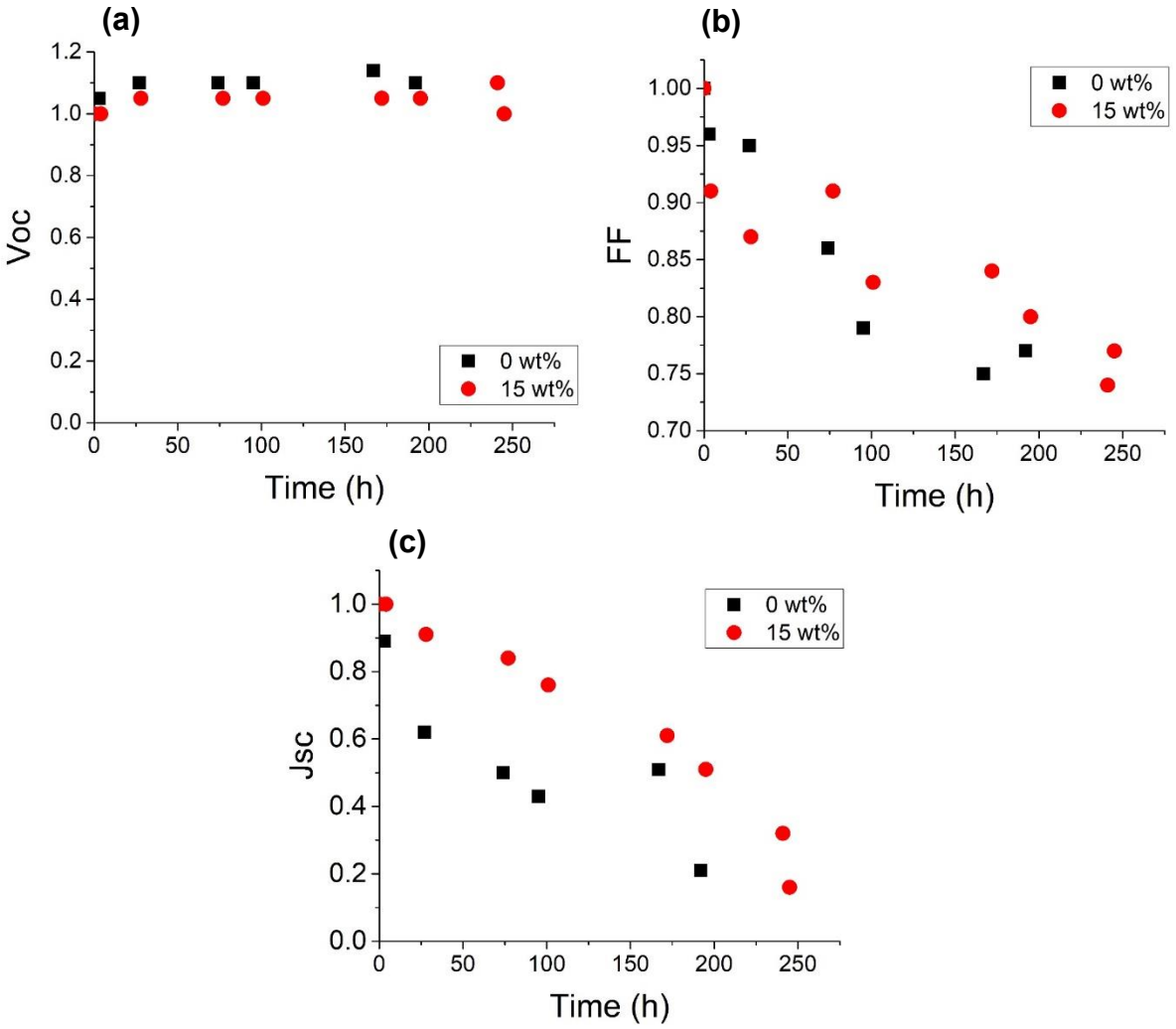

Figure 4.6 Normalised electrical characteristics showing the degradation of average binary P3HT:$PC_{61}BM$ (black squares) and ternary P3HT:$PC_{61}BM$:PMMA 15 wt% M_W 350 kg mol^{-1} (red circles) OPVs. (a) V_{OC}, (b) FF & (c) J_{SC}.

External quantum efficiency (EQE) measurements were also taken. EQE is the fraction of photons incident on the solar cell that create electron-hole pairs in the absorber, which are successfully collected, so it is related to J_{SC}, which degradation was slowed in the ternary OPVs. **Figure 4.7** shows the EQE degradation spectra of binary P3HT:$PC_{61}BM$ and ternary P3HT:$PC_{61}BM$:PMMA OPVs with increasing M_W. Although the devices with 15 kg mol^{-1} & 97 kg mol^{-1} M_W had a higher initial EQE than the 350 kg mol^{-1} M_W OPV, still this last one showed a much lower EQE degradation rate and outperformed the others in terms of lifetime (**Figure 4.4**). In all cases, the shape of the EQE curve did not change with degradation, rather its value was scaled. This suggests degradation is not related to light absorption of one component, rather

it appears the losses that happen during degradation are due to electronic recombination.[16]

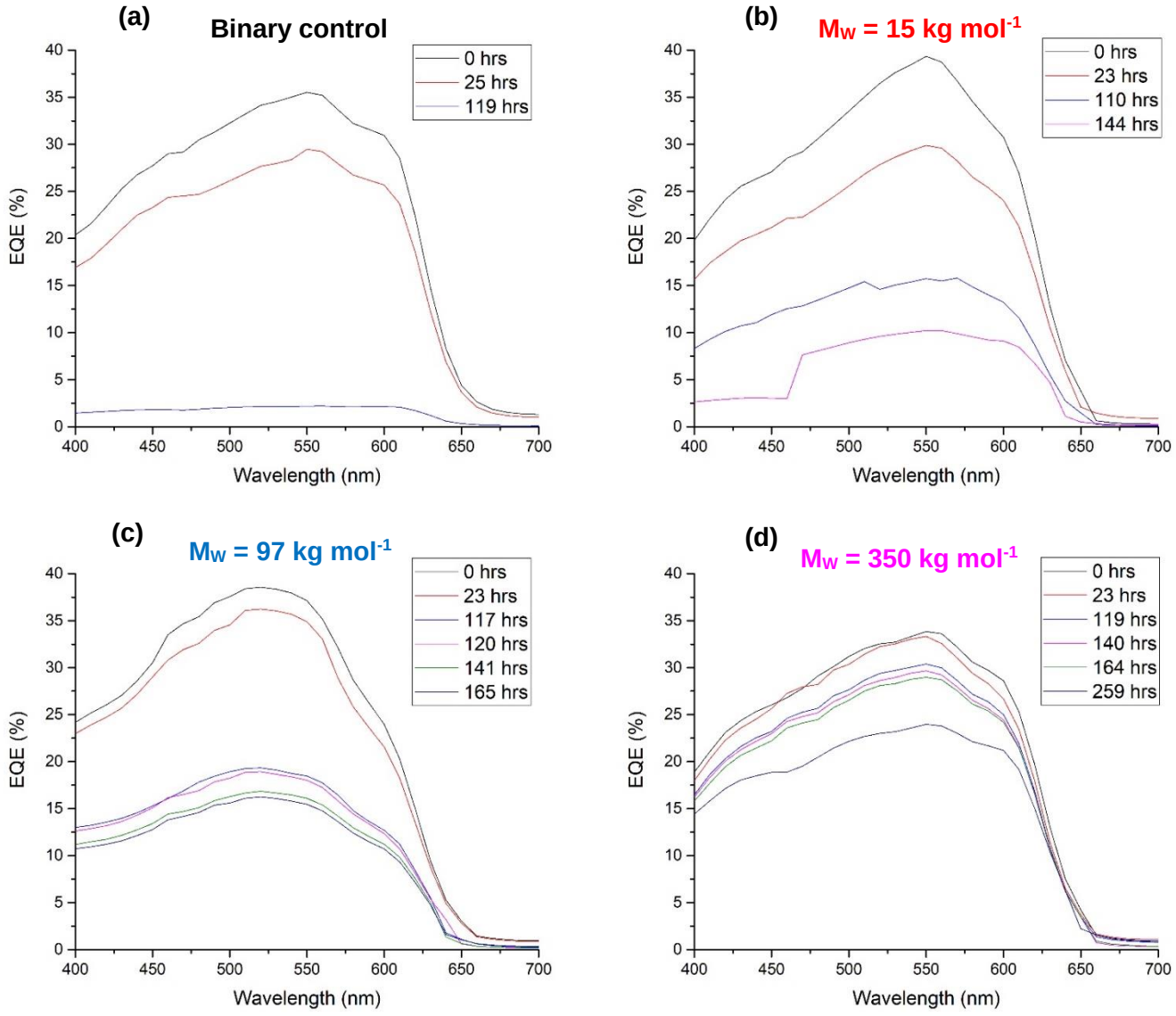

Figure 4.7 EQE degradation of (a) average binary P3HT:$PC_{61}BM$ binary blend and of P3HT:$PC_{61}BM$:PMMA ternary blends with 15 wt% of PMMA and (b) M_W = 15 kg mol^{-1} (c), M_W = 97 kg mol^{-1} & (d) M_W = 350 kg mol^{-1}.

Although the morphology role and benefits of PMMA to OPV lifetime are established by the data, the precise mechanism by which PMMA extends lifetime in OPVs is less clear. However, the gathered evidence is here evaluated. Al-Busaidi et al[26] demonstrated that adding PMMA to P3HT:$PC_{61}BM$ slowed the rate of OPV degradation resulting from atmospheric water vapour. Water may enter through

pinholes in the Al electrode[40] or by diffusion through the PEDOT:PSS layer. While there were no observable pinholes in the Al electrodes after fabrication, there was localised delamination in the form of bubbles after aging, as shown in **Figure 4.8**. Following aging in ambient air, similar bubbles on the cathode of organic LEDs were reported by Luo et al[41]. This was attributed to the formation of Hydrogen gas as a result of a reaction between water and Aluminium, which resulted in electrode delamination.[42] Further, Luo et al[41] found that PEDOT:PSS facilitated the formation of bubbles in the electrode, suggesting that the hygroscopic nature of PEDOT:PSS transported atmospheric water laterally through the device. Here, although bubbles appeared on the Al electrode of both aged ternary and binary OPVs, less bubbles were present in the ternary electrode. As a result, the data appear to be compatible with initial atmospheric water infiltration through the PEDOT:PSS, which is accelerated by the electrode rupturing due to Al-water reaction. More importantly, the physical process of electrode delamination is slowed down by the inclusion of PMMA in the ternary devices.

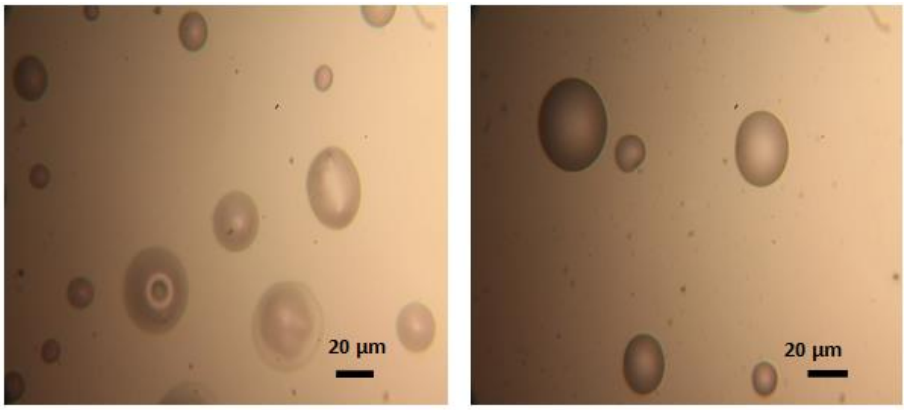

Figure 4.8 Optical micrographs of Al electrode following 24 hours exposure to 85% relative humidity ambient, corresponding to accelerated aging conditions. Left shows P3HT:$PC_{61}BM$ reference device whilst right shows P3HT:$PC_{61}BM$:PMMA ternary device with 14 wt% PMMA with M_W = 97 kg mol^{-1}.

Delamination in combination with aging also affects the PV performance parameters of the OPVs. The current findings demonstrate that changes in *FF* and J_{SC} are the primary cause of *PCE* deterioration, indicating that recombination increases over time. **Figure 4.4**d shows that V_{OC} is barely impacted with aging, hence these results are an indicative of shallow trapping (i.e. not recombination-active).

Shallow traps have been proven to form from clusters or simple traces of water,[43,44] limiting charge transport and increasing current voltage dependency.[43] This is in agreement with Al-Busaidi et al,[26] who utilised conductive AFM and observed reduced conductivity in aged devices, which underwent chemical changes that lead to increased trapping. However, despite the heterogeneity of the ternary blend, they also revealed that the loss of conductivity had negligible spatial dependence. Still, all the gathered data analysis shows that *PCE* degradation is a consequence of electrode and active layer chemical changes accelerated by atmospheric water vapour infiltration. More evident is that water has significant mobility in the buffer and active layers before interacting with Al or any of the active materials (P3HT and $PC_{61}BM$) and that PMMA regions can trap the water during this time of mobility, which consequently improves the lifetime of the OPVs.

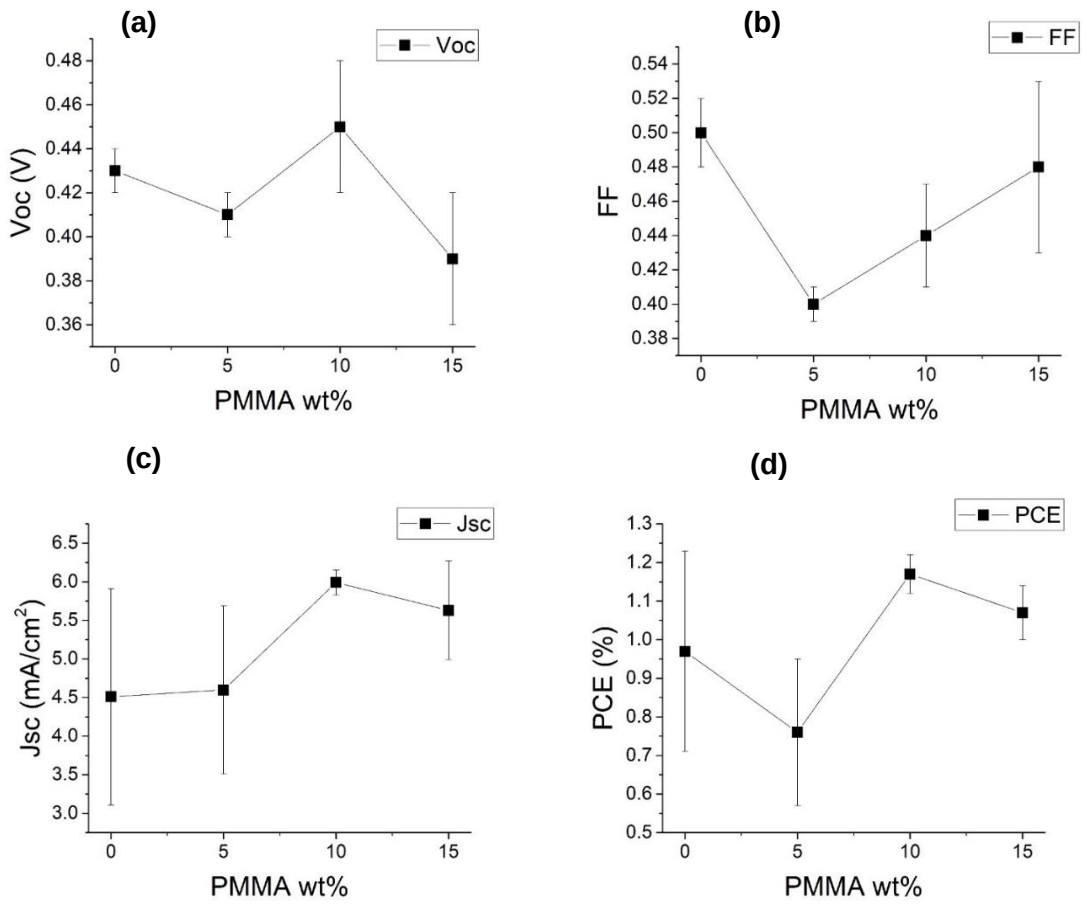

Figure 4.9 Initial electrical characteristics of binary P3HT:$PC_{61}BM$ films (0 wt%) and P3HT:$PC_{61}BM$:PMMA ternary films (5, 10 & 15 wt%) with PMMA M_W of 350 kg mol^{-1}. (a) V_{OC}, (b) FF, (c) J_{SC} & (d) PCE. Four devices of each wt% were measured to obtain these results.

Having established that PMMA can reduce the rate at which *PCE* degrades, now the impact of PMMA on initial absolute performance is considered. **Figure 4.9** and **Figure 4.10** show the impact of varying wt% and M_W of PMMA respectively upon the statistics of *PCE*, J_{SC}, V_{OC} and *FF*. No significant trend in *PCE* is observed in either series, with most devices displaying a *PCE* in the region of 0.8 to 1.2%, suggesting that adding PMMA does not have a significant impact in the initial performance of P3HT:PC_{61}BM OPVs. Instead, the initial efficiency range is attributed to batch to batch variations.

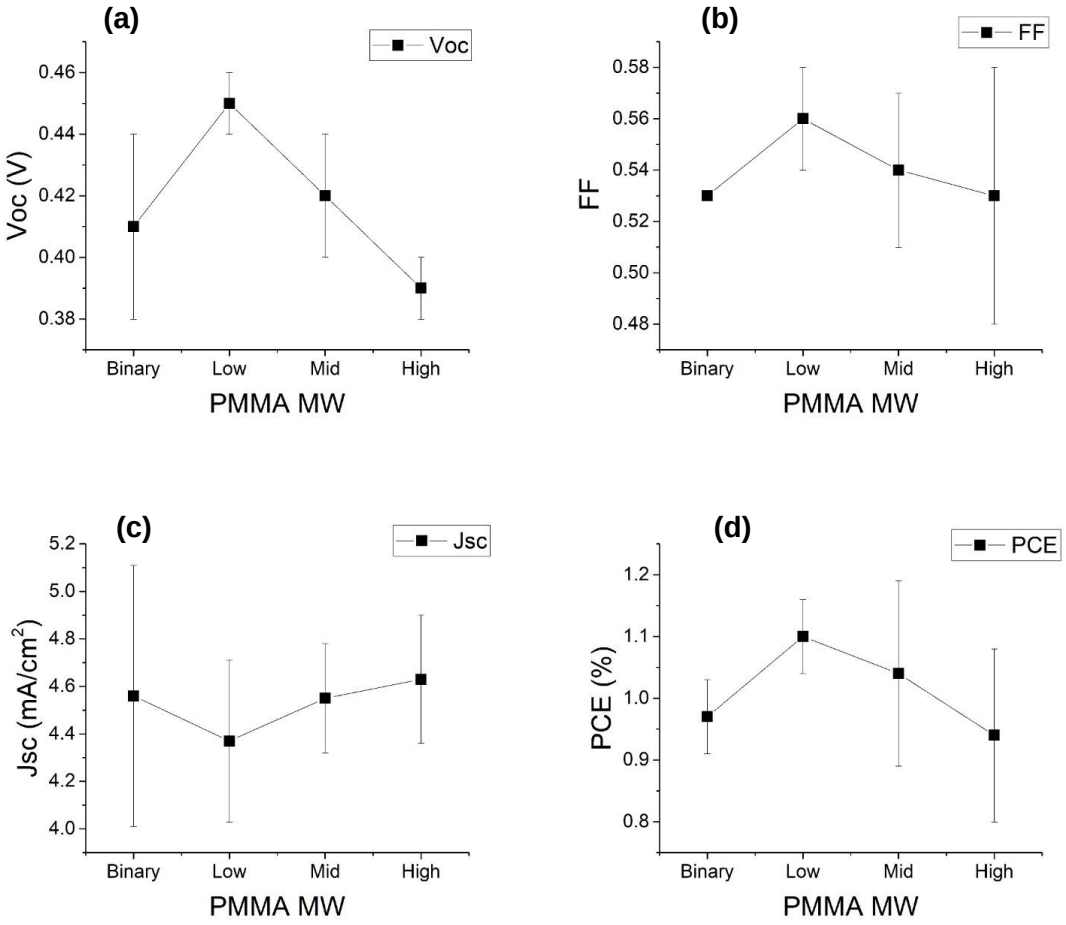

Figure 4.10 Initial electrical characteristics of P3HT:PC_{61}BM binary films (no PMMA) and of P3HT:PC_{61}BM:PMMA ternary films with a 15 wt% and 15 kg mol^{-1} (Low), 97 kg mol^{-1} (Mid) & 350 kg mol^{-1} (High) M_W of PMMA. (a) V_{OC}, (b) FF, (c) J_{SC} & (d) PCE. Four devices of each M_W were measured to obtain these results.

However, as observed in **Figure 4.11**, the inclusion of PMMA reduces reverse leakage current, which is attributed to a reduction in parallel current routes across the

PMMA-rich regions shown in **Figure 4.1**e. The reduction in reverse leakage current indicates that blending donor:acceptor materials with PMMA may also improve the detectivity of organic photodetectors.[45] These data add to those reported for organic field-effect transistors[46] and light-emitting diodes,[47] which show that devices containing inert polymers can perform as or better than those with polymer small molecule blends.

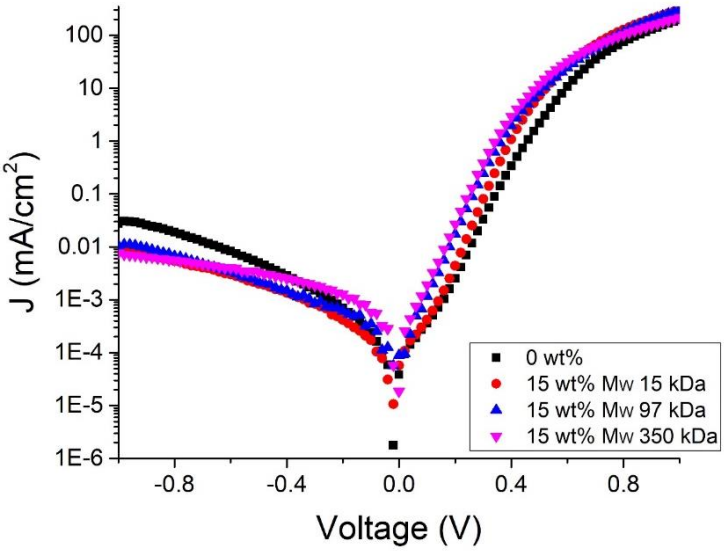

Figure 4.11 Dark J-V Curves for average binary P3HT:$PC_{61}BM$ blend (black squares), and ternary P3HT:$PC_{61}BM$:PMMA blend with 15wt% and a M_W of 15 kg mol^{-1} (red circles), 97 kg mol^{-1} (blue up triangles) and 350 kg mol^{-1} (pink down triangles) of PMMA.

4.4 Effectiveness of PMMA on PTB7:$PC_{71}BM$ system

To investigate whether incorporating PMMA into the active layer can increase the lifetime of other donor:acceptor systems, a series of OPVs were fabricated with PTB7 as donor and $PC_{71}BM$ as acceptor, being an OPV blend with different morphological characteristics[48] and higher performance[49] than previously analysed P3HT:$PCB_{61}BM$. The additive DIO is commonly used in binary PTB7:$PC_{71}BM$ OPVs to limit the size of fullerene aggregates and thereby maximise *PCE*,[48,50] hence, the initial consideration was to fabricate binary PTB7:$PC_{71}BM$ and ternary PTB7:$PC_{71}BM$:PMMA OPVs incorporating DIO as described in section 3.2 of Chapter 3. However, two different solvents (DCB & CB) with and without DIO were used in the preparation of PTB7:$PC_{71}BM$ OPVs to test which solvent resulted in higher initial

performance of binary devices before fabricating ternary OPVs. **Figure 4.12** illustrates the typical *J-V* curves under illumination for binary devices using DCB & CB solvents with and without the DIO additive. It is observed that adding the DIO additive to both solvents DCB & CB conducts to a significant increase in the J_{SC} (from 5 & 4 mA/cm^2 to ~8 & 11 mA/cm^2 respectively) and therefore an increase in the *PCE*. The positive effect of DIO is more pronounced when using CB, leading to good charge generation, attributed to uniform morphology with small phase separation in a previous study.[51] The improvement in J_{SC} is the reason why the following ternary batch was carried out with CB+DIO as the mixture solvent.

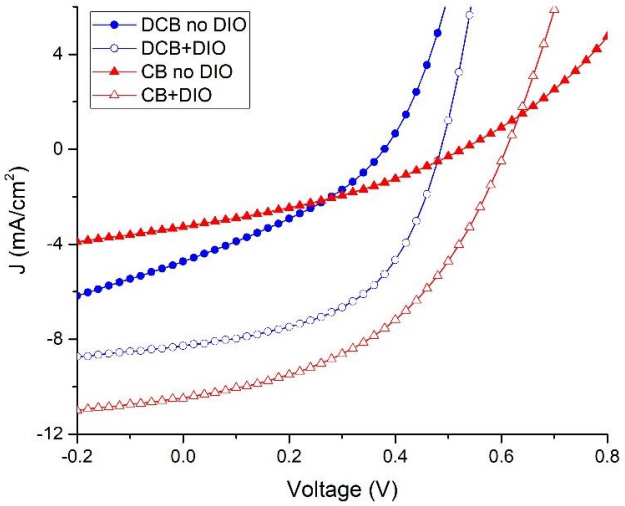

Figure 4.12 J-V Curves under illumination for average binary PTB7:$PC_{71}BM$ OPVs using DCB as solvent without DIO (filled blue circles) and with DIO (open blue circles), and using CB as solvent without DIO (filled red triangles) and with DIO (open red triangles).

Figure 4.13 shows ISOS-D-1 *PCE* degradation for ternary PTB7:$PC_{71}BM$:PMMA OPVs with 15 wt% of PMMA having M_W = 15, 97 and 350 kg mol^{-1}, compared to a binary PTB7:$PC_{71}BM$ OPV control. It is apparent that the lifetime of PTB7:$PC_{71}BM$-based devices is lower than that of P3HT:$PCB_{61}BM$ (**Figure 4.4**), and that addition of PMMA has no discernible impact on OPV lifetime. Furthermore, **Figure 4.14** shows that initial J_{SC} and *PCE* for ternary PTB7:$PC_{71}BM$:PMMA OPVs is less than half that of the binary counterpart initial performance. To investigate the underlying reasons of PMMA having an apparent negative effect in PTB7-based OPVs, further measurements and analysis are now presented.

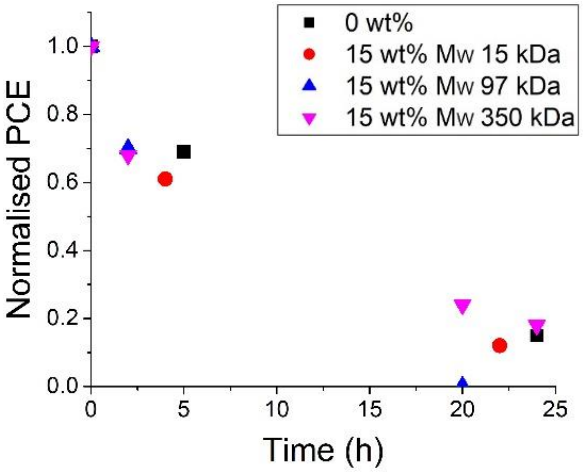

Figure 4.13 Normalised PCE as a function of time for average binary PTB7:$PC_{71}BM$ blend with DIO (black squares) and ternary PTB7:$PC_{71}BM$:PMMA blend with DIO and 15 wt% of PMMA and M_W = 15 kg mol^{-1} (red circles), 97 kg mol^{-1} (blue up triangles) and 350 kg mol^{-1} (pink down triangles). Initial PCE binary (not normalised): 3.0%. Initial PCE range ternary (not normalised): 0.5 - 0.8%.

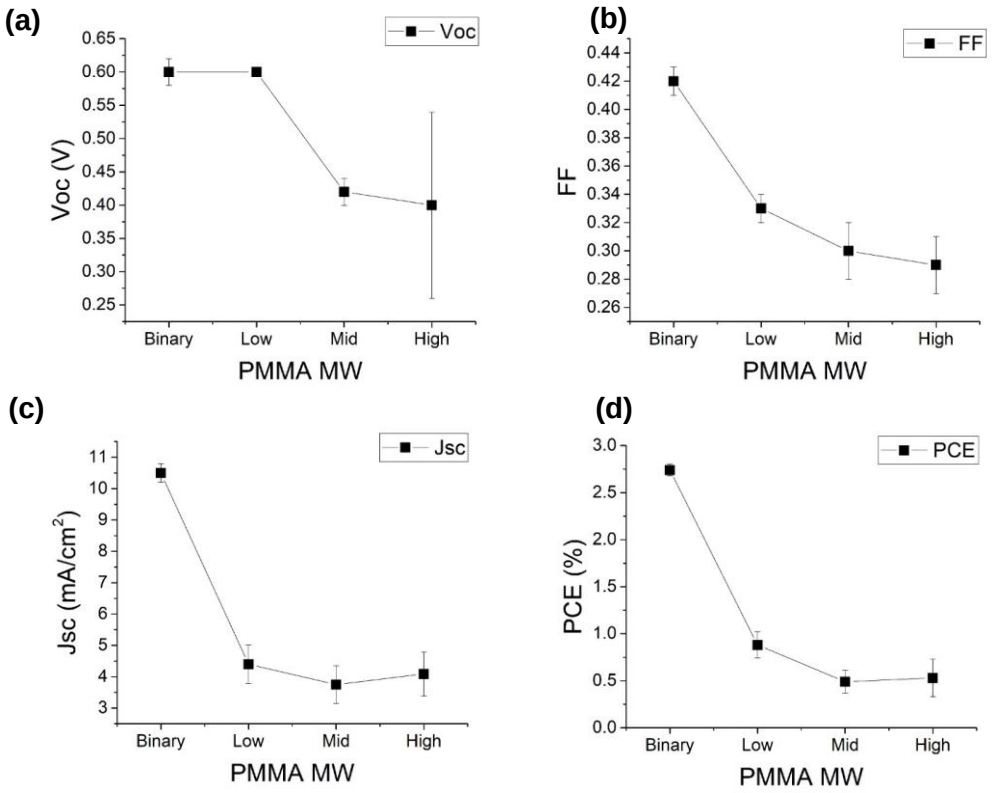

Figure 4.14 Initial electrical characteristics of PTB7:$PC_{71}BM$ binary films and of PTB7:$PC_{71}BM$:PMMA ternary films with a 15 wt% and 15 kg mol^{-1} (Low), 97 kg mol^{-1} (Mid) & 350 kg mol^{-1} (High) M_W of PMMA. All blends have DIO. (a) V_{OC}, (b) FF, (c) J_{SC} & (d) PCE. Four devices of each M_W were measured to obtain these results.

Figure 4.15 illustrates the typical dark *J-V* curves for ternary devices containing the same amount of PMMA (15 wt%) but different M_W. We note that an increase in series resistance (R_S) is not generally observed in P3HT:$PC_{61}BM$ OPVs when PMMA is added (~2 Ω cm^2 in **Figure 4.11**), while here it is observed that R_S increases when adding PMMA to PTB7:$PC_{71}BM$ OPVs (**Table 4.2**). Other studies have argued that increased R_S can reduce *FF*, and reduce the efficiency of charge collection, and hence J_{SC}.[52,53] Increased R_S may therefore be a reason PTB7:$PC_{71}BM$:PMMA ternary devices have lower performance than the PTB7:$PC_{71}BM$ binary controls possibly due to reduced charge generation, however the exact mechanism leading to this behaviour remains uncertain at this point.

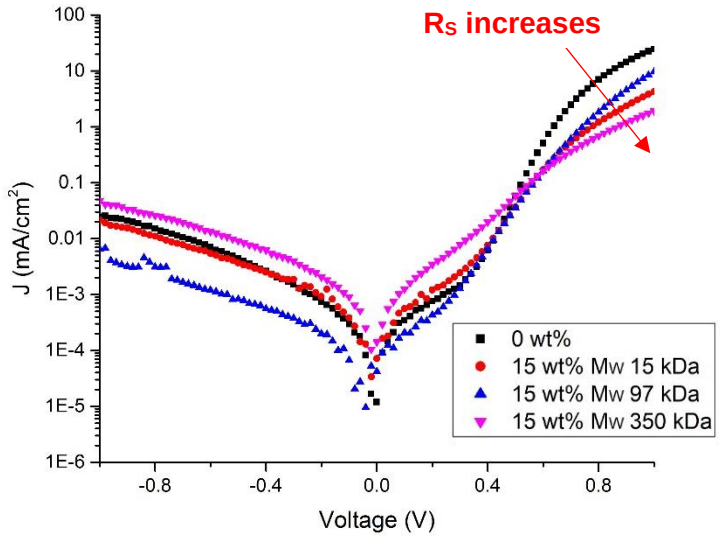

Figure 4.15 Dark J-V Curves for average binary PTB7:$PC_{71}BM$ blend (black squares), and ternary PTB7:$PC_{71}BM$:PMMA blend with a 15wt% and 15 kg mol^{-1} (red circles), 97 kg mol^{-1} (blue up triangles) & 350 kg mol^{-1} (pink down triangles) M_W of PMMA.

Table 4.2 Series resistance of average binary PTB7:$PC_{71}BM$ blend (0 wt%) and ternary PTB7:$PC_{71}BM$:PMMA blend with a 15 wt% and 15 kg mol^{-1}, 97 kg mol^{-1} & 350 kg mol^{-1} M_W of PMMA.

PTB7:$PC_{71}BM$:PMMA				
PMMA M_W (kg mol^{-1})	0 wt%	15	97	350
R_S (Ω cm^2)	13.6	80.4	33.3	191.7

The morphology of binary and ternary films was used to further study the reasons behind the affected performance of PTB7-based devices. When PMMA was added to the PTB7:$PC_{71}BM$ films, domed regions appeared, which grew in size as the M_W of the PMMA utilised was raised (**Figure 4.16**), similar to what was found with the P3HT:$PCB_{61}BM$:PMMA ternaries in **Figure 4.1**. PMMA had a very similar effect in both P3HT:$PCB_{61}BM$:PMMA and PTB7:$PC_{71}BM$:PMMA OPVs, indicating that morphology is unlikely to be the cause of the differences in initial performance and lifetime behaviour.

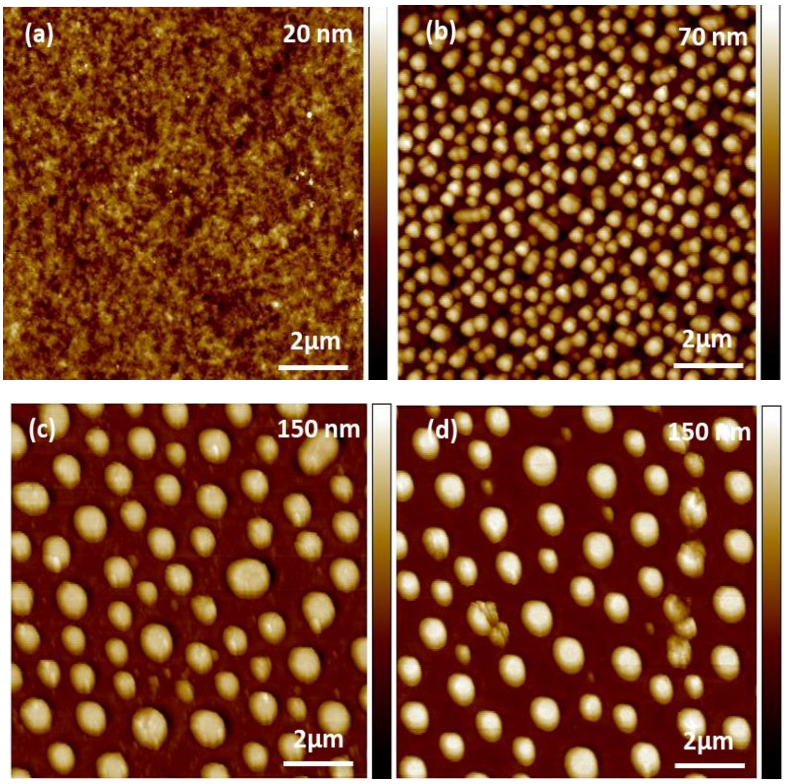

Figure 4.16 AFM topography images of (a) PTB7:$PC_{71}BM$, and of PTB7:$PC_{71}BM$:PMMA with 15 wt% of PMMA with (b) 15, (c) 97 and (d) 350 kg mol^{-1}.

One significant difference between the PTB7-based and P3HT-based devices is the use of DIO in the former. The use of processing additives has been proven to cause increased photo-bleaching.[54] Therefore, a hypothesis is that the short lifespan of PTB7:$PC_{71}BM$:PMMA ternary OPVs may be due to residual DIO which becomes trapped in the PMMA. This assertion was tested by fabricating further PTB7:$PC_{71}BM$

and PTB7:$PC_{71}BM$:PMMA OPVs without DIO, and subjecting them to the same ISOS-D-1 aging protocol, as shown in **Figure 4.17**. It can be seen that adding PMMA into the PTB7:$PC_{71}BM$ blend when DIO is absent improves lifetime, thereby recovering the result seen for the P3HT-based devices, however, it is noted that improvement is less pronounced. When PMMA is added to P3HT-based blends, the time it takes to decrease to 20% of the initial *PCE* is enhanced by up to a factor of ~2, while the improvement in lifetime for PTB7-based blends when PMMA is added is ~1.3. There are a number of possible reasons for this difference in behaviour. PTB7 contains a bridging O atom[54] which is not present in P3HT, and thus P3HT devices are more stable than their PTB7 counterparts.[55] Further, PTB7-based devices were fabricated with $PC_{71}BM$, while P3HT with $PC_{61}BM$. The larger size of $PC_{71}BM$ has an influence on phase segregation in the polymer–fullerene blend films,[56] which can lead to morphological changes with the passage of time, and may be one of the reasons for the poor ISOS-D-1 stability of $PC_{71}BM$-based devices.[57] The evidence that PMMA can extend the lifetime of PTB7:$PC_{71}BM$ OPVs, albeit slightly, suggests that water plays some role in these degradation mechanisms.

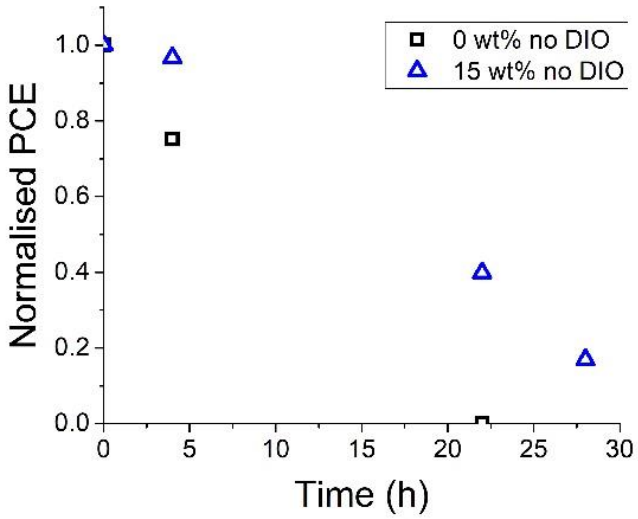

Figure 4.17 Normalised PCE as a function of time for average binary PTB7:$PC_{71}BM$ blend (open black squares) and ternary PTB7:$PC_{71}BM$:PMMA blend with 15 wt% of PMMA and M_W = 97 kg mol^{-1} (open blue up triangles). Devices were fabricated without DIO and were aged according to ISOS-D-1 standard. Initial PCE binary (not normalised): 0.65%. Initial PCE ternary (not normalised): 0.3%.

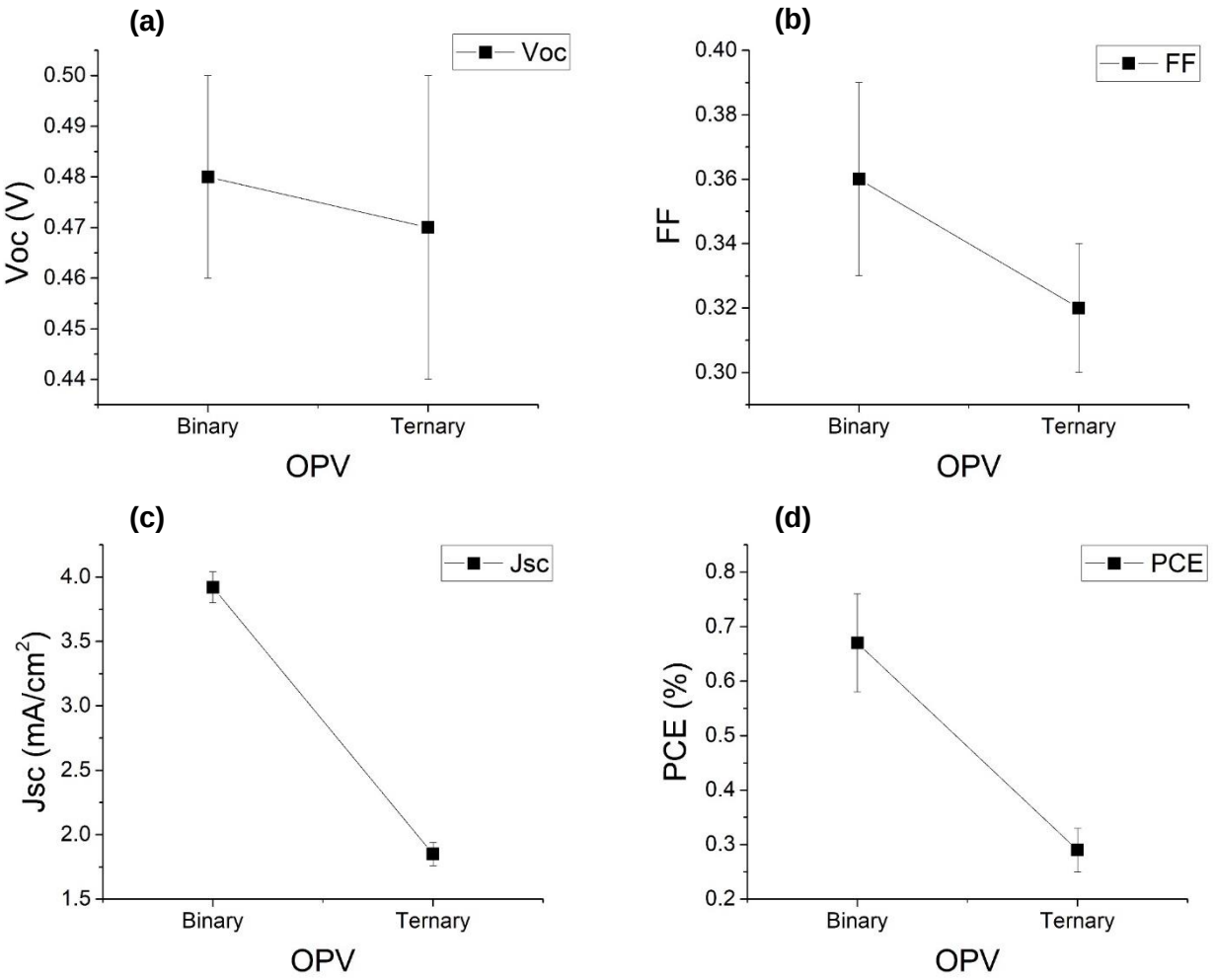

Figure 4.18 Initial electrical characteristics of PTB7:$PC_{71}BM$ binary films (no PMMA) and of PTB7:$PC_{71}BM$:PMMA ternary films with 15 wt% of 97 kg mol^{-1} M_W PMMA. Both blends have no DIO. (a) V_{OC}, (b) FF, (c) J_{SC} & (d) PCE. Four binary and four ternary devices were measured to obtain these results.

When compared to their binary counterparts, the PTB7:$PC_{71}BM$:PMMA OPVs with or without DIO show a decrease of >50% in initial J_{SC} and *PCE* when PMMA is added (**Figure 4.14** & **Figure 4.18**), indicating that PTB7-based devices initial performance is significantly affected by the addition of PMMA, as opposed to P3HT-based devices, which are almost unaffected as described in the previous section. **Figure 4.19** shows a decrease of ~24% in absorption of P3HT:$PC_{61}BM$:PMMA OPVs when compared to the binary control devices, while **Figure 4.20** shows a similar decrease of ~17-22% in absorption of PTB7:$PC_{71}BM$:PMMA OPVs when compared to their binary counterparts, suggesting that changes in absorption are not the root cause of the difference in initial behaviour.

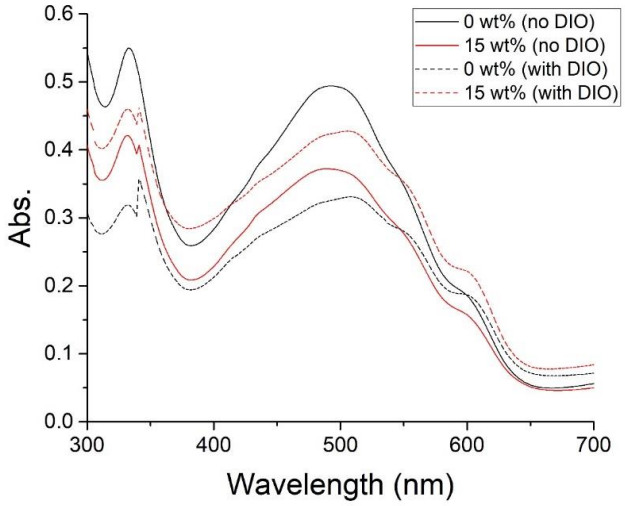

Figure 4.19 UV-vis absorption of average binary P3HT:$PC_{61}BM$ blends (black lines) and ternary P3HT:$PC_{61}BM$:PMMA blends (red lines) with 15 wt% of 97 kg mol^{-1} M_W PMMA (Solid lines for "no DIO" and dashed lines for "with DIO").

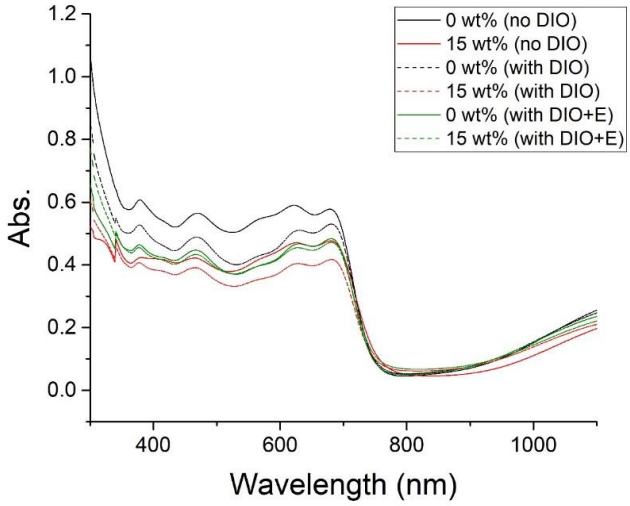

Figure 4.20 UV-vis absorption of average PTB7 based devices with different processing. Binary PTB7:$PC_{71}BM$ blends (black lines) and ternary PTB7:$PC_{71}BM$:PMMA blends (red lines) with 15 wt% of 97 kg mol^{-1} M_W PMMA (Solid lines for "no DIO" and dashed for "with DIO"). Binary blend with DIO plus ethanol wash (green solid line) and ternary blend with DIO plus ethanol wash (green dashed line).

Instead, it is here suggested that the differing impacts of PMMA upon initial performance of PTB7-based and P3HT-based devices is due to differences in microstructure. A previous study by Kumano et al.,[58] used time resolved microwave conductivity (TRMC) to show that adding an insulating molecule as a ternary component can enhance photoconductivity in crystalline polymers like P3HT and PffBT4T, and degrade photoconductivity in amorphous polymer PTB7, implying that insulating molecules/polymers are more compatible with crystalline than amorphous polymers. In other studies, energy filtered transmission electron microscopy (EFTEM) measurements have shown that P3HT:$PC_{61}BM$ films form nano fibrils; while there are no obvious PTB7 crystals in the PTB7:$PC_{71}BM$ films, only $PC_{71}BM$ aggregates.[59,60] These data suggest that the addition of insulating polymers/additives can disrupt charge transport in PTB7:$PC_{71}BM$:PMMA OPVs.[61,62] This provides a deeper understanding of how inert polymers may be utilised within OPV devices, as the data of this chapter suggest that PMMA can be effective in enhancing lifetime in different blend systems, but that it can also disrupt charge transport in amorphous donor polymers.

We now return to analyse P3HT based devices with the presence of DIO to see if the negative impact of the additive is present there also. To allow this, further P3HT:$PC_{61}BM$ devices were fabricated with DIO, to repeat similar experiments as those shown in **Figure 4.4**, although only considering one M_W with the addition of DIO for comparison. **Figure 4.21** shows ISOS-D-1 degradation of *PCE* for binary P3HT:$PC_{61}BM$ OPVs and ternary P3HT:$PC_{61}BM$:PMMA OPVs comprising 15 wt% of PMMA with M_W = 97 kg mol^{-1}, both of which included DIO as an additive. The addition of PMMA to the blend leads to very rapid reduction of OPV performance as compared to the binary control, which is the opposite behaviour to that observed in P3HT:$PC_{61}BM$ based devices when DIO is absent (**Figure 4.4**). It is concluded that while integrating PMMA as a ternary component can boost lifetime in a variety of donor:acceptor systems, its efficacy varies and is negatively impacted by the use of some processing additives.

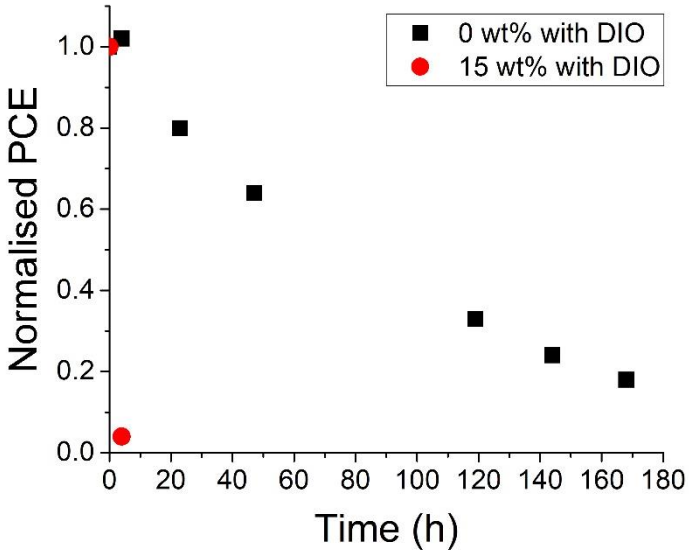

Figure 4.21 Normalised PCE as a function of time for average binary P3HT:$PC_{61}BM$ blend (black squares) and ternary P3HT:$PC_{61}BM$:PMMA blend with 15 wt% and a 97 kg mol^{-1} (red circles), both of which were processed with DIO. Initial PCE binary (not normalised): 1.6%. Initial PCE ternary (not normalised): 1.8%.

It is also noted that some studies have shown that washing the active layer with a small amount of an inert solvent with a low boiling point like methanol or ethanol can remove residual DIO and thus improve stability.[63,64] This approach was tested on the current devices to examine whether it could reduce or remove the negative impact of DIO on ternary OPVs. An ethanol washing treatment was used in an attempt to remove the negative lifetime impact of DIO. This treatment consisted in dropping 50 µL of low boiling point (~78 ^{o}C) ethanol onto the active layer. The ethanol was then spin-coated at 4000 rpm for 30 s and device fabrication was completed by Al evaporation and annealing of OPVs at 120 ^{o}C for 10 min in the glovebox prior to testing. However, **Figure 4.22** shows that the lifetime was not improved for the devices with the ethanol treatment, indicating that removal of residual DIO from the binary and ternary films was not successful. Further figures show that the ethanol treatment has no clear effect in the morphology (**Figure 4.23**), initial efficiency (**Figure 4.24**) and absorption (**Figure 4.20**). It is thus concluded that removing residual DIO is very difficult and may require more complex techniques than washing the active layer with ethanol, at least for the combination of blend films, additives and processing conditions considered in this thesis.

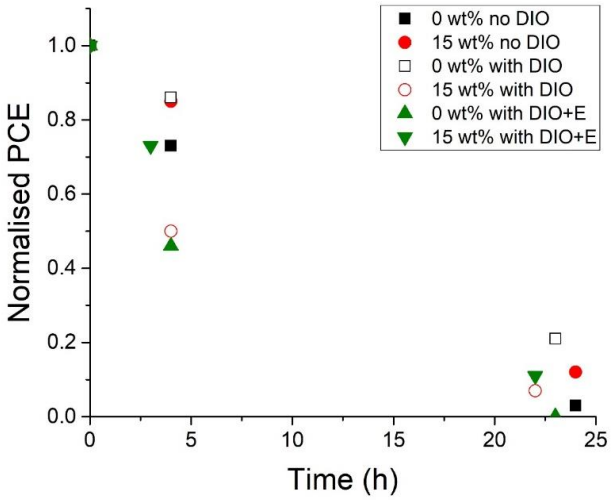

Figure 4.22 Normalised power conversion efficiency (PCE) as a function of time for average PTB7 based devices with different processing. Binary PTB7:$PC_{71}BM$ blends (black squares) and ternary PTB7:$PC_{71}BM$:PMMA blends (red circles) with 15 wt% of 97 kg mol^{-1} M_W PMMA (Solid symbols for "no DIO" and open for "with DIO"). Binary blend with DIO plus ethanol wash (green up triangles) and ternary blend with DIO plus ethanol wash (green down triangles). Initial PCE binary range (not normalised): 2.2 - 2.5%. Initial PCE ternary range (not normalised): 0.4 - 0.5%.

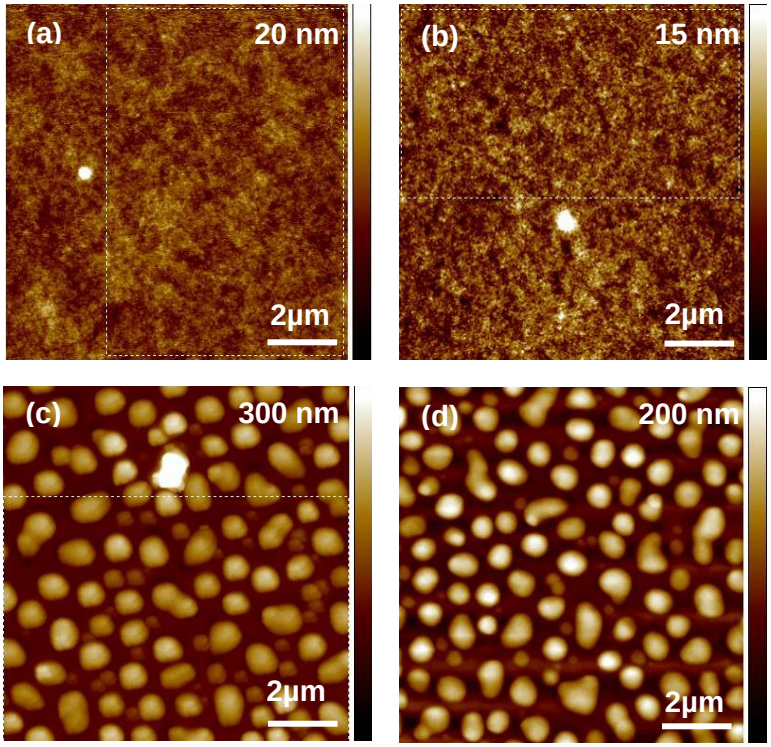

Figure 4.23 AFM topography images of DIO processed OPVs. PTB7:$PC_{71}BM$ binary films, with (a) and without ethanol wash (b). PTB7:$PC_{71}BM$:PMMA ternary films, with (c) and without (d) ethanol wash (15 wt% of 97 kg mol^{-1} M_W PMMA was used for both films).

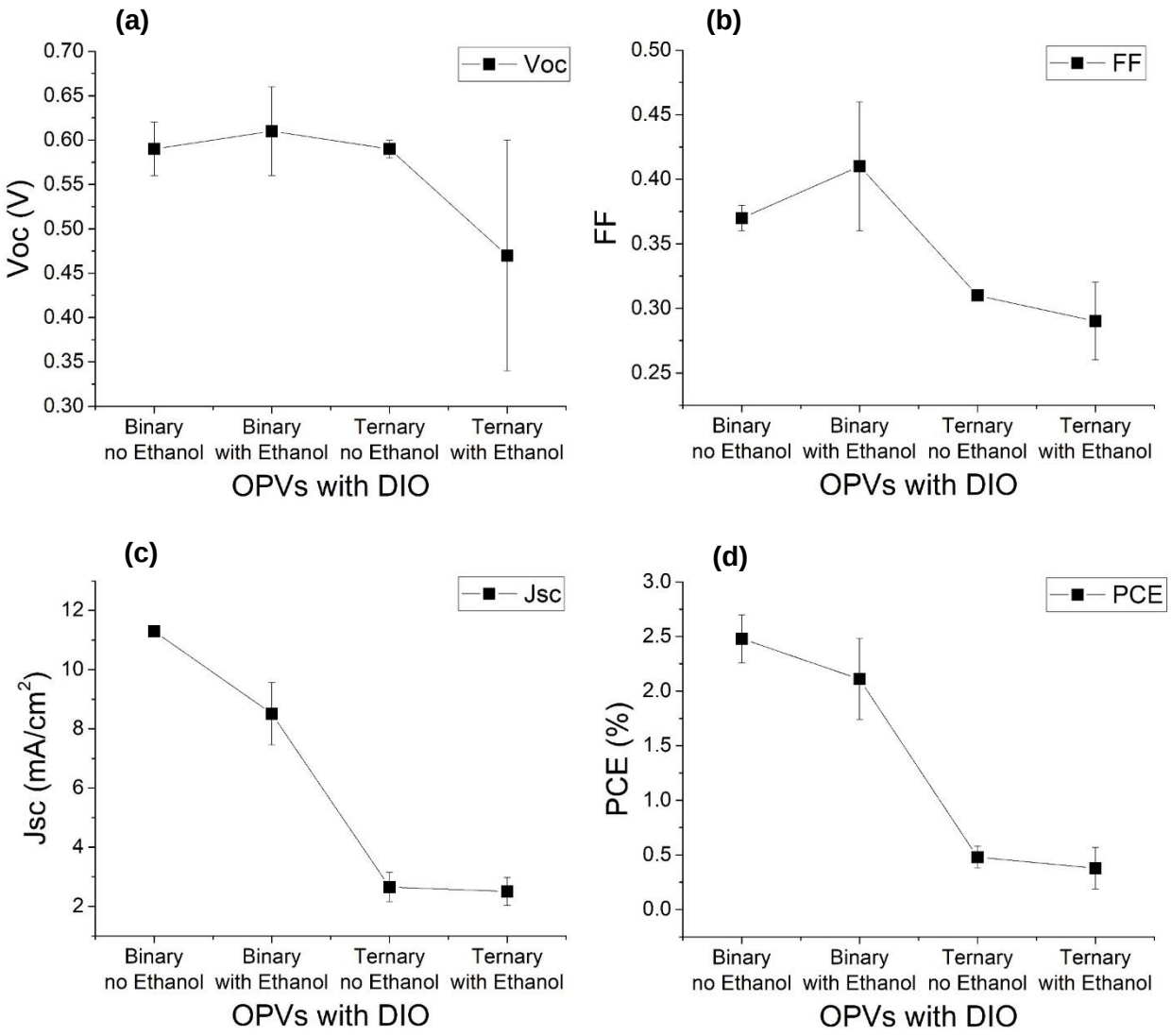

Figure 4.24 Initial electrical characteristics of DIO processed OPVs. PTB7:$PC_{71}BM$ binary blend, with and without ethanol wash, respectively; and PTB7:$PC_{71}BM$:PMMA ternary blend, with and without ethanol wash, respectively (15 wt% of 97 kg mol^{-1} M_W PMMA was used for both films). (a) V_{OC}, (b) FF, (c) J_{SC} & (d) PCE. Four devices of each combination were measured to obtain these results.

Table 4.3 Initial electrical characteristics and lifetime summary of average binary (0 wt%) and ternary ("x" wt%) P3HT:$PC_{61}BM$:PMMA OPVs with high content of PMMA and a 97 kg mol^{-1} M_W.

P3HT: $PC_{61}BM$:PMMA	Voc (V)	Jsc (mA/cm^2)	FF	PCE avg (%)	PCE best (%)	T_{80} (h)	T_{20} (h)
0 wt% (no DIO)	0.50 ± 0.04	-2.35 ± 0.39	0.53 ± 0.03	0.66 ± 0.09	0.75	4	42
15 wt% (no DIO)	0.53 ± 0.01	-3.15 ± 0.35	0.53 ± 0.01	0.93 ± 0.11	1.04	16	100
40 wt% (no DIO)	0.48 ± 0.02	-3.75 ± 0.62	0.56 ± 0.01	1.05 ± 0.20	1.25	80	256
50 wt% (no DIO)	0.41 ± 0.01	-2.59 ± 0.29	0.57 ± 0.01	0.61 ± 0.10	0.71	32	240

An additional limited set of P3HT:$PC_{61}BM$:PMMA devices were prepared with higher PMMA content (up to 50 wt%) to test if the initial electrical characteristics and lifetime continued to improve beyond 15 wt% (**Table 4.3**). These preliminary results show that the highest initial efficiency and longest lifetime was achieved by the 40 wt% devices, while the 50 wt% devices showed a comparable lifetime but a decrease in initial *PCE*. However, the limited number of devices tested (four for initial characteristics and one of each wt% for lifetime) in only one high PMMA content batch, emphasises the need for additional measurements to be taken. Due to laboratory constraints and the pandemic it was not possible to continue with these additional measurements.

4.5 Conclusions

Improvements in lifetime and cost of encapsulant technologies are required for commercial viability of OPVs. This chapter has shown that ternary blends incorporating PMMA can improve the ISOS-D-1 lifetime of OPVs. The data show that the improvement in lifetime is sensitive to the PMMA morphology, with larger, PMMA-rich domains providing the most benefit, thereby providing design rules for future devices. However, the efficacy of this technique varies depending on the donor:acceptor system. For example, the improvements in lifetime were as high as a factor of 2 without significantly effecting the initial efficiency of P3HT-based devices, while a lesser factor of 1.3 and an initial *PCE* drop of >50% was observed for PTB7-based devices. By analysing the gathered evidence from this and other studies, it is hypothesised that the compatibility between PMMA and the donor polymer is the reason why adding the inert polymer is more effective in some blend systems than in others, preferring crystalline polymers over amorphous polymers. Finally, it is also shown how the use of processing additives (here DIO) in addition to PMMA can have a negative impact on lifetime, indicating some limitations to the processing methodologies for ternary OPV devices with PMMA.

4.6 References

1 Manceau, M., Chambon, S., Rivaton, A., Gardette, J.-L., Guillerez, S. & Lemaître, N. (2010). Effects of long-term UV–visible light irradiation in the absence of oxygen on P3HT and P3HT:PCBM blend. *Sol. Energy Mater. Sol. Cells* 94, 1572-1577.

2 Razzell-Hollis, J., Wade, J., Tsoi, W. C., Soon, Y., Durrant, J. & Kim, J.-S. (2014). Photochemical stability of high efficiency PTB7:PC70BM solar cell blends. *J. Mater. Chem. A* 2, 20189-20195.

3 Rivaton, A., Tournebize, A., Gaume, J., Bussière, P.-O., Gardette, J.-L. & Therias, S. (2014). Photostability of organic materials used in polymer solar cells. *Polymer International* 63, 1335-1345.

4 Manceau, M., Rivaton, A., Gardette, J.-L., Guillerez, S. & Lemaître, N. (2009). The mechanism of photo- and thermooxidation of poly(3-hexylthiophene) (P3HT) reconsidered. *Polym. Degrad. Stab.* 94, 898-907.

5 Zhang, Y., Yi, H., Iraqi, A., Kingsley, J., Buckley, A., Wang, T. & Lidzey, D. G. (2017). Comparative indoor and outdoor stability measurements of polymer based solar cells. *Sci Rep* 7, 1305.

6 Tournebize, A., Bussiere, P.-O., Rivaton, A., Gardette, J.-L., Medlej, H., Hiorns, R. C., Dagron-Lartigau, C., Krebs, F. C. & Norrman, K. (2013). New insights into the mechanisms of photodegradation/stabilization of P3HT:PCBM active layers using poly(3-hexyl-d13- Thiophene). *Chem. Mater.* 25, 4522-4528.

7 Arredondo, B., Romero, B., Beliatis, M. J., del Pozo, G., Martín-Martín, D., Blakesley, J. C., Dibb, G., Krebs, F. C., Gevorgyan, S. A. & Castro, F. A. (2018). Analysing impact of oxygen and water exposure on roll-coated organic solar cell performance using impedance spectroscopy. *Solar Energy Materials and Solar Cells* 176, 397-404.

8 Wang, C., Ni, S., Braun, S., Fahlman, M. & Liu, X. (2019). Effects of water vapor and oxygen on non-fullerene small molecule acceptors. *Journal of Materials Chemistry C* 7, 879-886.

9 Peters, C. H., Sachs-Quintana, I. T., Kastrop, J. P., Beaupré, S., Leclerc, M. & McGehee, M. D. (2011). High efficiency polymer solar cells with long operating lifetimes. *Adv. Energy Mater.* 1, 491-494.

10 Sánchez, J. G., Balderrama, V. S., Estrada, M., Osorio, E., Ferré-Borrull, J., Marsal, L. F. & Pallarès, J. (2017). Stability study of high efficiency polymer solar cells using TiOx as electron transport layer. *Solar Energy* 150, 147-155.

11 Mateker, W. R. & McGehee, M. D. (2017). Progress in Understanding Degradation Mechanisms and Improving Stability in Organic Photovoltaics. *Adv Mater.* 29, 1-16.

12 Bartesaghi, D., Ye, G., Chiechi, R. C. & Koster, L. J. A. (2016). Compatibility of PTB7 and PC71BM as a key factor for the stability of PTB7:PC71BM solar cells. *Adv. Energy Mater.* 6, 1502338.

13 Turkovic, V., Engmann, S., Egbe, D. A. M., Himmerlich, M., Krischok, S., Gobsch, G. & Hoppe, H. (2014). Multiple stress degradation analysis of the active layer in organic photovoltaics. *Sol. Energy Mater. Sol. Cells* 120, 654-668.

14 Krebs, F. C. & Norrman, K. (2007). Analysis of the Failure Mechanism for a Stable Organic Photovoltaic During 10 000 h of Testing. *Prog. Photovoltaics* 15, 697-712.

15 Graff, G. L., Williford, R. E. & Burrows, P. E. (2004). Mechanisms of vapor permeation through multilayer barrier films: Lag time versus equilibrium permeation. *J. Appl. Phys.* 96, 1840-1849.

16 Dupont, S. R., Voroshazi, E., Heremans, P. & Dauskardt, R. H. (2012). The effect of anneal, solar irradiation and humidity on the adhesion/cohesion properties of P3HT: PCBM based inverted polymer solar cells. *38th IEEE Photovoltaic Specialists Conference , Austin, TX, Art. No* 6318272, 3259-3262.

17 Schafferhans, J., Baumann, A., Wagenpfahl, A., Deibel, C. & Dyakonov, V. (2010). Oxygen doping of P3HT:PCBM blends: Influence on trap states, charge carrier mobility and solar cell performance. *Organic Electronics* 11, 1693-1700.

18 Guerrero, A. & Garcia-Belmonte, G. (2017). Recent Advances to Understand Morphology Stability of Organic Photovoltaics. *Nanomicro Lett* 9, 10.

19 Sachs-Quintana, I. T., Heumüller, T., Mateker, W. R., Orozco, D. E., Cheacharoen, R., Sweetnam, S., Brabec, C. J. & McGehee, M. D. (2014). Electron Barrier Formation at the Organic-Back Contact Interface is the First Step in Thermal Degradation of Polymer Solar Cells. *Advanced Functional Materials* 24, 3978-3985.

20 Park, B., Kim, Y. J., Graham, S. & Reichmanis, E. (2011). Study of Conformational Change of P3HT Chains Using In-Situ Polarized Raman Spectroscopy. *ACS Appl. Mater. Interfaces* 3, 3545-3551.

21 Weaver, M. S., Michalski, L. A., Rajan, K., Rothman, M. A., Silvernail, J. A., Burrows, P. E., Graff, G. L., Gross, M. E., Martin, P. M., Hall, M. *et al.* (2002). Organic light-emitting devices with extended operating lifetimes on plastic substrates. *Appl. Phys. Lett.* 81, 2929-2931.

22 Meyer, J., Görrn, P., Bertram, F., Hamwi, S., Winkler, T., Johannes, H.-H., Weimann, T., Hinze, P., Riedl, T. & Kowalsky, W. (2009). Al2O3/ZrO2 Nanolaminates as Ultrahigh Gas-Diffusion Barriers—A Strategy for Reliable Encapsulation of Organic Electronics. 21, 1845-1849.

23 Ahmad, J., Bazaka, K., Anderson, L. J., White, R. D. & Jacob, M. V. (2013). Materials and methods for encapsulation of OPV: A review. *Renewable and Sustainable Energy Reviews* 27, 104-117.

24 Cros, S., de Bettignies, R., Berson, S., Bailly, S., Maisse, P., Lemaitre, N. & Guillerez, S. (2011). Definition of encapsulation barrier requirements: A method applied to organic solar cells. *Solar Energy Materials and Solar Cells* 95, S65-S69.

25 Machui, F., Hösel, M., Li, N., Spyropoulos, G. D., Ameri, T., Søndergaard, R. R., Jørgensen, M., Scheel, A., Gaiser, D., Kreul, K. *et al.* (2014). Cost analysis of roll-to-

roll fabricated ITO free single and tandem organic solar modules based on data from manufacture. *Energy & Environmental Science* 7.

26 Al-Busaidi, Z., C. Pearson, C. Groves, M.C. Petty. (2017). Enhanced lifetime of organic photovoltaic diodes utilizing a ternary blend including an insulating polymer. *Solar Energy Materials and Solar Cells* 160, 101-106.

27 Ogura, K., Fujii, A., Shiigi, H., Nakayama, M. & Tonosaki, T. (2000). Effect of Hygroscopicity of Insulating Unit of Polymer Composites on Their Response to Relative Humidity. *Journal of the Electrochemical Society* 147, 1105-1109.

28 Qin, D., Wang, W., Wang, M., Jin, S. & Zhang, J. (2014). The dependence of the cathode architecture on the photoactive layer morphology in bulk-heterojunction polymeric solar cells. *Semiconductor Science and Technology* 29, 125011.

29 O.Reese, M., Gevorgyan, S. A., Jørgensen, M., Bundgaard, E., Kurtz, S. R., Ginley, D. S., Olson, D. C., Lloyd, M. T., Morvillo, P., Katz, E. A. *et al.* (2011). Consensus stability testing protocols for organic photovoltaic materials and devices. *Solar Energy Materials and Solar Cells* 95, 1253-1267.

30 Gwyddion Software. (2019). http://gwyddion.net/download.php.

31 Amco Polymers - Molecular weight and its effects on polymer properties. (2018). https://www.amcopolymers.com/resources/blog/molecular-weight-and-its-effects-on-polymer-properties.

32 Polymer Database - Molecular Weight and Molecular Weight Distribution. (2021). https://polymerdatabase.com/polymer%20physics/Molecular%20Weight.html.

33 Andersson, H., Stading, M., Hjärtstam, J., Corswant, C. V. & Larsson, A. (2013). Effects of Molecular Weight on Phase Separated Coatings for Controlled Release of Drugs. *Annual Transactions of the Nordic Rheology Society* 21, 249-254.

34 Kuei, B. & Gomez, E. D. (2016). Chain conformations and phase behavior of conjugated polymers. *Soft Matter* 13, 49-67.

35 Scaccabarozzi, A. D. & Stingelin, N. (2014). Semiconducting: insulating polymer blends for optoelectronic applications-a review of recent advances. *J. Mater. Chem. A* 2, 10818-10824.

36 Li, X., Han, Y. & An, L. (2003). Surface morphology control of immiscible polymer-blend thin films. *Polymer* 44, 8155-8165.

37 Jones, M. L., Dyer, R., Clarke, N. & Groves, C. (2014). Are hot charge transfer states the primary cause of efficient free-charge generation in polymer:fullerene organic photovoltaic devices? A kinetic Monte Carlo study. *Physical Chemistry Chemical Physics* 16, 20310-20320.

38 Mandoc, M. M., Veurman, W., Koster, L. J. A., de Boer, B. & Blom, P. W. M. (2007). Origin of the Reduced Fill Factor and Photocurrent in MDMO-PPV:PCNEPV All-Polymer Solar Cells. 17, 2167-2173.

39 Groves, C., Blakesley, J. C. & Greenham, N. C. (2010). Effect of Charge Trapping on Geminate Recombination and Polymer Solar Cell Performance. *Nano Letters* 10, 1063-1069.

40 Hermenau, M., Riede, M., Leo, K., Gevorgyan, S. A., Krebs, F. C. & Norrman, K. (2011). Water and oxygen induced degradation of small molecule organic solar cells. *Solar Energy Materials and Solar Cells* 95, 1268-1277.

41 Luo, S.-C., Chung, H.-H., Pashuck, E. T., Douglas, E. P. & Holloway, P. H. (2005). Formation of bubbles on electrical contacts to polymer light-emitting diode devices. *Thin Solid Films* 478, 326-331.

42 Do, L.-M., Oyamada, M., Koike, A., Han, E.-M., Yamamoto, N. & Fujihira, M. (1996). Morphological change in the degradation of Al electrode surfaces of electroluminescent devices by fluorescence microscopy and AFM. *Thin Solid Films* 273, 209-213.

43 Kotadiya, N. B., Mondal, A., Blom, P. W. M., Andrienko, D. & Wetzelaer, G. A. H. (2019). A window to trap-free charge transport in organic semiconducting thin films. *Nat Mater* 18, 1182-1186.

44 Zuo, G., Linares, M., Upreti, T. & Kemerink, M. (2019). General rule for the energy of water-induced traps in organic semiconductors. *Nat Mater* 18, 588-593.

45 Ramuz, M., Bürgi, L., Winnewisser, C. & Seitz, P. (2008). High sensitivity organic photodiodes with low dark currents and increased lifetimes. *Organic Electronics* 9, 369-376.

46 Goffri, S., Muller, C., Stingelin-Stutzmann, N., Breiby, D. W., Radano, C. P., Andreasen, J. W., Thompson, R., Janssen, R. A. J., Nielsen, M. M., Smith, P. *et al.* (2006). Multicomponent semiconducting polymer systems with low crystallization-induced percolation threshold. *Nat. Mater.* 5, 950-956.

47 Kotadiya, N. B., Lu, H., Mondal, A., Ie, Y., Andrienko, D., Blom, P. W. M. & Wetzelaer, G.-J. A. H. (2018). Universal strategy for Ohmic hole injection into organic semiconductors with high ionization energies. *Nat. Mater.* 17, 329-334.

48 Collins, B. A., Li, Z., Tumbleston, J. R., Gann, E., McNeill, C. R. & Ade, H. (2012). Absolute Measurement of Domain Composition and Nanoscale Size Distribution Explains Performance in PTB7:PC71BM Solar Cells. *Advanced Energy Materials* 3, 65-74.

49 Liang, Y. Y., Xu, Z., Xia, J. B., Tsai, S. T., Wu, Y., Li, G., Ray, C. & Yu, L. P. (2010). For the Bright Future-Bulk Heterojunction Polymer Solar Cells with Power Conversion Efficiency of 7.4%. *Adv. Mater.* 22, E135-E138.

50 Roehling, J. D., Baran, D., Sit, J., Kassar, T., Ameri, T., Unruh, T., Brabec, C. J. & Moulé, A. J. (2016). Nanoscale Morphology of PTB7 Based Organic Photovoltaics as a Function of Fullerene Size. *Sci Rep.* 6, 30915-30926.

51 Liang, Y., Xu, Z., Xia, J., Tsai, S. T., Wu, Y., Li, G., Ray, C. & Yu, L. (2010). For the bright future-bulk heterojunction polymer solar cells with power conversion efficiency of 7.4%. *Adv Mater* 22, E135-138.

52 Li, G., Shrotriya, V., Huang, J., Yao, Y., Moriarty, T., Emery, K. & Yang, Y. (2005). High-efficiency solution processable polymer photovoltaic cells by self-organization of polymer blends. *Nat. Mater.* 4, 864-868.

53 Wu, L., Zang, H., Hsiao, Y.-C., Zhang, X. & Hu, B. (2014). Origin of the fill factor loss in bulk-heterojunction organic solar cells. *Applied Physics Letters* 104.

54 Kettle, J., Ding, Z., Horie, M. & Smith, G. C. (2016). XPS analysis of the chemical degradation of PTB7 polymers for organic photovoltaics. *Organic Electronics* 39, 222-228.

55 Shah, S. (2018). Investigating degradation pathways in organic solar cell materials. *Iowa State University PhD Dissertation* 16462, 1-90.

56 Zhang, F., Zhuo, Z., Zhang, J., Wang, X., Xu, X., Wang, Z., Xin, Y., Wang, J., Wang, J., Tang, W. *et al.* (2012). Influence of PC60BM or PC70BM as electron acceptor on the performance of polymer solar cells. *Sol. Energy Mater. Sol. Cells* 97, 71-77.

57 Chander, N., Jayaraman, E., Rawat, M., Bagui, A. & Iyer, S. S. K. (2018). Stability and Reliability of PTB7:PC71BM and PTB7:PC61BM Inverted Organic Solar Cells: A Comparative Study. *IEEE JOURNAL OF PHOTOVOLTAICS* 9, 183-193.

58 Kumano, M., Ide, M., Seiki, N., Shoji, Y., Fukushima, T. & Saeki, A. (2016). A ternary blend of a polymer, fullerene, and insulating self-assembling triptycene molecules for organic photovolatics. *Journal of Materials Chemistry A* 4, 18490-18498.

59 Hammond, M. R., Kline, R. J., Herzing, A. A., Richter, L. J., Germack, D. S., Ro, H.-W., Soles, C. L., Fischer, D. A., Xu, T., Yu, L. *et al.* (2011). Molecular Order in High-Efficiency Polymer-Fullerene Bulk Heterojunction Solar Cells. *ACS Nano* 5, 8248-8257.

60 Supasai, T., Amornkitbamrung, V., Thanachayanont, C., Tang, I. M., Sutthibutpong, T. & Rujisamphan, N. (2017). Visualizing nanoscale phase morphology for understanding photovoltaic performance of PTB7: PC71BM solar cell. *Applied Surface Science* 422, 509-517.

61 Ferenczi, T. A., Muller, C., Bradley, D. D., Smith, P., Nelson, J. & Stingelin, N. (2011). Organic semiconductor:insulator polymer ternary blends for photovoltaics. *Adv Mater* 23, 4093-4097.

62 Manion, J. G., Gao, D., Brodersen, P. M. & Seferos, D. S. (2017). Insulating polymer additives in small molecule and polymer photovoltaics: how they are tolerated and their use as potential interlayers. *Journal of Materials Chemistry C* 5, 3315-3322.

63 Ye, L., Jing, Y., Guo, X., Sun, H., Zhang, S., Zhang, M., Huo, L. & Hou, J. (2013). Remove the Residual Additives toward Enhanced Efficiency with Higher Reproducibility in Polymer Solar Cells. *J. Phys. Chem. C* 117, 14920−14928.

64 Li, N. & Brabec, C. J. (2015). Air-processed polymer tandem solar cells with power conversion efficiency exceeding 10%. *Energy Environ. Sci.* 8, 2902-2909.

CHAPTER 5
LCOE Model Development

5.1 Introduction

Due to their cheap cost of manufacture[1,2] and fast rising power conversion efficiency (*PCE*), organic and perovskite based emerging photovoltaic (PV) devices have the potential to be a breakthrough energy generation technology. However, a critical assessment of the resultant cost of energy is needed to evaluate the feasibility of these new technologies. The Levelized Cost of Energy (LCOE), which accounts for cumulative energy and related expenses throughout the life of a project, is the standard criterion by which energy generating systems are evaluated. Emerging PV faces a difficulty here, as energy yield degrades more quickly than existing silicon (Si) PV modules, which are typically warrantied to lose no more than 0.7% of their output each year over the course of their 25-year lifespan.[3] It is unclear how the competing impacts of cost, efficiency and degradation impact the current competitiveness of emerging PV, which complicates the selection of improvement paths to make newer technologies viable.

LCOE models are becoming more common as a tool for showing the commercial benefits of new PV devices as well as the problems they face. Several LCOE studies, for example, have used bottom-up approaches to assess the impact of cost of materials (e.g. active layer) and manufacturing processes at lab, upscaling and industry levels, revealing that potential bottlenecks to low-cost OPV production lie in cost of raw materials and not in processing costs.[4-6] A Monte Carlo approach has also been used in other studies to determine a range of costs for emerging PV devices, whilst also highlighting the importance of efficiency, lifetime and other parameters by a sensitivity analysis.[7,8] Additionally, the benefit of replacing panels when module performance increases quickly due to advancing technology has also been shown in an LCOE model.[9] However, one concern is that emerging PV LCOE models have assumed degradation similar to that of commercially established Si PV, rather than that of emerging PV. Others have shown the significant impacts of degradation on

LCOE in existing developed technologies,[10,11] but these models were not designed to capture the complex degradation behaviour of emerging PV.

The focus in this chapter is to show the development of a model which is based on degradation characteristics observed in real emerging PV devices for the first time. This new model of LCOE is able to quantify the impact of rapid degradation at the start of a module's life (burn-in) that is characteristic of emerging PV technologies, and makes it possible to quantify the relative impacts of realistic degradation, initial efficiency and module cost upon LCOE, as shown in the results Chapters 6-7.

5.2 Literature review of emerging PV degradation profile

A literature review of degradation profile of perovskite (PVK) and organic photovoltaic (OPV) devices was conducted to guarantee that the model could properly represent the degradation behaviour that is characteristic of emerging PV. The search engine Web of Science was used to perform a topic search for the terms 'lifetime,' 'degradation', 'burn-in,' 'photovoltaic,' 'solar cell,' and either 'organic' or 'OPV', or 'perovskite' on 8th Oct 2020, in the date range Jan 2013 to Jun 2020, returning 134 papers. A further topic search was conducted to ensure the state of the art was captured. In the new search, the terms 'stable' or 'stability' replaced lifetime related terms (lifetime or degradation or burn-in) and it was performed on 27th Jan 2021, with an extended date range from Jan 2013 to Dec 2020. Due to the large number of articles returned by the search, only the 100 most cited papers up to and including 2019, and 2020 papers with more than 15 cites (65 papers) were considered. The information related to degradation profile, device structure and measurement conditions was noted for each of the 299 examined papers returned by the searches, but only those papers which reported degradation behaviour in sufficient detail (burn-in studies needed to clearly indicate the burn-in period and loss, minimum aging of 200 hours to calculate degradation rate, aging protocol and test conditions specified, including if the device was encapsulated or unencapsulated so it could be categorised, UV-filters were acceptable although most studies did not indicate using them) were considered in the following analysis. **Table 5.1** summarizes the information obtained for the 38 OPV and 30 PVK datasets revealed by the search. These data were grouped into the following broad categories according to the measurement conditions:

- Light-soaking. Experiments which involved continuous illumination at or close to AM1.5G simulated sunlight with 1,000 W/m^2 intensity. The devices were either encapsulated in some manner (e.g. epoxy glued coverslips) or were tested in an atmosphere with reduced water vapour and oxygen content.
- Light-soaking without encapsulation. As light-soaking but without encapsulation and an ambient atmosphere similar to typical indoor conditions.
- Thermal aging: As light-soaking, but at elevated temperature of 85 °C.
- High-temperature storage: Devices were stored in the dark at elevated temperatures of 65/85 °C.
- Outdoor testing. Devices tested outdoors with either encapsulation or ambient atmosphere with reduced water vapour and oxygen content.

Only devices aged under light-soaking conditions were examined in the following analysis to reduce the impact of different measurement techniques. There were 29 OPV and 26 PVK devices in this smaller dataset. While the outdoor testing category is the most representative of real-world conditions, there are currently too few measurements reported to allow comparisons amongst candidate emerging PV devices. As a result, the light-soaking category was chosen since there is a wide variety of device and material data available, and the measurements under this protocol allow for the possibility of active materials photo-oxidation.

Table 5.1a Reported OPVs initial efficiency (PCE_i), burn-in (B) and degradation rate (D) in literature.

Testing conditions	Active layer	PCE_i (%)	B (%)	τB (h)	Test or Extrapolated Lifetime (h)	D (%/year)	Ref.	Year	Testing conditions	Active layer	PCE_i (%)	B (%)	τB (h)	Test or Extrapolated Lifetime (h)	D (%/year)	Ref.	Year
Light-soaking	PCDTBT: $PC_{70}BM$	5.60	39.0	250	14,500	2.76	[12]	2015	Light-soaking	P3HT: $PC_{60}BM$	3.03	23.0	500	2,000	20.0	[13]	2017
Light-soaking	P3HT: $PC_{60}BM$	3.70	35.0	1000	6,500	6.15	[14]	2013	Light-soaking	P3HT: IDTBR	6.05	0.00	0	4,500	8.89	[13]	2017
Light-soaking	P3HT: $PC_{60}BM$	2.80	0.00	0	12,000	1.67	[15]	2014	Light-soaking	L-PCDTBT: $PC_{71}BM$	7.21	0.00	0	20,000	2.00	[16]	2014
Light-soaking	PCDTBT: $PC_{70}BM$	5.50	20.0	1500	18,000	2.22	[17]	2013	Light-soaking	PTB7–Th: $PC_{71}BM$	8.81	25.0	400	N/A	N/A	[18]	2019
Light-soaking	PCDTBT: $PC_{71}BM$	5.30	40.0	3000	41,000	0.98	[19]	2015	Light-soaking	PTB7–Th: $PC_{71}BM$	8.80	40.0	300	800	50.0	[18]	2019
Light-soaking	PCDTBT: $PC_{71}BM$	5.10	40.0	4000	16,000	2.50	[19]	2015	High-temperature storage	PffBT4T-2OD: $PC_{60}BM$	4.42	40.0	2	N/A	N/A	[20]	2019
Light-soaking	PBDTTT-EFT: $PC_{71}BM$	6.00	60.0	5	N/A	N/A	[21]	2016	High-temperature storage	PffBT4T-2OD: $PC_{60}BM$	3.98	10.0	2	N/A	N/A	[20]	2019
Light-soaking	PBDTTT-EFT: $PC_{71}BM$	7.30	60.0	10	N/A	N/A	[21]	2016	Light-soaking	PBDB-T: ITIC-2F	7.78	7.00	200	11,000	3.64	[22]	2019
Light-soaking	PCDTBT: $PC_{70}BM$	5.40	16.4	60	N/A	N/A	[23]	2014	Light-soaking	PBDB-T: ITIC-Th	8.03	7.00	200	9,500	4.21	[22]	2019
Light-soaking	P3HT: $PC_{60}BM$	3.40	50.0	150	N/A	N/A	[24]	2014	Light-soaking	PBDB-T: ITIC-DM	8.23	60.0	200	200	200	[22]	2019
Light-soaking	PCDTBT: $PC_{70}BM$	5.70	40.0	150	N/A	N/A	[24]	2014	Light-soaking	P3HT: $SF(DPPB)_4$	3.00	38.0	192	N/A	N/A	[25]	2020
Light-soaking	DR3TSBDT: $PC_{71}BM$	9.60	47.0	990	5,600	7.14	[26]	2017	Light-soaking	P3HT: ICxA	2.92	40.0	96	N/A	N/A	[25]	2020
Light-soaking	DRCN5T: $PC_{71}BM$	9.80	47.0	770	5,200	7.69	[26]	2017	Light-soaking	P3HT: $PC_{60}BM$	2.82	17.0	48	N/A	N/A	[25]	2020
Light-soaking	F3: $PC_{61}BM$	7.30	41.0	1480	4,150	9.64	[26]	2017	Thermal aging	PBDTTT-OFT: IEICO-4F	13.0	0.00	0	1,050	38.10	[27]	2020
Light-soaking	X2: $PC_{61}BM$	6.30	44.0	1420	3,520	11.4	[26]	2017	Outdoor testing	PCE12: ITIC	3.24	20.0	120	N/A	N/A	[28]	2020
Light-soaking	DRCN7T: $PC_{71}BM$	9.10	31.0	1160	3,450	11.6	[26]	2017	Outdoor testing	PCE11: $PC_{60/70}BM$	2.50	60.0	120	N/A	N/A	[28]	2020
Outdoor testing	PFDT2BT-8: $PC_{71}BM$	5.90	38.0	1450	10,000	4.00	[29]	2017	Light-soaking	DBP: C_{70}	6.07	0.00	0	9,000	1.78	[30]	2019
Outdoor testing	PCDTBT: $PC_{71}BM$	6.24	20.0	450	6,200	6.45	[31]	2016	Light-soaking	PTB7-Th: IEICO-4F	10	0.00	0	34,000	1.18	[32]	2020
Thermal aging	PTB7: $PC_{71}BM$	7.30	40.0	500	N/A	N/A	[33]	2019	Thermal aging	PTB7: $PC_{71}BM$	4.63	6.00	500	N/A	N/A	[33]	2019

Table 5.1b Reported PVKs initial efficiency (PCE_i), burn-in (B) and degradation rate (D) in literature.

Testing conditions	Active layer	PCE_i (%)	B (%)	τB (h)	Test or Extrap. Lifetime (h)	D (%/yr)	Ref.	Year	Testing conditions	Active layer	PCE_i (%)	B (%)	τB (h)	Test or Extrap. Lifetime (h)	D (%/yr)	Ref.	Year
Light-soaking	$CH_3NH_3PbI_{3-x}Cl_x$/ $PC_{70}BM$	10.2	40.0	160	280	143	[34]	2018	Light-soaking	$PC_{61}BM$/ $(BA)_2(MA)_3Pb_4I_{13}$	12.5	0.00	0	2,500	0.00	[35]	2016
Light-soaking	$PC_{61}BM$/ $FA_{0.83}Cs_{0.17}$ $Pb(I_{0.6}Br_{0.4})_3$	15.1	12.5	150	3,350	11.9	[36]	2017	Light-soaking	$(5\text{-}AVA)_x(MA)_{1-x}PbI_3$/ TiO_2	12.8	0.00	0	1,000	0.00	[37]	2014
Light-soaking	$PC_{61}BM$/ $BA_{0.09}(FA_{0.83}$ $Cs_{0.17})_{0.91}$ $Pb(I_{0.6}Br_{0.4})_3$	15.5	12.5	150	3,800	10.3	[36]	2017	Light-soaking	SnO_2/ $FAPbI_3$	14.5	30.0	48	592	67.6	[38]	2018
Light-soaking	$MAPbI_3$/ $PC_{60}BM$	12.8	40.0	30	2,000	20.0	[39]	2018	Light-soaking	SnO_2/ $FA_{0.98}Cs_{0.02}PbI_3$	17.5	20.0	48	1,360	29.4	[38]	2018
Light-soaking	$MAPbI_3$/ $PC_{60}BM$	14.7	40.0	10	200	200	[39]	2018	Light-soaking	TiO_2-Cl/ CsMAFA	20.1	0.00	0	525	11.4	[40]	2017
Light-soaking	$MAPbI_3$/ $PC_{60}BM$	13.2	15.0	1500	N/A	N/A	[39]	2018	Light-soaking	$MAPbI_3$/ $PC_{60}BM$	15.0	0.00	0	1,000	20.0	[41]	2015
Light-soaking	$PC_{60}BM$:C_{60}:PFN/ $CH_3NH_3PbI_3$	19.3	30.0	150	1,060	16.5	[42]	2018	Light-soaking	$CH_3NH_3PbI_3$/ $PC_{61}BM$	19.7	0.00	0	1,000	20.0	[43]	2020
Light-soaking	TiO_2/ $CH_3NH_3PbI_3$	14.6	45.0	150	50	800	[42]	2018	Light-soaking	CsMAFA/ AALs	21.2	0.00	0	1,000	0.00	[44]	2020
Light-soaking	C_{60}/ $(HC(NH_2)_2)_{0.83}$ $Cs_{0.17}$ $Pb(I_{0.6}Br_{0.4})_3$	16.0	15.0	100	3,420	11.7	[45]	2016	Light-soaking	CsMAFA/ spiro-OMeTAD (PbI_2 1.18 M)	16.9	40.0	100	520	95.2	[46]	2020
Light-soaking without encapsulation	TiO_2/ $BA_{0.1}[Cs_{0.05}$ $(FA_{0.83}MA_{0.17})_{0.95}]_{0.9}$ $Pb(I_{0.83}Br_{0.17})_3$	20.6	20.0	100	1,170	34.1	[47]	2019	Light-soaking	CsMAFA/ spiro-OMeTAD (PbI_2 1.15 M)	17.6	0.00	0	520	3.85	[46]	2020
Light-soaking without encapsulation	TiO_2/ $Cs_{0.05}$ $(FA_{0.83}MA_{0.17})_{0.95}$ $Pb(I_{0.83}Br_{0.17})_3$	18.7	20.0	100	718	55.7	[47]	2019	Light-soaking	CsMAFA/ spiro-OMeTAD (PbI_2 1.12 M)	17.3	0.00	0	520	30.8	[46]	2020
Light-soaking	PCBM:PMMA/Rb_5 $Cs_{10}FAPbI_3$	18.7	6.00	35	1,000	2.00	[48]	2018	Light-soaking	$CH_3NH_3PbI_{3-x}Cl_x$/ Al_2O_3	12	50.0	200	500	0.00	[49]	2013
Light-soaking	m-SnO_2/ $FAIPbI_2MABrPb$ Br_2CsI	16.4	25.0	200	1,000	10.0	[50]	2018	Light-soaking	$(HOOC(CH_2)_4NH_3)_2PbI_4$/ $CH_3NH_3PbI_3$	11.9	0.00	0	1,000	0.00	[51]	2017
Light-soaking without encapsulation	$PC_{61}BM$/ $MAPbI_3$	11.6	60.0	24	250	160	[35]	2016	Light-soaking	$FAIPbI_2MABrPbBr_2$/ spiro-OMeTAD	18.7	0.00	0	4,320	0.93	[52]	2016
Light-soaking without encapsulation	$PC_{61}BM$/ $(BA)_2(MA)_3Pb_4I_{13}$	12.5	20.0	200	2,050	4.88	[35]	2016	Light-soaking	$PC_{61}BM$/ $MAPbI_3$	11.6	60.0	10	250	160	[35]	2016

Figure 5.1a depicts a typical degradation curve that represents the dataset behaviour over time. This degradation profile includes a quick phase of initial degradation, referred to as 'burn-in,' followed by a slower and consistent period of linear decay.[53] When exposed to light or heat, morphological changes in the blended materials of the active layer of emerging PV devices can induce burn-in,[54,55] as well as the interfacial resistance between the electron-transporting layer (ETL) and the photoactive layer.[20] Linear degradation, on the other hand, is mostly caused by the entry of water and oxygen into the device (as shown in Chapter 4 results), which can react with the organic layers under illumination, resulting in photo-bleaching or limited light-absorption capacity.[53] It is also important to comment on additional degradation behaviours not highlighted by the literature review. Some PVK devices have been demonstrated to have some burn-in recovery in the dark,[56] but it is unclear how much of this recovery would appear in a real-world environment, therefore it is not included here. However, it is pointed out that the approach given here can compute LCOE for degradation profiles with any temporal resolution, which would be required to account for such scenarios. Within the LCOE calculation, this could present itself as a lower effective burn-in than would be measured in an experiment with continuous illumination. The model could also be easily modified to adapt to even more rare devices presenting an inverse burn-in, i.e. devices with increasing efficiency in their initial aging period after fabrication. Returning to the literature review data, in around a quarter of the dataset devices (15), there was no burn-in, therefore their degradation profile was described by linear degradation only. While it is not expected that all emerging PV devices will be well-described by the parameterisation shown in **Figure 5.1**a, this degradation profile suits all 55 datasets captured by the literature review. Further discussion of how the LCOE model can be modified to account for arbitrary degradation profiles as required is available in section 5.3 (Model development).

Returning to the data, it is shown that 'burn-in' takes place over a period of time, τ_B that is typically of the order of hundreds of hours in full sun.[53] Here, PCE_i and PCE_B denote the initial and post burn-in efficiencies, respectively, with burn-in loss, B, denoting the percentage decrease in efficiency throughout the burn-in phase (e.g. if PCE_i = 10% and PCE_B = 8%, B = 20%). PCE_i (%) and B (%) values were taken directly as specified in the papers. However, the specific value of linear degradation is not usually mentioned in emerging PV studies. The linear degradation following burn-in is

parameterised by a degradation rate, *D*, which is defined as the fractional percentage loss of post-burn in efficiency per year of operation. To calculate the linear degradation rate, *D* (%/year) the difference between absolute post burn-in efficiency (PCE_b) and efficiency at the end of the test (PCE_{end}) was divided by the ratio of the intervening time period and the number of peak solar hours in a year, although in some cases, *D* was instead calculated by considering the extrapolated lifetime reported in the paper (often the estimated time for post burn-in efficiency to drop by 20%). It was necessary to convert the time spent under continuous illumination in a laboratory environment to a degradation rate per year, *D* (%/year), which reflects the diurnal and seasonal variance in sunshine in the project location for later LCOE calculations.[53] Each day was assumed to have 5.5 hours of direct full sunlight (equating to ~2,000 hours per year[19]) in this calculation, which was selected to be similar to the 1,889 annual peak solar hours for the chosen installation location (Suva, Fiji).[57] Given that the rate of aging in the dark is significantly lower than light aging, it was assumed that degradation only occurs during the hours of full sun.[58] The degradation rate was not calculated for those papers which did not provide enough detailed information about the test lifetime.

The values of PCE_i, *B* and *D* for emerging PV devices aged under light-soaking conditions only are plotted against one another in **Figure 5.1**b-d. The only clear distinction between OPVs and PVKs is that the datasets PCE_i in the former is lower than in the latter, but otherwise there appears to be little correlation amongst the datasets. **Table 5.2** shows the Pearson correlation coefficients of each pair of parameters in the light-soaking category attempting to clarify data relationships. Degradation rates of 30%/year or more were omitted from the analysis as unrepresentative outliers. OPVs had correlation coefficients close to zero (PCE_i vs *B* = 0.04, PCE_i vs *D* = -0.08, *D* vs *B* = 0.31), indicating negligible correlation between PCE_i, *B* and *D*. However, PVKs display a stronger negative correlation between PCE_i and burn-in (-0.46). This suggests that OPVs with high PCE_i will not necessarily have low *B* or *D*, whilst in PVKs, there is some correlation between initial performance and degradation as discussed elsewhere.[59-61] It is however noted that the certified record efficiencies for lab-scale PVK and OPV devices[62] are far in excess of the highest reported initial efficiency of lab-scale devices that have undergone degradation studies shown in **Figure 5.1**. This gap in performance is equivalent to a time-lag of ~7 years for OPV devices and ~3 years for PVK devices, and it emphasizes the need for

standardized degradation tests[63,64] on the latest PV materials and architectures to prove the viability of these technologies.

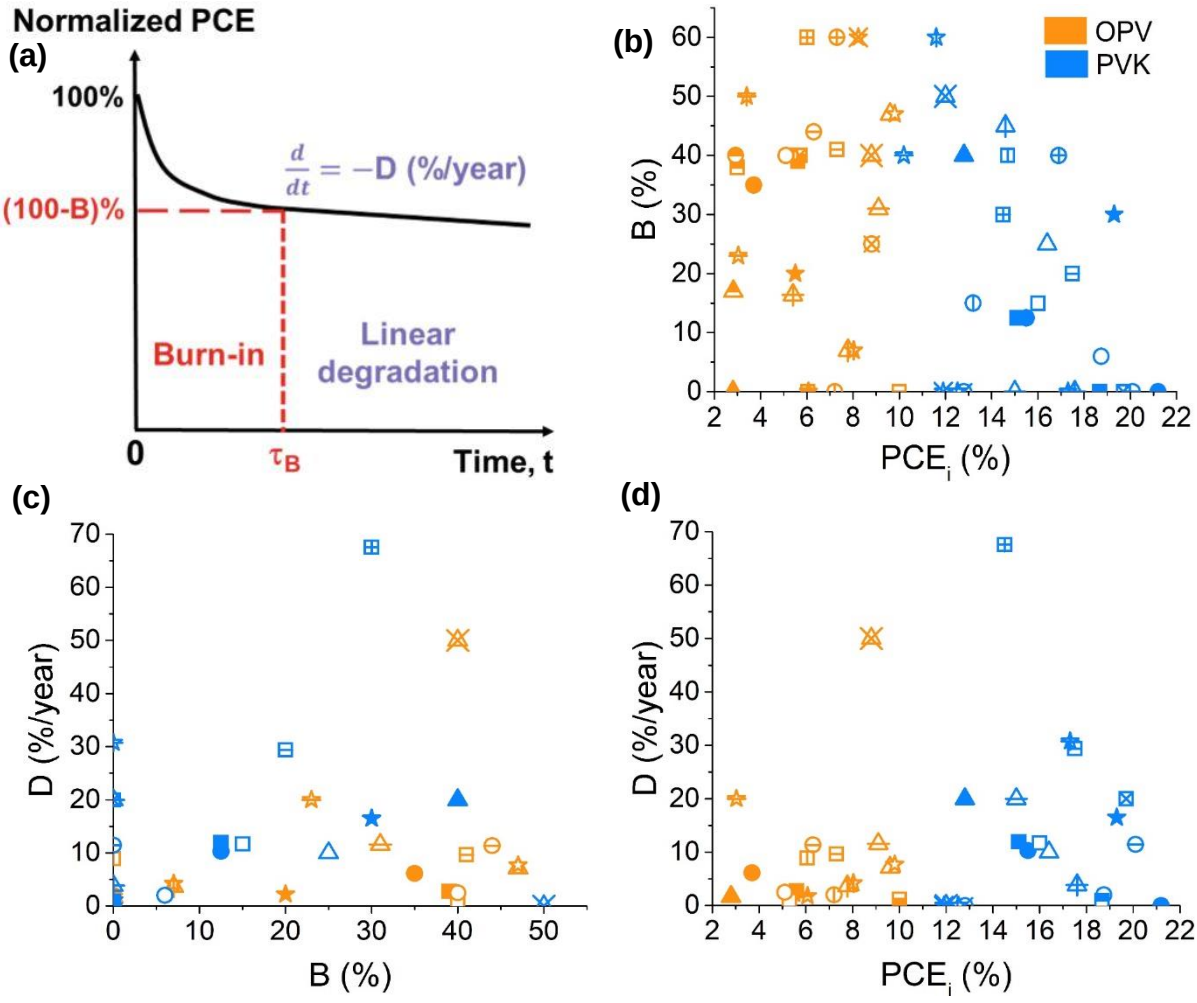

Figure 5.1 Emerging PV Characteristic Parameters from literature review

(a) Schematic representation of the typical evolution of PCE in OPV and PVK devices. Plots of (b) Burn-in vs PCE, (c) degradation rate vs burn-in, and (d) degradation rate vs PCE reported in the literature for PVK (blue) and OPV (orange) devices. Each symbol represents a unique device, the materials and architecture for which is listed in Table 6.1.

Table 5.2 Pearson coefficients and average characteristics of Figure 5.1 devices.

PV type	Pearson coefficients			Device characteristics		
	PCE_i vs B	**PCE_i vs D**	**D vs B**	**PCE_i (%)**	**B (%)**	**D (%/year)**
OPV	0.04	-0.08	0.31	6.2%	30%	6%
PVK	-0.46	0.20	0.26	16%	19%	9%

(Left) Pearson correlation coefficients of initial PCE (PCE_i), burn-in loss (B), and long-term degradation rate (D), and (Right) average device characteristics for OPV and PVK devices captured by the literature review.

5.3 Model development

The LCOE can be calculated by dividing the net present value (NPV) of the total costs incurred by the NPV of the total PV generation in the project lifetime:

$$LCOE = \frac{I_0 + \sum_{t=1}^{l} \frac{C_t}{(1+d)^t}}{\sum_{t=1}^{l} \frac{E_t}{(1+d)^t}} \qquad (5.1)$$

Here I_0 is the installation cost (USD); C_t are the total costs in year t (USD) comprising operating costs, and panel/inverter replacement costs at the end of their life; E_t is electricity generation in year t (kWh); l is the project life (years); and d is the discount rate (%).

PV modules (e.g. panel replacement year, panel cost or burn-in), PV project (e.g. project lifetime, inverter lifetime and land rental), and location (e.g. local discount rate, PV array tilt and peak solar hours per year) information are among the model input parameters. Section 5.3.1 shows a list of input parameters for PV modules and the project, together with justifications for values chosen, whilst location information can be found in section 5.3.2. The main project location of Suva, Fiji was selected due to its high yearly insolation and availability of underpinning data, although other arbitrary locations can be modelled using this approach (as shown in Chapter 7). Installation and balance of system costs scale with module efficiency to

reflect changing land-use, cabling and infrastructure requirements for the project. From these data, costs are calculated using equations shown in section 5.3.2, which in combination with the electricity generation model (section 5.3.3) allow to calculate the LCOE (equation 5.1).

5.3.1 Model inputs

Table 5.3 shows the estimated emerging PV module cost reported in the literature, although these technologies are not commercially available yet. Given that different studies consider different active layer combinations, encapsulation methods and even production scales (e.g. up-scaling or industry scale), there is a significant range between the reported module cost values. Taking this in consideration, a much wider range of module costs was used for LCOE predictions in Chapters 6-7, which allows the model to assess the importance of module cost and account for future improvements.

Table 5.3 Estimated emerging PV module cost reported in the literature.

PV type	Module cost ($/Wp)	Ref.	Year
OPV	0.43	[4]	2019
	0.23-0.34	[7]	2016
	0.10-1.08 (up-scaling)	[65]	2014
	0.06-0.72 (industrial scale)		
	0.14-0.27	[66]	2014
PVK	0.41	[6]	2017
	0.17	[5]	2018
	0.48 (Si-PVK)		
	0.21 (PVK-PVK)		
	0.21-0.28	[67]	2017

Table 5.4 provides input parameters used to calculate LCOE. The 'Cell info' parameters represent a standard emerging PV device and were selected according to the literature analysis of **Table 5.1**, but were varied as described in Chapters 6-7 to analyse improvements or specific state-of-the-art devices.

Table 5.4 Model input parameters.

Group	Id	Model Input	Default Value unless otherwise specified
Cell info	p_{rep}	Panel replacement year	5
	C_p	Panel cost, USD/Wp	0.245[68,69]
	PCE_i	Initial PCE, %	10
	G_{FF}	Geometric Fill Factor, %	98[70]
	D_P	Power density, Wp/m^2	98
	B	Burn-in degradation, %	40
	τ_B	Burn-in hours	500 (OPVs), 250 (PVKs)
	D	Degradation rate, %/year	10
Model info	Inv_l	Inverter life, years	10[71,72]
	l	Project Life, years	20[73,74]
	P_{arr}	Size of PV array, kWp	5,492
	A_p	Panel area (72 cell), m^2	1.95[75]
	C_{OP}	Fixed operating cost exc. replacements, USD/Wp	0.01[76,77]
	R	Rental per year, USD/m^2	0.5[78]
	I_G	Inflation, %	2.1[79]
	C_{ip}	Basecase install cost per panel (exc. panels), USD	200.04[80]
	C_{Inv}	Basecase Inverters cost, USD	519,095[69,80]

The ‘Model info’ parameters relate to project-specific parameters for the chosen 5.5 MWp PV installation in Fiji, as well as financial parameters such as discount rate. The assumptions used for these are as follows:

- The inverter life reflects a typical inverter warranty from major manufacturers.[71,72]
- A project life of 20 years, which requires a single inverter replacement during the project life. Note that Si PV panels may have a 25 or 30 year performance warranty,[73,74] but this results in sub-optimal inverter and panel replacement windows for emerging PV.
- Operating costs link to US inflation (2017-2019 average) for bankability.[79]
- The PV array size, inflation, rental and operating costs are based on advice from industry with respect to a realistic project size, and fall within the range of utility scale values reported elsewhere.[76-78,81] Basecase inverters cost and install cost

per panel take input from the Fraunhofer ISE/Agora[80] PV costs study and the NREL Q2/Q3 Solar Industry Update[69] report, as well as advice from industry.

- Discount rate is assumed to be 10%, same value used for non-OECD (Organisation for Economic Co-operation and Development) countries in the IRENA Renewable Power Generation Costs in 2019 report.[77]
- The refurbishment cost of panels (exc. panel cost) is assumed to be 10% of the initial capital cost based on advice from industry.

The model information data are either chosen to be specific values from the literature, or typical values within a practical range for the location or technology. In Chapter 7 some model info parameters are linked to a certain location and their impact is analysed (e.g. discount rate in section 7.6 and install costs in section 7.7). For Cell data, the taken approach was specifying typical values that may apply to either OPV or PVK devices as the literature review showed significant variation in performance within device types. Within Chapter 6, these defaults are changed to examine the impact of the range of reported values on LCOE (*D*, *B* and panel replacement year in section 6.2; module cost in 6.3; PCE_i in 6.3 and 6.4). However, specific state-of-the-art devices LCOE calculations are also available in Chapters 6-7 (sections 6.6 and 7.9) to understand how close are these devices to be market competitive if they are scaled up to module level.

5.3.2 Location data and calculated costs

Fiji is an island country in Oceania whose power needs are currently supplied mostly through fossil fuels (~45%) and hydropower (~50%).[82] However, the government of Fiji has the target of sourcing 100% of its power generation from renewable energy by 2030. In fact, a 15 MWp solar project was approved in late 2020 in Fiji (largest PV project of its kind in the Pacific).[82] Fiji's high insolation values and interest in PV installations therefore make it a very interesting case study.

Table 5.5 summarises PV yield, tilt, discount rate, array spacing and peak Solar hours in Fiji (unreferenced values provided through industry advice), whilst **Table 5.6** shows monthly variations in PV yield[83] and Peak Solar hours.[84]

Table 5.5 Location specific parameters.

Id	Location Parameter	Fiji
d	Discount rate, %	10[77]
Y	PV Yield (kWh/kWp) per year	1,237[83]
T_{deg}	Tilt based on latitude, deg	12
Sp_{arr}	Array spacing, m	5
S	Peak Solar Hours per year	1,889[84]

Table 5.6 Monthly and annual PV Yield[83] and Peak Solar Hours.[84]

Fiji	Jan	Feb	Mar	Apr	May	Jun	Jul	Aug	Sep	Oct	Nov	Dec	Annual
Yield (kWh/kWp)	123	108	119	105	96	85	91	98	95	104	101	112	1,237
Peak Solar Hours	196	171	174	139	127	112	122	137	155	176	183	196	1,889

Based on the input (section 5.3.1) and location (section 5.3.2) parameters, further variables are calculated that are used in the following calculated costs table, as well as in the electricity generation model (5.3.3) section. **Table 5.7** show variables related to the capital costs and those resulting from refurbishments (panels every p_{rep} years, and inverters every 10 years), annual operations & maintenance (O&M) and land rental costs, assuming a 2.1% inflation rate. The variable y denotes the current year (e.g. 1, 2,…20) in the inflation calculations.

Table 5.7 Calculated costs.

Id	Model Output	Formula
R_{tp}	Panel rating, W	$D_P A_{\mathrm{p}}$
A_{Lp}	Land area per panel, m^2	$(Sp_{arr} + 1.92\cos\left(radians\left(T_{deg}\right)\right)2)\,(\frac{0.99}{2})$
N_p	Required number of panels	$\frac{1000P_{arr}}{R_{tp}}$
A_{arr}	Array area, m^2	$A_{Lp}N_{\mathrm{p}}$
C_{iep}	Installation cost exc. Panels, USD	$N_p C_{\mathrm{ip}}$
C_{tp}	Total Panels Cost, USD	$1000P_{arr}C_{\mathrm{p}}$
I_0	Installation cost or capital cost, USD	$C_{iep} + C_{\mathrm{tp}}$
C_{PVref}	Refurbishment cost (panels - PV), USD	$1000P_{arr}C_{\mathrm{p}}$
C_{Oref}	Refurbishment cost (panels - other), USD	$(0.1 \times I_0)(1 + I_{\mathrm{G}})^{y-1}$
C_{pref}	Refurbishment cost (panels), USD	$C_{PVref} + C_{\mathrm{Oref}}$
C_{Invpct}	Inverter cost as % of C_{iep}, %	$\frac{C_{Inv}}{C_{iep}}$
C_{Invref}	Refurbishment cost (inverter), USD	$C_{invpct}C_{iep}(1 + I_{\mathrm{G}})^{y-1}$
C_{OM}	Annual O&M cost, USD	$(1000P_{arr}C_{OP})(1 + I_{\mathrm{G}})^{y-1}$
C_R	Land Rental, USD	$A_{arr}R$
C_t	Total costs, USD	$C_{pref} + C_{\mathrm{Invref}} + C_{OM} + C_R$

5.3.3 PCE time-dependant electricity generation model

Changes in PV capacity due to burn-in and subsequent linear degradation, as well as panel replacement, are accounted for in the power generation model. Under the consideration of degradation only occurring during the hours of full sun in the project location, the cumulative peak solar hours (S_c) were defined from the installation date to adjust PV capacity depending on the current panel period (either burn-in or linear degradation). The monthly peak solar hours in Fiji are shown in **Table 5.6**.

PCE's time-dependence was parameterised so that PV capacity could be calculated at any given time. The following functions were defined for B_F and D_F as the fractional loss in *PCE* as compared to the *PCE* at the start of the burn-in and linear degradation periods respectively, such that $PCE = PCE_i B_F$ during burn-in and $PCE = PCE_b D_F$ during linear degradation.

$$B_F(\%) = aS_c{}^2 + bS_c + 100 \qquad S_C \leq \tau_B \qquad (5.2)$$

$$D_F(\%) = d_L S_c + c + B \qquad S_C > \tau_B \qquad (5.3)$$

Table 5.8 Degradation coefficients.

Id	Model Coefficient	Formula
d_L	d_L, %/hr	$-\frac{D}{S_C}$
a	Coefficient a	$\frac{B-(d_L\tau_B)}{\tau_B{}^2}$
b	Coefficient b	$-d_L-(2a\tau_B)$
c	Coefficient c	$(100-B)-(d_L\tau_B)$

As shown in **Table 5.8**, burn-in (B) and linear degradation (D) values for the candidate PV modules are used to determine the variables dL, a, b, and c. The coefficients *a* and *b* describe a quadratic burn-in period, while d_L and *c* are the slope and intercept of a linear degradation region. These equations lead to a time-dependence of *PCE* of a form shown in **Figure 5.2**. Although equation 5.2 and 5.3 were selected as they described the general form of emerging PV degradation behaviour revealed in the literature review (section 5.2), it is noted that this framework could be modified to accept other arbitrary degradation functions that can represent OPVs and PVKs, or even other technologies if desired. The capacity to change panels at any moment over the project's lifetime is a characteristic of the model, reflecting the potential of supporting infrastructure having a longer lifespan than panels. While the panel replacement in emerging PV has been considered in a previous study,[9] the focus there was taking into account future improvements in efficiency that reduce balance of system (BOS) cost, whilst here the panel replacement is used to mitigate the impact of degradation. Whenever panels are replaced, S_c resets to zero so that the same PCE_i and degradation profile is applied to all panels. Setting τ_B =0 allows the model to account for cases in which *B* = 0%, such that linear degradation begins immediately after initial installation or panel replacement.

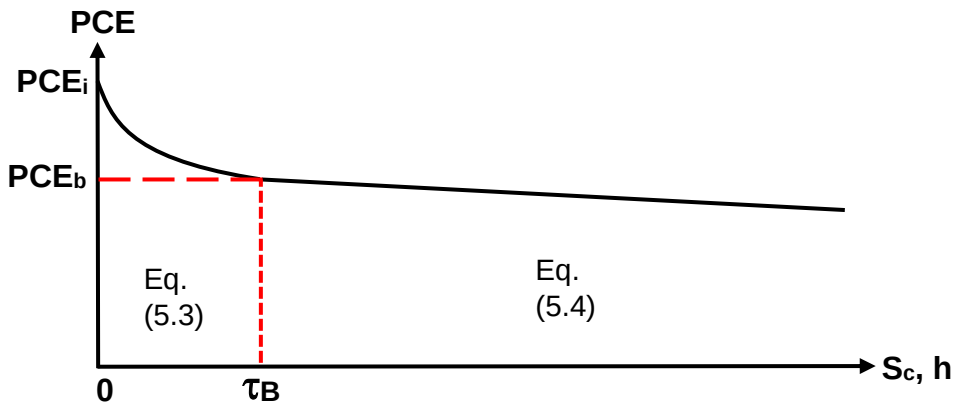

Figure 5.2 PCE degradation as a function of cumulative peak solar hours (S_C) showing regions of burn-in ($S_C < \tau_B$) and linear degradation ($S_C > \tau_B$).

The peak capacity of the PV array, P at any moment in time is thus represented as:

$$P = P_{arr} B_F \qquad S_C \leq \tau_B \qquad (5.4)$$

$$P = P_{arr} \frac{(100-B)}{100} D_F \qquad S_C > \tau_B \qquad (5.5)$$

Where P_{arr} is the size of PV array (**Table 5.4**) and *B* is the Burn-in degradation, %. Energy generation is calculated using the peak capacity at start of the project (P_{arr}), and the end of each month, *m* (P_m) according to equation (5.4) and (5.5). Since the resolution of the model is on a monthly scale, equation (5.5) is used to calculate P if the swap from burn-in to linear degradation happens in the middle of a month. For ease of notation, the initial size of the PV array P_{arr} is subsequently described as P_0. Electricity Generation in month *m* is thus calculated as follows:

$$E_m = Y_m \times \frac{P_m + P_{m-1}}{2} \qquad (5.6)$$

Where E_m = Electricity Generation at current month, Y_m = Yield at current month (from **Table 5.6**), and P_{m-1} = Peak capacity at previous month. Monthly electricity generation values are aggregated for each year of the project, and joined with yearly project costs, to calculate the LCOE using equation (5.1) for the 20-year project.

5.4 References

1 Chang, N. L., Ho-Baillie, A. W. Y., Vak, D., Gao, M., Green, M. A. & Egan, R. J. (2018). Manufacturing cost and market potential analysis of demonstrated roll-to-roll perovskite photovoltaic cell processes. *Solar Energy Materials and Solar Cells* 174, 314-324.

2 Li, N., McCulloch, I. & Brabec, C. J. (2018). Analyzing the efficiency, stability and cost potential for fullerene-free organic photovoltaics in one figure of merit. *Energy & Environmental Science* 11, 1355-1361.

3 Jordan, D. C. & Kurtz, S. R. (2013). Photovoltaic Degradation Rates-an Analytical Review. *Progress in Photovoltaics: Research and Applications* 21, 12-29.

4 Guo, J. & Min, J. (2019). A Cost Analysis of Fully Solution-Processed ITO-Free Organic Solar Modules. *Advanced Energy Materials* 9.

5 Li, Z., Zhao, Y., Wang, X., Sun, Y., Zhao, Z., Li, Y., Zhou, H. & Chen, Q. (2018). Cost Analysis of Perovskite Tandem Photovoltaics. *Joule* 2, 1559-1572.

6 Song, Z., McElvany, C. L., Phillips, A. B., Celik, I., Krantz, P. W., Watthage, S. C., Liyanage, G. K., Apul, D. & Heben, M. J. (2017). A technoeconomic analysis of perovskite solar module manufacturing with low-cost materials and techniques. *Energy & Environmental Science* 10, 1297-1305.

7 Gambhir, A., Sandwell, P. & Nelson, J. (2016). The future costs of OPV – A bottom-up model of material and manufacturing costs with uncertainty analysis. *Solar Energy Materials and Solar Cells* 156, 49-58.

8 Tran, T. T. D. & Smith, A. D. (2018). Incorporating performance-based global sensitivity and uncertainty analysis into LCOE calculations for emerging renewable energy technologies. *Applied Energy* 216, 157-171.

9 Jean, J., Woodhouse, M. & Bulović, V. (2019). Accelerating Photovoltaic Market Entry with Module Replacement. *Joule* 3, 2824-2841.

10 Jordan, D. C., Kurtz, S. R., VanSant, K. & Newmiller, J. (2016). Compendium of photovoltaic degradation rates. *Progress in Photovoltaics: Research and Applications* 24, 978-989.

11 Mulligan, C. J., Bilen, C., Zhou, X., Belcher, W. J. & Dastoor, P. C. (2015). Levelised cost of electricity for organic photovoltaics. *Solar Energy Materials and Solar Cells* 133, 26-31.

12 Bovill, E., Scarratt, N., Griffin, J., Yi, H., Iraqi, A., Buckley, A. R., Kingsley, J. W. & Lidzey, D. G. (2015). The role of the hole-extraction layer in determining the operational stability of a polycarbazole:fullerene bulk-heterojunction photovoltaic device. *Applied Physics Letters* 106.

13 Gasparini, N., Salvador, M., Strohm, S., Heumueller, T., Levchuk, I., Wadsworth, A., Bannock, J. H., de Mello, J. C., Egelhaaf, H.-J., Baran, D. *et al.* (2017). Burn-in Free Nonfullerene-Based Organic Solar Cells. *Advanced Energy Materials* 7.

14 Karpinski, A., Berson, S., Terrisse, H., Mancini-Le Granvalet, M., Guillerez, S., Brohan, L. & Richard-Plouet, M. (2013). Anatase colloidal solutions suitable for inkjet printing: Enhancing lifetime of hybrid organic solar cells. *Solar Energy Materials and Solar Cells* 116, 27-33.

15 Sapkota, S. B., Spies, A., Zimmermann, B., Dürr, I. & Würfel, U. (2014). Promising long-term stability of encapsulated ITO-free bulk-heterojunction organic solar cells under different aging conditions. *Solar Energy Materials and Solar Cells* 130, 144-150.

16 Kong, J., Song, S., Yoo, M., Lee, G. Y., Kwon, O., Park, J. K., Back, H., Kim, G., Lee, S. H., Suh, H. *et al.* (2014). Long-term stable polymer solar cells with significantly reduced burn-in loss. *Nat Commun* 5, 5688.

17 Roesch, R., Eberhardt, K.-R., Engmann, S., Gobsch, G. & Hoppe, H. (2013). Polymer solar cells with enhanced lifetime by improved electrode stability and sealing. *Solar Energy Materials and Solar Cells* 117, 59-66.

18 Oh, H., Sim, H. B., Han, S. H., Kwon, Y. J., Park, J. H., Kim, M. H., Kim, J. Y., Kim, W. S. & Kim, K. (2019). Reducing Burn-In Loss of Organic Photovoltaics by a Robust Electron-Transporting Layer. *Advanced Materials Interfaces* 6.

19 Mateker, W. R., Sachs-Quintana, I. T., Burkhard, G. F., Cheacharoen, R. & McGehee, M. D. (2015). Minimal Long-Term Intrinsic Degradation Observed in a Polymer Solar Cell Illuminated in an Oxygen-Free Environment. *Chemistry of Materials* 27, 404-407.

20 Yang, X.-Y., Niu, M.-S., Qin, C., Bi, P.-Q., Chen, Z.-H., Feng, L., Liu, J.-Q. & Hao, X.-T. (2019). Unraveling the unstable amorphous phase evolution effect on burn-in loss in polymer-fullerene solar cells. *Organic Electronics* 71, 156-163.

21 Pearson, A. J., Hopkinson, P. E., Couderc, E., Domanski, K., Abdi-Jalebi, M. & Greenham, N. C. (2016). Critical light instability in CB/DIO processed PBDTTT-EFT:PC 71 BM organic photovoltaic devices. *Organic Electronics* 30, 225-236.

22 Du, X., Heumueller, T., Gruber, W., Classen, A., Unruh, T., Li, N. & Brabec, C. J. (2019). Efficient Polymer Solar Cells Based on Non-fullerene Acceptors with Potential Device Lifetime Approaching 10 Years. *Joule* 3, 215-226.

23 Heumueller, T., Mateker, W. R., Sachs-Quintana, I. T., Vandewal, K., Bartelt, J. A., Burke, T. M., Ameri, T., Brabec, C. J. & McGehee, M. D. (2014). Reducing burn-in voltage loss in polymer solar cells by increasing the polymer crystallinity. *Energy Environ. Sci.* 7, 2974-2980.

24 Voroshazi, E., Cardinaletti, I., Conard, T. & Rand, B. P. (2014). Light-Induced Degradation of Polymer:Fullerene Photovoltaic Devices: An Intrinsic or Material-Dependent Failure Mechanism? *Advanced Energy Materials* 4.

25 Al-Ahmad, A. Y., Almayhi, F., Al-Mudhaffer, M. F., Griffith, M. J., Liu, W., Li, S., Sivunova, K., Elkington, D., Cooling, N. A., Feron, K. *et al.* (2020). A nuanced approach for assessing OPV materials for large scale applications. *Sustainable Energy & Fuels* 4, 940-949.

26 Cheacharoen, R., Mateker, W. R., Zhang, Q., Kan, B., Sarkisian, D., Liu, X., Love, J. A., Wan, X., Chen, Y., Nguyen, T.-Q. *et al.* (2017). Assessing the stability of high

performance solution processed small molecule solar cells. *Solar Energy Materials and Solar Cells* 161, 368-376.

27 Jiang, Z., Wang, F., Fukuda, K., Karki, A., Huang, W., Yu, K., Yokota, T., Tajima, K., Nguyen, T. Q. & Someya, T. (2020). Highly efficient organic photovoltaics with enhanced stability through the formation of doping-induced stable interfaces. *Proc Natl Acad Sci U S A* 117, 6391-6397.

28 Greenbank, W., Djeddaoui, N., Destouesse, E., Lamminaho, J., Prete, M., Boukezzi, L., Ebel, T., Bessissa, L., Rubahn, H.-G., Turkovic, V. *et al.* (2020). Degradation Behavior of Scalable Nonfullerene Organic Solar Cells Assessed by Outdoor and Indoor ISOS Stability Protocols. *Energy Technology*.

29 Zhang, Y., Yi, H., Iraqi, A., Kingsley, J., Buckley, A., Wang, T. & Lidzey, D. G. (2017). Comparative indoor and outdoor stability measurements of polymer based solar cells. *Sci Rep* 7, 1305.

30 Burlingame, Q., Huang, X., Liu, X., Jeong, C., Coburn, C. & Forrest, S. R. (2019). Intrinsically stable organic solar cells under high-intensity illumination. *Nature* 573, 394-397.

31 Zhang, Y., Bovill, E., Kingsley, J., Buckley, A. R., Yi, H., Iraqi, A., Wang, T. & Lidzey, D. G. (2016). PCDTBT based solar cells: one year of operation under real-world conditions. *Sci Rep* 6, 21632.

32 Xu, X., Xiao, J., Zhang, G., Wei, L., Jiao, X., Yip, H.-L. & Cao, Y. (2020). Interface-enhanced organic solar cells with extrapolated T80 lifetimes of over 20 years. *Science Bulletin* 65, 208-216.

33 Sung, Y.-M., Huang, Y.-C., Chien, F. S.-S. & Tsao, C.-S. (2019). Mechanism and Analysis of Thermal Burn-In Degradation of OPVs Induced by Evaporated HTL. *IEEE Journal of Photovoltaics* 9, 694-699.

34 Bracher, C., Freestone, B. G., Mohamad, D. K., Smith, J. A. & Lidzey, D. G. (2018). Degradation of inverted architecture CH3NH3PbI3-xClx perovskite solar cells due to trapped moisture. *Energy Science & Engineering* 6, 35-46.

35 Tsai, H., Nie, W., Blancon, J. C., Stoumpos, C. C., Asadpour, R., Harutyunyan, B., Neukirch, A. J., Verduzco, R., Crochet, J. J., Tretiak, S. *et al.* (2016). High-efficiency two-dimensional Ruddlesden-Popper perovskite solar cells. *Nature* 536, 312-316.

36 Wang, Z., Lin, Q., Chmiel, F. P., Sakai, N., Herz, L. M. & Snaith, H. J. (2017). Efficient ambient-air-stable solar cells with 2D–3D heterostructured butylammonium-caesium-formamidinium lead halide perovskites. *Nature Energy* 2.

37 Mei, A., Li, X., Liu, L., Ku, Z., Liu, T., Rong, Y., Xu, M., Hu, M., Chen, J., Yang, Y. *et al.* (2014). A hole-conductor-free, fully printable mesoscopic perovskite solar cell with high stability. *Science* 345, 295-298.

38 Lee, J. W., Dai, Z., Han, T. H., Choi, C., Chang, S. Y., Lee, S. J., De Marco, N., Zhao, H., Sun, P., Huang, Y. *et al.* (2018). 2D perovskite stabilized phase-pure formamidinium perovskite solar cells. *Nat Commun* 9, 3021.

39 Wong-Stringer, M., Game, O. S., Smith, J. A., Routledge, T. J., Alqurashy, B. A., Freestone, B. G., Parnell, A. J., Vaenas, N., Kumar, V., Alawad, M. O. A. *et al.* (2018). High-Performance Multilayer Encapsulation for Perovskite Photovoltaics. *Advanced Energy Materials* 8.

40 Tan, H., Jain, A., Voznyy, O., Lan, X., Garcia de Arquer, F. P., Fan, J. Z., Quintero-Bermudez, R., Yuan, M., Zhang, B., Zhao, Y. *et al.* (2017). Efficient and stable solution-processed planar perovskite solar cells via contact passivation. *Science* 355, 722-726.

41 Chen, W., Wu, Y., Yue, Y., Liu, J., Zhang, W., Yang, X., Chen, H., Bi, E., Ashraful, I., Gratzel, M. *et al.* (2015). Efficient and stable large-area perovskite solar cells with inorganic charge extraction layers. *Science* 350, 944-948.

42 Xie, J., Arivazhagan, V., Xiao, K., Yan, K., Yang, Z., Qiang, Y., Hang, P., Li, G., Cui, C., Yu, X. *et al.* (2018). A ternary organic electron transport layer for efficient and photostable perovskite solar cells under full spectrum illumination. *Journal of Materials Chemistry A* 6, 5566-5573.

43 Lv, Y., Zhang, H., Liu, R., Sun, Y. & Huang, W. (2020). Composite Encapsulation Enabled Superior Comprehensive Stability of Perovskite Solar Cells. *ACS Appl Mater Interfaces* 12, 27277-27285.

44 Zheng, X., Hou, Y., Bao, C., Yin, J., Yuan, F., Huang, Z., Song, K., Liu, J., Troughton, J., Gasparini, N. *et al.* (2020). Managing grains and interfaces via ligand anchoring enables 22.3%-efficiency inverted perovskite solar cells. *Nature Energy* 5, 131-140.

45 Wang, Z., McMeekin, D. P., Sakai, N., van Reenen, S., Wojciechowski, K., Patel, J. B., Johnston, M. B. & Snaith, H. J. (2017). Efficient and Air-Stable Mixed-Cation Lead Mixed-Halide Perovskite Solar Cells with n-Doped Organic Electron Extraction Layers. *Adv Mater* 29.

46 Tumen-Ulzii, G., Qin, C., Klotz, D., Leyden, M. R., Wang, P., Auffray, M., Fujihara, T., Matsushima, T., Lee, J. W., Lee, S. J. *et al.* (2020). Detrimental Effect of Unreacted PbI2 on the Long-Term Stability of Perovskite Solar Cells. *Adv Mater* 32, e1905035.

47 Liang, C., Zhao, D., Li, P., Wu, B., Gu, H., Zhang, J., Goh, T. W., Chen, S., Chen, Y., Sha, Z. *et al.* (2019). Simultaneously boost diffusion length and stability of perovskite for high performance solar cells. *Nano Energy* 59, 721-729.

48 Turren-Cruz, S.-H., Hagfeldt, A. & Saliba, M. (2018). Methylammonium-free, high-performance, and stable perovskite solar cells on a planar architecture. *Science* 362, 449-453.

49 Leijtens, T., Eperon, G. E., Pathak, S., Abate, A., Lee, M. M. & Snaith, H. J. (2013). Overcoming ultraviolet light instability of sensitized TiO(2) with meso-superstructured organometal tri-halide perovskite solar cells. *Nat Commun* 4, 2885.

50 Roose, B., Johansen, C. M., Dupraz, K., Jaouen, T., Aebi, P., Steiner, U. & Abate, A. (2018). A Ga-doped SnO2 mesoporous contact for UV stable highly efficient perovskite solar cells. *Journal of Materials Chemistry A* 6, 1850-1857.

51 Grancini, G., Roldan-Carmona, C., Zimmermann, I., Mosconi, E., Lee, X., Martineau, D., Narbey, S., Oswald, F., De Angelis, F., Graetzel, M. *et al.* (2017). One-Year stable perovskite solar cells by 2D/3D interface engineering. *Nat Commun* 8, 15684.

52 Bella, F., Griffini, G., Correa-Baena, J., Saracco, G., Gratzel, M., Hagfeldt, A., Turri, S. & Gerbaldi, C. (2016). Improving efficiency and stability of perovskite solar cells with photocurable fluoropolymers. *Science* 354, 203-206.

53 Mateker, W. R. & McGehee, M. D. (2017). Progress in Understanding Degradation Mechanisms and Improving Stability in Organic Photovoltaics. *Adv Mater* 29.

54 Li, Z., Wu, F., Lv, H., Yang, D., Chen, Z., Zhao, X. & Yang, X. (2015). Side-Chain Engineering for Enhancing the Thermal Stability of Polymer Solar Cells. *Adv. Mat.* 27, 6999-7003.

55 Baran, D., Gasparini, N., Wadsworth, A., Tan, C. H., Wehbe, N., Song, X., Hamid, Z., Zhang, W., Neophytou, M., Kirchartz, T. *et al.* (2018). Robust nonfullerene solar cells approaching unity external quantum efficiency enabled by suppression of geminate recombination. *Nat. Comm.* 9, 2059.

56 Saliba, M., Stolterfoht, M., Wolff, C. M., Neher, D. & Abate, A. (2018). Measuring Aging Stability of Perovskite Solar Cells. *Joule* 2, 1019-1024.

57 ArcGIS Web Application. (2020). https://power.larc.nasa.gov/data-access-viewer/.

58 Zhang, Y., Samuel, I. D. W., Wang, T. & Lidzey, D. G. (2018). Current Status of Outdoor Lifetime Testing of Organic Photovoltaics. *Adv Sci (Weinh)* 5, 1800434.

59 Grätzel, M. (2017). The Rise of Highly Efficient and Stable Perovskite Solar Cells. *Accounts of Chemical Research* 50, 487-491.

60 Bi, E., Tang, W., Chen, H., Wang, Y., Barbaud, J., Wu, T., Kong, W., Tu, P., Zhu, H., Zeng, X. *et al.* (2019). Efficient Perovskite Solar Cell Modules with High Stability Enabled by Iodide Diffusion Barriers. *Joule* 3, 2748-2760.

61 Wang, J., Zhang, J., Zhou, Y., Liu, H., Xue, Q., Li, X., Chueh, C. C., Yip, H. L., Zhu, Z. & Jen, A. K. Y. (2020). Highly efficient all-inorganic perovskite solar cells with suppressed non-radiative recombination by a Lewis base. *Nat Commun* 11, 177.

62 NREL Best Research-Cell Efficiency Chart. (2021). https://www.nrel.gov/pv/cell-efficiency.html.

63 Khenkin, M. V., Katz, E. A., Abate, A., Bardizza, G., Berry, J. J., Brabec, C., Brunetti, F., Bulović, V., Burlingame, Q., Di Carlo, A. *et al.* (2020). Consensus statement for stability assessment and reporting for perovskite photovoltaics based on ISOS procedures. *Nature Energy* 5, 35-49.

64 Reese, M. O., Gevorgyan, S. A., Jørgensen, M., Bundgaard, E., Kurtz, S. R., Ginley, D. S., Olson, D. C., Lloyd, M. T., Morvillo, P., Katz, E. A. *et al.* (2011). Consensus stability testing protocols for organic photovoltaic materials and devices. *Solar Energy Materials and Solar Cells* 95, 1253-1267.

65 Machui, F., Hösel, M., Li, N., Spyropoulos, G. D., Ameri, T., Søndergaard, R. R., Jørgensen, M., Scheel, A., Gaiser, D., Kreul, K. *et al.* (2014). Cost analysis of roll-to-roll fabricated ITO free single and tandem organic solar modules based on data from manufacture. *Energy & Environmental Science* 7.

66 Mulligan, C. J., Wilson, M., Bryant, G., Vaughan, B., Zhou, X., Belcher, W. J. & Dastoor, P. C. (2014). A projection of commercial-scale organic photovoltaic module costs. *Solar Energy Materials and Solar Cells* 120, 9-17.

67 Cai, M., Wu, Y., Chen, H., Yang, X., Qiang, Y. & Han, L. (2017). Cost-Performance Analysis of Perovskite Solar Modules. *Adv Sci (Weinh)* 4, 1600269.

68 Bloomberg NEF Solar PV reduction in cost per watt. (2018). http://www.rapidshift.net/solar-pv-shows-a-record-learning-rate-28-5-reduction-in-cost-per-watt-for-every-doubling-of-cumulative-capacity/.

69 NREL Q2/Q3 Solar Industry Update. (2019). https://www.nrel.gov/docs/fy20osti/75484.pdf.

70 Lucera, L., Machui, F., Kubis, P., Schmidt, H. D., Adams, J., Strohm, S., Ahmad, T., Forberich, K., Egelhaaf, H. J. & Brabec, C. J. (2016). Highly efficient, large area, roll coated flexible and rigid OPV modules with geometric fill factors up to 98.5% processed with commercially available materials. *Energy & Environmental Science* 9, 89-94.

71 Huawei Sun2000 Inverter Warranty. (2020). https://solar.huawei.com/en-AU/download?p=%2F~%2Fmedia%2FSolar%2Fattachment%2Fpdf%2Fau%2Fservice%2Fdownload%2FSUN2000_Inverter_Warranty.pdf.

72 SMA Extended Warranty. (2020). https://www.sma-uk.com/fileadmin/content/www.sma-uk.com/Service/Documents/PriceList.pdf.

73 JA Solar PV Double-Glass Modules. (2018). https://www.jasolar.com/uploadfile/2018/0518/20180518102313951.pdf.

74 CanadianSolar Photovoltaic KU Module Products. (2019). https://www.canadiansolar.com/wp-content/uploads/2019/12/PV_Ku_Module_Warranty_en.pdf.

75 370W PERC Double Glass Module JAM72D00 350-370/PR. (2018). https://www.jasolar.com/uploadfile/2018/0716/20180716031054317.pdf.

76 NREL New Best-Practices Guide for Photovoltaic System Operations and Maintenance. (2017). https://www.nrel.gov/docs/fy17osti/68281.pdf.

77 IRENA Renewable Power Generation Costs in 2019. (2020). https://www.irena.org/publications/2020/Jun/Renewable-Power-Costs-in-2019.

78 LDC Infrastructure Solar Farm Lease Rates Are on the Rise, But Why? (2020). https://ldcinfrastructure.com.au/solar-farm-lease-rates-are-on-the-rise-but-why/.

79 DataBank Inflation, consumer prices (annual %) - United States. (2020). https://data.worldbank.org/indicator/FP.CPI.TOTL.ZG?locations=US.

80 Fraunhofer ISE: Current and Future Cost of Photovoltaics. Long-term Scenarios for Market Development, System Prices and LCOE of Utility-Scale PV Systems. Study on behalf of Agora Energiewende. (2015). https://www.ise.fraunhofer.de/content/dam/ise/de/documents/publications/studies/AgoraEnergiewende_Current_and_Future_Cost_of_PV_Feb2015_web.pdf

81 Pv-magazine Swiss developer to install 7 MW solar system at Fijian gold mine. (2019). https://www.pv-magazine.com/press-releases/swiss-developer-to-install-7-mw-solar-system-at-fijian-gold-mine/.

82 Renew Economy Fiji set to build biggest solar project in Pacific Islands. (2020). https://reneweconomy.com.au/fiji-set-to-build-biggest-solar-project-in-pacific-islands-37084/.

83 Global Solar Atlas. (2020). https://globalsolaratlas.info/map.

84 ArcGIS Web Application. (2020). https://power.larc.nasa.gov/data-access-viewer/.

CHAPTER 6
Emerging PV degradation, efficiency and module cost impact on LCOE

6.1 Introduction

Levelized cost of energy (LCOE) models are frequently used to assess the economic competitiveness of established technologies. However, current literature models are not suitable for accurate LCOE calculation of emerging PV technologies because the degradation profile they consider is similar to that of silicon (Si) PV, instead of the one that characterises developing devices. This Chapter presents LCOE results from the novel model discussed in Chapter 5, which allowed quantifying the relative impacts of realistic degradation, initial efficiency and module cost upon LCOE of emerging PV devices for the first time. Further, the competitiveness of specific, state-of-the-art perovskite PV (PVK) and organic PV (OPV) reported in the literature are assessed for a realistic grid-scale PV installation in the case study location (Fiji), which was chosen due to its high insolation values, interest in adding PV capacity and availability of data required as input for the model. It is demonstrated that the approach used to optimise LCOE is highly dependent on the current state of the technology, i.e. module cost, initial power conversion efficiency (PCE_i), and subsequent degradation. It is also found that devices with high PCE_i do not necessarily result in low LCOE values (e.g. PCE_i = 20% with B = 40% & D = 10%/year results in an LCOE of 0.26 USD/kWh, while a device with PCE_i = 10% with B = 10% & D = 1%/year results in an LCOE of 0.17 USD/kWh), which is attributed to the largely uncorrelated degradation within devices from literature, therefore highlighting the importance of characterising lifetime energy yield in candidate emerging PV devices. PVK and OPV devices LCOE model predictions indicate that these emerging PV technologies have the potential to compete in wholesale electricity markets, but that the inter-relationship of cost, initial performance and degradation must be considered during research and pre-production stages. Additionally, a brief analysis of the emerging PV embodied carbon is presented and it is shown that if some devices can be scaled up to the module level they can offer reduced carbon emissions in comparison with Si PV.

6.2 Impact of degradation on LCOE

Silicon PV panels have dominated the PV market in the last few decades due to their well-established initial efficiency and proven low degradation. Therefore, a good understanding of the degradation profile of emerging PV devices is needed to critically assess the viability of these technologies (OPV and PVK). The impact of degradation in emerging PV devices is here analysed by separating the impacts of burn-in (i.e. short time degradation) and following linear degradation, as there is negligible correlation between them (Chapter 5 **Table 5.2**).

First we analyse the impact of linear degradation by considering specific cases of initial efficiency and burn-in. LCOE predictions are shown in **Figure 6.1** for emerging PV panels with PCE_i = 10% as a function of D with panel replacement after every 2, 5 or 10 years compared to no replacement in the 20-year project. Current champion PV modules for OPVs and PVKs have efficiencies of 11.7% and 17.9%[1] respectively, and by this reason most calculations in this chapter consider initial efficiencies of 10% and 20% to account for present technology status as well as realistic improvements in the near future. Regarding the burn-in, B = 10% and 40%, were chosen as the two main cases to represent typical values within the spread reported in the literature, as discussed in section 5.2 of Chapter 5. 40% represents the most repeated B value in the upper end of literature, whilst 10% represents a B value in the lower end of literature. However, specific literature devices with B = 0% are also considered in section 6.6. Moving on to analysing the impact of degradation, the LCOE sensitivity to D decreases with more frequent panel replacement, whilst increasing project costs. This behaviour leads to significant variations in the ideal panel replacement year as a function of degradation rate, D, for the project under consideration. An important note is that the optimal panel replacement year for the instances examined does not match the 'stabilised lifetime' (T_{S80}), which is defined as the time it takes for the post-burn-in efficiency to decline by 20%. Also, for specific installations, optimal replacement years are shown to be independent of PCE_i and B, since intersections between pairs of panel replacement curves (e.g. 20 years and 10 years at D = 3%) occur for the D when the project cost and PV yield fractional differences match. However, it is important to note that replacing panels too frequently may result in difficulties for the construction and installation sectors, due to complex transportation logistics and increased labour. Whilst emerging PV modules are expected to reduce embodied carbon dioxide as

compared to Si PV[2] (briefly explored in section 6.7), the recyclability impact, as well as the disposal and use of critical elements should be considered if emerging PV is to be commercialised, although this is out of the scope of this thesis.

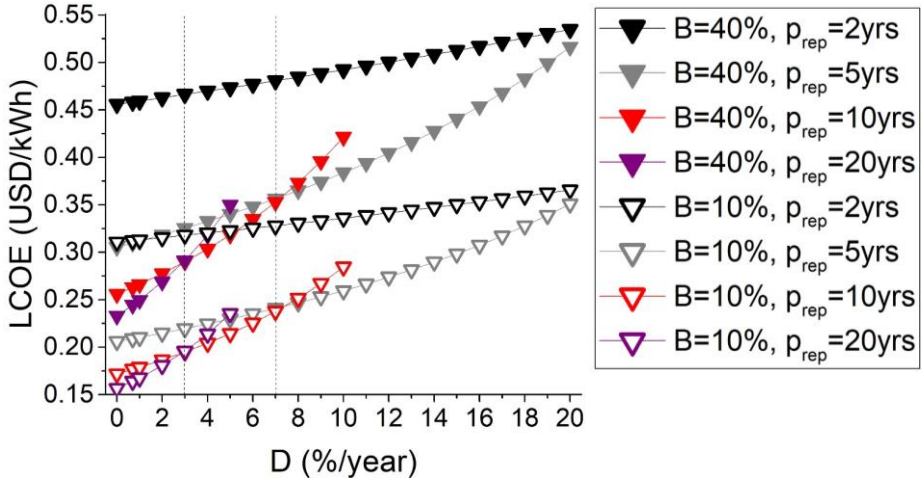

Figure 6.1 Impact of degradation rate in LCOE

Predictions of LCOE as a function of degradation rate, D for panel replacement years of 2 (black), 5 (grey), 10 (red) and no replacement within 20 year project (purple), with PCE_i = 10% and burn-in losses of 40% (solid) and 10% (open). A module cost matching Si PV (0.245 USD/Wp) was considered in all cases.

Now we move on to examine the impact of burn-in whilst considering panel replacement lessons learned from linear degradation. **Figure 6.2** illustrates LCOE projections as a function of burn-in loss, with *B* ranging from 5 to 40% for modules with PCE_i = 10% and four scenarios of *D* = 10, 4, 2, and 1%/year. Values of *B* and *D* are selected to be representative of the emerging PV literature spread from **Figure 5.1** (Chapter 5). According to the lowest LCOE for the value of *D* given in **Figure 6.1**, panel replacement is chosen to occur after 5 years, 10 years, or not at all throughout the 20-year project. LCOE predictions are shown to vary in a non-linear fashion with *B*, and when *B* and *D* values are close to the lower end of the considered ranges, LCOE approaches a local minimum. Because LCOE prioritises production and expenses early in the project life, the non-linearity with *B* is understandable as PV yield is significantly enhanced during the first months of panels operation when *B* is low. **Figure 6.2** also shows that potential materials and device structures might be chosen based on a good mix of short-term and long-term degradation, rather than 'champion'

status in one or the other (e.g. *D* = 4%/year & *B* = 20% better than *D* = 1%/year & *B* = 40%).

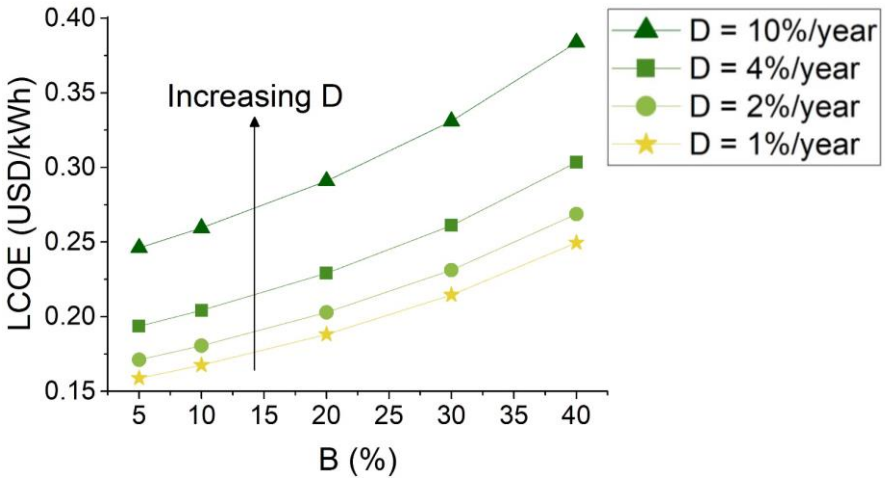

Figure 6.2 Impact of burn-in in LCOE

Predictions of LCOE as a function of burn-in, B for modules with PCE_i = 10% and D = 10%/year (up triangles), 4%/year (squares), 2%/year (circles) and 1%/year (stars). A module cost matching Si PV (0.245 USD/Wp) was considered in all cases.

6.3 Impact of module cost on LCOE

After determining the influence of the degradation profile on LCOE, our attention now moves to the possibility for reduced module cost, which is also a feature of emerging PV technologies. One issue however is that OPVs and PVKs are not commercialized yet, hence there are no specific values of module cost that can be taken directly from PV manufacturers. However, the module cost of emerging PV has been predicted in some literature studies, although they take different considerations (materials, processing, encapsulation, etc.) that lead to a significant range of predicted module costs for emerging PV, as shown in chapter 5 (**Table 5.3**). Therefore, to account for uncertainty and future improvements, the approach here taken does not specify a single module cost that is characteristic of a certain PV panel, but rather predicts LCOE over a significantly larger range of module costs than indicated in the literature. LCOE predictions are shown in **Figure 6.3** for emerging PV modules with PCE_i = 10%, *B* = 40% and *D* = 10%/year, 2%/year and 1%/year, representing values

within the spread reported in the literature. These modules with a range of *D* are compared to those with reduced burn-in (PCE_i = 10%, *B* = 10% and *D* = 10%/year) or increased initial efficiency (PCE_i = 20%, *B* = 40%, *D* = 10%/year). Modules with *D* = 10%/year are replaced every 5 years, and modules with *D* = 2 and 1%/year are not replaced within the 20-year project lifetime, following the optimal panel replacement years from **Figure 6.1**. It is important to note that Si PV module cost depends on materials, processing, transportation and importation of modules, while emerging PV module cost does not add any importation costs, as the model assumption is that emerging PV can be manufactured locally due to the ease of roll-to-roll processing.

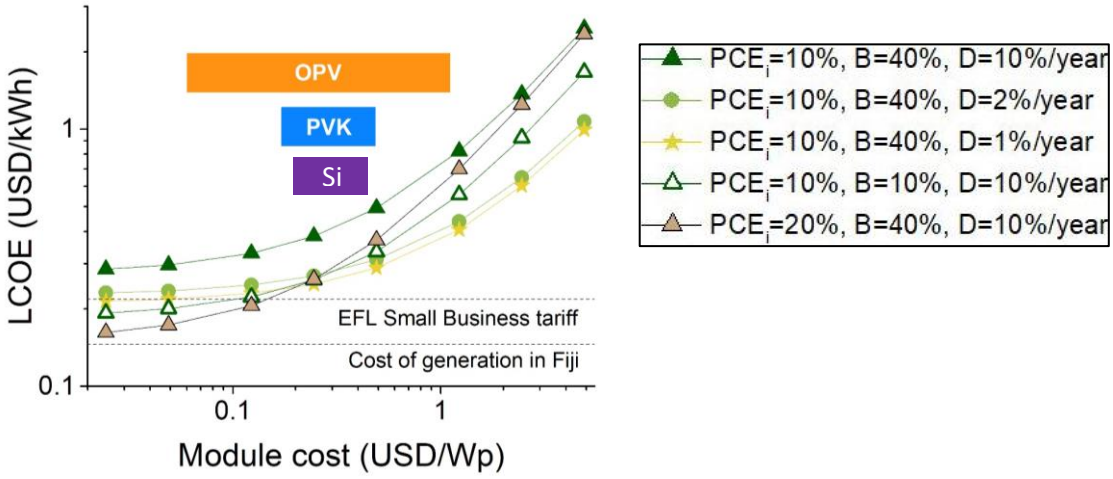

Figure 6.3 Impact of module cost in LCOE

Predictions of LCOE as a function of module cost for panels with PCE_i = 10% (shades of green) with burn-in B = 40% (closed) with D = 10%/year (triangles), 2%/year (circles) and 1%/year (stars). Compared to this are modules with PCE_i = 10%, B = 10% with D = 10%/year (green open triangles) and PCE_i = 20%, B = 40% with D = 10%/year (light brown triangles). Horizontal bars show range of literature estimated module costs for OPV and PVK technologies, as well as Si PV present market module costs range.

Due to the fixed costs of PV installation in the model, such as site establishment, grid connection, and so on, LCOE varies almost linearly with module cost above ~1 USD/Wp, but converges to a minimum value below ~0.2 USD/Wp. At low module cost, the minimum LCOE changes significantly with PCE_i and *B*, but is less effected by *D*. When module costs are high, however, doubling PCE_i has a smaller

impact. These findings show that the current model approach can provide targeted advice on the most efficient ways to reduce LCOE. For example, the LCOE of a device with a module cost of less than 0.2 USD/Wp can be improved by using a more expensive fluorinated encapsulation that reduces degradation.[3] However, if the module cost of a PV technology exceeds 2 USD/Wp, cost reductions in the module (e.g. by using lower cost materials or improving the efficiency of manufacturing processes), are expected to have a greater impact than any improvements in PCE_i. Therefore, it is noted that the dependence of LCOE on module cost varies substantially over the projected module cost range. Reducing burn-in, on the other hand, is always beneficial; for example, lowering burn-in from 40% to 10% reduces LCOE by ~32%. However, as observed in **Figure 6.3**, reducing *B* is recommended over reducing *D* when the module cost is low (<0.2 USD/Wp), and the contrary when the module cost is higher than 0.2 USD/Wp. These findings inspire additional research into determining the projected costs of commercially manufactured emerging PV modules, since this will allow for a more quantitative approach to LCOE optimisation.

6.4 Inter-relationship between PV metrics and LCOE

After looking at the effects of degradation, module cost, and initial efficiency in sections 6.2 and 6.3, we will now have a look at how these parameters interrelate. Pairwise functions of PCE_i, *B* and module cost are shown as contour plots of LCOE predictions in **Figure 6.4**a-c. Once again, the range of values for these parameters is selected considering the literature review as well as possible future improvements. Here, a degradation rate of D = 10%/year and panel replacement every 5 years are assumed, although qualitatively similar data is shown in Appendix A **Figure A1** for panels with improved degradation (D = 2%/year with no panel replacement) in the 20-year project. One benefit of having the data presented in this way is that it allows quantitative comparison of different technologies as a function of the PCE_i, *B* and module cost they provide. For example, a 7.5% PCE_i module with low module cost of 0.12 USD/Wp provides the same LCOE that achieves a 25% PCE_i module with high module cost of 0.75 USD/Wp. However, optimisation strategies would differ regardless of the equivalence in LCOE, since any reductions in module cost would have a low impact on the LCOE of the module with 7.5% PCE_i, whilst the 25% PCE_i

module would be greatly benefited with further module cost reductions. It is also observable that a low efficient module (PCE_i = 5%) is highly benefited from improvements in PCE_i, while a more established efficient module ($PCEi$ = 15%) would be more benefited from reductions in burn-in when the initial scenario has B = 40% for both modules. In a more general way, **Figure 6.4** show that the gradient of LCOE is a complex function of the lifetime energy yield, underlining the importance of using LCOE modelling to guide technological development.

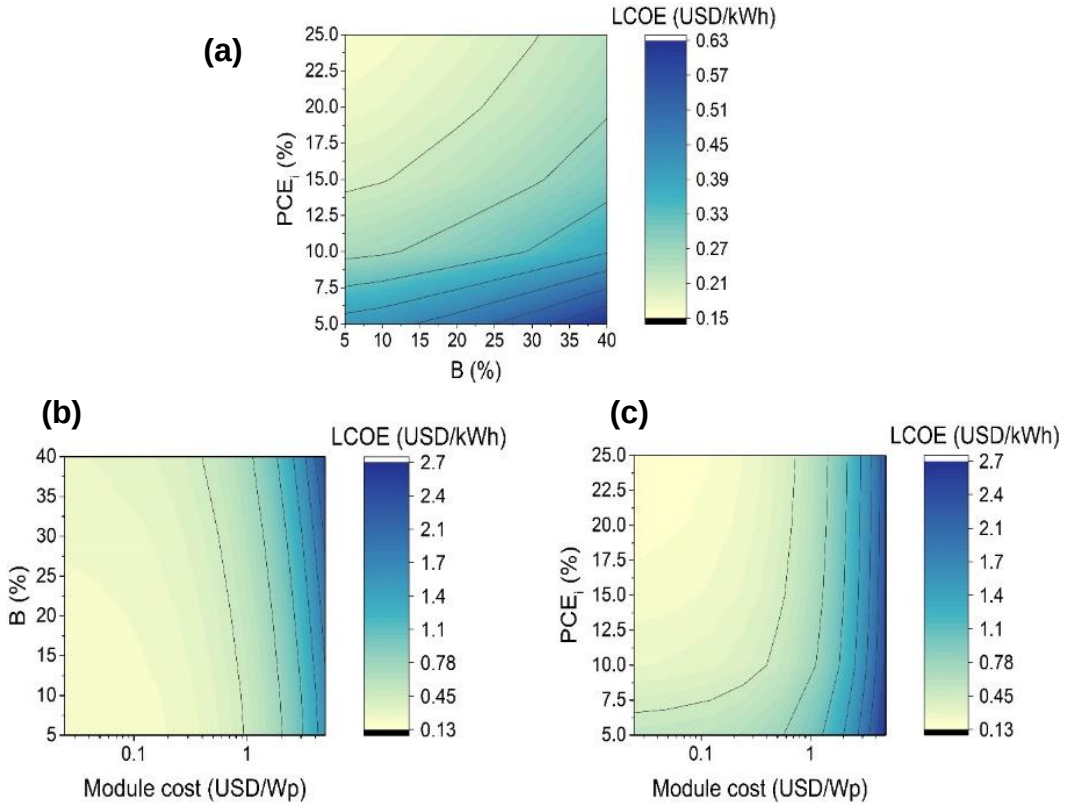

Figure 6.4 Inter-relationship between PV metrics and LCOE

Contour plots of predicted LCOE as a function of (a) PCE_i and burn-in, B assuming module cost 0.245 USD/Wp; (b) Module cost and burn-in, B assuming PCE_i = 10%; (c) PCE_i and module cost assuming burn-in, B = 40%. In all cases D is assumed = 10%/year with panel replacements every 5 years.

6.5 Contextualising LCOE within the electricity market

So far LCOE has been calculated for a wide range of emerging PV parameters, but comparing the resultant LCOE of different PV modules is not enough to prove the feasibility of these technologies. Therefore, the competitiveness of emerging PV LCOE values with respect to other energy generation technologies is now discussed. It is crucial to consider how LCOE compares to energy generation or supply costs from typical grid sources. As a result, LCOE estimates for low and high scenarios of energy generation and sale in Fiji are now taken into account. These values were calculated using similar parameters to the model (10% discount rate, 2.1% inflation and in this case a 25 years lifetime as a mature technology), based on the cost of generation from the Pacific Power Association report (0.1240 USD/kWh)[4] and the small business tariff of Energy Fiji Limited (EFL) (0.1849 USD/kWh)[5], which have an LCOE of 0.1461 USD/kWh and 0.2178 USD/kWh respectively. For context, electricity costs in Fiji are in general cheaper than in European countries (e.g. UK ~0.234-0.255 USD/kWh),[6] but not as cheap as in USA (~0.111-0.149 USD/kWh)[6] and other regions in America or Africa. However, it is important to clarify that the predicted LCOE values here are only applicable to Fiji, and that to comment on viability of emerging PV in other locations would require calculations with appropriate insolation and financial data for the location, which is later discussed in Chapter 7.

Although **Figure 6.3** shows that to compete with the Fiji electricity market reference values, most scenarios for emerging PV would require a module cost of less than 0.1 USD/Wp, **Figure A2** in Appendix A also shows that increasing PCE_i to 20% and 30%, as may be possible in high-performance single junction or tandem PVs,[7] would enable emerging PV competitiveness for a wider range of module costs and degradation parameters values. Panels with B = 40% and D = 2%, for example, are expected to beat the cost of generation for module costs less than 0.12 USD/Wp when PCE_i = 20%, and for module costs less than 0.25 USD/Wp when PCE_i = 30%, notwithstanding the high burn-in, which if also reduced would result in significantly lower LCOE values.

6.6 LCOE Assessment of state-of-the-art emerging PV devices

With previous sections analysing the impact of initial efficiency and degradation parameters (as well as their inter-relationship) upon LCOE for a 'typical' emerging PV module and expected improvements, it is now time to discuss LCOE projections for specific state-of-the-art PVK and OPV devices revealed in the literature review described in section 5.2 (Chapter 5) and listed in **Table 6.1** (note that partial derivatives are also included, but these are explained later on). Only devices which were tested under light-soaking conditions and some form of encapsulation or protective atmosphere (listed in Chapter 5 **Table 5.1**) are here considered, however, devices with degradation rates of 30%/year or more were omitted from the analysis as unrepresentative outliers. As mentioned in chapter 5 (section 5.2), the light-soaking category was chosen over the outdoor testing category because the former has been widely reported in emerging PV literature unlike the latter. Also, light-soaking protocols account for the possibility of active materials photo-oxidation, making it a real-world relevant degradation protocol. Furthermore, all considered OPV and PVK devices have a burn-in period τ_B that is equal to the average for that device type (OPVs τ_B = 500 hours & PVKs τ_B = 250 hours, as shown in Chapter 5 **Table 5.4**) to reduce the number of variables evaluated and facilitate the analysis. Once again, the assumed project was a 5.5 MWp PV installation in Fiji with a local discount rate of 10% and a 20-year project lifetime. Due to substantial variance in the projected module price for PVK and OPV devices, it is here assumed that their module cost is equal to silicon (0.245 USD/Wp), noting that this value fits within the range of expected module costs from **Table 5.3** (Chapter 5) literature review. Knowing that the optimal panel replacement year depends on the degradation parameters of a certain device, the LCOE was calculated for each device considering panel replacements every 2, 5, 10 and 20 years, to ensure obtaining the lowest possible LCOE value, which was ultimately the only LCOE prediction recorded for that particular device.

Table 6.1a Predicted LCOE and partial derivatives for literature OPV devices. The symbols in this table relate to datapoints shown in Figs 6.5 & 6.7.

Active layer	LCOE (USD/kWh)	$\frac{\delta LCOE}{\delta PCE_i}$ (USD/kWh%)	$\frac{\delta LCOE}{\delta B}$ (USD/kWh%)	$\frac{\delta LCOE}{\delta D}$ (USD year / kWh%)	$\frac{\delta LCOE}{\delta C_P}$ (Wp/kWh)	Ref.	Symbol
PCDTBT: $PC_{70}BM$	0.44	-1.8	10	0.15	0.014	[8]	■
P3HT: $PC_{60}BM$	0.68	-1.9	12	0.59	0.023	[9]	●
P3HT: $PC_{60}BM$	0.47	-1.1	0.0	0.10	0.0061	[10]	▲
PCDTBT: $PC_{70}BM$	0.33	-1.4	1.6	0.13	0.0079	[11]	★
PCDTBT: $PC_{71}BM$	0.41	-1.7	10	0.028	0.0096	[12]	□
PCDTBT: $PC_{71}BM$	0.48	-1.8	12	0.13	0.014	[12]	○
DR3TSBDT: $PC_{71}BM$	0.41	-2.6	15	1.1	0.020	[13]	△
DRCN5T: $PC_{71}BM$	0.41	-2.4	15	0.58	0.029	[13]	☆
F3: $PC_{61}BM$	0.48	-2.3	12	1.1	0.027	[13]	⊟
X2: $PC_{61}BM$	0.59	-2.5	18	1.9	0.030	[13]	⊖
DRCN7T: $PC_{71}BM$	0.37	-2.0	4.8	1.3	0.024	[13]	⧋
P3HT: $PC_{60}BM$	0.94	-2.0	5.9	3.2	0.044	[14]	✡
P3HT: IDTBR	0.33	-1.4	0.0	0.75	0.016	[14]	◫
L-PCDTBT: $PC_{71}BM$	0.21	-1.1	0.0	0.068	0.0063	[15]	◐
PBDB-T: ITIC-2F	0.23	-1.3	0.12	0.14	0.0098	[16]	⧊
PBDB-T: ITIC-Th	0.23	-1.3	0.12	0.19	0.010	[16]	✡
DBP: C_{70}	0.24	-1.1	0.0	0.06	0.0062	[17]	★
PTB7-Th: IEICO-4F	0.15	-1.0	1.0	0.016	0.0059	[18]	▬

Table 6.1b Predicted LCOE and partial derivatives for literature PVK devices. The symbols in this table relate to datapoints shown in Figs 6.5 & 6.7.

Active layer	LCOE (USD/kWh)	$\frac{\delta LCOE}{\delta PCE_i}$ (USD/kWh%)	$\frac{\delta LCOE}{\delta B}$ (USD/kWh%)	$\frac{\delta LCOE}{\delta D}$ (USD year / kWh%)	$\frac{\delta LCOE}{\delta C_P}$ (Wp/kWh)	Ref.	Symbol
$PC_{61}BM$/ $FA_{0.83}Cs_{0.17}Pb(I_{0.6}Br_{0.4})_3$	0.22	-1.7	0.39	0.92	0.020	[19]	■
$PC_{61}BM$/ $BA_{0.09}(FA_{0.83}Cs_{0.17})_{0.91}Pb(I_{0.6}Br_{0.4})_3$	0.21	-1.6	0.37	0.62	0.019	[19]	●
$MAPbI_3$/ $PC_{60}BM$	0.47	-3.2	11	6.7	0.038	[20]	▲
$PC_{60}BM$:C_{60}:PFN/ $CH_3NH_3PbI_3$/	0.29	-2.4	3.5	2.5	0.029	[21]	★
C_{60}/ $(HC(NH_2)_2)_{0.83}Cs_{0.17}Pb(I_{0.6}Br_{0.4})_3$	0.22	-1.7	0.57	0.86	0.021	[22]	□
PCBM:PMMA/ $Rb_5Cs_{10}FAPbI_3$	0.11	-1.2	0.043	0.035	0.0067	[23]	○
m-SnO_2/ $FAIPbI_2MABrPbBr_2CsI$	0.24	-1.8	1.9	0.64	0.022	[24]	△
$PC_{61}BM$ $(BA)_2(MA)_3Pb_4I_{13}$	0.12	-0.96	0.0	0.0	0.0054	[25]	☆
SnO_2/ $FA_{0.98}Cs_{0.02}PbI_3$	0.36	-2.3	1.7	3.5	0.049	[26]	⊟
TiO_2-Cl/ CsMAFA	0.17	-1.5	0.0	0.68	0.018	[27]	⊖
$MAPbI_3$/ $PC_{60}BM$	0.27	-2.0	0.0	4.3	0.024	[28]	⧋
CsMAFA/ spiro-OMeTAD (PbI_2 1.15 M)	0.13	-1.2	0.0	0.094	0.0093	[29]	⧊
$CH_3NH_3PbI_3$/ $PC_{61}BM$	0.24	-2.0	0.0	3.8	0.024	[30]	☒
$(5\text{-AVA})_x(MA)_{1-x}PbI_3$/ TiO_2	0.12	-0.96	0.0	0.0	0.0054	[31]	⊗
$CH_3NH_3PbI_{3-x}Cl_x$/ Al_2O_3	0.25	-1.9	11	0.0	0.011	[32]	⧆
$(HOOC(CH_2)_4NH_3)_2PbI_4$/ $CH_3NH_3PbI_3$	0.12	-0.96	0.0	0.0	0.0054	[33]	✶
$FAIPbI_2MABrPbBr_2$/ spiro-OMeTAD	0.098	-1.0	0.0	0.0065	0.0059	[34]	▬
CsFAMA/ AALs	0.085	-0.96	0.0	0.0	0.0054	[35]	◒

Both OPV and PVK devices are projected to have a broad distribution of LCOE values, as shown in **Figure 6.5**a. Although PVKs have a lower average LCOE than OPVs, the distributions overlap. Overall, two OPV devices and eight PVK devices result in LCOE values below the higher electricity selling price LCOE of 0.22 USD/kWh in Fiji, and seven of these PVK devices even beat the lower electricity sale price LCOE of 0.15 USD/kWh. While these LCOE predictions take into account cell level devices characteristics of LCOE, the performance of a real sized module would be expected to be worse. However, PV modules efficiency is also expected to improve in the future. Currently, certified record initial efficiencies for modules are ~5 years behind those of cells for both PVK and OPV devices.[1,36] Increasing the number of initial efficiency and degradation studies of emerging PV modules is therefore crucial to bridge the gap between research and commercial applications.

Figures 6.5b, c, and d depict the predicted LCOE's dependency on individual *B*, *D*, and PCE_i, respectively, with **Table 6.2** including the corresponding statistical data. It is observed that OPV and PVK devices with the highest initial efficiencies are not necessarily those with the lowest resultant LCOE values, which confirms the earlier supposition that emerging PV devices are more favoured from a balance of good efficiency and low burn-in and degradation rates, rather than having a 'champion' status in only one parameter. For example, the second highest PCE_i for OPVs within the dataset was 9.8%, but this device was predicted to have an LCOE of 0.41 USD/kWh because of high *B* and *D*, while an OPV with PCE_i of 7.2% was predicted to have a better LCOE of 0.21 USD/kWh as it had *D* = 2%/year degradation and minimal burn-in. While the finding that emerging PV devices with state-of-the-art initial efficiencies are not necessarily those with state-of-the-art LCOE is not necessarily surprising, it does highlight the importance of quantifying energy generation and associated costs over the lifespan of a device, as individual PV parameters do not provide a clear idea of the technology potential for grid-scale applications, as LCOE does.

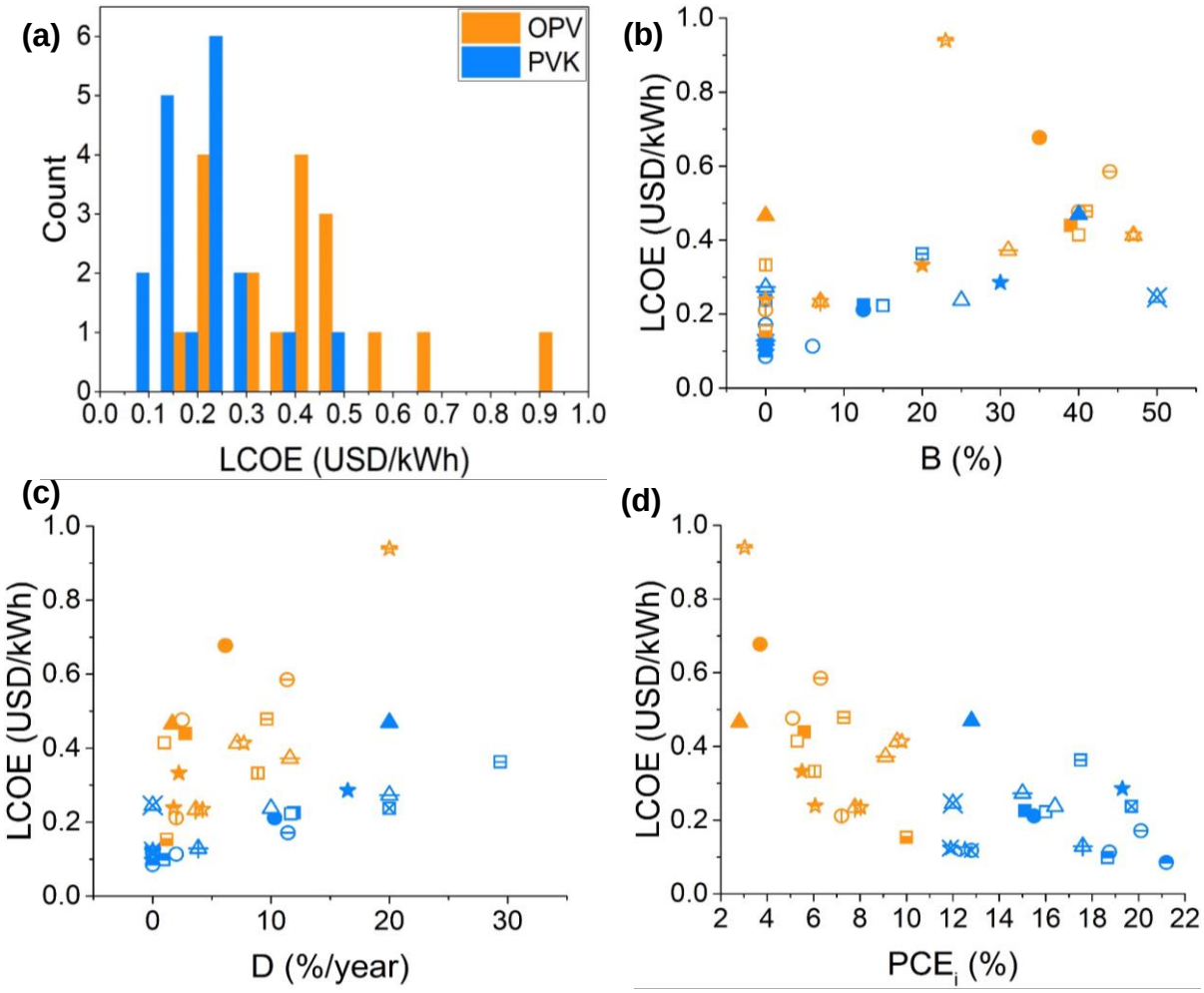

Figure 6.5 Predicted LCOE for specific state-of-the-art PVK and OPV devices

Predicted LCOE for PVK (blue) and OPV (orange) modules with parameters extracted from degradation measurements shown as (a) a histogram, and as a function of (b) B (c) D, and (d) PCE_i. Each symbol represents a unique device, the materials and architecture for which is listed in Table 6.1.

Table 6.2 Statistical analysis of data displayed in Figure 6.5.

PV type	Pearson coefficients			Average LCOE (USD/kWh)
	LCOE vs PCE_i	LCOE vs D	LCOE vs B	
OPV	-0.61	0.71	0.50	0.41
PVK	-0.19	0.82	0.70	0.21

Table 6.2 shows that both OPV and PVK devices have very high LCOE correlation with *D* (0.71 & 0.82 respectively), clearly indicating that devices with low degradation are likely to have a low LCOE. However, there are significant differences between the PCE_i and *B* correlation coefficients for PVK and OPV technologies, suggesting that optimal development strategies for emerging PVs may be different. **Figure 6.6** is used to further analyse this by presenting LCOE predictions for an average OPV or PVK device respectively (Chapter 5 **Table 5.2),** which is then subjected to various parameter improvements. Specifically, the average device for OPVs or PVKs is taken and either: PCE_i is increased by factor 2; burn in is reduced by factor 2; degradation rate is reduced by factor 2; burn-in and degradation rate are reduced by factor 2; or module cost is reduced by factor 2. These improvements represent ways in which average devices may develop by replacing active materials or using a certain methodology. For example, reducing the degradation by factor 2 was observed in P3HT:PC_{61}BM OPVs in Chapter 4 by the addition of the insulating polymer PMMA, and although this improvement was observed in shelf life, the concept is still applicable. All the previously mentioned improvements by factor 2 lead to LCOE predictions that are compared against the champion LCOE values for OPVs or PVKs, and values corresponding for commercial Si PV (PCE_i = 20%, *B* = 2%, *D* = 0.7%/year). It should be noted that the LCOE estimates for OPV and PVK correspond to cell-level devices parameters, thus these LCOE values are unlikely to be achieved by current modules of OPV and PVK technologies, although that might change in the future.

While doubling the PCE_i results in the greatest decrease in LCOE for both OPV and PVK devices, in the case of the PVK, the effectiveness of doubling initial efficiency is equivalent to halving burn-in and degradation. These findings could indicate that PVK devices are approaching a certain technological maturity, where future optimisation efforts should focus on reducing degradation rather than increasing efficiency. The fact that the champion PVK LCOE prediction is for a device with negligible burn-in and degradation backs up this theory. This champion cell-level PVK device even outmatches the LCOE of commercial silicon PV module, indicating that this technology can be cost-competitive in the near future if cell-level parameters can be scaled up to module-level.

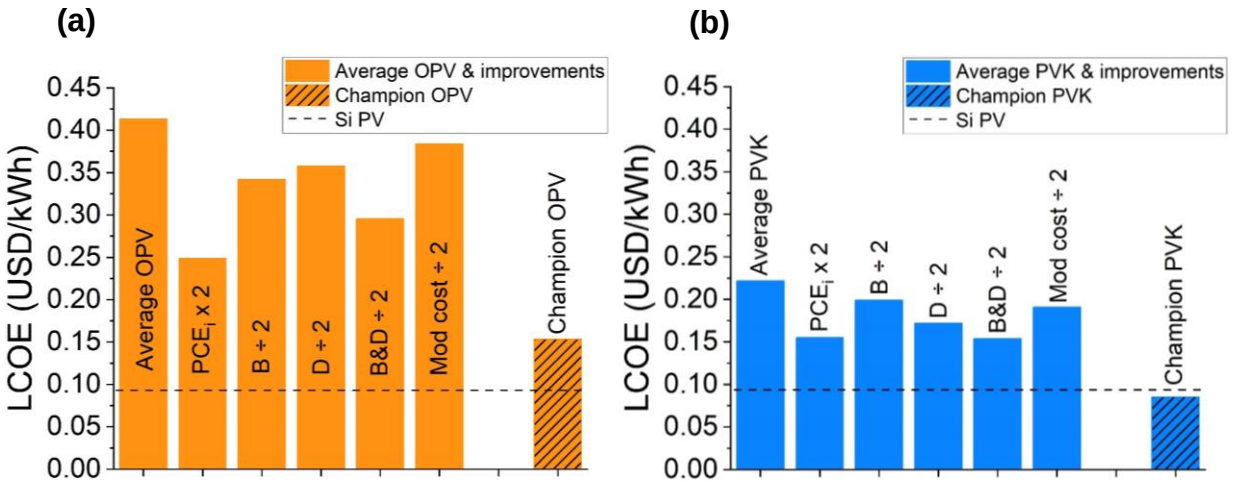

Figure 6.6 Average and Champion OPV & PVK vs Si PV LCOE

Comparison of literature review (a) Average OPV (PCE_i=6.2%, B=30%, D=6%/year) with improvements, Champion OPV (PCE_i=10%, B=0%, D=1.18%/year), and (b) Average PVK (PCE_i=16%, B=19%, D=9%/year) with improvements & Champion PVK (PCE_i=21.2%, B=0%, D=0%/year) vs a Si PV baseline (PCE_i=20%, B=2%, D=0.7%/year). Module cost assumed to be 0.245 USD/Wp for all, except when Mod cost ÷ 2 is indicated (0.1225 USD/Wp).

The partial derivatives of LCOE with respect to PCE_i, B, D and module cost at the point corresponding to each unique device (**Table 6.1**) were calculated numerically to further investigate optimal development strategies. These data are displayed as box plots in **Figure 6.7** and as pair-wise scatter plots in **Figure A3** of Appendix A. The partial derivatives of both PVK and OPV devices appear to differ substantially both between and within populations. This is a significant finding since it demonstrates that to provide quantitative suggestions on how to minimise LCOE, the lifetime energy yield of an individual PV design must be considered (quantified by PCE_i, B, and D). In light of this finding, it is worth noting that, while publications focusing on lifetime energy yield (e.g. ISOS[37,38] L or O standards) are becoming more common, those focusing on initial performance are far outnumbering them. Therefore, the focus of OPV and PVK studies must find a new balance that integrates the initial performance, degradation, and cost to fully realise the benefits of LCOE modelling to select and optimize emerging PV devices and modules.

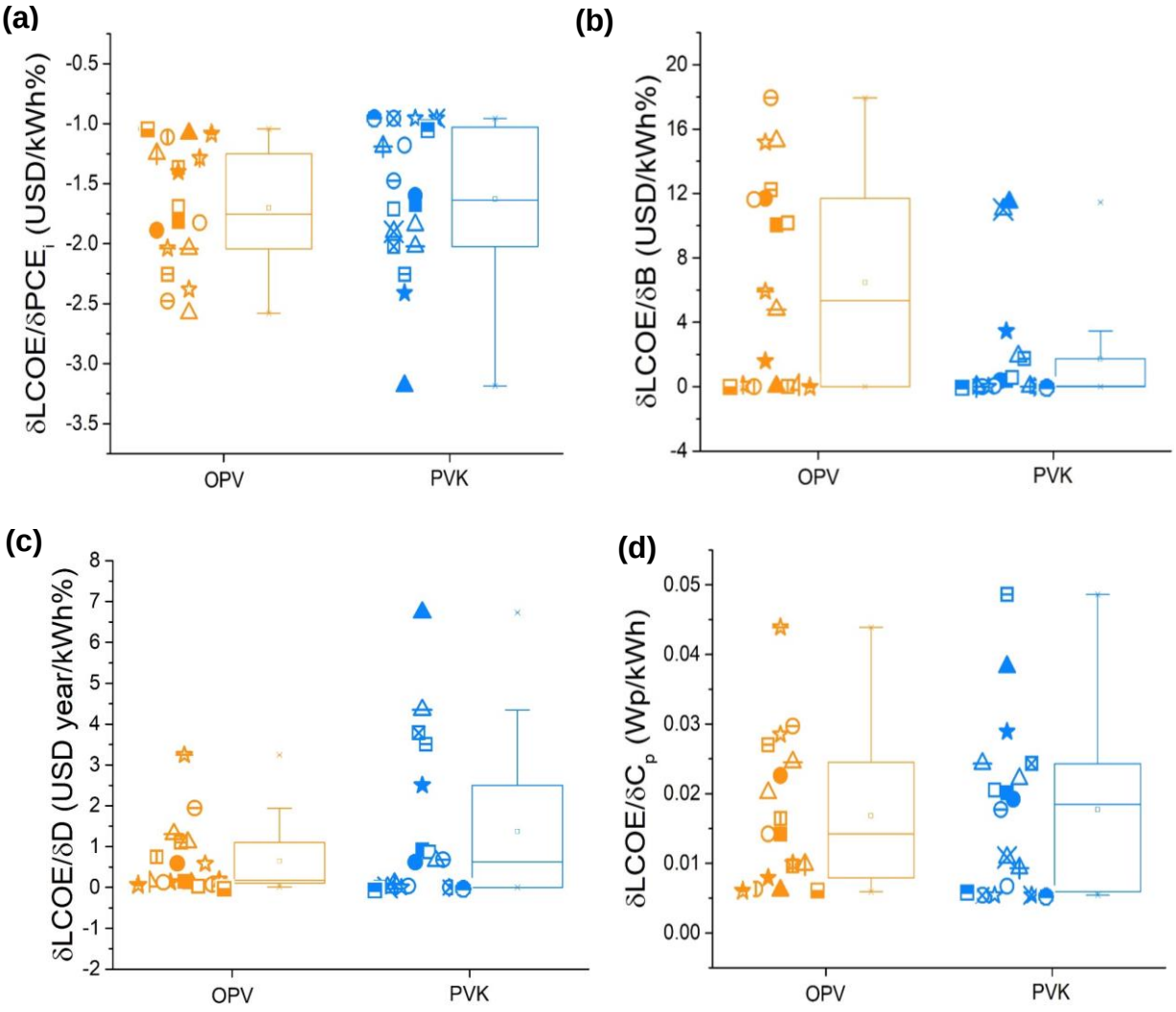

Figure 6.7 Partial derivatives of LCOE vs Emerging PV parameters

Statistical data for partial derivatives of LCOE with respect to (a) PCE_i, (b) B, (c) D and (d) C_p for OPV (orange) and PVK (blue) light-soaked devices. Each symbol represents a unique device, the materials and architecture for which is listed in Table 6.1.

6.7 Embodied carbon analysis of emerging PV

Having analysed the impacts of emerging PV parameters upon LCOE, we now focus our attention in a brief analysis of the embodied carbon provided by OPV and PVK devices. Embodied carbon refers to the carbon dioxide equivalent (CO_2e) emissions associated with materials and construction processes (extraction, transportation, manufacturing) throughout the whole lifecycle of a building or infrastructure, in other words, the carbon footprint of a product or project.[39] It is therefore important to know the embodied carbon of emerging PV technologies to

make a comparison with established Si PV. Although embodied carbon is commonly stated in g CO_2e per kWh, here we go one step back and consider literature values expressed in either kg CO_2e per kWp or kg CO_2e per m^2, which allows to account for differences in rated power or area required for specific devices. **Table 6.3** shows a range of literature embodied carbon values for Si and emerging PV technologies, which serve as input to calculate the total embodied carbon of the 20-year PV project in Fiji, as well as to express the carbon footprint values by units of electricity generation (g CO_2e per kWh) so a direct comparison can be made between the different PV technologies. It is important to note that in cases where panel replacements apply, the carbon emissions per area are multiplied by the corresponding factor to reflect the added effect of new panels. For example, replacing panels after 10 years within the 20-year project results in doubling the kg CO_2e per m^2 values, whilst replacing panels every 5 years would represent an increase by factor 4.

Table 6.3 Literature embodied carbon range of Si and emerging PV technologies expressed in kg CO_2e per kWp or per m^2.

PV type	kg CO_2e per kWp	kg CO_2e per m^2	Ref.
Si	1,500 - 2,560	- - -	[40-42]
OPV & PVK	- - -	14.52 - 52.23	[43-45]

Given that the base case 5.5 MWp Si PV plant generates more electricity than an equivalent 5.5 MWp emerging PV plant throughout its life (20 years) due to higher initial efficiency and lower degradation of the former, here we take a basis for comparison a rated amount of power generation of 152 GWh for the two technologies. **Figure 6.8** illustrate the required initial capacity (MWp) and array area (m^2) for OPV and PVK (average, improved and champion) devices to match the aforementioned Si PV generation. Although the required area for most OPV and PVK based installations is many times greater than for Si PV, it is shown that doubling the efficiency of average devices halves the area requirements. The PVK PCE_i improved device even matches Si PV array area, whilst the champion PVK requires even less land for its installation

due to having a slightly higher initial efficiency than the base case Si PV (21.2% vs 20%).

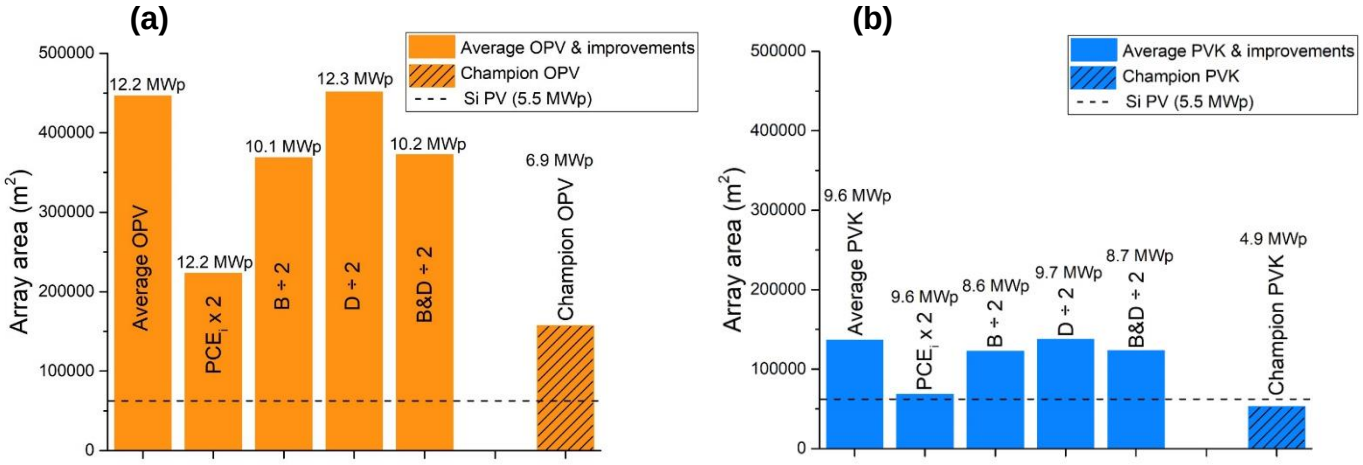

Figure 6.8 Average and Champion OPV & PVK vs Si PV Array Area

Comparison of literature review (a) Average OPV with improvements, Champion OPV, and (b) Average PVK with improvements & Champion PVK vs a Si PV baseline. The array area and indicated MWp initial capacity above each bar matches the total generation of a 5.5 MWp Si PV installation.

Having established the array area requirements for each device it is now possible to present the embodied carbon calculations. **Figure 6.9** show the predicted range of embodied carbon of each OPV and PVK device in floating bars, whilst the Si PV range is within the dashed lines. The corresponding array area from **Figure 6.8** was multiplied by the kg CO_2e per m^2 values from **Table 6.3** and then either multiplied by factor 2 or 4 to calculate the embodied carbon range of the average OPV and average PVK, respectively. Multiplying by factor 2 accounts for added emissions of replacing panels once at 10 years, whilst factor 4 accounts for panel replacements every 5 years during the 20-year project. Improving the PCE_i or B of average devices does not have an effect in the optimal panel replacement year, unlike reducing degradation ($D \div 2$ and $B\&D \div 2$), which doubles panel lifetime, therefore halving the multiplying factor involved in embodied carbon calculations. Champion OPV and PVK devices had a low enough D to avoid panel replacements (factor 1). Si PV also did not require any panel replacements, but its embodied carbon range was instead

calculated by multiplying its initial capacity (5.5 MWp) by the CO_2e values per kWp (**Table 6.3**).

Average embodied carbon reductions of ~50% are achieved either by doubling the initial efficiency or halving the degradation rate of average OPVs or PVKs (representing a lifetime reduction of 15,000 and 9,000 tonnes of CO_2e respectively), whilst halving burn-in only reduces the embodied carbon by 10-17%. However, the reason behind the considerable reductions is not the same in all cases. Doubling the efficiency reduces the required area, whilst halving degradation allows panels to be replaced less often, but both improvement paths lead to halving the embodied carbon. It is also shown that the lower end of the range of OPV devices can compete with the Si PV range (~50-90 g CO_2e per kWh), whilst even the upper end of PVK devices can. Champion OPV and PVK devices even beat the whole Si PV range, with values of ~15-54 and ~5-18 g CO_2e per kWh respectively, which denotes the potential of emerging PV technologies to reduce carbon emissions of utility scale installations.

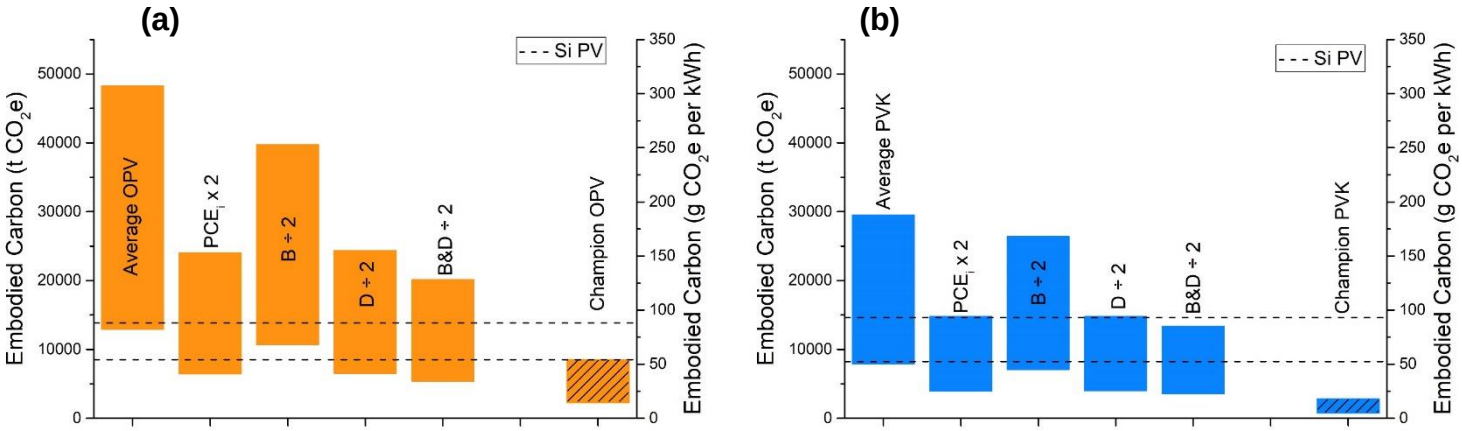

Figure 6.9 Average and Champion OPV & PVK vs Si PV Embodied Carbon

Comparison of literature review (a) Average OPV (PCE_i=6.2%, B=30%, D=6%/year) with improvements, Champion OPV (PCE_i=10%, B=0%, D=1.18%/year), and (b) Average PVK (PCE_i=16%, B=19%, D=9%/year) with improvements & Champion PVK (PCE_i=21.2%, B=0%, D=0%/year) vs a Si PV baseline (PCE_i=20%, B=2%, D=0.7%/year). Embodied carbon is expressed in t CO_2e and in g CO_2e per kWh.

6.8 Conclusions

This chapter presented and quantified the impacts of emerging PV parameters upon LCOE, utilising the novel time-resolved model developed in Chapter 5. A thorough literature review of state-of-the-art OPV and PVK devices captured the degradation behaviour of emerging PV devices, and this data was used to analyse the LCOE potential of these technologies in a realistic 5.5 MWp PV installation in Fiji. Ideal strategies to improve LCOE were found to depend on the current status of a device, which is characterised by initial efficiency, degradation and module cost. It is shown that panels with higher PCE_i are not necessarily those with 'champion' LCOE, as a good balance of efficiency and degradation can lead to lower LCOE values. These findings demonstrate that the feasibility analysis of new PV technologies should consider a holistic approach including degradation as well as costs, and not only the initial efficiency (current focus of many studies). The data also suggest OPV and PVK technologies can compete on wholesale electricity markets if cell-level parameters can be scaled up to module-level. Additionally, it is shown that emerging PV devices have the potential to compete with the embodied carbon values of Si PV, despite most emerging PV installations currently require larger areas and panel replacements due to their lower efficiencies and higher degradation rates. However, champion OPV and PVK devices already beat the embodied carbon values provided by Si PV, demonstrating that future PV installations may result in the reduction of thousands of tonnes of CO_2 equivalent emissions per 20-year project if modules can mimic the cell characteristics.

6.9 References

1 NREL Champion Photovoltaic Module Efficiency Chart. (2020). https://www.nrel.gov/pv/module-efficiency.html.

2 Tian, X., Stranks, S. D. & You, F. (2020). Life cycle energy use and environmental implications of high-performance perovskite tandem solar cells. *Sci. Adv.* 6, 1-10.

3 Uddin, A., Upama, M., Yi, H. & Duan, L. (2019). Encapsulation of Organic and Perovskite Solar Cells: A Review. *Coat.* 9.

4 PPA Benchmarking Report. (2018). https://www.ppa.org.fj/wp-content/uploads/2019/09/2018-FY-Benchmarking-Report_update_220719-FINAL.pdf.

5 Energy Fiji Limited Small Business Tariffs. (2019). http://efl.com.fj/your-business/electricity-tariffs-and-rates/small-business-tariffs/.

6 Global Electricity Prices. (2020). https://www.globalpetrolprices.com/electricity_prices/.

7 Oxford PV hits new world record solar cell. (2020). https://www.oxfordpv.com/news/oxford-pv-hits-new-world-record-solar-cell.

8 Bovill, E., Scarratt, N., Griffin, J., Yi, H., Iraqi, A., Buckley, A. R., Kingsley, J. W. & Lidzey, D. G. (2015). The role of the hole-extraction layer in determining the operational stability of a polycarbazole:fullerene bulk-heterojunction photovoltaic device. *Applied Physics Letters* 106.

9 Karpinski, A., Berson, S., Terrisse, H., Mancini-Le Granvalet, M., Guillerez, S., Brohan, L. & Richard-Plouet, M. (2013). Anatase colloidal solutions suitable for inkjet printing: Enhancing lifetime of hybrid organic solar cells. *Solar Energy Materials and Solar Cells* 116, 27-33.

10 Sapkota, S. B., Spies, A., Zimmermann, B., Dürr, I. & Würfel, U. (2014). Promising long-term stability of encapsulated ITO-free bulk-heterojunction organic solar cells under different aging conditions. *Solar Energy Materials and Solar Cells* 130, 144-150.

11 Roesch, R., Eberhardt, K.-R., Engmann, S., Gobsch, G. & Hoppe, H. (2013). Polymer solar cells with enhanced lifetime by improved electrode stability and sealing. *Solar Energy Materials and Solar Cells* 117, 59-66.

12 Mateker, W. R., Sachs-Quintana, I. T., Burkhard, G. F., Cheacharoen, R. & McGehee, M. D. (2015). Minimal Long-Term Intrinsic Degradation Observed in a Polymer Solar Cell Illuminated in an Oxygen-Free Environment. *Chemistry of Materials* 27, 404-407.

13 Cheacharoen, R., Mateker, W. R., Zhang, Q., Kan, B., Sarkisian, D., Liu, X., Love, J. A., Wan, X., Chen, Y., Nguyen, T.-Q. *et al.* (2017). Assessing the stability of high performance solution processed small molecule solar cells. *Solar Energy Materials and Solar Cells* 161, 368-376.

14 Gasparini, N., Salvador, M., Strohm, S., Heumueller, T., Levchuk, I., Wadsworth, A., Bannock, J. H., de Mello, J. C., Egelhaaf, H.-J., Baran, D. *et al.* (2017). Burn-in Free Nonfullerene-Based Organic Solar Cells. *Advanced Energy Materials* 7.

15 Kong, J., Song, S., Yoo, M., Lee, G. Y., Kwon, O., Park, J. K., Back, H., Kim, G., Lee, S. H., Suh, H. *et al.* (2014). Long-term stable polymer solar cells with significantly reduced burn-in loss. *Nat Commun* 5, 5688.

16 Du, X., Heumueller, T., Gruber, W., Classen, A., Unruh, T., Li, N. & Brabec, C. J. (2019). Efficient Polymer Solar Cells Based on Non-fullerene Acceptors with Potential Device Lifetime Approaching 10 Years. *Joule* 3, 215-226.

17 Burlingame, Q., Huang, X., Liu, X., Jeong, C., Coburn, C. & Forrest, S. R. (2019). Intrinsically stable organic solar cells under high-intensity illumination. *Nature* 573, 394-397.

18 Xu, X., Xiao, J., Zhang, G., Wei, L., Jiao, X., Yip, H.-L. & Cao, Y. (2020). Interface-enhanced organic solar cells with extrapolated T80 lifetimes of over 20 years. *Science Bulletin* 65, 208-216.

19 Wang, Z., Lin, Q., Chmiel, F. P., Sakai, N., Herz, L. M. & Snaith, H. J. (2017). Efficient ambient-air-stable solar cells with 2D–3D heterostructured butylammonium-caesium-formamidinium lead halide perovskites. *Nature Energy* 2.

20 Wong-Stringer, M., Game, O. S., Smith, J. A., Routledge, T. J., Alqurashy, B. A., Freestone, B. G., Parnell, A. J., Vaenas, N., Kumar, V., Alawad, M. O. A. *et al.* (2018). High-Performance Multilayer Encapsulation for Perovskite Photovoltaics. *Advanced Energy Materials* 8.

21 Xie, J., Arivazhagan, V., Xiao, K., Yan, K., Yang, Z., Qiang, Y., Hang, P., Li, G., Cui, C., Yu, X. *et al.* (2018). A ternary organic electron transport layer for efficient and photostable perovskite solar cells under full spectrum illumination. *Journal of Materials Chemistry A* 6, 5566-5573.

22 Wang, Z., McMeekin, D. P., Sakai, N., van Reenen, S., Wojciechowski, K., Patel, J. B., Johnston, M. B. & Snaith, H. J. (2017). Efficient and Air-Stable Mixed-Cation Lead Mixed-Halide Perovskite Solar Cells with n-Doped Organic Electron Extraction Layers. *Adv Mater* 29.

23 Turren-Cruz, S.-H., Hagfeldt, A. & Saliba, M. (2018). Methylammonium-free, high-performance, and stable perovskite solar cells on a planar architecture. *Science* 362, 449-453.

24 Roose, B., Johansen, C. M., Dupraz, K., Jaouen, T., Aebi, P., Steiner, U. & Abate, A. (2018). A Ga-doped SnO2 mesoporous contact for UV stable highly efficient perovskite solar cells. *Journal of Materials Chemistry A* 6, 1850-1857.

25 Tsai, H., Nie, W., Blancon, J. C., Stoumpos, C. C., Asadpour, R., Harutyunyan, B., Neukirch, A. J., Verduzco, R., Crochet, J. J., Tretiak, S. *et al.* (2016). High-efficiency two-dimensional Ruddlesden-Popper perovskite solar cells. *Nature* 536, 312-316.

26 Lee, J. W., Dai, Z., Han, T. H., Choi, C., Chang, S. Y., Lee, S. J., De Marco, N., Zhao, H., Sun, P., Huang, Y. *et al.* (2018). 2D perovskite stabilized phase-pure formamidinium perovskite solar cells. *Nat Commun* 9, 3021.

27 Tan, H., Jain, A., Voznyy, O., Lan, X., Garcia de Arquer, F. P., Fan, J. Z., Quintero-Bermudez, R., Yuan, M., Zhang, B., Zhao, Y. *et al.* (2017). Efficient and stable solution-processed planar perovskite solar cells via contact passivation. *Science* 355, 722-726.

28 Chen, W., Wu, Y., Yue, Y., Liu, J., Zhang, W., Yang, X., Chen, H., Bi, E., Ashraful, I., Gratzel, M. *et al.* (2015). Efficient and stable large-area perovskite solar cells with inorganic charge extraction layers. *Science* 350, 944-948.

29 Tumen-Ulzii, G., Qin, C., Klotz, D., Leyden, M. R., Wang, P., Auffray, M., Fujihara, T., Matsushima, T., Lee, J. W., Lee, S. J. *et al.* (2020). Detrimental Effect of Unreacted PbI2 on the Long-Term Stability of Perovskite Solar Cells. *Adv Mater* 32, e1905035.

30 Lv, Y., Zhang, H., Liu, R., Sun, Y. & Huang, W. (2020). Composite Encapsulation Enabled Superior Comprehensive Stability of Perovskite Solar Cells. *ACS Appl Mater Interfaces* 12, 27277-27285.

31 Mei, A., Li, X., Liu, L., Ku, Z., Liu, T., Rong, Y., Xu, M., Hu, M., Chen, J., Yang, Y. *et al.* (2014). A hole-conductor-free, fully printable mesoscopic perovskite solar cell with high stability. *Science* 345, 295-298.

32 Leijtens, T., Eperon, G. E., Pathak, S., Abate, A., Lee, M. M. & Snaith, H. J. (2013). Overcoming ultraviolet light instability of sensitized TiO(2) with meso-superstructured organometal tri-halide perovskite solar cells. *Nat Commun* 4, 2885.

33 Grancini, G., Roldan-Carmona, C., Zimmermann, I., Mosconi, E., Lee, X., Martineau, D., Narbey, S., Oswald, F., De Angelis, F., Graetzel, M. *et al.* (2017). One-Year stable perovskite solar cells by 2D/3D interface engineering. *Nat Commun* 8, 15684.

34 Bella, F., Griffini, G., Correa-Baena, J., Saracco, G., Gratzel, M., Hagfeldt, A., Turri, S. & Gerbaldi, C. (2016). Improving efficiency and stability of perovskite solar cells with photocurable fluoropolymers. *Science* 354, 203-206.

35 Zheng, X., Hou, Y., Bao, C., Yin, J., Yuan, F., Huang, Z., Song, K., Liu, J., Troughton, J., Gasparini, N. *et al.* (2020). Managing grains and interfaces via ligand anchoring enables 22.3%-efficiency inverted perovskite solar cells. *Nature Energy* 5, 131-140.

36 NREL Best Research-Cell Efficiency Chart. (2020). https://www.nrel.gov/pv/cell-efficiency.html.

37 Khenkin, M. V., Katz, E. A., Abate, A., Bardizza, G., Berry, J. J., Brabec, C., Brunetti, F., Bulović, V., Burlingame, Q., Di Carlo, A. *et al.* (2020). Consensus statement for stability assessment and reporting for perovskite photovoltaics based on ISOS procedures. *Nature Energy* 5, 35-49.

38 Reese, M. O., Gevorgyan, S. A., Jørgensen, M., Bundgaard, E., Kurtz, S. R., Ginley, D. S., Olson, D. C., Lloyd, M. T., Morvillo, P., Katz, E. A. *et al.* (2011). Consensus stability testing protocols for organic photovoltaic materials and devices. *Solar Energy Materials and Solar Cells* 95, 1253-1267.

39 Carbon Cure - What is Embodied Carbon? (2020). https://www.carboncure.com/concrete-corner/what-is-embodied-carbon/.

40 Circular Ecology - Solar PV Embodied Carbon. (2019). https://circularecology.com/solar-pv-embodied-carbon.html.

41 IEA-PVPS - Life Cycle Assessment of Future Photovoltaic Electricity Production from Residential-scale Systems Operated in Europe. (2015). https://iea-pvps.org/wp-content/uploads/2020/01/Future-PV-LCA-IEA-PVPS-Task-12-March-2015.pdf.

42 EU PVSEC - Energy and Carbon Analysis of Photovoltaic Systems in the UK. (2013). https://www.eupvsec-proceedings.com/proceedings?paper=25599.

43 Heliatek - Organic Photovoltaics – Truly Green Energy: “Ultra-Low Carbon Footprint”. (2020). https://www.heliatek.com/fileadmin/user_upload/pdf_documents/2020-10_Heliatek_Truly_Green_Energy_Ultra_Low_Carbon_Footprint_REV2.pdf.

44 Ibn-Mohammed, T., Koh, S. C. L., Reaney, I. M., Acquaye, A., Schileo, G., Mustapha, K. B. & Greenough, R. (2017). Perovskite solar cells: An integrated hybrid lifecycle assessment and review in comparison with other photovoltaic technologies. *Renewable and Sustainable Energy Reviews* 80, 1321-1344.

45 Tian, X., Stranks, S. D. & You, F. (2020). Life cycle energy use and environmental implications of high-performance perovskite tandem solar cells. *Science Advances* 6, eabb0055.

CHAPTER 7
Feasibility of Emerging PV at different locations

7.1 Introduction

Although Photovoltaic (PV) commercial technologies already provide low-cost energy generation with less carbon intensity than conventional energy sources (e.g. coal or natural gas),[1] regional cost differences in module cost, inverters and balance of system (BOS) persist.[2] Solar power prices are often cheaper in developed economies with solid policy frameworks and strong credit ratings in comparison to developing nations.[3] However, there have been an increasing number of cases in recent years of developing countries with impressively low power purchase agreements (PPAs).[3] As explored in Chapter 6, emerging PV technologies may be able to compete with silicon (Si) PV in the future due to improvements in efficiency, degradation and cost, however, that analysis only considered the base case location Fiji, and at this point it is uncertain the impact that emerging PV devices can have on different locations.

In this chapter, an emerging PV levelized cost of energy (LCOE) analysis is carried out for eight countries all around the world to cover a range of economies and insolation levels. This analysis considers the technological and economic improvements of emerging PV devices sourced from literature, to predict their feasibility in the utility scale solar market currently dominated by silicon. It is found that there is a very high correlation between the capital cost and the LCOE of emerging PV, indicating an area of opportunity to lower the LCOE in all locations, but especially in those with currently expensive costs. Average, champion and specific state-of-the-art organic PVs (OPVs) & perovskites (PVKs) LCOE results show that technological improvements effect the viability of PV in a country to different degrees (e.g. India less sensitive to changes in PCE_i than Japan). High-cost locations (i.e. countries with high total installation cost) are more benefited from improved initial efficiency, discount rate (DCR) and install costs, whilst low-cost locations are favoured from reductions in degradation rate and module cost. This emphasises the need to move away from a

'western centric' view of PV technology and ensure that the needs and circumstances of the location are considered at the point of research and development.

7.2 Country selection

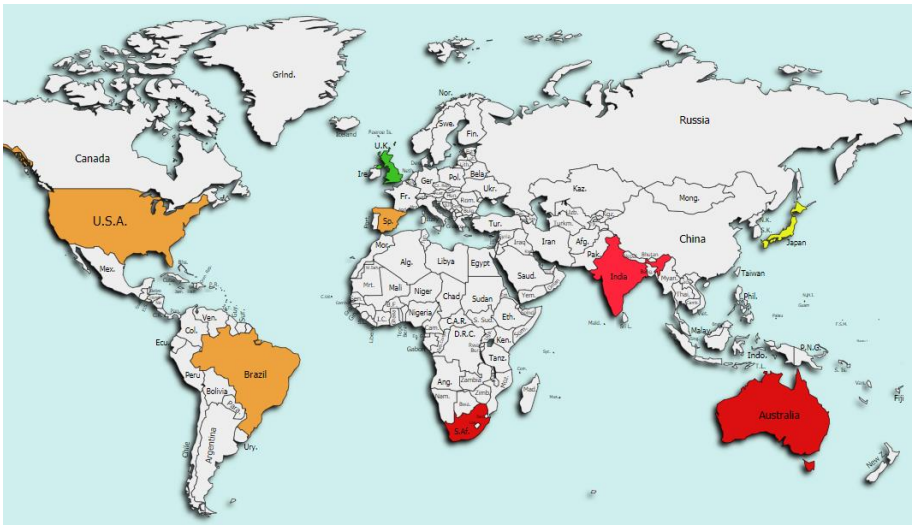

Figure 7.1 Chosen countries for LCOE analysis

World map with coloured countries considered in this study: USA (United States of America), JPN (Japan), IND (India), ZAF (South Africa), BRA (Brazil), ESP (Spain), GBR (United Kingdom) and AUS (Australia). Countries are identified by their ISO 3166 alpha-3 codes.[4]

To analyse the emerging PV LCOE behaviour in different locations of the world, at least one country per continent was considered (**Figure 7.1**). The 2019 IRENA Power Generation Costs Report[5] and the Solar Power Europe - Global Market Outlook 2020-2024 Report[6] were consulted to search for candidate countries with high PV installation activity or good solar potential, and available costing information. For this analysis, eight countries were chosen taking in consideration those sources as well as other PV yield[7,8] and DCR[9,10] relevant sources, to cover a range of economies and insolation levels. USA was chosen from North America as it is part of the top 3 PV markets in the world, while Brazil was chosen from South America to represent a location with high DCR. Australia was chosen from Oceania due to its high insolation. From Asia, India and Japan were chosen to represent locations with low and high installation costs, respectively. South Africa was chosen from Africa due to its high insolation, DCR and inflation rate. From Europe, United Kingdom (UK) and Spain were

chose to represent locations with low and high insolation levels, respectively. The following paragraphs explain how all the parameter values were carefully chosen, and these are all available in **Table B1** of Appendix B.

A 15-year period (2005-2019) average was considered for PV yield and peak sun hours values, and these were obtained using the Global Solar Atlas[7] and NASA Power Data tools,[8] respectively. South Africa and Australia showed the highest insolation values, whilst UK and Japan showed the lowest. Discount rate was selected from the 2018 Grant Thornton – Renewable Energy Survey Reports,[9,10] whilst inflation rate comes from the World Bank Data 2019 indicators.[11] It is noted that the countries with the highest inflation (IND, ZAF & BRA) also had the highest DCR, which suggests inflation is somehow related to risk in investments, although real reasons may be more complex than that.

The Si PV total installation costs, including inverter and module costs were chosen from the 2019 IRENA Power Generation Costs Report.[5] It is important to mention that Si PV module cost is different at all locations, given that most commercial panels are manufactured in China, so different transportation and importation costs apply. However, the selected base module cost for emerging PV reflects an average of various literature studies,[12-15] given that this technology is not commercial yet. Emerging PV module cost is kept the same at all locations so that focus can be made on technological interventions to modules. This reduced module cost also effects the total installation costs of emerging PV. All these specific values can be found in the **Table B1** of Appendix B. However, the effect of further decreasing module cost is also analysed in section 7.5.

7.3 LCOE and location parameters correlation

In **Figure 7.2**, the eight studied locations are split into maximum yield and average yield to cover places with the best PV potential and with an average PV potential within the country, respectively. All these locations consider the use of the same technology, which consists of ‘standard’ emerging PV with the following parameters: PCE_i= 10%, B= 40%, D= 10%/year; and they are compared with a reference silicon PV module (PCE_i= 20%, B= 2%, D= 0.7%/year). However, the LCOE

is very different between locations due to differing PV yield, peak sun hours, total installation cost, discount rate (DCR) and inflation rate. **Table 7.1** shows values normalised to the mean value of each parameter to allow quantifiable comparisons between countries.

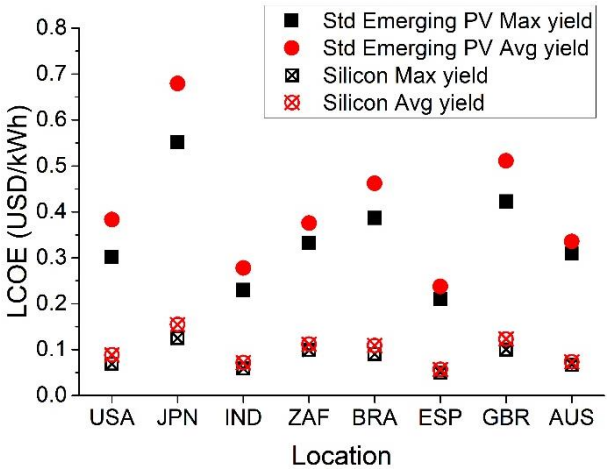

Figure 7.2 Location specific Standard Emerging PV and Si PV LCOE

Standard Emerging PV (PCE_i = 10%, D = 10%/year, B = 40%) and Si PV (PCE_i = 20%, D = 0.7%/year, B = 2%) LCOE of maximum and average yield locations within each country from Figure 7.1.

Table 7.1 Location parameters normalised to mean value.

Location	PV Yield avg location[7]	Peak sun hours avg location[8]	Basecase Utility-scale Emerging PV Total Installation Cost[5]	DCR[9,10]	Inflation rate[11]	Emerging PV LCOE avg yield
USA	1.04	1.02	1.04	0.91	0.66	0.94
Japan	0.81	0.81	1.75	0.56	0.18	1.67
India	1.04	1.10	0.55	1.26	2.83	0.68
South Africa	1.22	1.19	0.95	1.61	1.50	0.92
Brazil	1.04	1.10	1.12	1.26	1.36	1.13
Spain	1.04	0.99	0.64	0.77	0.26	0.58
UK	0.61	0.58	0.84	0.81	0.62	1.25
Australia	1.20	1.20	1.11	0.81	0.59	0.82

From **Table 7.1**, it is observed that low values of LCOE can be achieved notwithstanding high DCR, as shown by India which has the second highest DCR (1.26) and the second best LCOE (0.68) at the same time. It is also observed that the country with least insolation (UK) still results in a lower LCOE than Japan (1.25 vs 1.67). This shows that a lower or higher parameter may not be definitive to predict the LCOE. However, a correlation analysis is conducted later on to quantify the probability of these predictions. As shown in **Figure 7.2**, emerging PV are closer to market in some places than others. This is why it is important to identify the key challenges to reduce their implementation gap. The challenge for each location may be different, as for example Japan would be greatly benefited by cost reductions, whereas in South Africa reducing risk in installations may reduce DCR, which ultimately reduces LCOE. Also, their reduction goal would be different considering that the silicon PV LCOE values vary from country to country.

From a more general perspective, in **Table 7.2** is shown that emerging PV and Si PV LCOE share similar correlation values with insolation and costs. However, DCR and inflation rate correlation increases on emerging PV devices, which could be due to an increased time dependence because of more need for panel replacements as a consequence of having higher degradation rates than Si PV. Still, emerging PV LCOE correlation with DCR (-0.34) and inflation rate (-0.37) is much lower than its positive correlation with total installation costs (0.81), or its also high negative correlation with PV yield and peak sun hours (~-0.60). This remarks the importance of these parameters and indicates a high likelihood of having a low LCOE in locations with low installation costs, whilst DCR or inflation rate would be a less obvious indicative. Also, even if the installation costs are important for both, Si and emerging PV, the former is already well optimised, whereas the latter may still have room to improve, as emerging PV panels are compatible with ready-to-use film solution with self-adhesive backside, and preconfigured wiring that can be easily mounted to decrease installation time and labour.[16] By these reasons, three countries have been chosen to represent locations with cheap (IND), average (USA) and expensive (JPN) total installation costs, and most of the main figures will focus on them. However, discussion still considers the eight studied locations and additional figures can be found in Appendix B.

Table 7.2 Location parameters correlation with LCOE.

Correlation of LCOE vs	Standard Emerging PV	Silicon PV
PV Yield	-0.62	-0.57
Peak sun hrs	-0.59	-0.53
Total Inst. Cost	0.81	0.76
DCR	-0.34	-0.10
Inflation rate	-0.37	-0.24

7.4 Sensitivity analysis of emerging PV parameters

Figure 7.3 show the impact of technological advances in each location. The following improvements were selected to represent values in the lower end (*D* and *B*) and higher end (PCE_i) of the literature review from Chapter 5, although champion devices with even better characteristics are discussed in sections 7.9 and 7.10. Improving the burn-in from 40% to 10% always results in an LCOE decrease of ~33% regardless of the location. One interesting observation is that for most locations it is slightly better to double the *PCEi* (10% to 20%), rather than reducing *D* from 10%/year to 1%/year, with India, UK and Spain being the exception, as they are more benefited from *D* improvements. This indicates that different locations require optimisation strategies. For example, the LCOE reductions in India are of 28% and 40% when improving *PCEi* or *D*, respectively. This behaviour is attributed to India's lower costs and is explained in more detail in the following module cost section. However, improving *D* & *B* at the same time in the 'standard' devices is always better than doubling PCE_i, regardless of the location, with LCOE reductions in the range of 54-60% as observed in **Figure 7.3**. Still, one needs to consider a balance of improvements to make emerging PV competitive against current commercial technologies, and here it is shown that the relative importance of those changes depends on the location.

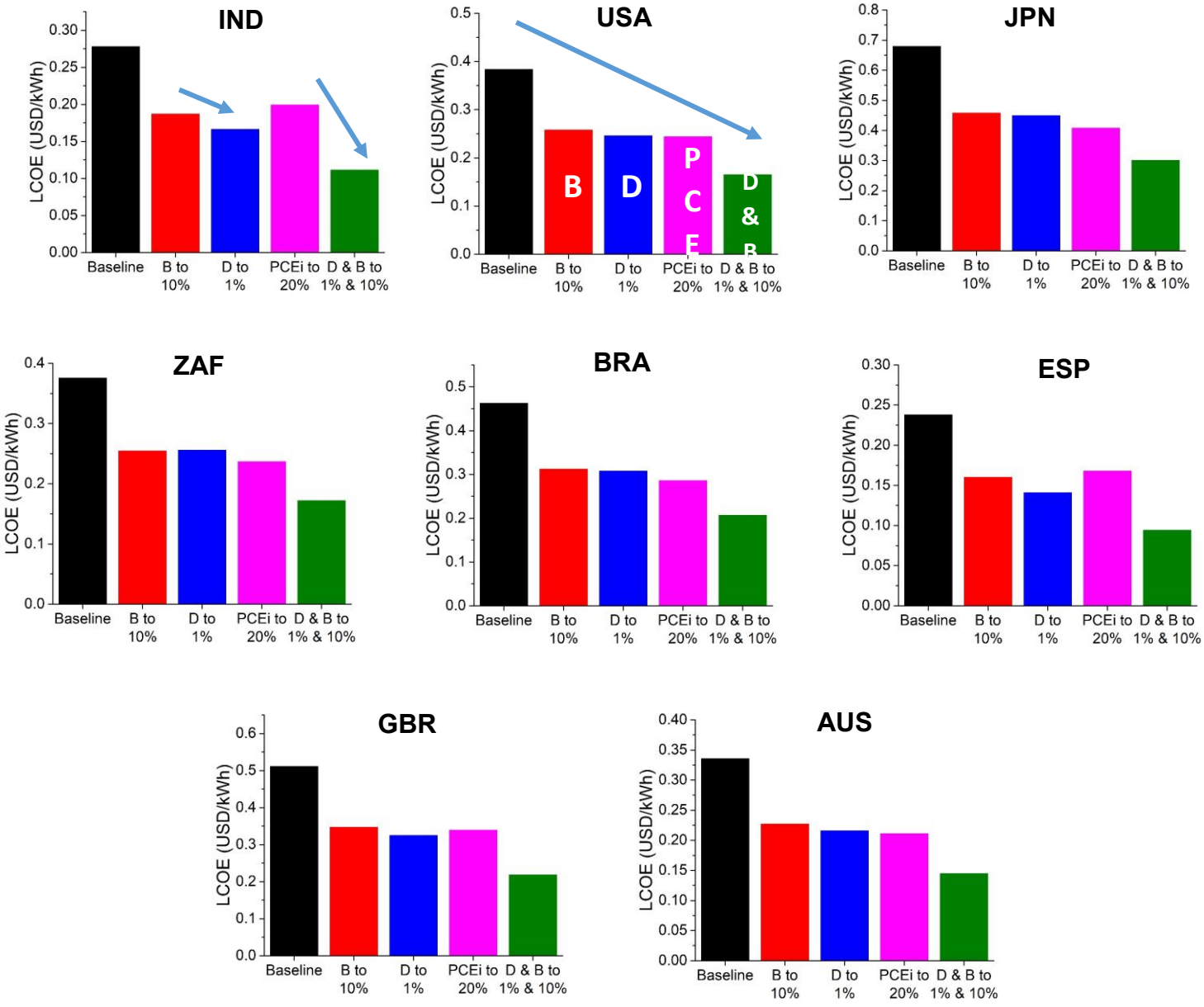

Figure 7.3 Sensitivity analysis of standard emerging PV and its improvements

Baseline emerging PV device (PCE_i = 10%, D = 10%/year, B = 40%) LCOE (black) and its reduction by either improving B to 10% (red), D to 1%/yr (blue), PCE_i to 20% (pink), or D & B to 1%/yr & 10% at the same time (green).

7.5 Effects of improving module cost in different locations

A major factor in the interest in emerging PV is the potential low cost, hence it is important to quantify its impact in location-specific LCOE predictions to test the economic viability of panels with reduced cost. Here the LCOE is calculated for

specific combinations of PCE_i, *D* & *B*, while varying the module cost, and compare the LCOE values to understand the relative importance of module cost upon LCOE for different technology scenarios. **Figure 7.4** show that reducing module cost below the 'standard' module cost here considered to be 0.245 USD/Wp (value within those reported in literature),[12-15] results in steeper curves when both, degradation rate and burn-in are high, regardless of the initial efficiency (closed triangles). This means that reducing the module cost is especially critical for devices with low stability, as it compensates for the abrupt decrease in efficiency and need for often panel replacements due to the high levels of *B* and *D*. As we can see, standard module cost devices with reduced *B* or *D* are better than devices with doubled PCE_i in India, but the order is reversed in Japan, indicating a greater importance of degradation in low cost locations. This happens because having a low install cost per panel, results in a lower ratio against module cost. For example, if India had the costs of Japan, the PCE_i would have priority over *D* or *B* (Appendix B **Table B2**), but if Japan has the costs of India, then the degradation has priority over PCE_i (Appendix B **Table B3**). This indicates that costs are the key for this behaviour, considering that both countries have very different insolation levels, DCR and inflation rate. Taking this in consideration, we can observe that if the module cost keeps falling, the trend becomes the same for all countries, with *D* & *B* combined reductions being better than PCE_i improvements, but the latter being more effective than alone *D* or *B* reductions.

Reducing the module cost at low *D* (1%/year) has a lower impact in LCOE than at high *D* (10%/year). This can be explained by knowing that only high *D* panels need to be replaced during the 20-year project lifetime, therefore reducing the panel's refurbishment costs, which do not apply to the low *D* modules. At 10% PCE_i the LCOE improvement by module cost reductions goes from 3-16% for low *D* modules, and from 7-29% for high *D* modules, depending on the country. India, Spain and UK show the best improvements in LCOE, as these are the countries with lower utility costs. At 20% PCE_i the LCOE reductions are even greater, with a range of 5-24% for low *D* modules, and of 12-40% for high *D* modules, which is a consequence of the installing costs ratio variation with respect of the module cost. Therefore, it is concluded that devices with increasing PCE_i are more benefitted from module cost reductions than devices with lowering *D* & *B*.

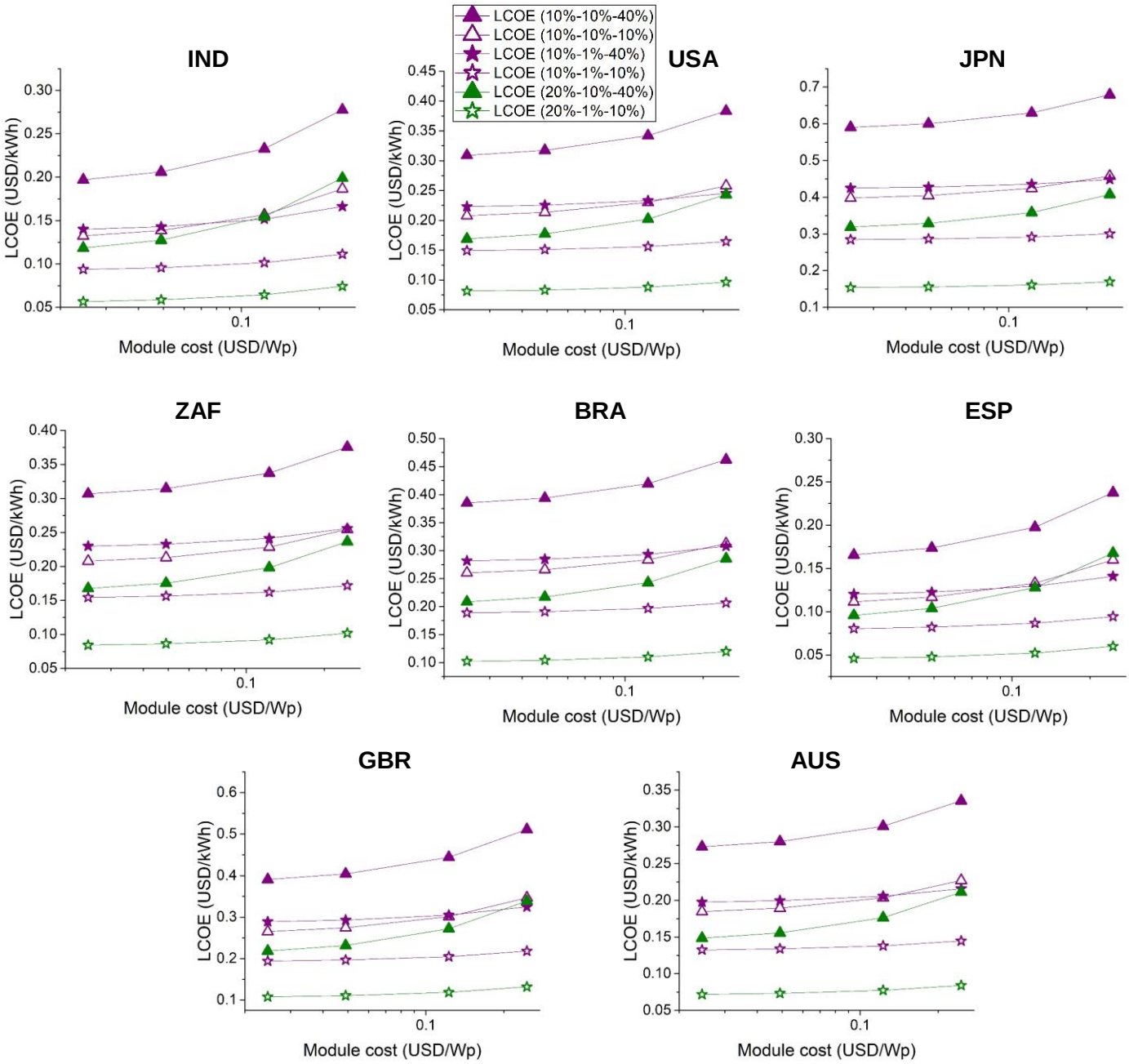

Figure 7.4 Module cost impact in LCOE

Predictions of LCOE as a function of module cost for devices with PCE_i = 10% (purple) or PCE_i = 20% (green), D = 10%/year (up triangles) or 1%/year (stars), and B = 40% (open symbols) or B = 10% (closed symbols).

7.6 Impact of DCR on LCOE

A key factor that is not often considered in the viability of new PV technology is the impact of financing on viability. This is especially important for emerging PV in

which panel replacement changes the typical operations and maintenance (O&M) cost, and for which the competing impacts of cost versus efficiency are not yet known. One important parameter related to risk in investment is the discount rate, and now we focus our attention into the impact of this parameter. For this section, the locations with the highest DCR have been chosen: South Africa – 11.5%, India – 9% and Brazil – 9%, as these are the least similar to Europe and North America, where most emerging PV activity is located. I focus on changes in DCR as this may be impacted by, for example, favourable financing by governments or non-governmental organisations (NGOs). I am therefore asking the question, is favourable finance or further improvements in device performance most beneficial to making emerging PV viable?

In **Figure 7.5** we can see that technical improvements in panels are better than economic improvements (i.e. reducing DCR). This correlates with **Table 7.2** findings (low LCOE vs DCR correlation value), which indicates that a low DCR is far from being an indicative of low LCOE. However, the benefit of having a lower DCR is still observable even without technological improvements, and varies depending of the location. At *D* = 1%/year, major reductions in LCOE of 14% in India, 28% in South Africa and 20% in Brazil are observed when the DCR is decreased from nominal values to 5%, suggesting that the DCR is sensitive to changes in degradation. And although these three countries in principle share a high PV Yield, DCR and inflation rate, only India has very low total installation costs (**Table 7.1**), which lead us to the conclusion that reducing the DCR is more effective in locations with higher PV costs.

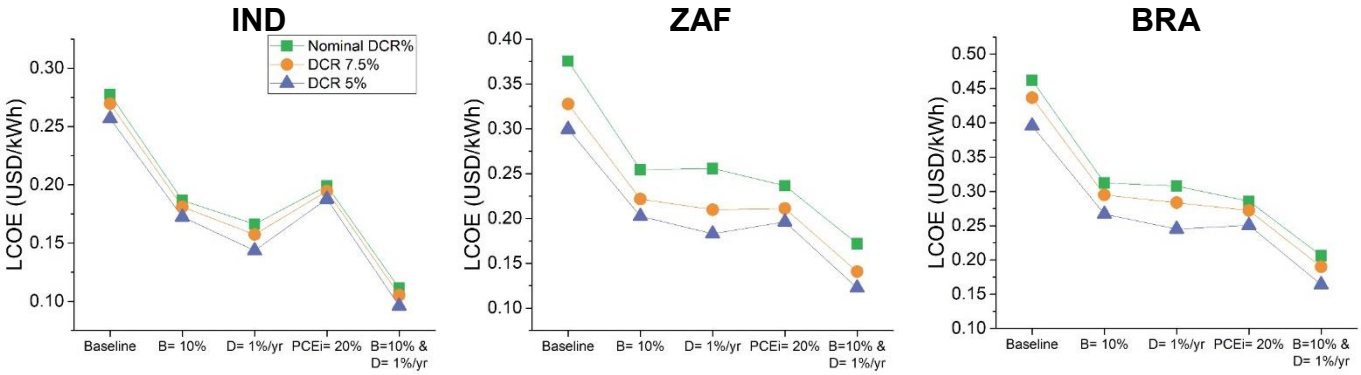

Figure 7.5 DCR impact in LCOE

Predictions of LCOE by improving DCR from nominal (green squares) to 7.5% (orange circles) and 5% (purple triangles) for different technology scenarios.

7.7 Impact of install costs on LCOE

Here I look at install costs because emerging PV have the potential to result in cheaper installations than those of Si PV, but to what extent this is beneficial is unknown as emerging PV is not commercial yet and therefore there is no record of their installation costs from the PV industry. Install costs play an important role in the LCOE calculation, because if they are expensive a solar PV plant installation may not be feasible, even if the location has good insolation and efficient panels. **Figure 7.6** show the impact of reducing by 10% and 20% the install cost per panel, and the reasons behind these analysed reductions relate to the potential of emerging PV for cheaper mounting and mechanical installation, to name a few examples.

From the eight studied locations the LCOE average total reductions go from ~4-8% by 10% install cost reduction, and from ~9-15% by 20% install cost reduction. Japan has the greatest reductions and India the lowest, due to their expensive and cheap installation costs, respectively. Still, Japan would need greater reductions to compete with the LCOE of India due to the high difference in utility costs (**Figure 7.6** & **Table B1** from Appendix B). There are many reasons of why utility costs vary so much from country to country. For example, Japan is affected by limited land availability and expensive construction and soft costs,[6] whilst India benefits from lower costs due to the government role in the solar market, price sensitivity and low cost of labour.[17]

Of course emerging PV has a long way to go to become competitive against Si PV, but the aim of this chapter is to identify how far, and what route emerging PV should take in each location. Reducing the install cost per panel is useful for improving emerging PV LCOE, however, the resultant LCOE can only reach similar Si PV LCOE levels if technological improvements are also addressed (PCE_I=20%, D=1%/year, B=10%), regardless of the location.

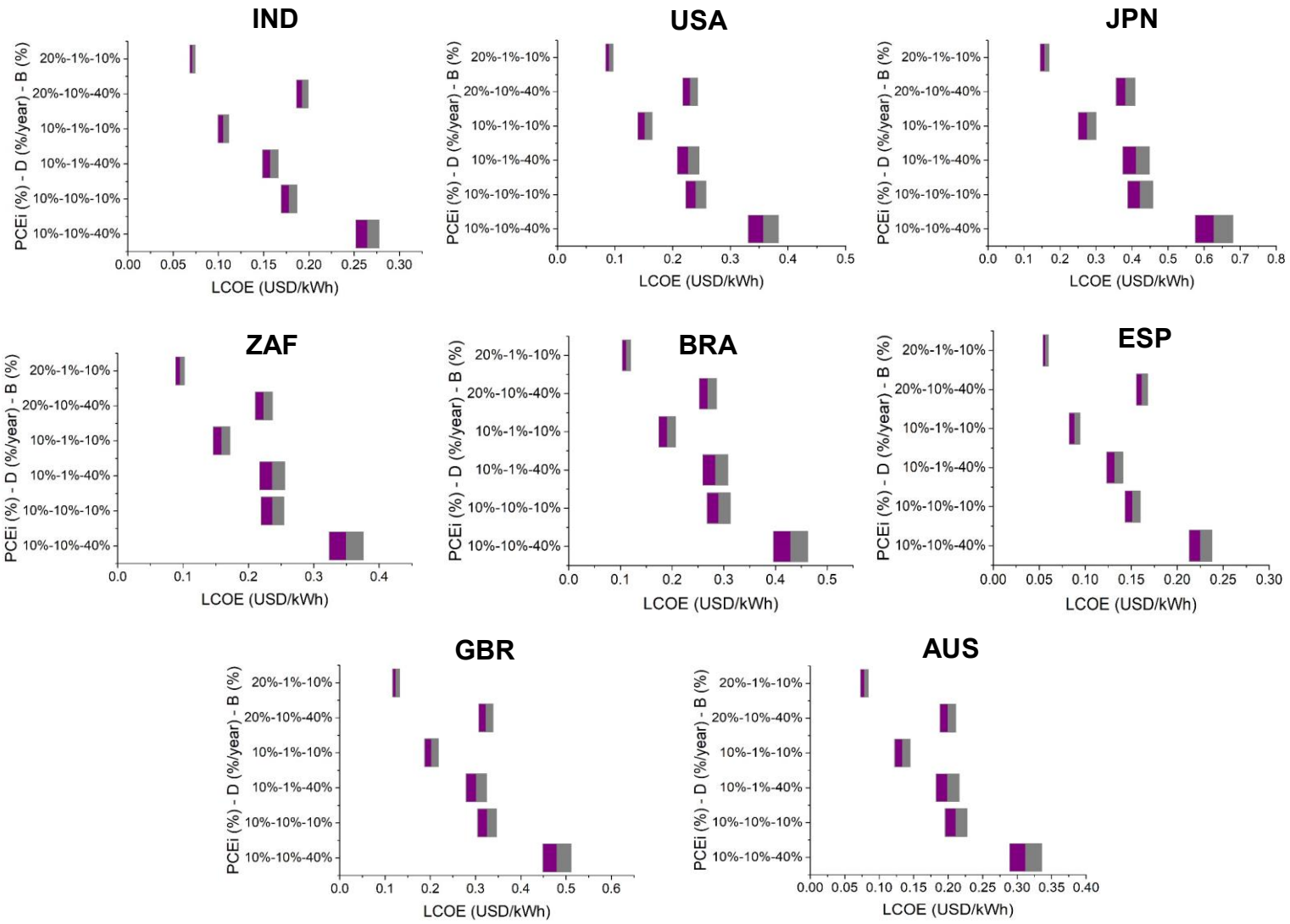

Figure 7.6 Install cost per panel impact in LCOE

Predictions of LCOE of devices with typical install costs (right gray edge), reduced by 10% (gray and purple intersection), and reduced by 20% (left purple edge) for different technology scenarios.

7.8 Combined technological and economic improvements

It is now time to analyse the total LCOE reduction by combining all the technological and economic improvements from the previous sections. This analysis is distinct from the individual sensitivity analysis of section 7.4, as the aim of this section is to accumulate the improvements to see whether the additive improvements can 'beat' Si PV LCOE. **Figure 7.7** show a step by step LCOE reduction by improved *D*, *B*, PCE_i, Module cost, DCR and Install cost per panel. Only Japan did not benefit

from further DCR reductions, as it already has a lower DCR (4%) than the suggested improvement (5%) for the rest of the locations. It is observed that emerging PV can be competitive against silicon PV (red arrows) in all locations by technological and economic improvements.

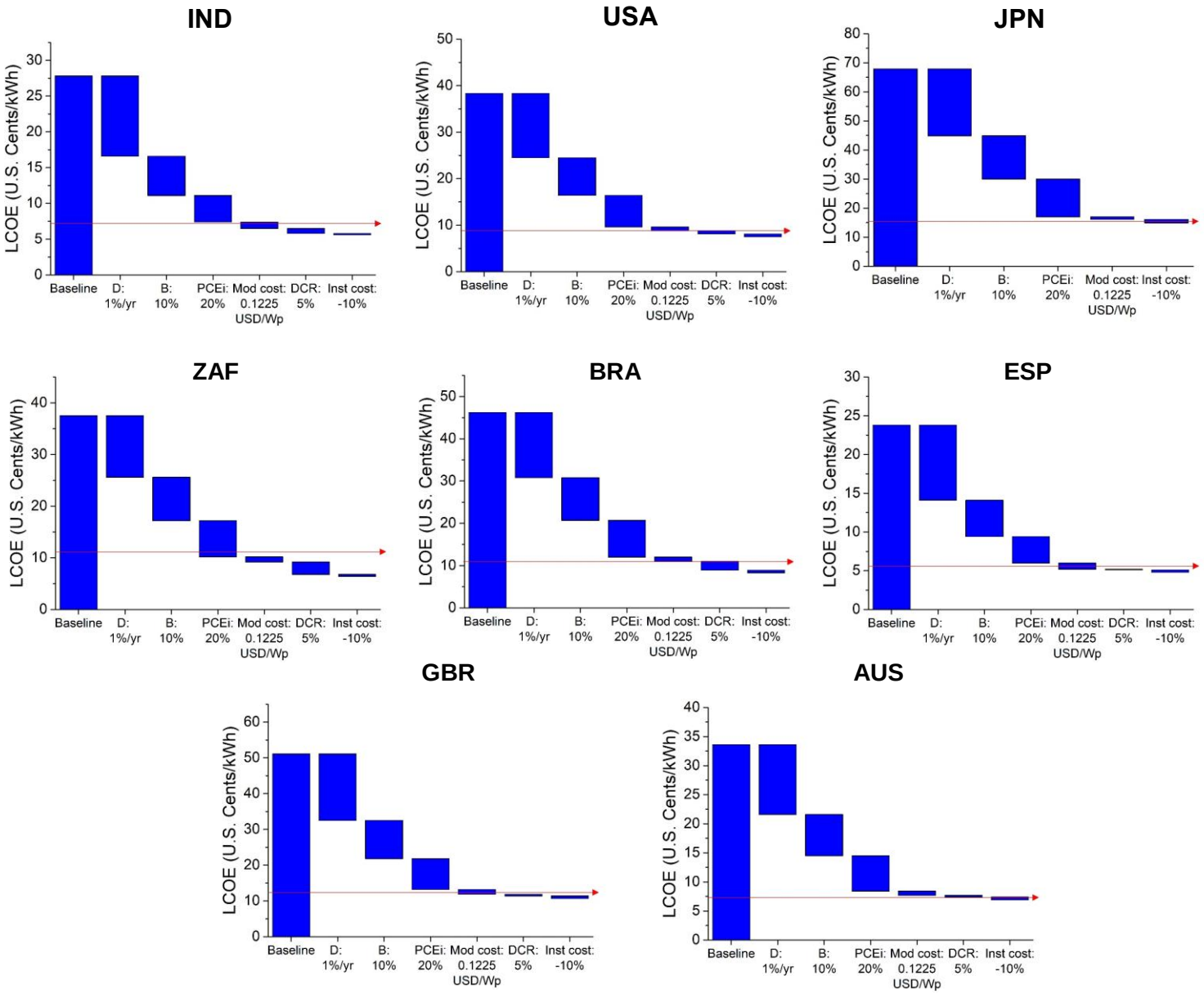

Figure 7.7 Step by step LCOE reduction

Baseline emerging PV device (PCEi = 10%, B = 40%, D = 10%/year) LCOE and its reduction by subsequently improving D to 1%/year, B to 10%, PCE_i to 20%, Module cost to 0.1225 USD/Wp, DCR to 5% and Install cost per panel by 10%. Red arrows indicate the reference Si PV (PCEi = 20%, B = 2%, D = 0.7%/year) LCOE of each location for comparison.

Emerging PV in India and South Africa can match Si PV LCOE just by addressing *D*, *B* and PCE_i, and the rest of the countries by further improving the module cost. In the case of India it is attributed to having the cheapest costs of the eight studied locations, and for South Africa it is attributed to the major difference of its silicon PV module cost and the suggested emerging PV module cost (Appendix B **Table B1**). By also improving the DCR there is a total LCOE reduction of 6% for South Africa, 4% for Brazil and of only 1-2% for the remaining locations, which indicates the importance of reducing the % in places with a high DCR, even if using modules with high efficiency and low degradation. Further reducing by 10% the install cost per panel only contributes with a total LCOE reduction of 1-2% in all locations, but we need to keep in mind that at this point everything else has been improved, so the reductions are expected to be much lower. Still, install cost per panel reductions is a high area of opportunity for improvement, and previous section explored 10% and 20% install cost per panel reductions, but even greater reductions could be achieved by emerging PV, although more research is needed to validate the assumptions. Finally, combining all technological and economic improvements result in a total LCOE reduction of ~79-83% compared to the baseline of each location.

7.9 Location-specific LCOE analysis of state-of-the-art emerging PVs

Having analysed the separate and combined impact of many factors and their improvements on the LCOE of the different locations, it is now time to present LCOE results for specific state-of-the-art OPVs and PVKs. The analysed devices were chosen from an 8-year literature review (Jan 2013 - Dec 2020)[18-59] fully described in Chapter 5. Only devices which were tested under light-soaking conditions and some form of encapsulation or protective atmosphere were considered and are listed in **Table 6.1** of Chapter 6. Project lifetime (20 years), initial capacity (5.5 MWp) and module cost (0.245 USD/Wp) was kept the same for all locations, whilst specific location data such as PV yield, peak sun hours, inflation, DCR and other costs can be found in Appendix B **Table B1**.

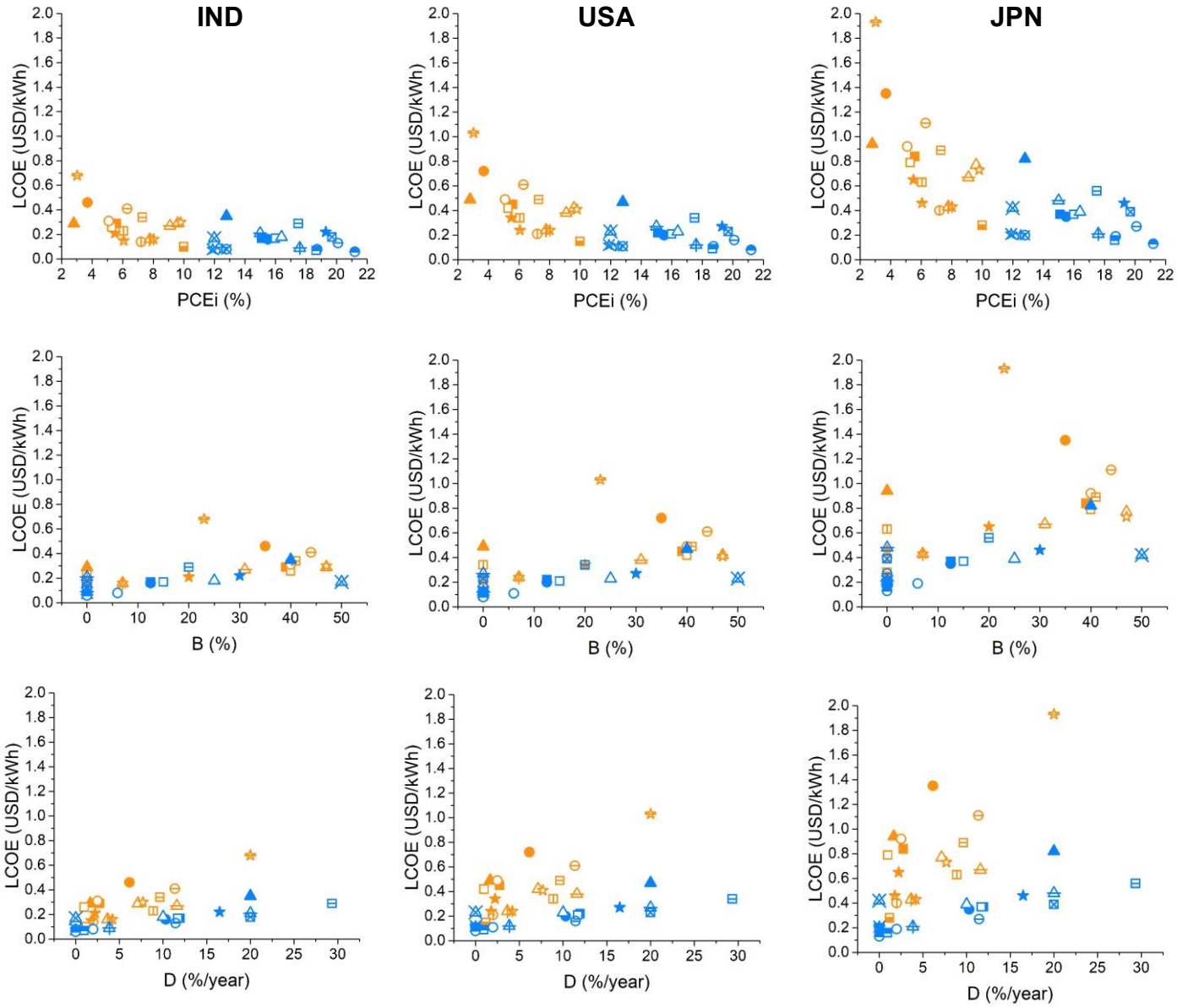

Figure 7.8 Predicted LCOE for specific state-of-the-art OPV and PVK devices

Predicted LCOE for OPV (orange) and PVK (blue) modules with parameters extracted from degradation measurements shown as a function of (1st row) PCE_i, (2nd row) B, and (3rd row) D for (1st column) India, (2nd column) USA, and (3rd column) Japan. Each symbol represents a unique device, the materials and architecture for which is listed in Table 6.1 of Chapter 6.

Figure 7.8 shows the predicted LCOE values of specific emerging devices installed in India, USA and Japan, and **Appendix B Figure B1** presents the same information but normalised to the lowest LCOE of each location. It is clear that PVKs have a lower LCOE than OPVs in general, due to the high difference in efficiency of

the reported devices. Also, there are some apparent trends in PCE_i, D and B with respect to LCOE, however, it is not clear to what extent is LCOE dependent on these parameters, and if the dependency is higher on OPV or PVK devices. To clarify this, **Table 7.3** and **Table 7.4** show the correlation of the PV parameters with LCOE on OPVs and PVKs respectively. These data make it clear that the functional dependence of LCOE on the PV parameters of emerging PV devices is different in different locations. Although the PCE_i correlation with LCOE is much higher on OPVs than in PVKs due to the greater efficiency of PVK devices, the correlation value increases in both technologies when going from India to Japan, suggesting that locations with high costs are more sensitive to changes in efficiency. In the case of B, the behaviour is not so obvious but higher correlation values are observed in the PVK devices, which could be due to having more devices with 0% burn-in than OPVs in the dataset of **Figure 7.8**. However, the highest correlation values are those involving the degradation rate. Here, the correlation value decreases when going from India to Japan, indicating that reducing degradation has a higher impact in low-cost locations. These data are aligned with observations from the previous sections, demonstrating that different optimisation strategies may apply depending on the location.

Table 7.3 Statistical analysis of OPV data displayed in Figure 7.8.

OPVs LCOE correlation vs	IND	USA	JPN
PCE_i	-0.54	-0.62	-0.65
B	0.50	0.46	0.44
D	0.77	0.71	0.69

Table 7.4 Statistical analysis of PVK data displayed in Figure 7.8.

PVKs LCOE correlation vs	IND	USA	JPN
PCE_i	-0.13	-0.21	-0.24
B	0.65	0.69	0.70
D	0.86	0.81	0.78

7.10 Champion and average OPV & PVK LCOE

Figure 7.9 shows the predicted LCOE fractional difference of average and champion OPV (orange) and PVK (blue) devices against the silicon PV LCOE of each location. Appendix B **Figure B2** shows a complementary graph with the specific LCOE predictions, rather than a fractional reference. The analysed devices were chosen from the literature review, with champion devices being identified in **Figure 7.9** with closed symbols and average devices with open symbols. It is observed that current average OPVs are far to compete with the silicon PV LCOE. With champion OPVs and average PVKs, the LCOE difference becomes smaller, but their predicted LCOE is still ~1.4-2.6 times higher than that of silicon PV.

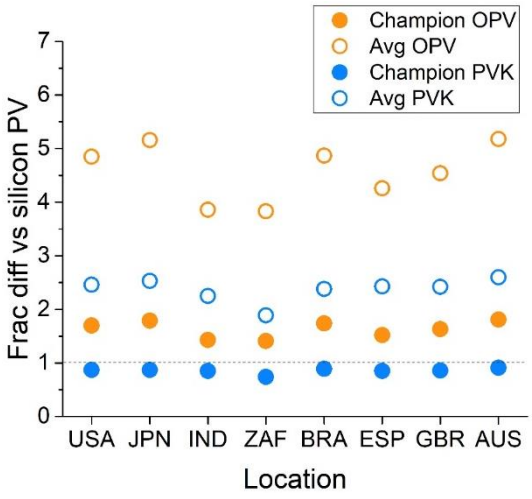

Figure 7.9 Fractional difference of OPVs & PVKs vs Si PV LCOE

Champion (closed symbols) and average (open symbols) OPV (orange) & PVK (blue) devices fractional difference vs Si PV LCOE. Dashed line indicates parity with Si PV. **Champion OPV (PCE_i, D, B):** 10% - 1.18%/yr - 0%, **Avg OPV (PCE_i, D, B):** 6.2% - 6%/yr - 30%, **Champion PVK (PCE_i, D, B):** 21.2% - 0%/yr - 0%, **Avg PVK (PCE_i, D, B):** 16% - 9%/yr - 19%.

Although PVK devices are generally better than OPVs, their distributions overlap and champion OPV devices beat average PVK ones. One can note that at all locations the champion OPV with 10% PCE_i achieves a better LCOE than the average PVK with a high 16% PCE_i, due to the low *D* & *B* of the former (1.18%/yr & 0%)

compared to the latter (9%/yr & 19%). This is very important, because it shows that significantly decreasing degradation after a certain threshold is better than alone improvements in efficiency, even in high-cost locations like Japan. However, it is still noted that low-cost locations like India and Spain are even more favoured by these improvements in stability, denoted by the greater gap between champion OPV and average PVK devices in **Figure 7.9**. In the case of the champion PVK here analysed, its LCOE even beats the silicon PV, due to its high PCE_i (21.2%) and negligible *D* & *B*. These results are encouraging, taking in consideration that further improvements in module cost, DCR and install cost per panel reductions could lower the LCOE even more. However, it is important to note that here cell-size devices are considered, which would need to be scaled up to module size preserving its efficiency and degradation parameters. Also, with champion PVKs the LCOE difference between maximum yield and average yield locations becomes minimal (Appendix B **Figure B2**), making the technology equally viable all across the same country. This would be a significant advantage for emerging PV deployment, because there would be less land restrictions as installing PV plants lead to a similar LCOE regardless of the chosen location within a country.

7.11 LCOE optimisation using a genetic algorithm

Additionally, a genetic algorithm (GA) coded by Cai Williams (Engineering Department of Durham University) was used in conjunction with the LCOE model, to simulate the process of technology development, as a way of demonstrating an LCOE focussed approach to optimising PV technology. A GA is a heuristic search algorithm used to solve search and optimisation problems by employing the concept of natural selection and genetics.[60] The considerations and outcome of the GA used in this thesis are explained in the following paragraphs.

To make use of the GA it was needed to establish an initial population of sets of emerging PV parameters that represent current status and potential improvements. Each individual parameter represents a gene, while each set of parameters represents a chromosome (**Figure 7.10**). The 36 devices from literature review (**Table 6.1** of Chapter 6) were upscaled to 200 chromosomes to have a larger population that allowed for a more widespread representation of parameters that could take place in

the real world. The 200 candidate OPV/PVK devices were created, in addition to those found in the literature review, to provide a suitable population of devices to 'evolve'. These devices were created in line with the statistics reported for real devices – e.g. the PCE_i was drawn at random from a Gaussian distribution with the same mean and standard deviation as that in the literature. In the case the value of a gene was beyond the chosen parameter limits, the value was limited at the appropriate bound. The bounds of each parameter were chosen according to the literature review maximum and minimum values, except in the case of PCE_i, where its upper bound was increased to 30% to account for physical limits. For module cost the bounds were chosen from the industrial scale range shown in **Table 5.3** of Chapter 5. All parameters bounds are specified in **Table 7.5**.

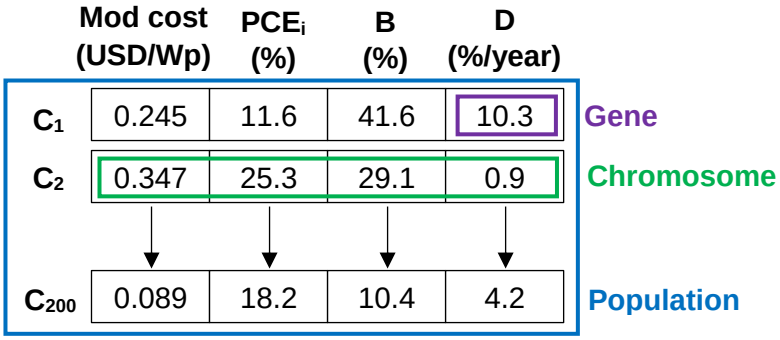

Figure 7.10 Population components in the GA

Each emerging PV parameter (mod cost, PCE_i, B & D) value represents a gene within a chromosome Cx. A chromosome contains a set of four parameter values, which represent a unique device. The sum of all chromosomes conforms the population (C_1-C_{200} in this case).

Table 7.5 GA parameter bounds.

Parameter	Lower bound	Upper bound	Mean	Standard deviation
Mod cost (USD/Wp)	0.06	0.7	0.3275	0.088
PCE_i (%)	2.8	30.0	17.56	17.85
B (%)	0.0	50.0	7.59	7.34
D (%/year)	0.0	30.0	11.42	5.49

Once the initial generation was formed (G_0), the LCOE was calculated for each chromosome considering panel replacements every 2, 5, 10 and 20 years, and only the lowest LCOE value was kept. After this, the fitness function expressed in Equation 7.1 was used to calculate the fitness score of each chromosome. The fitness score indicates how "fit" or how "good" the solution is with respect to the problem, which in this case is trying to minimise the LCOE as close to zero as possible.

$$f(C_x) = \frac{\frac{LCOE_{max} - LCOE_{Cx}}{LCOE_{max} - LCOE_{min}}}{\sum_{i=1}^{200} \frac{LCOE_{max} - LCOE_{Ci}}{LCOE_{max} - LCOE_{min}}} \qquad (7.1)$$

Where:

$f(C_x)$ = fitness of current chromosome

$LCOE_{max}$ = maximum LCOE in current generation

$LCOE_{min}$ = minimum LCOE in current generation

$LCOE_{Cx}$ = LCOE of current chromosome

The top 10 performing devices were then selected (highest fitness) and passed over to the next generation. For the rest of the places (190) in the subsequent generation of candidate PVs, crossover occurs. Crossover is essentially the creation of offspring from two 'parent' PV devices in the previous generation. This might represent, for example, an acceptor compound with superior characteristics being used in a new context, or the translation of a processing methodology to a new type of device. Parents are chosen randomly, but in a way that is weighted by the parent's fitness (i.e. such that more fit parents are more likely to generate offspring). The fitness values of each generation are made to sum to unity. When making the weighted choice the fitness is the probability that the device will be selected, and each selection of a member is independent from all the others. So, a device may be selected more than once, hence be a parent more than once. A random number selects how many of the genes are inherited from the 'mother' and 'father' devices to create the next generation members along with the top performing devices.

Additionally, any of the devices in the next generation may undergo mutation of a gene. Whether mutation occurs is determined by a random number, which if it exceeds (1-mutation rate), which here is 0.25, mutation of a single gene occurs. Which gene is randomly selected, and a new value is selected from the population distribution as for the creation of the initial population. However, there is an exception for the gene representing module cost of devices. A random sample of a normal distribution of a set standard deviation (0.088 from Chapter 5 **Table 5.3**) is used, as the module cost in the initial data was considered the same for all devices (0.245 USD/Wp). This exception is made as there is not any statistical data on emerging PV costs. Each gene value is then checked against the bounds and clipped where needed. **Figure 7.11** summarises the genetic algorithm process, which was iterated for 50 generations. It is noted that the population size, number of generations, mutation rate, crossover and number of top performing devices can be modified to match the evolution of technology.

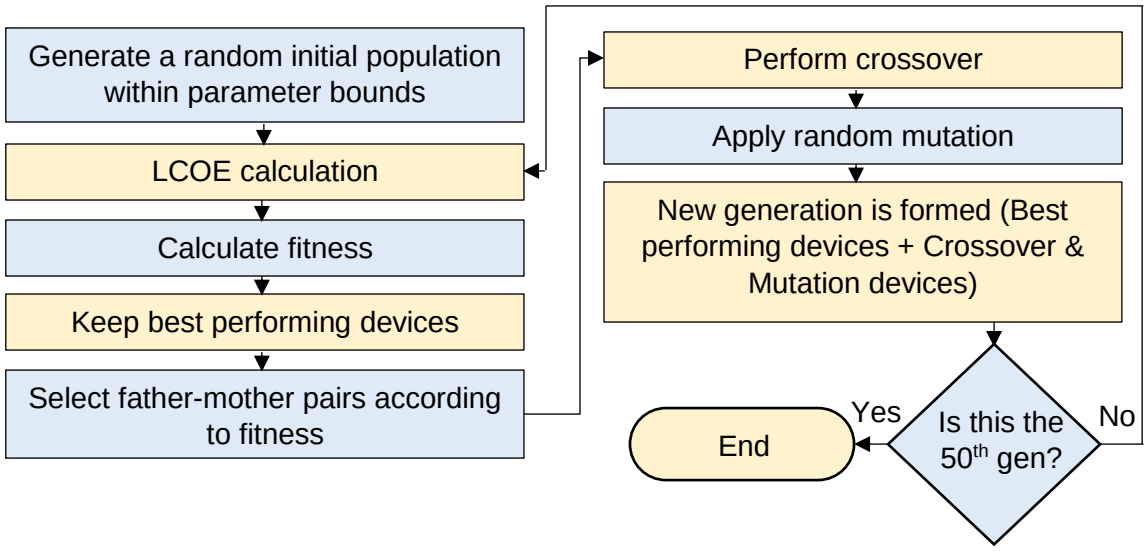

Figure 7.11 Genetic algorithm process

Figure 7.12 shows the GA results after 50 generations in a graphic way. To populate this figure, the average value of the 200 genes associated with a parameter (Mod cost, PCE_i, B or D) was calculated for every generation and for every location, so each average value represents a single point within the graphs. This allows to see the evolution of each parameter from generation to generation, and observe the

differences between countries. A difference in the progression of the parameters observed in **Figure 7.12**, demonstrates that the course of a technology to optimal LCOE is different, and so indicates that technology development is local to each country. During the first generations the differences are not very clear, as the GA is learning and adapting to achieve better LCOEs. However, some differences can be observed in the mid generations, before all the values converge in the last generations, when the GA has optimised all parameters close to the lower or upper bound values from **Table 7.6**. By these reasons, the analysis focus in the mid generations.

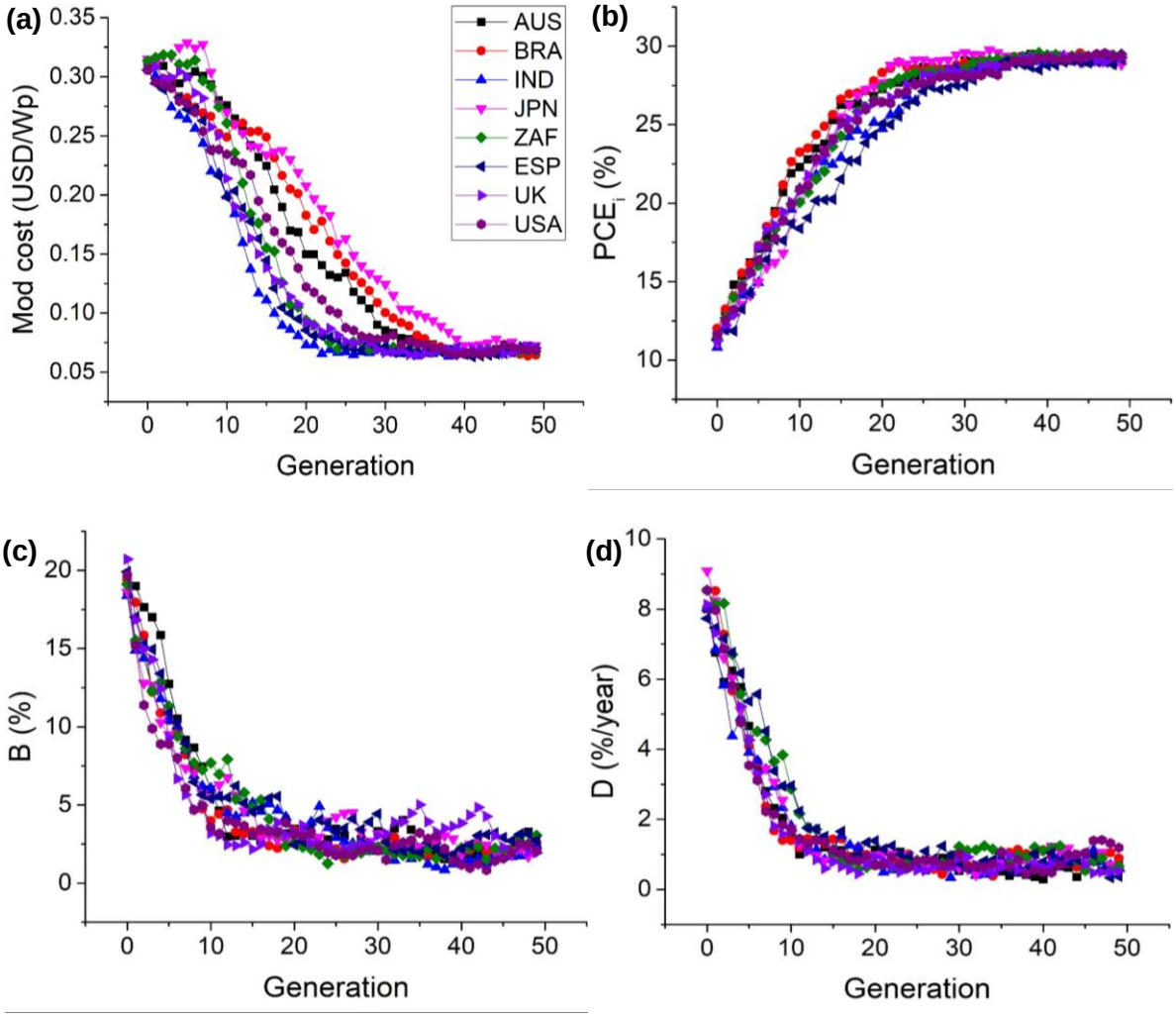

Figure 7.12 Genetic Algorithm Generations

GA average parameter results: (a) module cost, (b) PCE_i, (c) B and (d) D of the 50 generations.

The most notable difference is observed in the module cost parameter, as it is shown that module cost is quickly reduced in India and Spain (low-cost locations), while its reduction is much slower in Japan and Brazil (high-cost locations). This indicates that module cost is a more effective route to lower the objective function (LCOE) in some cases than others. Specifically, those countries with low install costs (e.g. IND) benefit from low module prices as modules represent a larger proportion of the costs than in a country with larger install costs (e.g. JPN). It is noted that this trend is reversed in *PCE* data, with countries having a high install cost showing the greatest rate of change in PCE_i, indicating that PCE_i is a more favourable route to reduce LCOE. This can be understood as the calculation assumes panel is already bought, and therefore LCOE benefits mostly from increases in PCE_i.

By contrast, while there are differences between pairs of countries in the *B* and *D* data, it is noted that the curves change at roughly the same rate. This indicates that impact of degradation on the LCOE is somewhat similar in the cases observed. The difference between these data and those earlier may be due to: 1.The variation in panel replacement year, which is optimised in each case in the GA, which may act to reduce the impact of degradation generally, or 2.Degradation having a higher correlation with LCOE than PCE_i, which leads to an accelerated transition to lower *B* and *D* values regardless of the location. For example, after only 10 generations most locations have *B* values below 5% and *D* values below 2%/year. Although degradation differences between countries are more difficult to highlight, it is however noted that the GA quickly reducing *B* and *D* suggests that improving stability of devices is of utmost importance at all locations to enable commercialisation of emerging PV technologies. Thus, technology improvements should not only focus in efficiency, as the impact of degradation and cost is crucial to determine the viability of new PV technologies at a given location.

7.12 Conclusions

This chapter presents an LCOE analysis that evaluates the potential of Emerging PV technologies in eight different countries. The optimisation strategies are mostly linked with the utility costs of each country, given that install costs have a high correlation with LCOE (~0.80). Low-cost locations are more favoured from reductions in the degradation rate and module cost, whilst high-cost locations are more benefited from improvements in initial efficiency, lower discount rates and reductions in install costs. Also, some improvements in location parameters show greater LCOE reductions depending on the device parameters. For example, devices with low degradation rate are more benefited from DCR reductions than devices with high PCE_i, but devices with increasing PCE_i are more benefited from module cost reductions than devices with decreasing D or B. Ultimately, Emerging PV modules with a good balance of initial efficiency and degradation like the devices here analysed, can deliver competitive LCOE values even in locations like UK with very low PV yield, Japan with very high utility costs, or South Africa with very high DCR. These LCOE values can be reduced even further if they are combined with reductions in the parameters from the previous sections (module cost, DCR and install cost per panel), making OPVs and PVKs a very interesting option in the up-scaling electricity global market. Additionally, it was shown that machine learning methods can be useful to help assessing the feasibility of emerging PV technologies at different locations.

7.13 References

1 Pehl, M., Arvesen, A., Humpenöder, F., Popp, A., Hertwich, E. G. & Luderer, G. (2017). Understanding future emissions from low-carbon power systems by integration of life-cycle assessment and integrated energy modelling. *Nature Energy* 2, 939-945.

2 IRENA Renewable Power Generation Costs in 2019. (2020). https://www.irena.org/publications/2020/Jun/Renewable-Power-Costs-in-2019.

3 Solar Power Europe - Global Market Outlook 2020 - 2024. (2020). https://www.solarpowereurope.org/global-market-outlook-2020-2024/.

4 ISO 3166 - Country Codes. (2021). https://www.iso.org/iso-3166-country-codes.html.

5 IRENA Power Generation Costs. (2019). https://www.irena.org/-/media/Files/IRENA/Agency/Publication/2020/Jun/IRENA_Power_Generation_Costs_2019.pdf.

6 Solar Power Europe - Global Market Outlook 2020-2024. (2020). https://www.solarpowereurope.org/global-market-outlook-2020-2024/.

7 Global Solar Atlas. (2020). https://globalsolaratlas.info/map.

8 ArcGIS Web Application. (2020). https://power.larc.nasa.gov/data-access-viewer/.

9 Renewable energy discount rate survey results. (2018). https://www.grantthornton.co.uk/globalassets/1.-member-firms/united-kingdom/pdf/documents/renewable-energy-discount-rate-survey-results-2018.pdf.

10 Africa renewable energy discount rate survey. (2018). https://www.grantthornton.co.uk/globalassets/1.-member-firms/united-kingdom/pdf/documents/africa-renewable-energy-discount-rate-survey-2018.pdf.

11 The World Bank - Inflation, consumer prices (annual %). (2020). https://data.worldbank.org/indicator/FP.CPI.TOTL.ZG.

12 Cai, M., Wu, Y., Chen, H., Yang, X., Qiang, Y. & Han, L. (2017). Cost-Performance Analysis of Perovskite Solar Modules. *Adv Sci (Weinh)* 4, 1600269.

13 Gambhir, A., Sandwell, P. & Nelson, J. (2016). The future costs of OPV – A bottom-up model of material and manufacturing costs with uncertainty analysis. *Solar Energy Materials and Solar Cells* 156, 49-58.

14 Li, Z., Zhao, Y., Wang, X., Sun, Y., Zhao, Z., Li, Y., Zhou, H. & Chen, Q. (2018). Cost Analysis of Perovskite Tandem Photovoltaics. *Joule* 2, 1559-1572.

15 Mulligan, C. J., Wilson, M., Bryant, G., Vaughan, B., Zhou, X., Belcher, W. J. & Dastoor, P. C. (2014). A projection of commercial-scale organic photovoltaic module costs. *Solar Energy Materials and Solar Cells* 120, 9-17.

16 World's largest BIOPV installation on a roof – France. (2020). https://www.heliatek.com/projects/biopv-la-rochelle/.

17 How India in a short period of time has become the cheapest producer of solar power. (2019). https://economictimes.indiatimes.com/small-biz/productline/power-generation/how-india-in-a-short-period-of-time-has-become-the-cheapest-producer-of-solar-power/articleshow/70325301.cms?from=mdr.

18 Al-Ahmad, A. Y., Almayhi, F., Al-Mudhaffer, M. F., Griffith, M. J., Liu, W., Li, S., Sivunova, K., Elkington, D., Cooling, N. A., Feron, K. *et al.* (2020). A nuanced approach for assessing OPV materials for large scale applications. *Sustainable Energy & Fuels* 4, 940-949.

19 Bella, F., Griffini, G., Correa-Baena, J., Saracco, G., Gratzel, M., Hagfeldt, A., Turri, S. & Gerbaldi, C. (2016). Improving efficiency and stability of perovskite solar cells with photocurable fluoropolymers. *Science* 354, 203-206.

20 Bovill, E., Scarratt, N., Griffin, J., Yi, H., Iraqi, A., Buckley, A. R., Kingsley, J. W. & Lidzey, D. G. (2015). The role of the hole-extraction layer in determining the operational stability of a polycarbazole:fullerene bulk-heterojunction photovoltaic device. *Applied Physics Letters* 106.

21 Bracher, C., Freestone, B. G., Mohamad, D. K., Smith, J. A. & Lidzey, D. G. (2018). Degradation of inverted architecture CH3NH3PbI3-xClx perovskite solar cells due to trapped moisture. *Energy Science & Engineering* 6, 35-46.

22 Burlingame, Q., Huang, X., Liu, X., Jeong, C., Coburn, C. & Forrest, S. R. (2019). Intrinsically stable organic solar cells under high-intensity illumination. *Nature* 573, 394-397.

23 Cheacharoen, R., Mateker, W. R., Zhang, Q., Kan, B., Sarkisian, D., Liu, X., Love, J. A., Wan, X., Chen, Y., Nguyen, T.-Q. *et al.* (2017). Assessing the stability of high performance solution processed small molecule solar cells. *Solar Energy Materials and Solar Cells* 161, 368-376.

24 Chen, W., Wu, Y., Yue, Y., Liu, J., Zhang, W., Yang, X., Chen, H., Bi, E., Ashraful, I., Gratzel, M. *et al.* (2015). Efficient and stable large-area perovskite solar cells with inorganic charge extraction layers. *Science* 350, 944-948.

25 Du, X., Heumueller, T., Gruber, W., Classen, A., Unruh, T., Li, N. & Brabec, C. J. (2019). Efficient Polymer Solar Cells Based on Non-fullerene Acceptors with Potential Device Lifetime Approaching 10 Years. *Joule* 3, 215-226.

26 Gasparini, N., Salvador, M., Strohm, S., Heumueller, T., Levchuk, I., Wadsworth, A., Bannock, J. H., de Mello, J. C., Egelhaaf, H.-J., Baran, D. *et al.* (2017). Burn-in Free Nonfullerene-Based Organic Solar Cells. *Advanced Energy Materials* 7.

27 Grancini, G., Roldan-Carmona, C., Zimmermann, I., Mosconi, E., Lee, X., Martineau, D., Narbey, S., Oswald, F., De Angelis, F., Graetzel, M. *et al.* (2017). One-Year stable perovskite solar cells by 2D/3D interface engineering. *Nat Commun* 8, 15684.

28 Greenbank, W., Djeddaoui, N., Destouesse, E., Lamminaho, J., Prete, M., Boukezzi, L., Ebel, T., Bessissa, L., Rubahn, H.-G., Turkovic, V. *et al.* (2020). Degradation Behavior of Scalable Nonfullerene Organic Solar Cells Assessed by Outdoor and Indoor ISOS Stability Protocols. *Energy Technology*.

29 Heumueller, T., Mateker, W. R., Sachs-Quintana, I. T., Vandewal, K., Bartelt, J. A., Burke, T. M., Ameri, T., Brabec, C. J. & McGehee, M. D. (2014). Reducing burn-in voltage loss in polymer solar cells by increasing the polymer crystallinity. *Energy Environ. Sci.* 7, 2974-2980.

30 Jean, J., Woodhouse, M. & Bulović, V. (2019). Accelerating Photovoltaic Market Entry with Module Replacement. *Joule* 3, 2824-2841.

31 Jiang, Z., Wang, F., Fukuda, K., Karki, A., Huang, W., Yu, K., Yokota, T., Tajima, K., Nguyen, T. Q. & Someya, T. (2020). Highly efficient organic photovoltaics with enhanced stability through the formation of doping-induced stable interfaces. *Proc Natl Acad Sci U S A* 117, 6391-6397.

32 Karpinski, A., Berson, S., Terrisse, H., Mancini-Le Granvalet, M., Guillerez, S., Brohan, L. & Richard-Plouet, M. (2013). Anatase colloidal solutions suitable for inkjet printing: Enhancing lifetime of hybrid organic solar cells. *Solar Energy Materials and Solar Cells* 116, 27-33.

33 Kong, J., Song, S., Yoo, M., Lee, G. Y., Kwon, O., Park, J. K., Back, H., Kim, G., Lee, S. H., Suh, H. *et al.* (2014). Long-term stable polymer solar cells with significantly reduced burn-in loss. *Nat Commun* 5, 5688.

34 Lee, J. W., Dai, Z., Han, T. H., Choi, C., Chang, S. Y., Lee, S. J., De Marco, N., Zhao, H., Sun, P., Huang, Y. *et al.* (2018). 2D perovskite stabilized phase-pure formamidinium perovskite solar cells. *Nat Commun* 9, 3021.

35 Leijtens, T., Eperon, G. E., Pathak, S., Abate, A., Lee, M. M. & Snaith, H. J. (2013). Overcoming ultraviolet light instability of sensitized TiO(2) with meso-superstructured organometal tri-halide perovskite solar cells. *Nat Commun* 4, 2885.

36 Liang, C., Zhao, D., Li, P., Wu, B., Gu, H., Zhang, J., Goh, T. W., Chen, S., Chen, Y., Sha, Z. *et al.* (2019). Simultaneously boost diffusion length and stability of perovskite for high performance solar cells. *Nano Energy* 59, 721-729.

37 Lv, Y., Zhang, H., Liu, R., Sun, Y. & Huang, W. (2020). Composite Encapsulation Enabled Superior Comprehensive Stability of Perovskite Solar Cells. *ACS Appl Mater Interfaces* 12, 27277-27285.

38 Mateker, W. R., Sachs-Quintana, I. T., Burkhard, G. F., Cheacharoen, R. & McGehee, M. D. (2015). Minimal Long-Term Intrinsic Degradation Observed in a Polymer Solar Cell Illuminated in an Oxygen-Free Environment. *Chemistry of Materials* 27, 404-407.

39 Mei, A., Li, X., Liu, L., Ku, Z., Liu, T., Rong, Y., Xu, M., Hu, M., Chen, J., Yang, Y. *et al.* (2014). A hole-conductor-free, fully printable mesoscopic perovskite solar cell with high stability. *Science* 345, 295-298.

40 Oh, H., Sim, H. B., Han, S. H., Kwon, Y. J., Park, J. H., Kim, M. H., Kim, J. Y., Kim, W. S. & Kim, K. (2019). Reducing Burn-In Loss of Organic Photovoltaics by a Robust Electron-Transporting Layer. *Advanced Materials Interfaces* 6.

41 Pearson, A. J., Hopkinson, P. E., Couderc, E., Domanski, K., Abdi-Jalebi, M. & Greenham, N. C. (2016). Critical light instability in CB/DIO processed PBDTTT-EFT:PC 71 BM organic photovoltaic devices. *Organic Electronics* 30, 225-236.

42 Roesch, R., Eberhardt, K.-R., Engmann, S., Gobsch, G. & Hoppe, H. (2013). Polymer solar cells with enhanced lifetime by improved electrode stability and sealing. *Solar Energy Materials and Solar Cells* 117, 59-66.

43 Roose, B., Johansen, C. M., Dupraz, K., Jaouen, T., Aebi, P., Steiner, U. & Abate, A. (2018). A Ga-doped SnO2 mesoporous contact for UV stable highly efficient perovskite solar cells. *Journal of Materials Chemistry A* 6, 1850-1857.

44 Sapkota, S. B., Spies, A., Zimmermann, B., Dürr, I. & Würfel, U. (2014). Promising long-term stability of encapsulated ITO-free bulk-heterojunction organic solar cells under different aging conditions. *Solar Energy Materials and Solar Cells* 130, 144-150.

45 Sung, Y.-M., Huang, Y.-C., Chien, F. S.-S. & Tsao, C.-S. (2019). Mechanism and Analysis of Thermal Burn-In Degradation of OPVs Induced by Evaporated HTL. *IEEE Journal of Photovoltaics* 9, 694-699.

46 Tan, H., Jain, A., Voznyy, O., Lan, X., Garcia de Arquer, F. P., Fan, J. Z., Quintero-Bermudez, R., Yuan, M., Zhang, B., Zhao, Y. *et al.* (2017). Efficient and stable solution-processed planar perovskite solar cells via contact passivation. *Science* 355, 722-726.

47 Tsai, H., Nie, W., Blancon, J. C., Stoumpos, C. C., Asadpour, R., Harutyunyan, B., Neukirch, A. J., Verduzco, R., Crochet, J. J., Tretiak, S. *et al.* (2016). High-efficiency two-dimensional Ruddlesden-Popper perovskite solar cells. *Nature* 536, 312-316.

48 Tumen-Ulzii, G., Qin, C., Klotz, D., Leyden, M. R., Wang, P., Auffray, M., Fujihara, T., Matsushima, T., Lee, J. W., Lee, S. J. *et al.* (2020). Detrimental Effect of Unreacted PbI2 on the Long-Term Stability of Perovskite Solar Cells. *Adv Mater* 32, e1905035.

49 Turren-Cruz, S.-H., Hagfeldt, A. & Saliba, M. (2018). Methylammonium-free, high-performance, and stable perovskite solar cells on a planar architecture. *Science* 362, 449-453.

50 Voroshazi, E., Cardinaletti, I., Conard, T. & Rand, B. P. (2014). Light-Induced Degradation of Polymer:Fullerene Photovoltaic Devices: An Intrinsic or Material-Dependent Failure Mechanism? *Advanced Energy Materials* 4.

51 Wang, Z., Lin, Q., Chmiel, F. P., Sakai, N., Herz, L. M. & Snaith, H. J. (2017). Efficient ambient-air-stable solar cells with 2D–3D heterostructured butylammonium-caesium-formamidinium lead halide perovskites. *Nature Energy* 2.

52 Wang, Z., McMeekin, D. P., Sakai, N., van Reenen, S., Wojciechowski, K., Patel, J. B., Johnston, M. B. & Snaith, H. J. (2017). Efficient and Air-Stable Mixed-Cation Lead Mixed-Halide Perovskite Solar Cells with n-Doped Organic Electron Extraction Layers. *Adv Mater* 29.

53 Wong-Stringer, M., Game, O. S., Smith, J. A., Routledge, T. J., Alqurashy, B. A., Freestone, B. G., Parnell, A. J., Vaenas, N., Kumar, V., Alawad, M. O. A. *et al.* (2018). High-Performance Multilayer Encapsulation for Perovskite Photovoltaics. *Advanced Energy Materials* 8.

54 Xie, J., Arivazhagan, V., Xiao, K., Yan, K., Yang, Z., Qiang, Y., Hang, P., Li, G., Cui, C., Yu, X. *et al.* (2018). A ternary organic electron transport layer for efficient and

photostable perovskite solar cells under full spectrum illumination. *Journal of Materials Chemistry A* 6, 5566-5573.

55 Xu, X., Xiao, J., Zhang, G., Wei, L., Jiao, X., Yip, H.-L. & Cao, Y. (2020). Interface-enhanced organic solar cells with extrapolated T80 lifetimes of over 20 years. *Science Bulletin* 65, 208-216.

56 Yang, X.-Y., Niu, M.-S., Qin, C., Bi, P.-Q., Chen, Z.-H., Feng, L., Liu, J.-Q. & Hao, X.-T. (2019). Unraveling the unstable amorphous phase evolution effect on burn-in loss in polymer-fullerene solar cells. *Organic Electronics* 71, 156-163.

57 Zhang, Y., Bovill, E., Kingsley, J., Buckley, A. R., Yi, H., Iraqi, A., Wang, T. & Lidzey, D. G. (2016). PCDTBT based solar cells: one year of operation under real-world conditions. *Sci Rep* 6, 21632.

58 Zhang, Y., Yi, H., Iraqi, A., Kingsley, J., Buckley, A., Wang, T. & Lidzey, D. G. (2017). Comparative indoor and outdoor stability measurements of polymer based solar cells. *Sci Rep* 7, 1305.

59 Zheng, X., Hou, Y., Bao, C., Yin, J., Yuan, F., Huang, Z., Song, K., Liu, J., Troughton, J., Gasparini, N. *et al.* (2020). Managing grains and interfaces via ligand anchoring enables 22.3%-efficiency inverted perovskite solar cells. *Nature Energy* 5, 131-140.

60 Section IO - The Basics of Genetic Algorithms in Machine Learning. (2021). https://www.section.io/engineering-education/the-basics-of-genetic-algorithms-in-ml/.

CHAPTER 8
CONCLUSIONS

8.1 Conclusions

Emerging PV technologies such as OPVs and PVKs have the potential to disrupt the PV market due to their ease of fabrication (compatible with cheap roll-to-roll processing) and installation, as well as their significant efficiency improvements over the last few years. However, rapid degradation is still an issue present in many emerging PV devices, and it must be addressed so these new solar harvesting technologies can become widely commercialised. This thesis focused on showing an OPV lifetime enhancing technique by adding the insulating polymer PMMA to the active layer, and quantifying the impact of degradation (alongside efficiency and cost) upon LCOE in real world emerging PV installations. A summary of the main conclusions is presented below.

The effectiveness of an ISOS-D-1 lifetime enhancing technique was studied by varying the concentration (wt%) and molecular weight (M_W) of PMMA added as a ternary component in P3HT:$PC_{61}BM$ OPVs. It was found that either increasing the wt% or M_W of PMMA lead to larger PMMA-rich domains. This resulted in a total higher volume of isolated PMMA, which provided increased protection against water vapour, which would otherwise cause increased trapping and charge recombination, and thus effect J_{SC} and *FF*. However, these parameters had a slower degradation when PMMA wt% or M_W was increased. These findings suggested that large, widely spread PMMA-rich zones are most effective at extending OPV lifetime, thus providing design criteria for future ternary OPV devices.

The efficacy of the ternary PMMA technique was also tested on a different OPV system consisting of PTB7:$PC_{71}BM$, but the results were not as good as those achieved by P3HT:$PC_{61}BM$ OPVs. For example, the improvements in lifetime were as high as a factor of 2 without significantly effecting the initial efficiency of P3HT-based devices, while a lesser factor of 1.3 and an initial *PCE* drop of >50% was observed for PTB7-based devices. The morphology was discarded as the cause of the differences in initial performance and lifetime behaviour, because adding PMMA to PTB7-based

OPVs resulted in the appearance of domed regions which grew in size when the PMMA M_W was raised, similar to what was observed in P3HT-based devices. One significant difference between the initial set of PTB7-based and P3HT-based devices was the use of the additive DIO in the former. The addition of DIO has been proven to cause increased photo-bleaching and shortened the lifetime of the PTB7-based devices. When further PTB7-based OPVs were fabricated without DIO, the lifetime enhancement by PMMA was again observed, although not to the same extent that it was observed in P3HT-based OPVs. By analysing the gathered evidence from this and other studies, it was hypothesised that the compatibility between PMMA and the donor polymer is the reason why adding the inert polymer is more effective in some blend systems than in others, preferring crystalline polymers (P3HT) over amorphous polymers (PTB7).

While integrating PMMA as a ternary component can boost lifetime in a variety of donor:acceptor systems, its efficacy varied and was negatively impacted by the use of the processing additive DIO. An ethanol washing treatment was used in an attempt to remove the negative lifetime impact of DIO, but was not successful, as it had no clear effect in the morphology, initial efficiency, degradation or absorption of the OPVs. It was thus concluded that removing residual DIO is very difficult and may require more complex techniques than washing the active layer with ethanol, at least for the combination of blend films, additives and processing conditions considered in this thesis.

To quantify the impact of emerging PV degradation upon LCOE in real world installations, a novel model was developed taking into account realistic degradation profile sourced from an eight-year (Jan 2013 - Dec 2020) literature review of state-of-the-art OPV and PVK devices. Further, the competitiveness of these emerging PV devices were assessed for a realistic grid-scale PV installation of 5.5 MWp in the case study location (Fiji), which was chosen due to its high insolation values, interest in adding PV capacity and availability of data required as input for the model. It was found that optimal strategies to improve LCOE depend on the present characteristics of a device (i.e. initial efficiency, burn-in, degradation rate and module cost). For example, a 7.5% PCE_i module with low module cost of 0.12 USD/Wp provides the same LCOE that achieves a 25% PCE_i module with high module cost of 0.75 USD/Wp, but only the latter would be greatly benefited with further module cost reductions.

The LCOE model results also showed that panels with a good balance of efficiency and degradation were in many cases better than panels with higher PCE_i but higher degradation as well, demonstrating that to provide quantitative suggestions on how to minimise the LCOE of new PV technologies, a holistic approach including degradation and costs must be considered, and not only the initial efficiency (current focus of many studies). LCOE results of specific OPV and PVK devices also suggested that these technologies can compete on wholesale electricity markets if cell-level parameters can be scaled up to module-level.

The environmental impact of emerging PV panels was also briefly analysed. It was shown that emerging PV devices have the potential to compete with the embodied carbon values of Si PV, despite most emerging PV installations currently require larger areas and panel replacements due to their lower efficiencies and higher degradation rates. However, the embodied carbon values provided by Si PV were beaten by the champion OPV and PVK devices, showing that future PV installations may result in the reduction of thousands of tonnes of CO_2 equivalent emissions per 20-year project if modules can mimic the cell characteristics.

Finally, an LCOE analysis was carried out for eight countries all around the world to cover a range of economies and insolation levels, and evaluate the potential of emerging PV in each place. The optimisation strategies were mostly linked with the utility costs of each country, given that total install costs had a high correlation with LCOE (~0.80). Average, champion and specific state-of-the-art OPVs & PVKs LCOE results showed that technological improvements effect different countries to different degrees, e.g., Installations in India are less sensitive to changes in PCE_i than in Japan. In general, it was found that low-cost locations were more favoured from reductions in the degradation rate and module cost, whilst high-cost locations were more benefited from improvements in initial efficiency, lower discount rates and reductions in install costs. For example, if shelf life improvement by factor 2 from Chapter 4 P3HT:PC_{61}BM:PMMA OPVs can be kept in operational lifetime of Chapter 6-7 standard emerging PV (PCE_i=10%, B=40%, D=10%/year to D=5%/year), while reducing module cost (e.g., from 0.245 to 0.1225 USD/Wp) due to PMMA reducing active material requirements, different levels of alone efficiency improvement would be required to match the resultant LCOE depending on the location. India would require improving PCE_i to ~21.3%, whereas Japan would only require improving PCE_i

to ~13.7%. These findings showed that locations had different ideal optimisation strategies, and that tuning parameters of future commercial emerging PV panels may be necessary to achieve the lowest possible LCOE of a given location.

8.2 Future research suggestions

Emerging PV is currently an exciting field of research and there are many aspects that can be studied and improved to accelerate its commercialisation. Two future work suggestions are presented below:

Ternary OPVs by adding insulating polymers to devices with Non-Fullerene Acceptors (NFAs)

The discovery of the non-fullerene acceptor (NFA) material, ITIC in 2015 was a breakthrough in the OPV field and has allowed a rapid increase in device efficiency over the last few years.[1] However, recent review articles have focused in highlighting the importance of reducing degradation, as NFA OPVs instability is one of the major barriers to their commercialisation.[2-4] These reviews show that degradation arising from oxygen, irradiation and interfaces has been tried to be reduced by different strategies, such as molecule design and passivation of interlayers. However, stability improvements have not been enough to reach commercial levels. Therefore, using a ternary approach like the one described in Chapter 4 of this thesis could be an interesting option to improve the lifetime of NFA OPVs. Previous findings such as insulating polymer (PMMA) large domains and compatibility with crystalline polymers should be considered, but experiments could be taken further by for example, pushing PMMA amount to a maximum limit without losing its benefits and encapsulating the devices for accelerated aging tests. Combining the effects of the PMMA method with other literature strategies may result in NFA OPV devices with a lifetime long enough to be considered for real life applications.

LCOE assessment with updated costs for building integrated applications

LCOE models are becoming more popular as a technique for demonstrating both the commercial benefits and the issues that new PV devices face. Previous models[5-8] have been used to assess the impacts of module efficiency, manufacturing processes and panel replacements, although none of them have considered the complex degradation behaviour of emerging PV. Unlike those models, the LCOE model developed in Chapter 5 did consider realistic degradation characteristic of emerging PV devices, and was useful to quantify the economic and environmental impact of emerging PV parameters (Chapter 6) as well as to identify ideal optimisation strategies depending on the location (Chapter 7). However, this model can still be updated and applied in different applications. For example, researchers and industry partnering can lead to the development of novel materials and more efficient processing, thus impacting the manufacturing and installations costs of emerging PV. These inputs could be applied in the LCOE model not only for typical ground-mounted or roof installations, but also for more rare applications like building integrated panels. Updating the model with more specific cost information could result in LCOE analysis demonstrating the feasibility of emerging PV in certain building integrated applications where a higher degradation and lower efficiency than Si PV is acceptable, as long as panels are cheap, flexible and easily installed. Ultimately, publishing well-validated results in the right channels may attract the attention of investors and accelerate the commercialisation of emerging PV, even if only at niche markets.

8.3 References

1 Ossila Non-Fullerene Acceptors. (2021). https://www.ossila.com/collections/non-fullerene-acceptors.

2 Li, Y., Li, T. & Lin, Y. (2021). Stability: next focus in organic solar cells based on non-fullerene acceptors. *Materials Chemistry Frontiers* 5, 2907-2930.

3 Speller, E. M., Clarke, A. J., Luke, J., Lee, H. K. H., Durrant, J. R., Li, N., Wang, T., Wong, H. C., Kim, J.-S., Tsoi, W. C. *et al.* (2019). From fullerene acceptors to non-fullerene acceptors: prospects and challenges in the stability of organic solar cells. *Journal of Materials Chemistry A* 7, 23361-23377.

4 Yan, C., Barlow, S., Wang, Z., Yan, H., Jen, A. K. Y., Marder, S. R. & Zhan, X. (2018). Non-fullerene acceptors for organic solar cells. *Nature Reviews Materials* 3, 18003.

5 Guo, J. & Min, J. (2019). A Cost Analysis of Fully Solution-Processed ITO-Free Organic Solar Modules. *Advanced Energy Materials* 9.

6 Jean, J., Woodhouse, M. & Bulović, V. (2019). Accelerating Photovoltaic Market Entry with Module Replacement. *Joule* 3, 2824-2841.

7 Li, Z., Zhao, Y., Wang, X., Sun, Y., Zhao, Z., Li, Y., Zhou, H. & Chen, Q. (2018). Cost Analysis of Perovskite Tandem Photovoltaics. *Joule* 2, 1559-1572.

8 Song, Z., McElvany, C. L., Phillips, A. B., Celik, I., Krantz, P. W., Watthage, S. C., Liyanage, G. K., Apul, D. & Heben, M. J. (2017). A technoeconomic analysis of perovskite solar module manufacturing with low-cost materials and techniques. *Energy & Environmental Science* 10, 1297-1305.

Appendix A

LCOE base case location (Fiji) - Additional figures

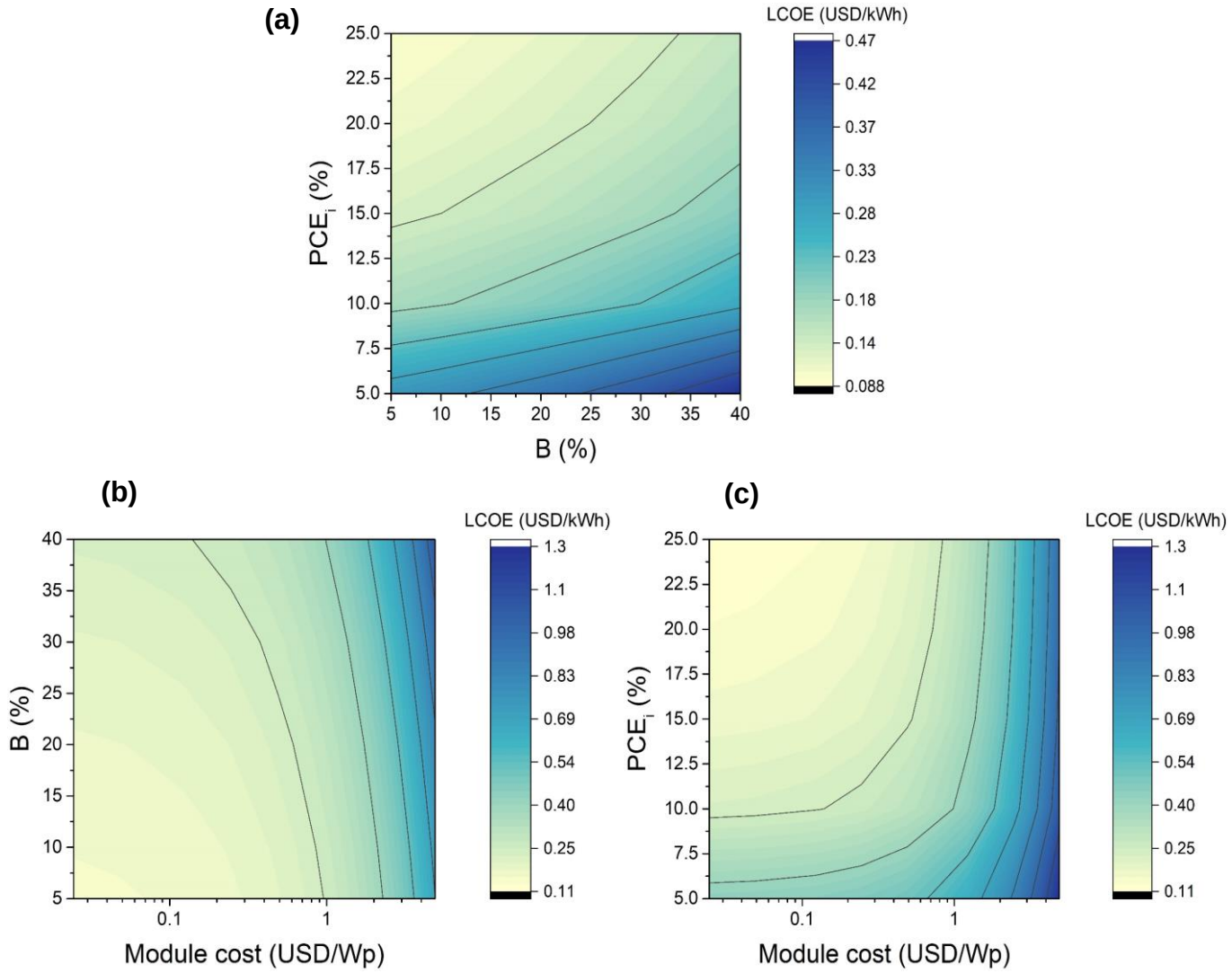

Figure A1 Contour plots of predicted LCOE as a function of (a) initial efficiency, PCE_i and burn-in, B assuming module cost 0.245 USD/Wp; (b) Module cost and B assuming PCE_i = 10%; (c) PCE_i and module cost assuming B = 40%. In all cases D = 2%/year is assumed with no panel replacement in 20-year project.

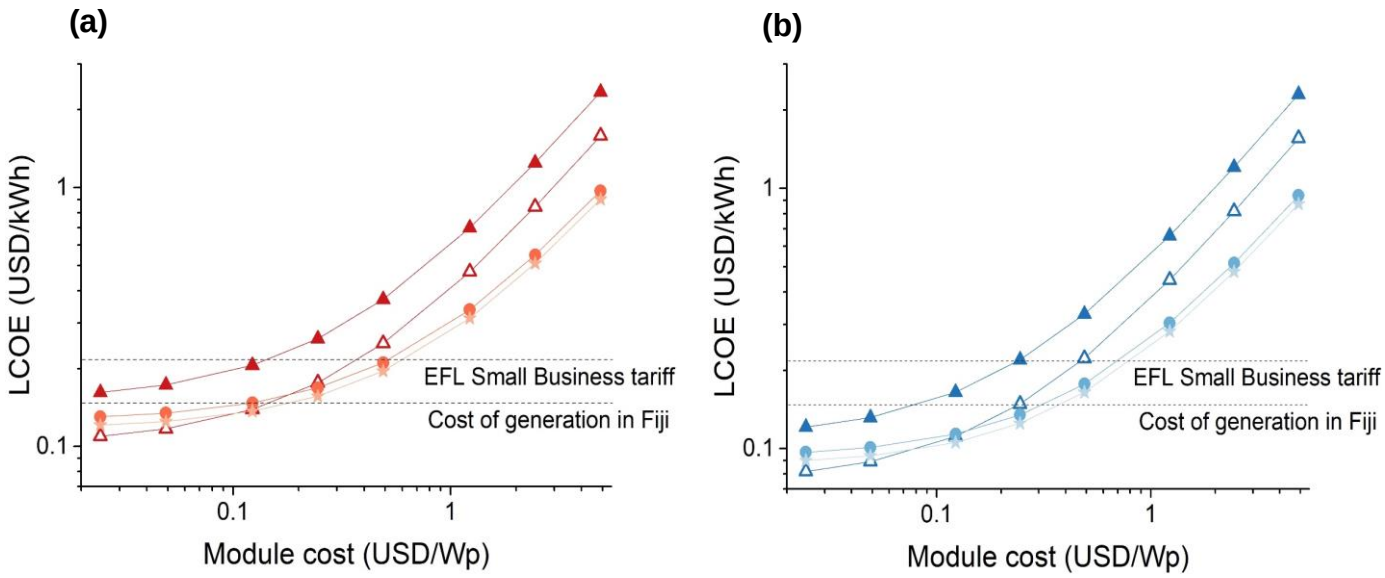

Figure A2 Predictions of LCOE as a function of module cost for panels with (a) PCE_i = 20% and (b) 30% assuming burn-in B = 40% (closed) or 10% (open), with D = 10%/year (triangles), 2%/year (circles) and 1%/year (stars). Panels with D = 10%/year are replaced every 5 years, and the remaining have no panel replacement in 20-year project.

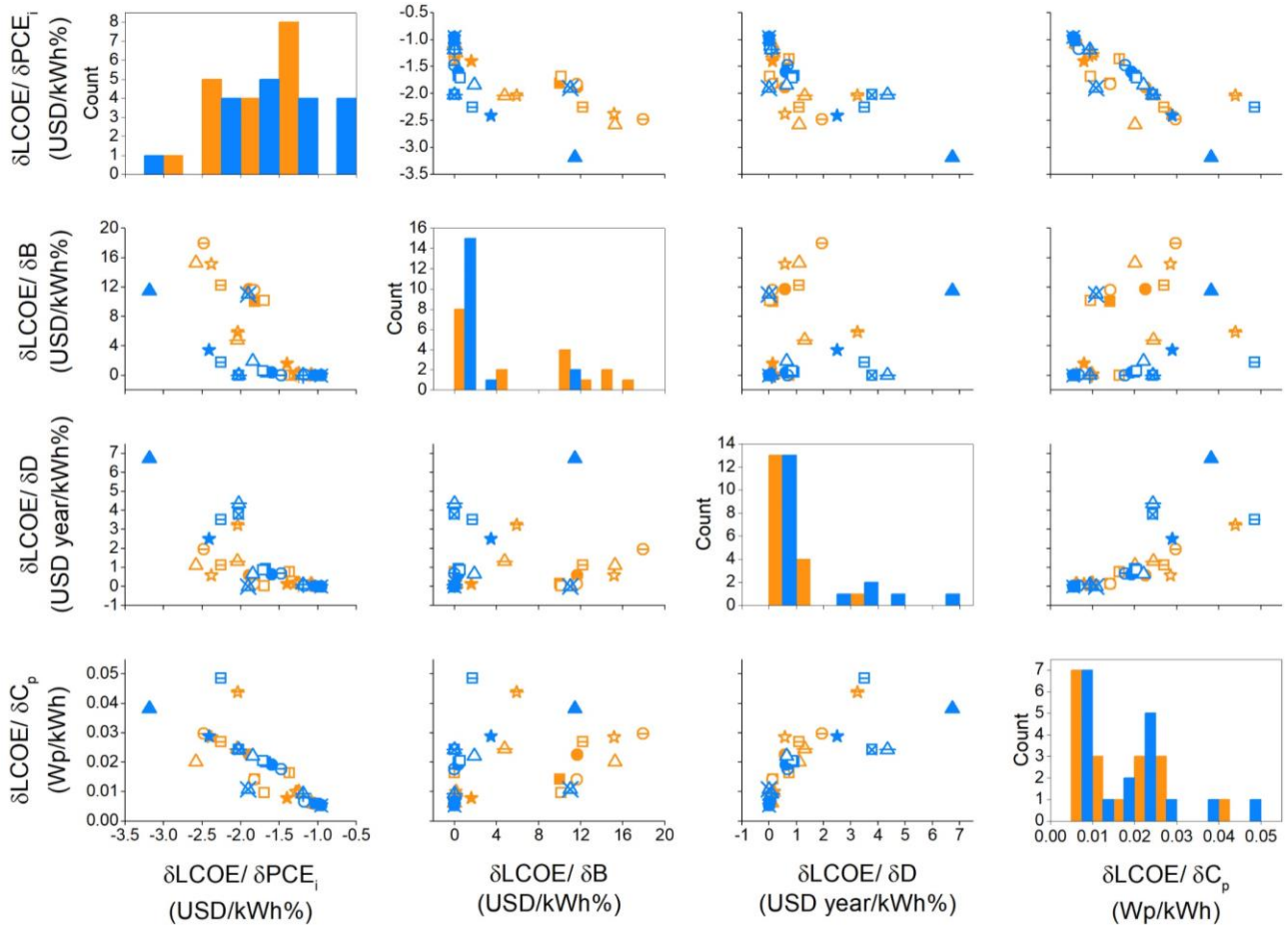

Figure A3 Pair-wise scatter plots and histograms of partial derivatives of LCOE with respect to PCE_i, burn-in (B), degradation rate (D) and module cost (C_p) for OPV (orange) and PVK (blue) light-soaked devices.

Appendix B

Location-specific LCOE - Additional information

Table B1 Location parameters individual values.

Location	PV Yield max[1]	PV Yield avg location[1]	Peak sun hours max[2]	Peak sun hours avg location[2]	Basecase Utility-scale Silicon PV Total Installation Cost (USD/kW)[3]	Basecase Utility-scale Emerging PV Total Installation Cost (USD/kW)[3]	Module cost Silicon PV (USD/kW)[3]	Module cost Emerging PV (USD/kW)[4-7]
USA	1997	1558	2049	1710	1221	1107	358	245
Japan	1512	1223	1419	1346	2070	1864	451	
India	1886	1568	2022	1842	618	585	278	
South Africa	2074	1826	2241	1994	1321	1009	557	
Brazil	1886	1562	2166	1829	1255	1194	306	
Spain	1788	1568	1773	1649	800	685	360	
UK	1119	913	1189	976	1018	900	362	
Australia	1978	1802	2341	2010	1236	1187	294	

Location	Install cost per panel Silicon PV (exc. panels)[3]	Install cost per panel Emerging PV (exc. panels)[3]	Inverter cost (USD/kW)[3]	DCR (%)[8,9]	Inflation rate (%)[10]	Emerging PV LCOE max yield (USD/kWh)	Silicon PV LCOE max yield (USD/kWh)	Emerging PV LCOE avg yield (USD/kWh)	Silicon PV LCOE avg yield (USD/kWh)
USA	353.83	353.62	68.4	6.5	1.8	0.3014	0.0690	0.3833	0.0885
Japan	663.79	663.82	223.7	4	0.5	0.5516	0.1250	0.6793	0.1545
India	139.40	139.56	44.4	9	7.7	0.2298	0.0589	0.2777	0.0715
South Africa	313.24	313.24	89.8	11.5	4.1	0.3325	0.0987	0.3755	0.1118
Brazil	389.09	389.24	71.2	9	3.7	0.3869	0.0903	0.4622	0.1088
Spain	180.40	180.58	57.4	5.5	0.7	0.2094	0.0499	0.2376	0.0569
UK	268.96	268.69	54.8	5.75	1.7	0.4228	0.1004	0.5111	0.1230
Australia	386.22	386.21	62.5	5.75	1.6	0.3092	0.0669	0.3356	0.0733

Table B2 LCOE and project costs of India with higher install cost per panel (same as JPN).

PCEi	D	B	LCOE (USD/kWh)	Module cost (USD/Wp)	Panel cost, USD	Install cost per panel (exc. panels)	Project price exc. panels, USD	Project price with these panels, USD	NPV Total Costs, USD	NPV Total Generation, kWh
10	10	40	0.8477	0.245	1,345,656	748.25	21,480,875	22,826,532	33,271,791	39,250,128
20	10	40	0.4872				10,740,438	12,086,094	19,124,279	39,250,128
10	10	10	0.5700				21,480,875	22,826,532	33,271,791	58,369,576
10	1	40	0.5507				21,480,875	22,826,532	25,381,915	46,093,522

Table B3 LCOE and project costs of Japan with lower install cost per panel (same as IND).

PCEi	D	B	LCOE (USD/kWh)	Module cost (USD/Wp)	Panel cost, USD	Install cost per panel (exc. panels)	Project price exc. panels, USD	Project price with these panels, USD	NPV Total Costs, USD	NPV Total Generation, kWh
10	10	40	0.2681	0.245	1,345,656	152.93	4,390,338	5,735,994	11,945,441	44,563,428
20	10	40	0.1964				2,195,169	3,540,825	8,753,585	44,563,428
10	10	10	0.1806				4,390,338	5,735,994	11,945,441	66,132,898
10	1	40	0.1543				4,390,338	5,735,994	7,950,019	51,536,644

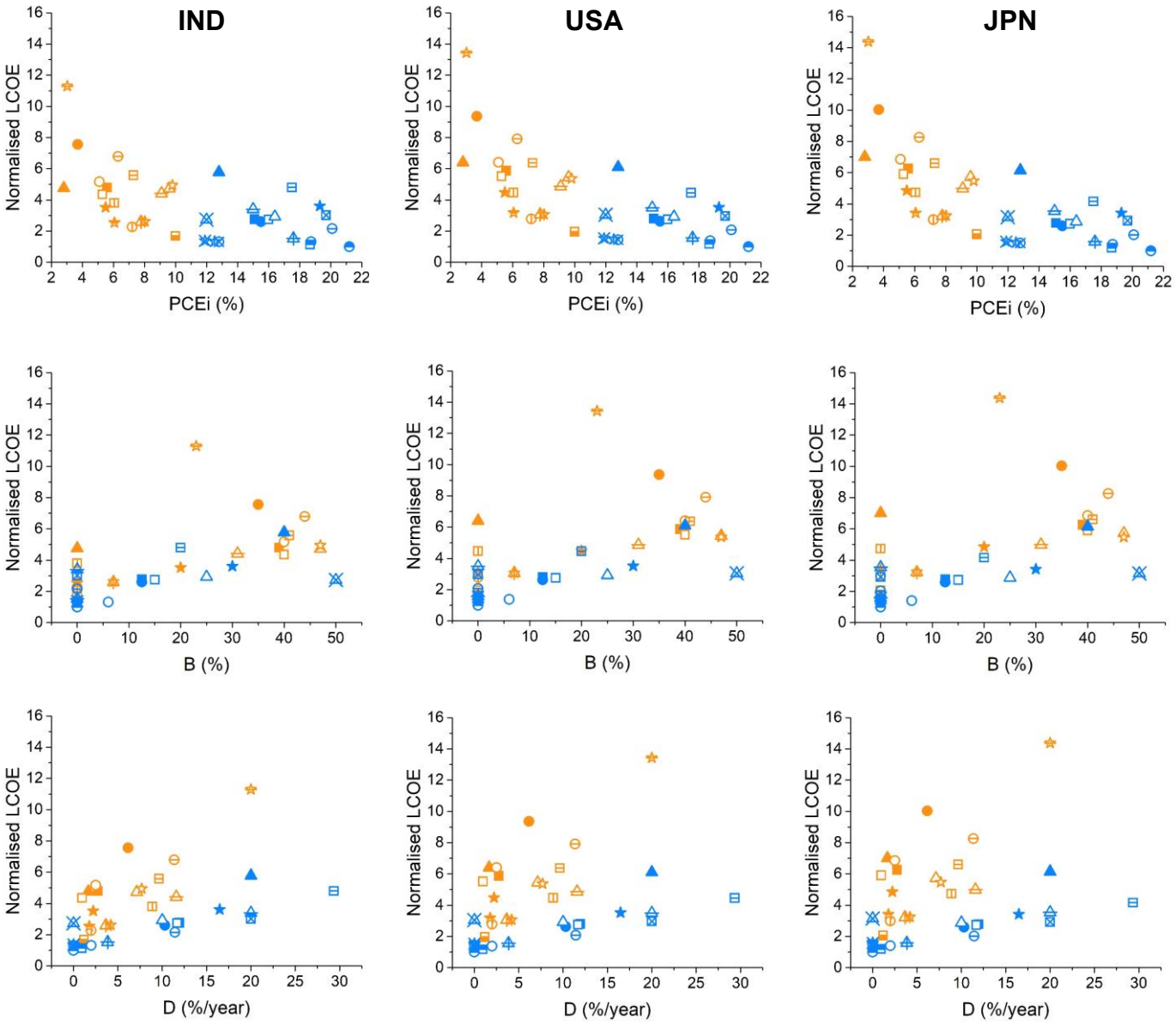

Figure B1 Normalised LCOE for *specific* state-of-the-art OPVs and PVKs

LCOE normalised to the lowest value of each location for OPV (orange) and PVK (blue) modules with parameters extracted from degradation measurements shown as a function of (1st row) PCE_i, (2nd row) B, and (3rd row) D for (1st column) India, (2nd column) USA, and (3rd column) Japan. Each symbol represents a unique device, the materials and architecture for which is listed in Table 6.1 of Chapter 6.

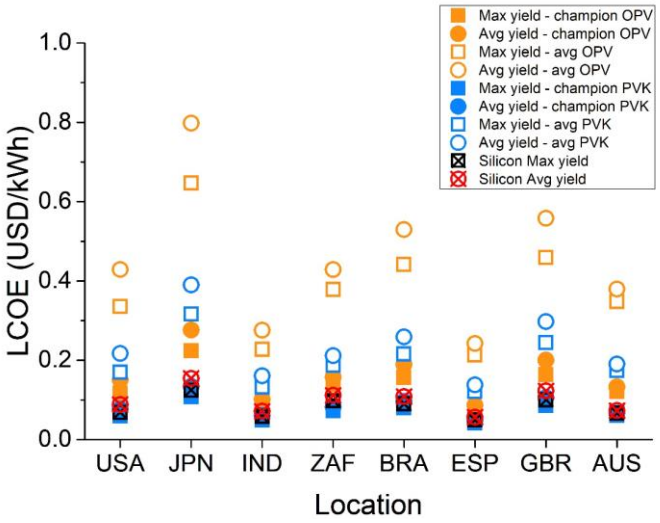

Figure B2 Location specific OPVs, PVKs and Si PV LCOE

Champion (closed symbols) and average (open symbols) OPV (orange) and PVK (blue) devices LCOE compared with Si PV (crossed symbols) LCOE of maximum (squares) and average (circles) yield locations within USA (United States of America), JPN (Japan), IND (India), ZAF (South Africa), BRA (Brazil), ESP (Spain), GBR (United Kingdom) and AUS (Australia).

Appendix B References

1 Global Solar Atlas. (2020). https://globalsolaratlas.info/map.

2 ArcGIS Web Application. (2020). https://power.larc.nasa.gov/data-access-viewer/.

3 IRENA Power Generation Costs. (2019). https://www.irena.org/-/media/Files/IRENA/Agency/Publication/2020/Jun/IRENA_Power_Generation_Costs_2019.pdf.

4 Cai, M., Wu, Y., Chen, H., Yang, X., Qiang, Y. & Han, L. (2017). Cost-Performance Analysis of Perovskite Solar Modules. *Adv Sci (Weinh)* 4, 1600269.

5 Gambhir, A., Sandwell, P. & Nelson, J. (2016). The future costs of OPV – A bottom-up model of material and manufacturing costs with uncertainty analysis. *Solar Energy Materials and Solar Cells* 156, 49-58.

6 Li, Z., Zhao, Y., Wang, X., Sun, Y., Zhao, Z., Li, Y., Zhou, H. & Chen, Q. (2018). Cost Analysis of Perovskite Tandem Photovoltaics. *Joule* 2, 1559-1572.

7 Mulligan, C. J., Wilson, M., Bryant, G., Vaughan, B., Zhou, X., Belcher, W. J. & Dastoor, P. C. (2014). A projection of commercial-scale organic photovoltaic module costs. *Solar Energy Materials and Solar Cells* 120, 9-17.

8 Renewable energy discount rate survey results. (2018). https://www.grantthornton.co.uk/globalassets/1.-member-firms/united-kingdom/pdf/documents/renewable-energy-discount-rate-survey-results-2018.pdf.

9 Africa renewable energy discount rate survey. (2018). https://www.grantthornton.co.uk/globalassets/1.-member-firms/united-kingdom/pdf/documents/africa-renewable-energy-discount-rate-survey-2018.pdf.

10 The World Bank - Inflation, consumer prices (annual %). (2020). https://data.worldbank.org/indicator/FP.CPI.TOTL.ZG.